MUNI
FACULTY
OF MEDICINE

Mass spectrometry in bioanalytical and clinical applications

Habilitation thesis

by

Ondřej Peš

2022

This page is intentionally left blank

All likelihood-based models are Bayesian models in which the prior distribution is an appropriately selected uniform prior, and as the size of the data gets large they are identical given any finite appropriate prior. So such empirical researchers are really Bayesian; they just do not know it yet.

— Jeff Gill and Christopher Witko

This page is intentionally left blank

Originality and conflict of interest statement

The author performed the original research presented in the habilitation thesis in cooperation with his colleagues, students, and members of the cooperating research groups; all of them are appropriately quoted as coauthors of the manuscripts. Funding of the research was supported by the following projects:

I hereby declare that I have no conflict of interest.

Preface

This cumulative habilitation thesis consists of 9 original and 2 review articles published in years 2008–2020 and focuses on the development and applications of mass spectrometry techniques in bioanalytical, medicinal, and clinical chemistry. The entire thesis has been thematically divided into three parts, as follows.

1. **Mass spectrometry hyphenated via an offline interface**

   Many fields of chemistry, biology, or medicine usually require more than a simple approach in observing critical processes and inferring specific conclusions. Usually, mass spectrometry on its own is not capable of providing answers to complex questions. It is thus beneficial to employ different platform setups to achieve a maximum gain of information entropy.

2. **Mass spectrometry as a tool in identification and characterization**

   Unambiguous identification of a compound belongs to tasks, which have been haunting chemists for centuries. Any chemical compound may be essentially classified as a known unknown (its structure has already been *de novo* elucidated) or an unknown unknown (no records exist about the structure). Mass spectrometry is a compelling and still readily available technique capable of identifying and characterizing chemical substances, provided they might be ionized. Fragmentation techniques and different types of detection may orthogonal information, leading to minimizing ambiguity in the compound's identity.

3. **Mass spectrometry as a sensitive and specific detector**

   Recent developments in mass spectrometry allow detection of very low amounts while keeping very high specificity. Theoretical limits of common and abundant mass spectrometric detectors (under optimal conditions) are as low as a few femtograms in a single injection. Additional coupling with a separation technique may enhance the limits even further. Hence, it is reasonable to exploit such a feature in quantitative research, especially when sensitivity and specificity of other methods applied so far may have been reaching their limits.

Acknowledgments

I would like to thank all my colleagues, students, and others involved in my research career. The presented thesis would never have existed without their support and encouragement. Mainly, I would like to express my gratitude to the following people (in alphabetical order):

Mirka Bittová, Jiří Dostál, Pavla Foltynová, Jana Gregorová, Martina Hanousková, Jan Juřica, Viktor Kanický, Katarína Kostolanská, Michaela Králíková, Pavel Krásenský, Lenka Kubinyiová, Josef Kučera, Adam Midlik, Miriam Minaříková, Lenka Nerudová, Lucie Novotná, Hana Paulová, Jan Preisler, Jan Přikryl, Jiří Schlaghamerský, Kristýna Šebrlová, Lucie Šimoníková, Jiří Slanina, Pavel Šmak, Jindra Smutná, Eva Táborská, Petr Táborský, Tomáš Vaculovič, Tomáš Vašina, Michaela Vašinová-Galiová, Ondřej Zendulka

I would like to thank my family as well.

Contents

1 Introduction

Originally, mass spectrometry (MS) was developed to measure atom masses, and its first scientific contribution was to demonstrate the existence of isotopes. At that time, MS was anticipated to fade from science when all isotopes were discovered. Fortunately, petroleum chemists in the 1940s were using MS to measure small hydrocarbons, and in the 1960s, the complex fragmentation processes were studied and a range of possible applications was apprehended. Currently, mass spectrometry has been with scientists for more than a hundred years although it was doomed several times since its inception.

The discoverer of MS, Sir Joseph John Thomson, made the discovery involuntarily while studying a phenomenon of cathode rays. Over 50 years, the cathode rays were continuously debated whether they were made of particles or waves. Those who believed in particles reasoned that their mass should be evidenced. With his laboratory assistant Ebenezer Everett, Thomson first measured the charge-to-mass ratio (e/m) of the cathodic rays – electrons in 1897, for which Thomson received the 1906 Nobel Prize.[1] Ultimately, Thomson, with Francis Aston's help, built the first mass spectrometer to measure masses of charged particles by deflecting them using electric and magnetic fields onto a photographic plate.[2] The beginning of the 20th century might be viewed as a hunt to improve the resolving power to refine the accuracy of measurements of the relative abundance and masses of the elements and their isotopes and broaden the MS applications outside the realm of physics. The practicality of MS fully showed in the 1940s when Alfred Nier built several MS instruments capable of preparing ^{13}C-enriched carbon.[3] Enrico Fermi, John Dunning, and Alfred Nier began the nuclear era when nanogram quantities of ^{235}U were prepared. Since 1940, MS has been used quantitatively to control production processes although the mass spectrum-to-molecular structure relationship was not known and thus extensively studied. The operating principle of the quadrupole mass spectrometer was made in 1953 by Wolfgang Paul and Helmut Steinwedel,[4] for which Paul received the 1989 Nobel Prize. However, it wasn't until the 1970s that the quadrupole found its true calling in computerized gas chromatography coupled to MS in enviromental analysis.

In the 1960s, Fred McLafferty, Klaus Biemann, and Carl Djerassi were methodologically drawing out fragmentation mechanisms allowing chemists to employ MS to determine structures of unknown molecules.[5–7] Ultrahigh resolving power instruments came around 1970 when Melvin Comisarow and Alan Marshall applied Fourier transform to ion cyclotron resonance (ICR),[8] developed in 1949 by John Hipple.[9] The discovery of time-of-flight (TOF) MS in 1946 is given to William Stephens, who pioneered a conceptually simple mass analyzer with theoretically unlimited mass range and the ability to capture the entire spectrum at once.[10] Absence of inherently pulsed ionization techniques left TOF MS inapplicable until its renaissance about thirty years later when laser desorption made its appearance. By the 1980s, small organic molecules were routinely being analyzed by MS. The area of elemental analysis was further strengthened by development of inductively coupled plasma (ICP) in 1980, which enables to measure nearly all of the elements of the periodic table when interfaced to MS.[11] However, macromolecules such as proteins, nucleic acids, and complex carbohydrates were challenging as the macromolecules could not be ionized without being too fragmented. Techniques like fast atom bombardment, plasma desorption, secondary ion MS or thermospray were making little progress as they worked only with small proteins at high concentrations. In 1988, the discovery of the electrospray ionization (ESI) interface by John Fenn revolutionized biological MS.[12] Fenn was awarded the

2002 Nobel Prize together with Koichi Tanaka, who shared the prize for using a laser desorption technique in a 1988 analysis of proteins.[13] Fenn gave a lot of credit to Malcolm Dole who demonstrated that nonvolatile solutes, when dissolved in volatile solvents, produced highly charged droplets in which they stayed intact even if transferred into the gaseous phase.[14] On the other hand, the lifetime effort of Michael Karas and Franz Hillenkamp, who are considered the inventors of matrix-assisted laser desorption ionization (MALDI), was not rewarded by any prize whatsoever.[15] The development of ESI and MALDI opened the MS field to new researchers pursuing protein and peptide investigations. Analysis of neonatal dried blood spot samples for a range of inborn errors of metabolism was a primary early application for liquid chromatography (LC)–ESI MS, which persevered to current times.[16] Bacterial identification and diagnosis is currently driven by MALDI fingerprinting.[17] ESI and MALDI are considered competing and complementary at the same time.

The 21st century has brought significant innovations in the design of TOF MS and multiple collector ICP MS; ESI techniques evolved into ambient ionization techniques – desorption electrospray ionization (DESI)[18] and direct analysis in real time (DART)[19], and the orbital ion trap (Orbitrap) analyzer was introduced. Orbitrap, which was first given as a proof-of-principle in the 1990s by Alexander Makarov, was commercialized in 2005.[20,21] The history of ion mobility spectrometry (IMS) goes back to Thomson and Rutherford who conceptualized the technique in 1896.[22] In the 1960s IMS was more commonly known as plasma chromatography and used to gas-phase separate a wide variety of substances, *e.g.*, many airport explosives detectors are currently based upon IMS. The introduction of a routine IMS MS instrument in 2006 drove the technology from research to analytical laboratories.[23] Since then many manufactures have developed their own IMS MS platform based on unique mobility separations, thereby adding the analytical power of IMS to MS for challenging systems in complex mixtures.[24,25]

The unique ability to separate the ionized molecules themselves according to m/z has driven advances across science over a hundred years, and at the same time, it is the primary reason why mass spectrometry has become one of the dominant analytical methodologies of the 21st century.

2 Mass spectrometry hyphenated via an offline interface

MS itself is a very powerful technique; however, complex mixtures can easily overcome the power in terms of resolution, sensitivity, or ion suppression. Coupling MS to separation techniques, which may decrease the complexity of a sample, is an additional and sometimes a mandatory step to increase the reliability and efficiency of qualitative and quantitative analysis. Such hyphenation may be performed online, inline, or completely offline. While the online coupling of chromatography to MS using ESI is the predominating technique it still possesses shortcomings originating from the time constraints of MS measurements. Particularly, a short time frame limits the analysis of all components in highly resolved peaks. In some cases, the entire analysis has to be repeated to complete data acquisition on missed analytes. Or the duration of online analysis is given by the time in which the entire separation is accomplished; however, in the offline arrangement, the separation, which may take hours, can be stored and analyzed (repeatedly) in minutes. The offline coupling of MS to separation techniques presents a significant advantage in actual decoupling the processes of separation and detection, which both may be performed under their optimal conditions. Sometimes, an online interface is lacking, such as in 1D/2D gel electrophoresis (GE), or thin-layer chromatography (TLC). MALDI is generally less responsive to ion suppression than ESI, and furthermore, since singly-charged ions are typically formed in MALDI, simpler spectra are produced than those in ESI. Yet, the offline coupling of chromatography to MS represents a minority of publications indexed by the Web of Science, as seen in Figure 1.
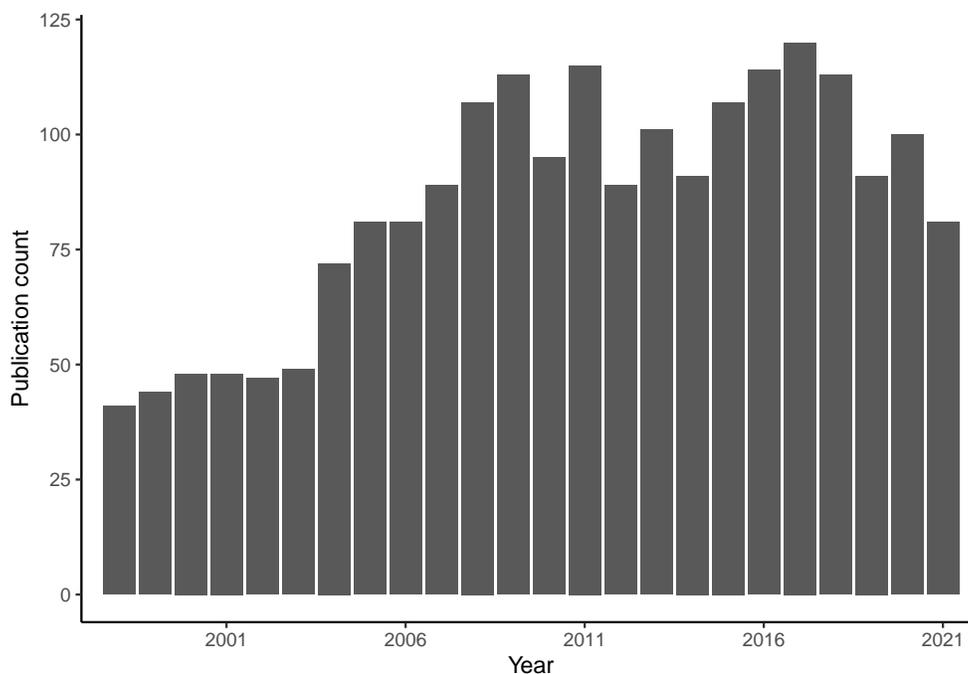

Figure 1: Publication results in 2021 on the Web of Science for a query: "(offline OR off-line) chromatography mass spectrometry"

Microcolumn techniques such as capillary LC (cLC) or capillary electrophoresis (CE) may be easily recorded and

stored without fabricating complex and fragile online interfaces. The classification of junctions between the separation column and the deposition probe and the deposition mechanisms are given in Figure 2. Generally, a sheath flow from a T-junction is commonplace in LC; a liquid junction with a separation buffer addition is a viable alternative in CE. When a separation technique is coupled offline, the sheath liquid is usually evaporated and is thus not part of the sample.
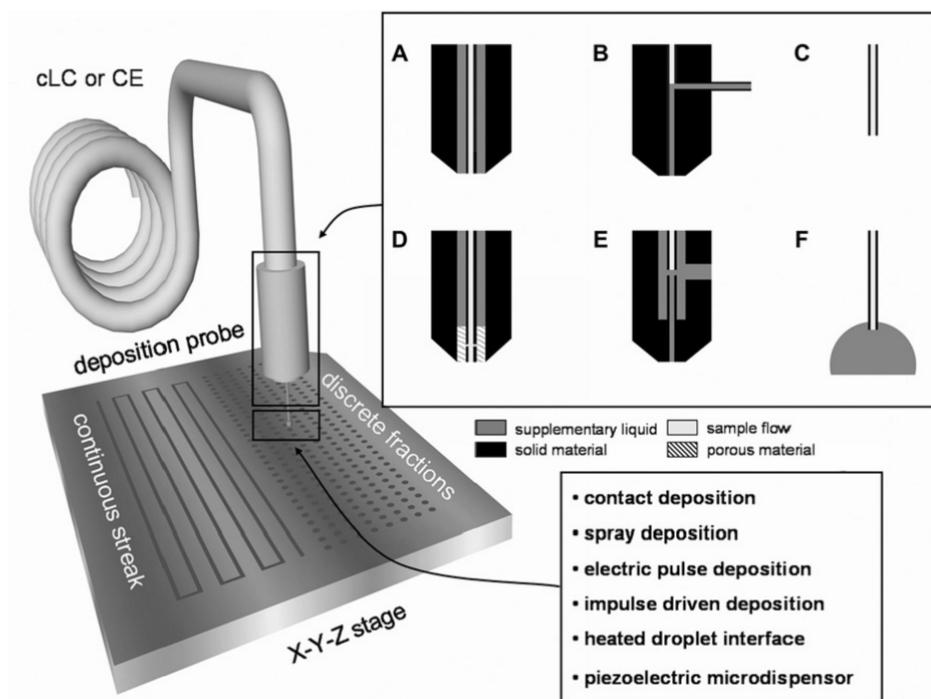
Figure 2: Off-line coupling scheme. Junctions used for coupling of microcolumn techniques include (A) coaxial sheath flow, (B) T-junction, (C) sheathless, (D) porous junction, (E) liquid junction (F) droplet electrocoupling.

Another great advantage lies in the availability to archive the separation, perform on target reactions, or employ different detection techniques avoiding the throughput mismatch when the separation and detection techniques are not compatible in their data acquisition rates. In other words, a detection technique working at a slow acquisition rate, *e.g.*, MS/MS acquisition or a high resolving power instrument, may be employed in an offline design without compromised efficiency due to time constraints. The availability of commercial mass spectrometers equipped with <1 kHz lasers capable of high data acquisition speeds in both MS and MS/MS modes pushes the advantages of offline coupling even further.

2.1 Offline coupling of microcolumn separations to desorption mass spectrometry

Essentially, the simplest mode of coupling LC to desorption MS is offline, which could be achieved by manual fractionation and collection into vials or tubes, followed by concentration and spotting for desorption analysis. The majority of offline systems includes MALDI or LDI as an ionization source although other techniques like

desorption/ionization on silicon, material-enhanced laser desorption/ionization, laser ablation, surface-assisted laser desorption were described. Direct fraction collection via automated robotic interfaces is far more reliable in terms of labor and repeatability. The effluent is deposited by a needle mounted in a z-axis direction to the spotting target. The fraction collection itself may be classified from various points of view. The deposition of the continuous streak has proven to be beneficial only in fast separations. In other separations, the mass spectra are accumulated along a finite trace segment which provides an average spectrum similar to that obtained from a discrete fraction. A slight decrease in chromatographic resolution due to the segmented acquisition is usually negligible. However, chromatographic resolution may deteriorate as a result of axial diffusion in the case of a relatively long evaporation time of the streak. Hence, the discrete spot fractionation is the main mode of operation in commercial spotting devices. The effluent deposition could be performed either contact or contactless. Many spotting devices rely on contact deposition even as it suffers from significant memory effects as the advancing needle remains wet from the previous fraction. Most of the time, addition of sheath liquid in microcolumn separations incurred a problem of sensitivity loss due to significant dilution caused by a much larger volume of the supplemental liquid. A predesigned sample support with hydrophobic surface could concentrate the analyte in the deposited sample. Contactless deposition modes are scarcer and include spraying (ESI, nebulizer), dispensing (piezoelectric, impulse-driven), heated droplet deposition or deposition assisted by electric field. Later, as ambient MS have become available, for instance, DESI, desorption atmospheric pressure chemical ionization (DAPCI), desorption atmospheric pressure photoionization (DAPPI), DART, paper spray ionization (PSI), or diode laser thermal vaporization (DLTV), they helped in disease diagnosing and drug monitoring tasks[26]. Their contribution can as well be traced to the analysis of recorded separations.[27–30] Several step-wise processes of transferring the solid analytes into the gaseous state of charged particles have given a name to a range of techniques used in the analysis of solid samples across different fields of science.[31] Many commercially-available spotting devices have become available, and the authors made an effort to review and summarize all of the manufacturers, interfaces, and their applications to date.

Review

Off-line coupling of microcolumn separations to desorption mass spectrometry

Ondřej Peš, Jan Preisler *

Department of Chemistry and Department of Experimental Biology, Faculty of Science, Masaryk University, Kotlářská 2, 611 37, Brno, Czech Republic

ARTICLE INFO

ABSTRACT

The presented review provides comprehensive and detailed characteristics on microcolumn separation techniques off-line coupled to mass spectrometry. Major attention is paid to the classification of junctions between the separation column and the deposition needle and to the process by which the liquid is transferred onto the target. Both contact and non-contact deposition techniques are covered. In order to emphasize the significance of the topic of off-line separations, current commercially available devices have been compared in terms of their potential utilization in analytical chemistry with a summarization of applications used over the past few years.

© 2010 Elsevier B.V. All rights reserved.

Contents

1. Introduction

Mass spectrometry (MS) is a powerful technique capable of obtaining essential data about a wide range of samples. However, not even mass spectrometry is able to provide the required results when applied to complex sample mixtures without prior separation. To reduce sample complexity, coupling mass spectrometry to one or more available separation techniques, in either an on-line or off-line arrangement, is unavoidable.

Microcolumn separation techniques, such as capillary liquid chromatography (cLC, μLC) or capillary electrophoresis (CE), are among the most important analytical tools in separation science. The advantages of these techniques include high separation efficiency, low limits of detection, minute sample size requirements and economical operating costs. With MS detection, both LC and CE belong to the most powerful solutions for the identification of unknown substances in complex matrices.

Whilst the common on-line, in-line (at-line) approaches have been comprehensively covered by many reviewers [1–6], challenges resulting from time scales imposed by analyzing complex mixtures on-line seem to be a major driving force for technological advances in the field of off-line coupling. Basically, the separation

is recorded on a target plate in the form of a solid as either discrete fractions or a continuous track. Such a separation record is predestined for desorption techniques capable of effective introduction of the sample into a mass spectrometer. The majority of off-line systems includes matrix-assisted laser desorption/ionization (MALDI) [7] or laser desorption/ionization (LDI) as an ionization source. The sample introduction techniques further include desorption/ionization on silicon (DIOS) [8], material-enhanced laser desorption/ionization (MELDI) [9], desorption electrospray ionization (DESI) [10], laser ablation (LA) [11], or the recently presented surface-assisted laser desorption inductively coupled plasma (SALD ICP) [12]. As MALDI MS is amongst the leading ionization techniques nowadays, most examples of off-line coupling discussed in this paper pertain to the proteomic area. The principles and applications, however, can be extended to the other desorption techniques and analyte types.

Historically, many proteomic studies have relied on 2D gel electrophoresis (GE) followed by excision of spots from the gel. The proteins contained within the spot are then subjected to protease digestion, and MS/MS is used to identify the peptides [3]. Although 2D gels have been widely used, they are limited by presence of not always advantageous gel matrix [13]. In brief, proteins with extreme values of molecular mass and/or pI tend to be underrepresented. Variations in the protein charge and size is affected by post-translational modifications which may result in several bands of the same protein over a wide pH range. Protein bands may not be detected due to a low expression of the protein, *i.e.* the dynamic range of gels is limited. Last but not least, 2D gels can be time consuming to prepare, run and analyze; these gels suffer from variable reproducibility and a skilled operator is required to run them successfully.

Alternative approaches may employ 1D GE followed by LC of peptides from proteolytically digested bands on-line coupled to tandem MS, also known as Gel-C-MS/MS [14], multidimensional protein identification technology (MudPIT) [15,16] and column or microcolumn separations. As these techniques are complementary and do not suffer from the limitations of 2D gels, they could become the method of choice in many proteomic applications.

Published reviews mostly cover only a part of the topic, such as CE–MS [2,17], or quantitative proteomics [18]. The aim of this review is to provide a comprehensive view on microcolumn separation techniques coupled off-line to MS. It includes the classification of junctions between the separation column and the deposition probe, deposition mechanisms as well as characterization and availability of commercial spotters. In the last part of the review, a list of applications mapping the area of off-line coupling is given.

2. Off-line *vs.* on-line interfacing

Due to the inherent nature of liquid column separations, electrospray ionization [19] (ESI) offers easier and more straightforward on-line coupling, relative to MALDI. While being the predominating technique, it still possesses shortcomings originating from the time constraints of MS measurements. Particularly, there is a short time available for the analysis of all components in highly resolved peaks, *i.e.* by the time MS/MS of a selected compound has been carried out, co-eluting or closely eluting compounds may have been skipped. In some cases, the entire LC–MS analysis has to be repeated in order to collect data on missed analytes.

Generally, the simplest mode of coupling LC to desorption MS is off-line, which has the advantage of completely decoupling the two techniques, enabling separate optimization of each. MALDI is, relative to ESI, less responsive to traces of additives in the separation medium, such as sodium dodecylsulphate, trifluoroacetic acid, or salts. Furthermore, since singly charged ions are typically formed

in MALDI, it is known to produce simpler spectra than ESI. Compared to on-line interfacing, papers dealing with off-line coupling of microcolumn techniques are less frequent, presumably due to the requirement of a relatively complex deposition interface and early expansion of MS/MS-capable mass spectrometers equipped with ESI. It is important to note that stable deposition depends on many variables, such as effluent flow rate, temperature and viscosity, concentration of organic solvents in effluent, substrate surface, surface tension, or environment pressure. On the other hand, the key difference between time-dependent and result-driven analyses [20] is constantly being equalized by increasing the power of data acquisition and processing hardware. Although on-line coupling prevails, the off-line approach is capable of combining the advantages of column (ruggedness) and gel (archiving) separations. The ability to store the eluted fractions on a MALDI plate and expose them to another spectrometric technique has appeared to be rewarding, *e.g.* in metallomics, where both species, metal and bio-ligand, are expected to be determined together [12,21].

In combination with multicolumn separation, the off-line approach offers improved sample throughput and cost-effective exploitation of a mass spectrometer. In the on-line approach, the duration of MS analysis is given by the time in which the entire liquid separation is accomplished. In the off-line arrangement LC separations, which may take hours, can be stored on a MALDI target and analyzed repeatedly, under various conditions, in minutes. Alternatively, multiple samples, separated and deposited on a target in parallel, can be analyzed by a single mass spectrometer without compromising separation and mass spectrometry performance as demonstrated by in-line capillary array electrophoresis (CAE) MALDI MS of eight protein digests [22]. This concept is valid also for off-line workflow [23–25]. Separation records obtained from multiple columns can be analyzed with a single high-throughput mass spectrometer which is usually the most expensive part of the setup. The throughput of axial MALDI TOF MS is, up to a certain limit (∼10 kHz), proportional to the rate at which individual spectra can be acquired; this rate being primarily a function of the laser repetition rate.[26] Reliable solid-state UV lasers with fast repetition rates (0.1–5 kHz), power density and pulse-to-pulse stability adequate for MALDI applications have become available, which may significantly reduce the time required for MS analysis of large sample arrays [27]. Recently, the introduction of commercial mass spectrometers equipped with a 1 kHz laser capable of high data acquisition speeds in both MS and MS/MS modes has been announced [28,29].

3. Effluent collection

Off-line LC–MS can simply be achieved by manual fractionation and collection into microtubes, followed by concentration and spotting for traditional MALDI analysis. This process is labor intensive and can result in sample loss [30,31]. This review will focus on direct fraction collection on a sample target. In addition, off-line coupling to CE requires an electrical contact to be maintained at both ends of the capillary during the separation. Typically, the capillary output end is located in an electrolyte reservoir acting as a conductor and pH buffer. In order to prevent degradation of the CE resolution, intake and outflow of the auxiliary buffer has to be arranged in such a manner as to prevent the induction of laminar flow in the separation capillary.

Naturally, in CE and after the introduction of nanoflow separation techniques such as cLC, sample volumes from both systems are directly compatible with spotting onto a MALDI target without any preconcentration [3]. However, low flow rates may require supplementary liquid for the cLC or CE effluent to be deposited with it. Viable connections as well as available deposition interfaces are
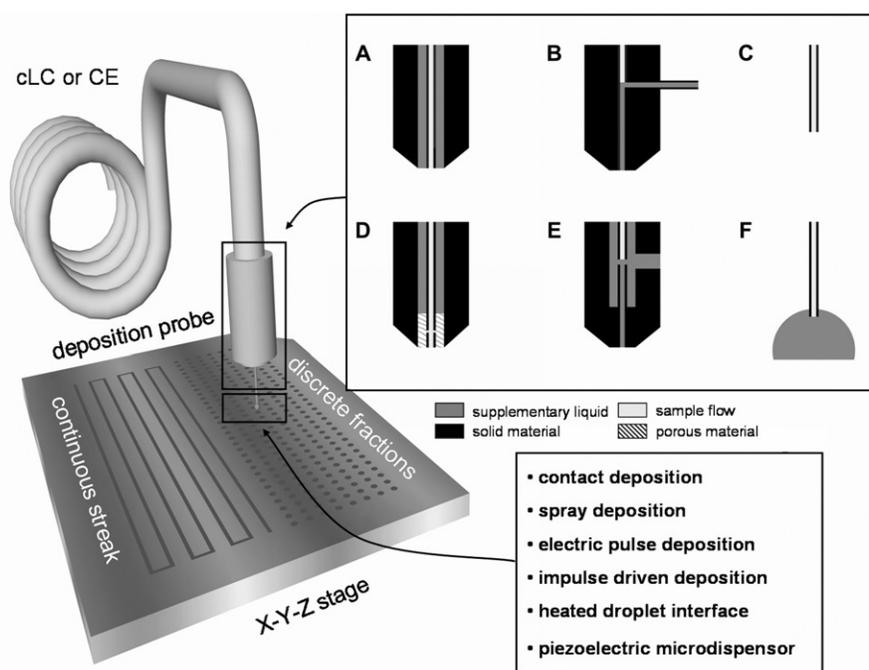
Fig. 1. Off-line coupling scheme showing supplementary liquid addition and deposition mechanisms. Junctions used for coupling of microcolumn techniques include (A) coaxial sheath flow, (B) T-junction, (C) sheathless, (D) porous junction, (E) liquid junction (F) droplet electrocoupling. (A)–(C) are typical for cLC whereas (D)–(F) are common in CE.

shown in Fig. 1. Generally, a sheath flow from a T-junction is preferred in LC; a liquid junction with a separation buffer addition is a viable alternative in CE. Alternatively, the voltage may be switched off, the vial at the cathode end removed and the desired peak eluted by applying pressure at the inlet end [32,33]. Because prior knowledge of the analyte retention time is required, the pressure method relies on an on-line detector for the separation to be stopped at the appropriate point. Disadvantages include prolongation of the analysis time and difficulty in handling small analyte volumes that are produced at flow rates of a few nanoliters per second. The addition of supplementary liquid at the capillary output has been used to overcome this problem [34–36].

The fraction collection itself may be classified from various points of view. As previously mentioned, effluent can be collected in the form of discrete fractions or a continuous streak. The deposition of the continuous streak has proven to be beneficial only in fast separations where the peak widths are as low as 2 s [37,38]. In other separations, the mass spectra are accumulated along a finite trace segment which provides an average spectrum similar to that obtained from a discrete fraction. A slight decrease in chromatographic resolution due to the segmented acquisition is usually negligible. However, chromatographic resolution may deteriorate as a result of axial diffusion in the case of a relatively long evaporation time of the streak. Therefore, most spotters only aim at discrete spot fractionation which fulfills most common needs. The spotting devices have been sorted according to the principles of operation.

4. Contact deposition

The simplest way to transfer the liquid is assumed to be the deposition needle or rather the droplet formed underneath, that touches the target plate surface and most commercial devices work on this principle. Although mechanically simple, the contact deposition may suffer from significant memory effects as the advancing needle remains wet from the previous fraction. Takigiku et al. [39] presented the use of a previously described porous glass joint [40] near the cathodic end of the CE column to collect fractions for

desorption MS; later it was used by Keough et al. [41] for the determination of proteins. Next, off-line microcolumn separation techniques coupled to MALDI MS involved elution onto the sample target by the addition of a supplementary liquid. It included cLC [42–45], CE [34–36,46–50], capillary isoelectric focusing (CIEF) [51–55], capillary electrochromatography (CEC) [56] and 2D LC CE [57]. Whilst being effective, a problem of sensitivity loss could occur due to significant dilution caused by a much larger volume of supplemental liquid from the junction. To address this issue, a prestructured sample support [58] was used for fraction collection [59]. In this design, dilution by the matrix/buffer solution was counteracted by the concentrating effect of the hydrophobic Teflon surface. In 1998, Stevenson et al. designed a device comprising a modified pen plotter programmed to apply the HPLC effluent directly to a membrane that was attached to the MALDI sample target stage and used it for N-terminal sequencing of peptides via automated microblotting onto membrane substrates [60,61].

Rejtar et al. introduced continuous vacuum fraction collection from CE coupled to MALDI MS [43], which arose from an on-line vacuum deposition device introduced by the same group in 1998 [37]. They were able to produce ∼100 μm of wide streaks, only discrete segments of which were consumed in MS. After data analysis the rest of the sample, containing unidentified peptides as well as several species chosen for sequence confirmation, was re-analyzed in the MS/MS mode. An example of the 3D MS-chromatogram with highly resolved peaks in both directions is shown in Fig. 2. Moreover, a similar principle, sub-atmospheric deposition interface, was used in 2008 for coupling of CE to ICP MS [12]. Although the vacuum (sub-atmospheric) interface demands a large deposition chamber, it allows for the generation of smaller spots or a narrower streak due to the solvent evaporating more rapidly than in the case of deposition at atmospheric pressure.

A device for contact deposition developed by Nagele and Vollmer [62] read the actual flow rate of the mobile phase from the pump's flow sensor in order to adjust the draw speed of the deposition probe. If the liquid volume per spot was greater than 500 nL,
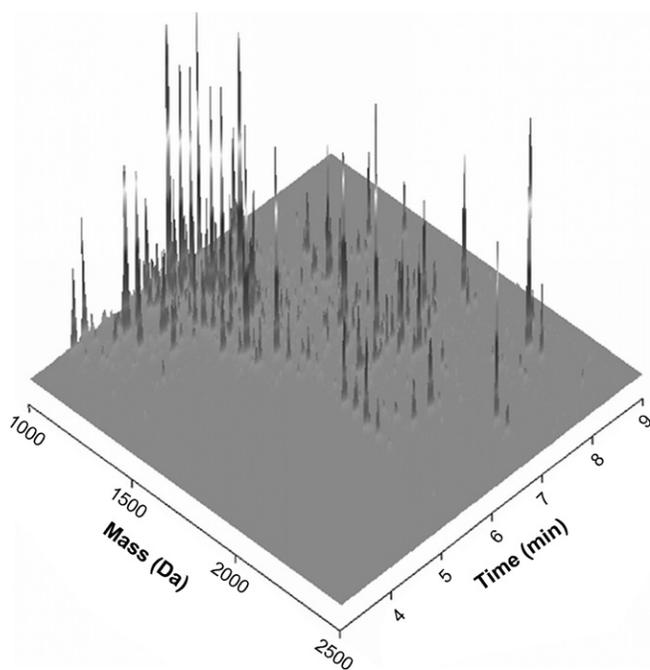
Fig. 2. 3D MS-chromatogram of an in-gel digest of an excised 40–50 kDa SDS-PAGE band of a yeast lysate, analyzed by continuous deposition MALDI MS analysis. Reproduced with permission from [38].

the capillary tip started to move continuously upwards, keeping the droplet in contact with the surface.

In 2008, Hattan et al. deposited LC effluent onto both conventional MALDI plates and plates with collimated-hole structures (CHS) [63]. These plates contained monolithic chromatography media filling the holes and provided additional capacity for capturing and concentrating samples. Using these three-dimensional targets, they achieved about a 30-fold enrichment of sample concentration in the matrix crystals on the surface in comparison to the conventional stainless steel MALDI targets.

An off-line interface incorporating sheathless flow and counter-flow balance was developed to couple CE to MALDI Fourier-transform ion-cyclotron resonance (FT-ICR) MS for neuropeptide analysis of complex tissue samples [64]. The interface integrated a porous cellulose acetate membrane joint constructed near the capillary outlet for the electrical circuit completion which simplified the CE interface by eliminating a coaxial sheath-liquid. The electro-osmotic flow (EOF) at reversed polarity (negative) CE mode was balanced and reversed by a pressure-initiated capillary siphoning (PICS), which generated a low flow (<100 nL/min) for fraction collection. Thus, the sample deposition occurs at a speed appropriate to chromatography giving enough time for FT-ICR MS to record high-resolution spectra.

4.1. Target electrocoupling

A few off-line CE interfaces involving no supplemental sheath flow have been introduced. The electrical circuit was maintained by deposition onto a conductive target. Such fraction collection of CE effluent was first performed by Zhang and Caprioli in 1996 [65]. A sample track was produced by linear movement of the target during the electrophoretic separation and subsequently analyzed by MALDI MS.

In 2001, the capillary was put into a droplet of buffer solution or matrix solution in order to make an electrical connection and to apply a high voltage between the metallic sample plate and the counter pole of CE [66]. The applied high voltage was automati-

cally turned off during the transfer of the capillary outlet between droplets. Separated components were collected and concentrated in droplets on the plate.

Another example of droplet electrocoupling (DEC) for CE MALDI MS with a structurally silicone coated target was presented by Jacksén et al. [67] The migration times from a UV-electropherogram were used to pinpoint the fractionation start time and the number of fractions needed to cover all UV-detected peaks. With a transfer time of ~0.05 s between two fractions, evaporation during this short transfer time resulted in a minute concentration of analytes and the voltage was not turned off during the transfer. To avoid the formation of a sparking spray-like sample transfer or air bubbles, the capillary was positioned as close to the MALDI plate as possible without actually touching it.

In 2006 an elastomeric device reversibly sealed on the MALDI target, capable of concentrating and purifying samples directly on the MALDI target, was described [68]. A poly(dimethyl siloxane) (PDMS) sample concentrator with an array of wells was sealed on the MALDI target; sample solutions were deposited in the wells that match the spots on the MALDI target. The device was used for the collection of sialylated glycopeptides separated by CE on the MALDI target [69].

A special case of DEC was described by Chiu et al. [70]; the capillary outlet was coated with conductive epoxy thus requiring no capillary fracture, liquid junction, or sheath-liquid. Busnel et al. [71] modified the setup by painting the outer outlet part of the separation capillary with a silver conducting paste to adapt the interface to neutrally coated capillaries producing no significant electro-osmotic flow.

5. Non-contact deposition

5.1. Electrospray

A conductive spraying technique was used to spray the CE effluent onto a matrix-coated MALDI target, which moved periodically underneath the spraying tip [72–74]. A steel plate with a small hole in it prevented the aerosol from overspreading. However, the masked sample was lost and this contributed to the relatively low sensitivity of the method, especially due to dilution effects and the excessively wide sample distribution. Signal intensity and sample homogeneity would have been enhanced if the entire sprayed output had been collected into sample wells [75].

Off-line narrow-bore size exclusion chromatography (SEC) MALDI MS analysis was performed by Lou and van Dongen [76]. The SEC effluent, as well as a suitable matrix solution added coaxially through a T-junction with no dead volume, was directly deposited on the MALDI plate.

DeVault et al. [77] modified the conditions to produce a narrow (20 μm) liquid filament (electrofilament), which was capable of depositing spatially preserved bands with ~100 μm track widths. Even though it was not coupled to MS, it enabled recording CE separations without decreasing its efficiency.

Electrospray deposition was also used to couple LC with DIOS MS. A spatially preserved linear track of the separated sample was generated on a specially designed DIOS chip [78].

Wei et al. [79] electrosprayed nanoliter volumes of matrix/analyte mixture from a high voltage (1–2 kV) fused-silica capillary onto a grounded MALDI plate mounted 100–500 μm from the capillary outlet. Electrospray deposition with these conditions produced sample spots 200–300 μm in diameter.

5.2. Nebulizers

Wall et al. presented a heated nebulizer interface, where LC effluent was continuously collected as linear tracks on a MALDI

target [80]. MALDI target plates were pre-coated with a matrix prior to sample deposition and a fine mist of droplets that rapidly evaporated was sprayed onto the target plate. The heated capillary nebulizer provided rapid on-line desolvation of effluent from flow rates of 200 nL/min up to 50 μL/min which permitted splitless, continuous deposition of LC separations of peptide and protein digest samples at nanoflow and capillary scales.

A simple interface based on an oscillating capillary nebulizer (OCN) [81], was first used for deposition of a post-column mixture of cLC effluent and MALDI matrix onto a MALDI target [82]. Later, the effluent from a thermal field-flow fractionation system was pre-mixed with a matrix and deposited directly and continuously onto a moving MALDI probe [83]. The result was a continuous sample track representative of the separation process. Subsequent off-line MALDI MS was performed in automated and manual modes.

5.3. Piezoelectric dispensers

In 1998, a piezoelectric flow-through microdispenser system was introduced for the detection of attomole amounts of proteins from a single droplet of analyte mixed with a matrix; the droplets, ranging from 30 to 200 pL, were formed at a frequency 500 Hz on a MALDI target plate [84]. In 2000, the piezoelectric microdispenser was modified to interface capillary LC with MALDI for the identification of biomolecules [85]. The MALDI target plate was placed on a computer-controlled high-resolution x–y stage on to which the column of effluent was deposited as discrete spots. The entire target plate was sprayed with a homogeneous layer of α-cyano-4-hydroxy-cinnamic acid mixed with nitrocellulose using an airbrush. Multiple (1800) droplets of 1 nM peptide mixture deposited on the same target spot, corresponding to ∼100 amol, could be detected. Application of the method was extended to the identification of phosphopeptides generated from a trypsin digest of recombinant autophosphorylated ZAP-70; chromatography and on-line tandem mass spectrometry were combined to ascertain the identity of peptides [86,87].

5.4. Electric field-assisted

An automated platform for high-throughput proteomics combining LC and MALDI FT-ICR was developed in 2002 by introducing a charge induction mechanism which transferred the column of effluent to a MALDI plate by applying a negative potential to the plate [23,88]. The effluent from the LC formed an electrically grounded droplet. An electric field formed by the application of a negative voltage (−2 kV) pulse to a MALDI target (positioned 2–5 mm from the outlet) polarized the droplet and pulled it onto the target. This resulted in a series of droplets of precisely controlled volume. Surface-modified targets were used to facilitate concentration and precise positioning of samples. High ionic strength solutions and pure organic solvents could be deposited, enabling their use in various modes of chromatography as well as on-plate automated recrystallizations. Moreover, the deposition platform was capable of electrospraying the effluent as continual streams.

5.5. Heated droplet

LC–MS coupling using a heated droplet interface developed by Zhang et al. [89] was based on the formation of hanging droplets at the outlet of an LC effluent transfer tube. The transfer tube and the MALDI plate were heated in a controlled manner in order to evaporate the carrier solvent without spraying, ionizing, nebulizing, splattering or uncontrolled boiling of the carrier solvent. Even with liquid flow rates of up to 50 μL min⁻¹, about 800 μm analyte spots were formed on the MALDI plate.

Similar to the heated droplet interface, heated sheath gas and a capillary nozzle were used to remove most of the mobile phase as well as deposit the GPC-LC effluent onto the pre-coated matrix on a moving MALDI plate [90].

5.6. Impulse driven

Another non-contact interface introduced by the same group [91] involved a pulsed voltage operated solenoid, which generated impulses that transported hanging droplets from the LC outlet directly to a MALDI plate via a momentum transfer process. This impulse-driven system is claimed to be compatible with solvents of varying polarity and viscosity and hydrophobic and hydrophilic MALDI matrices. The generated droplets with volumes ranging from 20 nL to 2 μL make the interface useful for depositing the effluent from a capillary LC column that typically operates at flow rates below 2 μL min⁻¹. In 2007, the interface was integrated with the heated droplet interface resulting in an impulse driven heated droplet system, which could accommodate a wide range of LC flow rates giving the user greater flexibility in choosing the methodology to suit the experimental requirements [92]. The maximum flow rate of about 5 μL min⁻¹ at room temperature could be extended to a relatively high flow rate of up to 50 μL min⁻¹ with heating.

Recently, a solenoid valve and a He-pressurized pump have been used to dispense sample and matrix for coupling CE to MALDI MS [93].

5.7. Chip-based systems

The concept of rapid open-access channel electrophoresis has been introduced with sample mixtures being separated in open microchannels cut into glass microchips [94]. With a matrix added to the buffer solution prior to separation, the channel yielded a complete MALDI sample and was ready for analysis at the end of the separation after solvent evaporation. The laser was then used to raster the channel providing mass spectra as a function of channel position.

CIEF separation on three model proteins in a pseudo-closed microchannel built on a polymethylmethacrylate (PMMA) chip was performed in 2003 [95]. The chip consisted of a base with separation channels and a cover. The cover minimized sample drying and the effects of atmospheric carbon dioxide. Sample drying was also reduced by cooling down the chip on a thermoelectric cooler. After completion of CIEF, the cover was removed and the solvent evaporated. The base was put onto a commercial MALDI target using a home-made adapter; a MALDI matrix was deposited by syringe pump on top of the focused sample in the channel, and a protein signal was recorded along the channel.

Matrix-free infra-red (IR) LDI of polypeptides and proteins directly from a polyacrylamide gel after electrophoretic separation in a microfluidic chip fabricated from PMMA was performed by Xu et al. [96]. A simple T-structure of gel was prepared on a PMMA chip and covered with an annealed PDMS cover. After electrophoresis, the gel could be analyzed when attached either to the PDMS cover or to the PMMA chip.

MALDI MS in an open microchannel has advanced to off-line hyphenation between CE and MALDI MS in the so-called closed-open-closed microchannel system [97]. Two fused-silica capillaries were connected via a silicon chip comprising an open microcanal, which was utilized as a MALDI detection window within the CE capillary system. With a MALDI target integrated in the electrophoresis setup, electrocoupling was assured and the external sample transfer from the CE capillary to the target was avoided.

It is worth noting a technique with the potential for coupling a microseparation to MS—the microfluidic compact disk (CD) described by Gustafsson et al. [98]. The device involved parallel

Table 1
Commercially available microfraction collectors—spotters.

Manufacturer	Model	Max. spotting rate/Hz	Min. fraction volume/nL	Plate capacity[a]	Flow rate	Matrix flow rate	Positioning precision (X/Y/Z axis/μm)	Spotting needle	T-junction volume	Deposition	Manufacturer's comments
Agilent	1200 Series Micro collector/spotter	0.33	100	4 MTP	100 μL/min	100 μL/min total flow	Not specified	Quartz, 360 μm O.D.	29 nL	Discrete	Possibility of two spotters connected via a micro valve.
Applied Biosystems	TempoLC MALDI spotter	4	0.8	8 ABI large/16 ABI small	200 nL–3 μL/min	200 nL–20 μL/min	10	Teflon coated fused silica, 360 μm O.D., 50 μm I.D.	Less than 500 nL	Discrete/ continuous	Tested with monolith columns.
Bruker Daltonics	Proteineer fcII	0.3	200	4 Bruker MTP	200 nL–50 μL/min	1000 nL–120 μL/min	100	Fused silica, 50 μm I.D.	Few nL	Discrete	Controlled by HyStar-Software Package.
CTC Analytics	PAL MALDI Option	0.33	5	23 shallow/11 deepwell MTP	20 nL–300 μL/min	20 nL–300 μL/min	100	Stainless steel capillary, 50 μm I.D.	10 nL–3 μL	Discrete	
Dionex	ProBot	0.25	5	2 MTP/6 ABI small	200 nL/min	248 nL–308 μl/min.	20	Fused silica, 30 μm or 100 μm I.D.	30 nL	Discrete/ continuous	
Eksigent Technologies	Ekspot	0.25	25	8 MTP/16 ABI small/4 deepwell MTP	200 nL–4 μL/min	400 nL–50 μL/min	100	Fused silica	17 nL	Discrete	Possibility to collect into MT plates at low flow rates due to a sideway capillary movement once lowered into a well.
Gilson	223 fraction collector	0.555	200	1 Bruker MTP	1000 nL–100 μL/min	5000 nL–50 μL/min	250	Spring loaded probe, 1/32" O.D., 200 μm I.D.	3 μL	Discrete	
Shimadzu	AccuSpot	0.33	10	9 MTP/18 ABI small	50 nL–10 μL/min	100 nL–10 μL/min	100/120/0[b]	Fused silica, 285 μm O.D., 25 μm I.D.	On-target matrix addition	Discrete	A plate sensor controlling the distance of the tip to the metal target.
SunChrom	SunCollect MALDI Spotter	1	2	4 MTP	1 nl–100 μL/min	1 nL–10 μL/min	30/125/39	Quartz, 360 μm O.D.	100 nL	Discrete/ continuous	Tissue spray option, tested for MALDI imaging, 260 μm O.D. needle; micro fraction collection into any MTP of fractions from 2 nL up to 1 mL.

[a] MTP: microtitration well plate-sized target (any manufacturer), ABI small: dimensions 44 mm × 44 mm, ABI large: dimensions 123 mm × 81 mm.
[b] With a plate sensor employed.

sample preparation and MALDI MS of 96 samples with volumes ranging from one to several microliters. Centrifugal force was applied to move liquid through multiple microstructures, each containing a 10-nL reversed phase chromatography column. The peptides in the digests were concentrated, desalted, and subsequently eluted from the columns directly into MALDI target areas on the CD using a solvent containing the MALDI matrix. After crystallization, the target areas of the CD were inserted into the MALDI instrument for peptide mass fingerprinting and database identification. The microfluidic disk was also used for the detection of phosphorylated peptides with combined immobilized metal affinity chromatography (IMAC) and enzymatic dephosphorylation [99]. Phosphoproteins were digested with trypsin, processed by nanoliter scale IMAC on the CD with and without subsequent in situ alkaline phosphatase treatment and detected in MALDI MS.

An automated proteolytic digestion bioreactor and droplet deposition system was constructed with a PMMA microfluidic device for off-line interfacing to MALDI MS [100]. The bioreactor was mounted in the micro fraction collector for protein digestion and deposition of the digests with a matrix solution on the MALDI plate.

At-line coupling of LC to chip electrospray MS was performed using a commercially available Advion TriVersa Nanomate® chip electrospray system [101–105]. In the case of ultra-high pressure LC (UPLC) coupled to FT-ICR MS [102], the LC gradient effluent was collected in microliter fractions onto a 96-port plate which was put into the autosampler of a chip-based nanoelectrospray ionization system serving the FT-ICR MS. The approach maintained the advantage of off-line coupling; i.e. the time difference between the separation speed of UPLC and the data acquisition speed of the FT-ICR MS buffered to preserve the high efficiency of both methods. The fractions of target components were collected manually for greater flexibility which is needed during gradient elution.

6. Commercial spotters

Automated robotic interfaces allow direct collection and transfer onto MALDI plates. The analyte, with or without a matrix, is deposited by a capillary needle which is mounted in a z-axis direction. In most systems the needle is held stationary while the MALDI target plate moves underneath. Generally, all commercially available instruments are flexible in using various types of MALDI target plates. The connection between separation output and deposition input is usually provided by a T-junction. The matrix solution can be instantly mixed with the separation effluent from a side input of the T-junction, deposited onto a target before sample introduction or added to fractions in a separate step. In the first approach, the deposited mixture is ready for MALDI MS immediately after evaporation. However, in CE, a matrix addition inside the T-junction can result in a change of separation electrolyte composition inside the separation capillary, thus affecting the migration times and peak resolution.

Table 1 lists, to the best of our knowledge, all current commercially available spotters and information collected from the manufacturers. Although the commercial spotters are primarily intended for interfacing LC to MALDI MS, a slight modification of the LC–MS spotting device, involving sheath flow interface grounding, allows off-line CE–MS to be performed. Nevertheless, most of the spotters used for off-line CE–MS are laboratory-built.

7. Applications

Previous reviews [106,107] covering off-line coupling of column separations and MS were mostly focused on the development
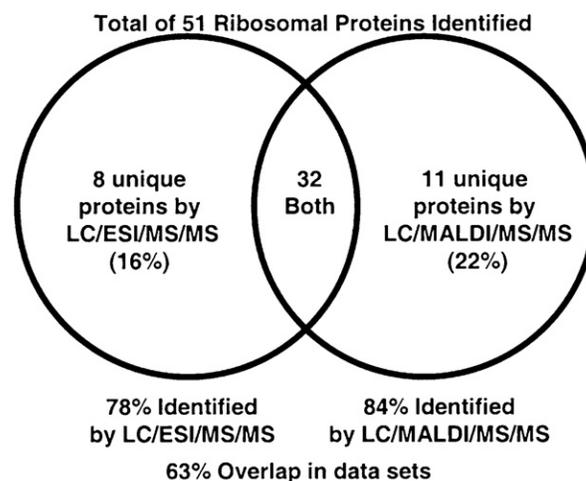

Fig. 3. Comparison of the number of overlapping and unique protein assignments obtained by LC/ESI/MS/MS and LC/MALDI/MS/MS analysis of the 39S subunit of bovine mitochondrial ribosomes. Reproduced with permission from [110].

of interfaces which were tested on model samples. As the field matured and the number of commercial spotters in the separation community grew, off-line systems were applied to solve many real problems, especially in the proteomic area. In addition to papers dealing with the interface development for off-line coupling, we have listed the applications in Table 2. The table does not include the off-line systems using columns with an I.D. larger than 300 μm and applications in which fractions of microcolumn effluent are collected into a relatively large volume (>5 μL) in microvials prior to MS processing.

Utilization of microcolumn separation techniques off-line coupled to MS is suitable in peptidomics, proteomics, metallomics, as well as in low mass screening applications such as metabolomics, pharmacokinetics, and drug development. Although the ESI MS interface is unquestionably easier to implement [108], the off-line systems have spread rapidly in recent years. Although various interfaces for on target liquid spotting have been developed, the majority of applications are performed by cLC MALDI MS using a T-junction and contact deposition. CE MALDI MS may be an attractive choice for certain areas. For instance, Amon et al. have shown that CE–MS can be considered as a competitive and complementary method to capillary reversed phase HPLC MS for glycopeptide mapping [109]. Detection limits for the glycopeptides were found to be near 100 fmol for CE ESI MS and 50–300 fmol for CE MALDI MS. In the latter case, it was strongly dependent on the size of the glycopeptide.

Analytical schemes combining off- and on-line approaches have been performed by many groups. For instance Bodnar et al. evaluated the improvement in proteome coverage of complex protein mixtures gained by analyzing samples using both LC ESI MS/MS and LC MALDI MS/MS [110]. Parallel analyses of a single sample were accomplished by interfacing a commercially available fractionation system (Probot) with a nanoscale LC system. The Probot was configured to perform a post-column split so that a fraction (20%) of the column effluent was sent for on-line LC ESI MS/MS data acquisition and the majority of the sample (80%) was mixed with a matrix solution and deposited onto the MALDI target plate. The split-flow approach takes advantage of the concentration sensitive character of ESI and provides sufficient quantity of sample for MALDI/MS/MS; the complementary nature of the ionization techniques results in a significantly improved protein coverage, as seen in Fig. 3.

Table 2
Applications of microcolumn separations coupled to desorption MS.

Analyte	Sample/objective	Instrumentation	Fractionation	Year	Reference
Protein digest	*Escherichia coli*	SCX cRPLC MALDI	Probot	2009	[111]
Protein digest	*Corynebacterium glutamicum*	RP cRPLC MALDI	Probot	2009	[108]
Protein digest	Ventricular cerebrospinal fluid	CE MALDI	Probot	2009	[112]
Proteins digest	Cervical-vaginal fluid	cRPLC MALDI		2009	[113]
Protein digest	*Escherichia coli*	cRPLC MALDI		2009	[114]
Protein, protein digest	Follicular fluid	IEF CE MALDI	Probot	2009	[115]
Protein digest	Bax HCT116 clones	SCX cRPLC MALDI	Impulse-driven heated droplet	2009	[116]
Peptides, proteins	Saliva	cRPLC MALDI	Probot	2009	[117]
Melanoma-specific markers, protein digest	Plasma	SCX cRPLC MALDI	Probot	2009	[118]
Protein digest	Honeybee royal jelly	cRPLC MALDI	Laboratory-built contact	2009	[119]
Protein digest	Ribosomal subunit of *Escherichia coli*, human protein mixture, HEK293 cells	cRPLC MALDI	1100 Series	2009	[120]
Protein digest	Neuronal cells	cSCX cRPLC MALDI	Probot	2009	[121]
Protein digest	Yeast mitochondria, bovine serum albumin	cRPLC MALDI		2009	[122]
Protein digest	Aqueous humor	cRPLC MALDI	1100 Series	2009	[123]
Protein digest	Mouse cortex	cRPLC MALDI	Probot	2009	[124]
Protein digest	Bovine milk	cRPLC MALDI	Probot	2009	[125]
Protein digest	Tumor-bearing kidneys	cRPLC MALDI	Probot	2009	[126]
Neuropeptides	*Rhodnius prolixus*	cRPLC MALDI	Probot	2009	[127]
Small molecules	Yeast	CE MALDI	Laboratory-built contact	2009	[128]
Myoglobin digest		Sphingomyelin-coated CE MALDI	1100 Series	2009	[129]
Neuropeptides	*Cancer borealis*	CE MALDI	PICS	2009	[130]
Small molecules	*Sophora japonica*	CE MALDI	Laboratory-built non-contact	2009	[131]
^{15}N-labeled protein digest	*Methanococcus maripaludis*	cRPLC MALDI FT-ICR	Probot	2009	[132]
Neuropeptides	*Cancer borealis*	CE MALDI FT-ICR	PICS	2009	[133]
Hepatocyte proteins	Human liver	RP cRPLC MALDI	Probot	2009	[134]
Chromium species		CE SALD ICP	Laboratory-built sub-atmospheric contact	2008	[12]
Oligosaccharides		cNPLC MALDI	Probot	2008	[135]
Peptides	Blood cells	cRPLC MALDI		2008	[136]
Glycosphingolipids	Erythrocytes	cRPLC MALDI	Proteineer fc	2008	[137]
Laminin β1 digest		cRPLC MALDI	Proteineer	2008	[138]
Proteins	Liver tissue	SCX cRPLC MALDI	Probot	2008	[139]
Phosphorylated peptides, protein digest		cRPLC MALDI	Probot	2008	[140]
Proteins, peptides	Urine	cRPLC MALDI	Probot	2008	[141]
Proteins		cRPLC MALDI	Tempo LC MALDI	2008	[142]
Protein digest	*Arabidopsis*	cRPLC MALDI	Probot	2008	[143]
Protein digest	*Escherichia coli*	cRPLC MALDI	Probot	2008	[144]
Protein digest	*Porphyromonas gingivalis*	cRPLC MALDI	Proteineer fc	2008	[145]
Protein digest	Cerebrospinal fluid	cRPLC MALDI	Probot	2008	[146]
Protein digest	Bovine conceptus fluids	cRPLC MALDI	1100 Series	2008	[147]
Man-6-P glycoprotein digests and glycopeptides	Mouse serum	SCX cRPLC MALDI	Probot	2008	[148]
Protein, protein digest	Follicular fluid	IEF cRPLC MALDI	1100 Series	2008	[149]
Fiber connexins	Bovine lens	cRPLC MALDI	Laboratory-built contact	2008	[150]
Arabinoxylans		cNPLC MALDI	Probot	2007	[151]
Protein digest	White spot syndrom virus	cRPLC MALDI	Probot	2007	[152]
Glycated peptides	Serum albumin	cRPLC MALDI	AccuSpot	2007	[153]
Peptides	Serum	cRPLC MELDI	1100 Agilent	2007	[154]
Peptides, protein digest		cRPLC MALDI	AccuSpot	2007	[155]
Protein digest	D20 liver cancer tissue	SCX cRPLC MALDI	Probot	2007	[156]
Protein digest	Apoptotic Jurkat T cells	cRPLC MALDI	Probot	2007	[157]
Protein digest	Vitreous humor	cRPLC MALDI	Probot	2007	[158]
Protein digest	*Arabidopsis thaliana* seed extracts	cRPLC MALDI	Probot	2007	[159]
Protein digest	Breast-cancer cell lines MCF-7/WT	cRPLC MALDI	Micro-FC, G1364D	2007	[160]
Protein digest	Red blood cell membrane proteins	SCX cRPLC MALDI	Probot	2007	[161]
Protein digest	*Sinorhizobium fredii*	cRPLC MALDI	Probot	2007	[162]
Protein digest		cRPLC MALDI	1100 Series	2007	[163]
Proteins	Examination of DropStop foil	CE MALDI	Probot	2007	[164]
Peptide mixture	Prediction of retention times	cRPLC MALDI	Laboratory-built contact	2007	[165]
Glycoprotein, proteinase P69B	Tomato	cRPLC MALDI	Laboratory-built contact	2006	[166]

Table 2 (*Continued*).

Analyte	Sample/objective	Instrumentation	Fractionation	Year	Reference
Sialylated glycopeptides	Bovine α_1-acid glycoprotein	CE MALDI	Target electrocoupling	2006	[69]
Serum constituents	Serum	cRPLC MELDI	Probot	2006	[167]
Protein digest	Plasma and serum	cRPLC MALDI	Probot	2006	[168]
Proteins	Esophageal adenocarcinoma epithelium	cRPLC MALDI	Laboratory-built non-contact piezoelectric	2006	[169]
Proteins, protein digest		cRPLC MALDI	Probot	2006	[170]
N-glycans	Honey bee phospholipase A$_2$	cNPLC MALDI	Probot	2006	[171]
Peptide biomarkers	Urine	CE MALDI	Probot	2006	[172]
Bovine serum albumin digest		Microchip LC MALDI	Laboratory-built electric field-assisted	2006	[173]
Protein digest	Singapore grouper iridovirus	cRPLC MALDI	Probot	2006	[174]
Glycopeptides	Plasma	CE MALDI	Probot	2006	[109]
Proteins	Rat liver tissue	cRPLC CIEF MALDI	Probot	2006	[175]
Protein digest	HCT116 cell lysate	cSCX cRPLC MALDI	Laboratory-modified FC204	2006	[176]
Glycated serum albumin		cRPLC MALDI	AccuSpot	2006	[177]
Protein digest	*Candida albicans*	cRPLC MALDI		2006	[178]
Protein digest	Rat liver proteasome	cRPLC MALDI	1100 Series	2006	[179]
Colicin E9 protein digest	*Escherichia coli*	cRPLC MALDI	Probot	2006	[180]
Protein digest	Multipotent adult progenitor cell line	SCX RP cRPLC MALDI	1100 Series	2006	[181]
Proteins	Rat liver	SCX cRPLC MALDI	Probot	2006	[182]
Neuropeptides	Brain rat tissue	cRPLC MALDI	Laboratory-built electric field-assisted	2006	[183]
Peptide mixtures	Kinetics of deamidation	cRPLC MALDI	Laboratory-built contact	2006	[184]
Peptide mixtures	Prediction of retention times	cRPLC MALDI	Laboratory-built contact	2006	[185]
Protein digest	*Escherichia coli*	Multi cRPLC MALDI	Laboratory-built	2005	[24]
Protein digest	Squamous carcinoma cells	SCX cRPLC MALDI	Heated droplet	2005	[186]
Protein digest	*Escherichia coli*	cRPLC MALDI	Heated droplet	2005	[187]
Polydisperse fluorosurfactant FC134		CE MALDI	Laboratory-built	2005	[188]
Protein digest	Yeast	SCX/SAX/cSCX cRPLC MALDI	Probot	2005	[189]
Tumor peptides	Renal cell carcinoma	cRPLC MALDI	1100 series spotter and Probot	2005	[190]
Proteins	Blood serum	CIEF MALDI	Laboratory-built	2005	[54]
Protein digest	Milk	cRPLC MALDI	Heated droplet	2005	[191]
Protein digest	GST fusion proteins	cRPLC MALDI	Laboratory-built contact	2005	[192]
Protein digest	Human serum	cRPLC MALDI	Probot	2005	[193]
Protein digest	teratocarcinoma cell lines	cRPLC MALDI	Probot	2005	[194]
Protein digest	*Escherichia coli*	cRPLC MALDI	Laboratory-built contact	2005	[195]
Membrane protein digest	*Staphylococcus aureus* N315	cRPLC MALDI	Laboratory-built	2005	[196]
Membrane protein digest	HT29 cells	cRPLC MALDI	Heated droplet interface	2004	[197]
Proteins	Tear fluid	CE MALDI	Probot	2004	[46]
Penicillin-binding proteins, digest	*Escherichia coli*	SCX cRPLC MALDI	Probot	2004	[198]
Glycopeptides	Asialofetuin digest	cRPLC MALDI	Probot	2004	[199]
Lectin affinity purified glycoprotein digest	K562 cells	cRPLC MALDI	Laboratory-built contact	2004	[200]
Peptide mixtures	Prediction of retention times	cRPLC MALDI	Laboratory-built contact	2004	[201]
Peptide mixtures	Site-specific glycosylation	cRPLC MALDI	Laboratory-built contact	2004	[202]
Protein digest	Murine brain prion protein, tracheal epithelium gland secretion	SCX cRPLC MALDI	Probot	2003	[203]
Protein digest	Bovine mitochondrial ribosomes	cRPLC MALDI	Probot	2003	[110]
Nonionic emulsifiers	Cremophor EL	CE MALDI	Probot	2002	[204]

8. Conclusions

Recent technological advancements, namely increased repetition rate of desorption experiments and faster data acquisition and processing promote the expansion of microcolumn technique off-line interfacing. The inability to adequately sample all proteins in a complex matrix due to the high dynamic range of protein concentrations and to identify the same proteins reproducibly in different laboratories using different MS platforms re-enables the off-line systems to enter the science foreground. Ultimately, a similar degree of automation as with LC ESI MS may allow researchers to take full advantage of the benefits offered by the off-line interface. While ESI is still considered the foremost ionization technique in MS coupling, off-line coupling has increased utilization in various fields of chemistry, especially due to dissimilar ionization efficiencies of ESI and MALDI and the decoupling of separation and MS.

It includes avoiding a throughput mismatch where a too slow or a too fast mass spectrometer is coupled on-line to LC. Since the MS is performed separately, the use of high speed MS, such as TOF, can significantly decrease the time needed for analysis and re-analysis of the separation record. Moreover, the separation can be archived and/or exposed to other analytical techniques, such as laser ablation/desorption ICP MS. Alternatively, it can be subjected to on-target chemical reactions prior to MS.

Acknowledgments

References

[1] A. Gaspar, M. Englmann, A. Fekete, M. Harir, P. Schmitt-Kopplin, Electrophoresis 29 (2008) 66.
[2] A. Staub, J. Schappler, S. Rudaz, J.-L. Veuthey, Electrophoresis 30 (2009) 1610.
[3] E. Edwards, J. Thomas-Oates, Analyst 130 (2005) 13.
[4] R. Haselberg, G.J. de Jong, G.W. Somsen, J. Chromatogr. A 1159 (2007) 81.
[5] C.W. Huck, R. Bakry, L.A. Huber, G.K. Bonn, Electrophoresis 27 (2006) 2063.
[6] F.E. Ahmed, J. Chromatogr. B 877 (2009) 1963.
[7] M. Karas, F. Hillenkamp, Anal. Chem. 60 (1988) 2299.
[8] Z.X. Shen, J.J. Thomas, C. Averbuj, K.M. Broo, M. Engelhard, J.E. Crowell, M.G. Finn, G. Siuzdak, Anal. Chem. 73 (2001) 612.
[9] I. Feuerstein, M. Rainer, K. Bernardo, G. Stecher, C.W. Huck, K. Kofler, A. Pelzer, W. Horninger, H. Klocker, G. Bartsch, G.K. Bonn, J. Proteome Res. 4 (2005) 2320.
[10] Z. Takats, J.M. Wiseman, B. Gologan, R.G. Cooks, Science 306 (2004) 471.
[11] A.L. Gray, Analyst 110 (1985) 551.
[12] O. Pes, P. Jungova, R. Vyhnanek, T. Vaculovic, V. Kanicky, J. Preisler, Anal. Chem. 80 (2008) 8725.
[13] R.J. Simpson, L.M. Connolly, J.S. Eddes, J.J. Pereira, R.L. Moritz, G.E. Reid, Electrophoresis 21 (2000) 1707.
[14] J.E. Froehlich, C.G. Wilkerson, W.K. Ray, R.S. McAndrew, K.W. Osteryoung, D.A. Gage, B.S. Phinney, J. Proteome Res. 2 (2003) 413.
[15] A.J. Link, J. Eng, D.M. Schieltz, E. Carmack, G.J. Mize, D.R. Morris, B.M. Garvik, J.R. Yates, Nat. Biotechnol. 17 (1999) 676.
[16] M.P. Washburn, D. Wolters, J.R. Yates, Nat. Biotechnol. 19 (2001) 242.
[17] B.R. Fonslow, J.R. Yates, J. Sep. Sci. 32 (2009) 1175.
[18] J.Z. Bereszczak, F.L. Brancia, Chem. Combinatorial, Comb. Chem. High Throughput Screen. 12 (2009) 185.
[19] J.B. Fenn, M. Mann, C.K. Meng, S.F. Wong, C.M. Whitehouse, Science 246 (1989) 64.
[20] A. Graber, P.S. Juhasz, N. Khainovski, K.C. Parker, D.H. Patterson, S.A. Martin, Proteomics 4 (2004) 474.
[21] T. Hasegawa, Y. Wakita, Y.B. Zhu, H. Matsuura, H. Haraguchi, T. Umemura, Bull. Chem. Soc. Jpn. 80 (2007) 503.
[22] J. Preisler, P. Hu, T. Rejtar, E. Moskovets, B.L. Karger, Anal. Chem. 74 (2002) 17.
[23] C. Ericson, Q.T. Phung, D.M. Horn, E.C. Peters, J.R. Fitchett, S.B. Ficarro, A.R. Salomon, L.M. Brill, A. Brock, Anal. Chem. 75 (2003) 2309.
[24] H.S. Chen, T. Rejtar, V. Andreev, E. Moskovets, B.L. Karger, Anal. Chem. 77 (2005) 7816.
[25] H. Lee, T.J. Griffin, S.P. Gygi, B. Rist, R. Aebersold, Anal. Chem. 74 (2002) 4353.
[26] E. Moskovets, J. Preisler, H.S. Chen, T. Rejtar, V. Andreev, B.L. Karger, Anal. Chem. 78 (2006) 912.
[27] M.L. Vestal, J. Mass Spectrom. 44 (2009) 303.
[28] A. Booy, K. Lewis-Torpey, C. Hunter, www.appliedbiosystems.com, 2009.
[29] R. Schafer, LC GC Eur. (2009) 26.
[30] S. Udiavar, A. Apffel, J. Chakel, S. Swedberg, W.S. Hancock, E. Pungor, Anal. Chem. 70 (1998) 3572.
[31] T.J. Griffin, S.P. Gygi, B. Rist, R. Aebersold, A. Loboda, A. Jilkine, W. Ens, K.G. Standing, Anal. Chem. 73 (2001) 978.
[32] J.P. Barry, D.R. Radtke, W.J. Carton, R.T. Anselmo, J.V. Evans, J. Chromatogr. A 800 (1998) 13.
[33] G. Choudhary, J. Chakel, W. Hancock, A. Torres-Duarte, G. McMahon, I. Wainer, Anal. Chem. 71 (1999) 855.
[34] P.A. Vanveelen, U.R. Tjaden, J. Vandergreef, A. Ingendoh, F. Hillenkamp, J. Chromatogr. 647 (1993) 367.
[35] W. Weinmann, C.E. Parker, L.J. Deterding, D.I. Papac, J. Hoyes, M. Przybylski, K.B. Tomer, J. Chromatogr. A 680 (1994) 353.
[36] K.L. Walker, R.W. Chiu, C.A. Monnig, C.L. Wilkins, Anal. Chem. 67 (1995) 4197.
[37] J. Preisler, F. Foret, B.L. Karger, Anal. Chem. 70 (1998) 5278.
[38] H.S. Chen, T. Rejtar, V. Andreev, E. Moskovets, B.L. Karger, Anal. Chem. 77 (2005) 2323.
[39] R. Takigiku, T. Keough, M.P. Lacey, R.E. Schneider, Rapid Commun. Mass Spectrom. 4 (1990) 24.
[40] R.A. Wallingford, A.G. Ewing, Anal. Chem. 59 (1987) 1762.
[41] T. Keough, R. Takigiku, M.P. Lacey, M. Purdon, Anal. Chem. 64 (1992) 1594.
[42] E. Mirgorodskaya, C. Braeuer, P. Fucini, H. Lehrach, J. Gobom, Proteomics 5 (2005) 399.
[43] T. Rejtar, P. Hu, P. Juhasz, J.M. Campbell, M.L. Vestal, J. Preisler, B.L. Karger, J. Proteome Res. 1 (2002) 171.
[44] S. Hsieh, K. Dreisewerd, R.C. van der Schors, C.R. Jimenez, J.R. Stahl-Zeng, F. Hillenkamp, J.W. Jorgenson, W.P.M. Geraerts, K.W. Li, Anal. Chem. 70 (1998) 1847.
[45] O. Krokhin, Y. Qian, J.R. McNabb, V. Spicer, K.G. Standing, W. Ens, Proceedings of the 50th ASMS Conference on Mass Spectrometry and Allied Topics, Orlando, FL, USA, 2002.
[46] A. Zuberovic, S. Ullsten, U. Hellman, K.E. Markides, J. Bergquist, Rapid Commun. Mass Spectrom. 18 (2004) 2946.
[47] J.S. Page, S.S. Rubakhin, J.V. Sweedler, Anal. Chem. 74 (2002) 497.
[48] S.S. Rubakhin, J.S. Page, B.R. Monroe, J.V. Sweedler, Electrophoresis 22 (2001) 3752.
[49] J.S. Page, S.S. Rubakhin, J.V. Sweedler, Analyst 125 (2000) 555.
[50] H. Suzuki, O. Muller, A. Guttman, B.L. Karger, Anal. Chem. 69 (1997) 4554.
[51] M. Lechner, A. Seifner, A.M. Rizzi, Electrophoresis 29 (2008) 1974.
[52] L.H.H. Silvertand, J.S. Torano, G.J. de Jong, W.P. van Bennekom, Electrophoresis 30 (2009) 1828.
[53] A. Chartogne, M. Gaspari, S. Jespersen, B. Buscher, E. Verheij, R. van der Heijden, U. Tjaden, J. van der Greef, Rapid Commun. Mass Spectrom. 16 (2002) 201.
[54] T.A. Crowley, M.A. Hayes, Proteomics 5 (2005) 3798.
[55] N.G. Weiss, N.L. Zwick, M.A. Hayes, J. Chromatogr. A 1217 (2010) 179.
[56] T.J. Tegeler, Y. Mechref, K. Boraas, J.P. Reilly, M.V. Novotny, Anal. Chem. 76 (2004) 6698.
[57] J. Zhang, H.L. Hu, M.X. Gao, P.Y. Yang, X.M. Zhang, Electrophoresis 25 (2004) 2374.
[58] M. Schuerenbeg, C. Luebbert, H. Eickhoff, M. Kalkum, H. Lehrach, E. Nordhoff, Anal. Chem. 72 (2000) 3436.
[59] T. Johnson, J. Bergquist, R. Ekman, E. Nordhoff, M. Schurenberg, K.D. Kloppel, M. Muller, H. Lehrach, J. Gobom, Anal. Chem. 73 (2001) 1670.
[60] T.I. Stevenson, J.A. Loo, K.D. Greis, Anal. Biochem. 262 (1998) 99.
[61] T.I. Stevenson, J.A. Loo, LC GC-Mag. Sep. Sci. 16 (1998) 54.
[62] E. Nagele, M. Vollmer, Rapid Commun. Mass Spectrom. 18 (2004) 3008.
[63] S.J. Hattan, M.L. Vestal, Anal. Chem. 80 (2008) 9115.
[64] J. Wang, M. Ma, R. Chen, L. Li, Anal. Chem. 80 (2008) 6168.
[65] H.Y. Zhang, R.M. Caprioli, J. Mass Spectrom. 31 (1996) 1039.
[66] N. Ojima, T. Shingaki, T. Yamamoto, T. Masujima, Electrophoresis 22 (2001) 3478.
[67] J. Jacksén, T. Redeby, A. Emmer, J. Sep. Sci. 29 (2006) 288.
[68] X.X. Chen, A. Murawski, G. Kuang, D.J. Sexton, W. Galbraith, Anal. Chem. 78 (2006) 6160.
[69] S.I. Snovida, V.C. Chen, O. Krokhin, H. Perreault, Anal. Chem. 78 (2006) 6556.
[70] R.W. Chiu, K.L. Walker, J.J. Hagen, C.A. Monnig, C.L. Wilkins, Anal. Chem. 67 (1995) 4190.
[71] J.M. Busnel, J. Josserand, N. Lion, H.H. Girault, Anal. Chem. 81 (2009) 3867.
[72] R.R. Hensel, R.C. King, K.G. Owens, Rapid Commun. Mass Spectrom. 11 (1997) 1785.
[73] G.S. McLeod, J. Axelsson, R. Self, P.J. Derrick, Rapid Commun. Mass Spectrom. 11 (1997) 214.
[74] J. Axelsson, A.M. Hoberg, C. Waterson, P. Myatt, G.L. Shield, J. Varney, D.M. Haddleton, P.J. Derrick, Rapid Commun. Mass Spectrom. 11 (1997) 209.
[75] G.S. McLeod, J. Axelsson, R. Self, P.J. Derrick, 22nd Annual British Mass Spectrometry Conference, Swansea, Wales, 1996, p. 214.
[76] X.W. Lou, J.L.J. van Dongen, J. Mass Spectrom. 35 (2000) 1308.
[77] G.L. DeVault, M.J. Sepaniak, Electrophoresis 21 (2000) 1320.
[78] J.E. Prenni, Z.X. Shen, S. Trauger, W. Chen, G. Siuzdak, Spectroscopy 17 (2003) 693.
[79] H. Wei, K. Nolkrantz, D.H. Powell, J.H. Woods, M.C. Ko, R.T. Kennedy, Rapid Commun. Mass Spectrom. 18 (2004) 1193.
[80] D.B. Wall, S.J. Berger, J.W. Finch, S.A. Cohen, K. Richardson, R. Chapman, D. Drabble, J. Brown, D. Gostick, Electrophoresis 23 (2002) 3193.
[81] J. Perez, C.J. Petzold, M.A. Watkins, W.E. Vaughn, H.I. Kenttamaa, J. Am. Soc. Mass Spectrom. 10 (1999) 1105.
[82] K.Y.C. Fung, S. Askovic, F. Basile, M.W. Duncan, Proteomics 4 (2004) 3121.
[83] F. Basile, G.E. Kassalainen, S.K.R. Williams, Anal. Chem. 77 (2005) 3008.
[84] P. Onnerfjord, J. Nilsson, L. Wallman, T. Laurell, G. Marko-Varga, Anal. Chem. 70 (1998) 4755.
[85] T. Miliotis, S. Kjellstrom, J. Nilsson, T. Laurell, L.E. Edholm, G. Marko-Varga, J. Mass Spectrom. 35 (2000) 369.
[86] T. Miliotis, P.O. Ericsson, G. Marko-Varga, R. Svensson, J. Nilsson, T. Laurell, R. Bischoff, J. Chromatogr. B 752 (2001) 323.
[87] T. Miliotis, S. Kjellstrom, P. Onnerfjord, J. Nilsson, T. Laurell, L.E. Edholm, G. Marko-Varga, J. Chromatogr. A 886 (2000) 99.
[88] E.C. Peters, A. Brock, D.M. Horn, Q.T. Phung, C. Ericson, A.R. Salomon, S.B. Ficarro, L.M. Brill, LC GC Eur. 15 (2002) 423.
[89] B.Y. Zhang, C. McDonald, L. Li, Anal. Chem. 76 (2004) 992.
[90] S.D. Hanton, X.M. Liu, Anal. Chem. 72 (2000) 4550.
[91] J.B. Young, L. Li, J. Am. Soc. Mass Spectrom. 17 (2006) 325.
[92] J.B. Young, L. Li, Anal. Chem. 79 (2007) 5927.
[93] M.W. Vannatta, C.D. Whitmore, N.J. Dovichi, Electrophoresis 30 (2009) 4071.
[94] J. Liu, K. Tseng, B. Garcia, C.B. Lebrilla, E. Mukerjee, S. Collins, R. Smith, Anal. Chem. 73 (2001) 2147.

[95] M.L.S. Mok, L. Hua, J.B.C. Phua, M.K.T. Wee, N.S.K. Sze, Analyst 129 (2004) 109.
[96] Y.C. Xu, M.W. Little, K.K. Murray, J. Am. Soc. Mass Spectrom. 17 (2006) 469.
[97] J. Johan, T. Frisk, T. Redeby, V. Parmar, W. van der Wijngaart, G. Stemme, A. Emmer, Electrophoresis 28 (2007) 2458.
[98] M. Gustafsson, D. Hirschberg, C. Palmberg, H. Jornvall, T. Bergman, Anal. Chem. 76 (2004) 345.
[99] D. Hirschberg, T. Jagerbrink, J. Samskog, M. Gustafsson, M. Stahlberg, G. Alvelius, B. Husman, M. Carlquist, H. Jornvall, T. Bergman, Anal. Chem. 76 (2004) 5864.
[100] J. Lee, H.K. Musyimi, S.A. Soper, K.K. Murray, J. Am. Soc. Mass Spectrom. 19 (2008) 964.
[101] L.J. Yu, Y. Chen, M.P. DeNinno, T.N. O'Connell, C. Hop, Drug Metab. Dispos. 33 (2005) 484.
[102] X. Li, A. Fekete, M. Englmann, C. Frommberger, S. Lv, G. Chen, P. Schmitt-Kopplin, Anal. Bioanal. Chem. 389 (2007) 1439.
[103] A. Lu, L.F. Waanders, R. Almeida, G.Q. Li, M. Allen, R. Cox, J.V. Olsen, T. Bonaldi, M. Mann, Int. J. Mass Spectrom. 268 (2007) 158.
[104] S. Kim, R.P. Rodgers, G.T. Blakney, C.L. Hendrickson, A.G. Marshall, J. Am. Soc. Mass Spectrom. 20 (2009) 263.
[105] K. Geddes, G. Adamson, N. Dube, S. Crathern, R.C. King, Rapid Commun. Mass Spectrom. 23 (2009) 1303.
[106] T. Wehr, LC GC N. Am. 21 (2003) 974.
[107] F. Foret, J. Preisler, Proteomics 2 (2002) 360.
[108] M. Lasaosa, N. Delmotte, C.G. Huber, K. Melchior, E. Heinzle, A. Tholey, Anal. Bioanal. Chem. 393 (2009) 1245.
[109] S. Amon, A. Plematl, A. Rizzi, Electrophoresis 27 (2006) 1209.
[110] W.M. Bodnar, R.K. Blackburn, J.M. Krise, M.A. Moseley, J. Am. Soc. Mass Spectrom. 14 (2003) 971.
[111] M.A. Kuzyk, L.B. Ohlund, M.H. Elliott, D. Smith, H. Qian, A. Delaney, C.L. Hunter, C.H. Borchers, Proteomics 9 (2009) 3328.
[112] A. Zuberovic, M. Wetterhall, J. Hanrieder, J. Bergquist, Electrophoresis 30 (2009) 1836.
[113] G. Zegels, G.A.A. Van Raemdonck, E.P. Coen, W.A.A. Tjalma, X.W.M. Van Ostade, Proteome Sci. 7 (2009).
[114] H. Neubert, T.P. Bonnert, K. Rumpel, B.T. Hunt, E.S. Henle, I.T. James, J. Proteome Res. 7 (2008) 2270.
[115] J. Hanrieder, A. Zuberovic, J. Bergquist, J. Chromatogr. A 1216 (2009) 3621.
[116] P. Wang, A. Lo, J.B. Young, J.H. Song, R. Lai, N.M. Kneteman, C.H. Hao, L. Li, J. Proteome Res. 8 (2009) 3403.
[117] R. Vitorino, A. Barros, A. Caseiro, P. Domingues, J. Duarte, F. Amado, Proteome Clin. Appl. 3 (2009) 528.
[118] M. Takikawa, Y. Akiyama, T. Ashizawa, A. Yamamo, N. Yamazaki, Y. Kiyohara, N. Oku, K. Yamaguchi, Proteom. Clin. Appl. 3 (2009) 552.
[119] K. Bilikova, E. Mirgorodskaya, G. Bukovska, J. Gobom, H. Lehrach, J. Simuth, Proteomics 9 (2009) 2131.
[120] A. Zerck, E. Nordhoff, A. Resemann, E. Mirgorodskaya, D. Suckau, K. Reinert, H. Lehrach, J. Gobom, J. Proteome Res. 8 (2009) 3239.
[121] M.V. Muetzelburg, F. Hofmann, I. Just, A. Pich, J. Chromatogr. B 877 (2009) 1344.
[122] P. Kouvonen, L.A. McDonnell, R.M.A. Heeren, G.L. Corthals, Proteomics 9 (2009) 1662.
[123] E. Hardenborg, A. Botling-Taube, J. Hanrieder, M. Andersson, A. Alm, J. Bergquist, Proteom. Clin. Appl. 3 (2009) 299.
[124] P. Klemmer, A.B. Smit, K.W. Li, J. Proteome Res. 72 (2009) 82.
[125] D. Molle, J. Jardin, M. Piot, M. Pasco, J. Leonil, V. Gagnaire, J. Chromatogr. A 1216 (2009) 2424.
[126] H. Kamada, T. Fugmann, D. Neri, C. Roesli, Proteomics 9 (2009) 783.
[127] S. Ons, F. Richter, H. Urlaub, R.R. Pomar, Proteomics 9 (2009) 788.
[128] A. Amantonico, P.L. Urban, R. Zenobi, Analyst 134 (2009) 1536.
[129] K. Jurcic, K.K.C. Yeung, Electrophoresis 30 (2009) 1817.
[130] M.M. Ma, J.H. Wang, R.B. Chen, L.J. Li, J. Proteome Res. 8 (2009) 2426.
[131] K. Helmja, M. Borissova, T. Knjazeva, M. Jaanus, U. Muinasmaa, M. Kaljurand, M. Vaher, J. Chromatogr. A 1216 (2009) 3666.
[132] L. Jing, K. Amster, Int. J. Mass Spectrom. 287 (2009) 27.
[133] J.H. Wang, X.Y. Jiang, R.M. Sturm, L.J. Li, J. Chromatogr. A 1216 (2009) 8283.
[134] M. Worner, K. Melchior, N. Delmotte, K.H. Hwang, K. Monostory, C.G. Huber, R. Bernhardt, J. Sep. Sci. 32 (2009) 1165.
[135] G. Ridlova, J.C. Mortimer, S.L. Maslen, P. Dupree, E. Stephens, Rapid Commun. Mass Spectrom. 22 (2008) 2723.
[136] E. Stodulkova, P. Novak, S.O. Deininger, P. Man, J. Capkova, D. Kavan, E. Ivaskova, M. Flieger, Immunol. Lett. 116 (2008) 79.
[137] M. Zarei, S. Kirsch, J. Muthing, L. Bindila, J. Peter-Katalinic, Anal. Bioanal. Chem. 391 (2008) 289.
[138] S. Kalkhof, S. Haehn, C. Ihling, M. Paulsson, N. Smyth, A. Sinz, Rapid Commun. Mass Spectrom. 22 (2008) 1933.
[139] M.X. Gao, W.J. Yu, Y. Zhang, G.Q. Yan, C.H. Deng, P.Y. Yang, X.M. Zhang, Analyst 133 (2008) 1261.
[140] V.C. Chen, C.C. Chou, H.Y. Hsieh, H. Perreault, K.H. Khoo, J. Mass Spectrom. 43 (2008) 1649.
[141] K. Benkali, P. Marquet, J.P. Rerolle, Y. Le Meur, L.N. Gastinel, BMC Genomics 9 (2008).
[142] M. Getie-Kebtie, P. Franke, R. Aksamit, M.A. Alterman, J. Proteome Res. 7 (2008) 3697.
[143] C. Manzano, Z. Abraham, G. Lopez-Torrejon, J.C. Del Pozo, Plant Mol. Biol. 68 (2008) 145.
[144] M. Dong, L.L. Yang, K. Williams, S.J. Fisher, S.C. Hall, M.D. Biggin, J. Jin, H.E. Witkowska, J. Proteome Res. 7 (2008) 1836.
[145] C.S. Ang, P.D. Veith, S.G. Dashper, E.C. Reynolds, Proteomics 8 (2008) 1645.
[146] S. Pan, J. Rush, E.R. Peskind, D. Galasko, K. Chung, J. Quinn, J. Jankovic, J.B. Leverenz, C. Zabetian, C. Pan, Y. Wang, J.H. Oh, J. Gao, J.P. Zhang, T. Montine, J. Zhang, J. Proteome Res. 7 (2008) 720.
[147] G.A. Riding, A. Jones, M.K. Holland, J.R. Hill, S.A. Lehnert, Proteomics 8 (2008) 160.
[148] M.Q. Qian, D.E. Sleat, H.Y. Zheng, D. Moore, P. Lobel, Mol. Cell. Proteomics 7 (2008) 58.
[149] J. Hanrieder, A. Nyakas, T. Naessen, J. Bergquist, J. Proteome Res. 7 (2008) 443.
[150] D. Shearer, W. Ens, K. Standing, G. Valdimarsson, Invest. Ophthalmol. Vis. Sci. 49 (2008) 1553.
[151] S.L. Maslen, F. Goubet, A. Adam, P. Dupree, E. Stephens, Carbohydr. Res. 342 (2007) 724.
[152] Z.J. Li, Q.S. Lin, J. Chen, J.L. Wu, T.K. Lim, S.S. Loh, X.H. Tang, C.L. Hew, Mol. Cell. Proteomics 6 (2007) 1609.
[153] A. Lapolla, F.L. Brancia, J. Bereszczak, D. Fedele, L. Baccarin, R. Seraglia, P. Traldi, Mol. Nutr. Food Res. 51 (2007) 456.
[154] M. Rainer, M. Najam-ul-Haq, R. Bakry, C.W. Huck, G.K. Bonn, J. Proteome Res. 6 (2007) 382.
[155] F.L. Brancia, J.Z. Bereszczak, E. Piatkowska, D. Delneri, Rapid Commun. Mass Spectrom. 21 (2007) 3069.
[156] C.L. Liu, X.M. Zhang, J. Chromatogr. A 1139 (2007) 191.
[157] F. Schmidt, H.K. Hustoft, M. Strozynski, C. Dimmler, T. Rude, B. Thiede, Electrophoresis 28 (2007) 4359.
[158] T. Kim, S.J. Kim, K. Kim, U.B. Kang, C. Lee, K.S. Park, H.G. Yu, Y. Kim, Proteomics 7 (2007) 4203.
[159] E. Oliveira, I. Amara, D. Bellido, M.A. Odena, E. Dominguez, M. Pages, A. Goday, J. Mass Spectrom. 42 (2007) 1485.
[160] S.S. Park, D.S. Kim, K.S. Park, H.J. Song, S.Y. Kim, Proteom. Clin. Appl. 1 (2007) 555.
[161] H.M. Zhang, Q.S. Lin, S. Ponnusamy, N. Kothandaraman, T.K. Lim, C.Q. Zhao, H.S. Kit, B. Arijit, M. Rauff, C.L. Hew, M.C.M. Chung, S.B. Joshi, M. Choolani, Proteomics 7 (2007) 1654.
[162] J.A. Rodrigues, F.J. Lopez-Baena, F.J. Ollero, J.M. Vinardell, M.D. Espuny, R.A. Bellogin, J.E. Ruiz-Sainz, J.R. Thomas, D. Sumpton, J. Ault, J. Thomas-Oates, J. Proteome Res. 6 (2007) 1029.
[163] W.R. Alley, Y. Mechref, I. Klouckova, M.V. Novotny, J. Proteome Res. 6 (2007) 124.
[164] J. Rechthaler, A. Rizzi, G. Allmaier, Int. J. Mass Spectrom. 268 (2007) 131.
[165] V. Spicer, A. Yamchuk, J. Cortens, S. Sousa, W. Ens, K.G. Standing, J.A. Wilkins, O.V. Krokhin, Anal. Chem. 79 (2007) 8762.
[166] N.V. Bykova, C. Rampitsch, O. Krokhin, K.G. Standing, W. Ens, Anal. Chem. 78 (2006) 1093.
[167] R.M. Vallant, Z. Szabo, L. Trojer, M. Najam-ul-Haq, M. Rainer, C.W. Huck, R. Bakry, G.K. Bonn, J. Proteome Res. 6 (2007) 44.
[168] S.J. Hattan, K.C. Parker, Anal. Chem. 78 (2006) 7986.
[169] C. Yoo, J. Zhao, M. Pal, K. Hersberger, C.G. Huber, D.M. Simeone, D.G. Beer, D.M. Lubman, Electrophoresis 27 (2006) 3643.
[170] C. Hunzinger, A. Schrattenholz, S. Poznanovic, G.P. Schwall, W. Stegmann, J. Chromatogr. A 1123 (2006) 170.
[171] S. Maslen, P. Sadowski, A. Adam, K. Lilley, E. Stephens, Anal. Chem. 78 (2006) 8491.
[172] P. Zurbig, M.B. Renfrow, E. Schiffer, J. Novak, M. Walden, S. Wittke, I. Just, M. Pelzing, C. Neususs, D. Theodorescu, K.E. Root, M.M. Ross, H. Mischak, Electrophoresis 27 (2006) 2111.
[173] K.W. Ro, H. Liu, D.R. Knapp, J. Chromatogr. A 1111 (2006) 40.
[174] W.J. Song, Q.S. Lin, S.B. Joshi, T.K. Lim, C.L. Hew, Mol. Cell. Proteomics 5 (2006) 256.
[175] W.J. Yu, Y. Li, C.H. Deng, X.M. Zhang, Electrophoresis 27 (2006) 2100.
[176] H. Saito, Y. Oda, T. Sato, J. Kuromitsu, Y. Ishihama, J. Proteome Res. 5 (2006) 1803.
[177] F.L. Brancia, J.Z. Bereszczak, A. Lapolla, D. Fedele, L. Baccarin, R. Seraglia, P. Traldi, J. Mass Spectrom. 41 (2006) 1179.
[178] J.E. Melanson, K.A. Chisholm, D.M. Pinto, Rapid Commun. Mass Spectrom. 20 (2006) 904.
[179] F. Schmidt, B. Dahlmann, K. Janek, A. Kloss, M. Wacker, R. Ackermann, B. Thiede, P.R. Jungblut, Proteomics 6 (2006) 4622.
[180] A. Scholten, N.F.C. Visser, R.H.H. van den Heuvel, A.J.R. Heck, J. Am. Soc. Mass Spectrom. 17 (2006) 983.
[181] K. Gevaert, J. Pinxteren, H. Demol, K. Hugelier, A. Staes, J. Van Damme, L. Martens, J. Vandekerckhove, J. Proteome Res. 5 (2006) 1415.
[182] M.X. Gao, J. Zhang, C.H. Deng, P.Y. Yang, X.M. Zhang, J. Proteome Res. 5 (2006) 2853.
[183] H. Wei, K. Nolkrantz, M.C. Parkin, C.N. Chisolm, J.P. O'Callaghan, R.T. Kennedy, Anal. Chem. 78 (2006) 4342.
[184] O.V. Krokhin, M. Antonovici, W. Ens, J.A. Wilkins, K.G. Standing, Anal. Chem. 78 (2006) 6645.
[185] O.V. Krokhin, S. Ying, J.P. Cortens, D. Ghosh, V. Spicer, W. Ens, K.G. Standing, R.C. Beavis, J.A. Wilkins, Anal. Chem. 78 (2006) 6265.
[186] C.J. Ji, L.J. Li, M. Gebre, M. Pasdar, L. Li, J. Proteome Res. 4 (2005) 1419.
[187] C.J. Ji, L. Li, J. Proteome Res. 4 (2005) 734.
[188] S.Y. Al-Jarah, J. Sjodahl, A. Woldegiorgis, A. Emmer, J. Sep. Sci. 28 (2005) 239.
[189] S.J. Hattan, J. Marchese, N. Khainovski, S. Martin, P. Juhasz, J. Proteome Res. 4 (2005) 1931.

[190] S. Hofmann, M. Gluckmann, S. Kausche, A. Schmidt, C. Corvey, R. Lichtenfels, C. Huber, C. Albrecht, M. Karas, W. Herr, Mol. Cell. Proteomics 4 (2005) 1888.
[191] C.J. Ji, N. Guo, L. Li, J. Proteome Res. 4 (2005) 2099.
[192] E. Mirgorodskaya, E. Wanker, A. Otto, H. Lehrach, J. Gobom, J. Proteome Res. 4 (2005) 2109.
[193] J.Y. Kim, J.H. Lee, G.W. Park, K. Cho, K.H. Kwon, Y.M. Park, S.Y. Cho, Y.K. Paik, J.S. Yoo, Proteomics 5 (2005) 3376.
[194] S.B. Scheurer, C. Roesli, D. Neri, G. Elia, Proteomics 5 (2005) 3035.
[195] A. Pashkova, H.S. Chen, T. Rejtar, X. Zang, R. Giese, V. Andreev, E. Moskovets, B.L. Karger, Anal. Chem. 77 (2005) 2085.
[196] A. Scherl, P. Francois, M. Bento, J.M. Deshusses, Y. Charbonnier, W. Converset, A. Huyghe, N. Walter, C. Hoogland, R.D. Appel, J.C. Sanchez, C.G. Zimmermann-Ivol, G.L. Corthals, D.F. Hochstrasser, J. Schrenzel, J. Microbiol. Methods 60 (2005) 247.
[197] N. Zhang, N. Li, L. Li, J. Proteome Res. 3 (2004) 719.
[198] Y.J. Zhen, N.F. Xu, B. Richardson, R. Becklin, J.R. Savage, K. Blake, J.M. Peltier, J. Am. Soc. Mass Spectrom. 15 (2004) 803.
[199] G. Lochnit, R. Geyer, Biomed. Chromatogr. 18 (2004) 841.
[200] D. Ghosh, O. Krokhin, M. Antonovici, W. Ens, K.G. Standing, R.C. Beavis, J.A. Wilkins, J. Proteome Res. 3 (2004) 841.
[201] O.V. Krokhin, R. Craig, V. Spicer, W. Ens, K.G. Standing, R.C. Beavis, J.A. Wilkins, Mol. Cell. Proteomics 3 (2004) 908.
[202] O. Krokhin, W. Ens, K.G. Standing, J. Wilkins, H. Perreault, Rapid Commun. Mass Spectrom. 18 (2004) 2020.
[203] K.C. Hansen, G. Schmitt-Ulms, R.J. Chalkley, J. Hirsch, M.A. Baldwin, A.L. Burlingame, Mol. Cell. Proteomics 2 (2003) 299.
[204] T. Meyer, D. Waidelich, A.W. Frahm, Electrophoresis 23 (2002) 1053.

2.2 Off-Line Coupling of Capillary Electrophoresis to Substrate-Assisted Laser Desorption Inductively Coupled Plasma Mass Spectrometry

Interfacing different MS techniques to separation methods have always been challenging by means of online coupling. Flow splitting or additional detectors connected in series may deteriorate the entire method's sensitivity, robustness, or applicability. A throughput mismatch may be an issue if too slow or too fast detection technique is used in an online-hyphenated separation. Another option is recording the separation on a suitable target, which may serve for archiving or reanalysis by a complementary technique. Analysis of metalloproteins is very challenging due to the presence of a low molecular metal (or a metal-containing group) and a large molecule of protein – both requiring a hard and soft ionization technique to be determined by MS. A sub-atmospheric chamber, originally capable of depositing microcolumn separations and analyzing them by MALDI MS, was developed in 2000.[32,33] Nowadays, many commercial spotting devices capable of storing liquid separations for different analyses have been readily available.[34]

A specific type of disposable, co-polymer target has been tested in assisting the laser ablation process in laser ablation (LA) ICP MS. This surface-assisting process resulted in mere desorption of the deposited sample rather than ablation of the bulk material. Since the laser energies may have been kept as low as tens of $MW \cdot cm^{-2}$, the limits of detection (LOD) reached approximately an order of magnitude lower than in the case of common LA ICP MS involving high energies (units to tens of $GW \cdot cm^{-2}$). Even at low laser energies, a reliable transfer of the sample to an ICP cell was assured. This surface-assisted laser desorption (SALD) mechanism has been proposed, investigated, and finally applied in a model speciation analysis to demonstrate the feasibility of a complementary analysis of metalloproteins. The SALD technique was further applied in myeloid leukemia cells,[35] improved by cold plasma,[36] employed in analysis of nanoparticles,[37] or analysis of sterols.[38]

Off-Line Coupling of Capillary Electrophoresis to Substrate-Assisted Laser Desorption Inductively Coupled Plasma Mass Spectrometry

Ondřej Peš, Pavla Jungová, Radek Vyhnánek, Tomáš Vaculovič, Viktor Kanický, and Jan Preisler*

Department of Chemistry, Faculty of Science, Masaryk University, Kotlářská 2, 611 37, Brno, Czech Republic

A novel off-line coupling of capillary electrophoresis (CE) and inductively coupled plasma mass spectrometry (ICPMS) is reported here. The coupling interface is based on the connection of a separation capillary to a deposition capillary via a liquid junction maintaining high separation efficiency and sample utilization due to the self-focusing effect and lack of pressure-induced flow in comparison with nebulizer-like interfaces. The separation is recorded in the form of droplets of CE effluent on a suitable substrate − a poly(ethylene terephthalate) glycol (PETG) sample plate placed inside a partially evacuated chamber. Substrate-assisted laser desorption (SALD) is used to vaporize the sample fractions and to enable further transfer to the ICPMS. The mechanism of SALD is examined using model samples deposited on a variety of substrates. The highest response is obtained for a PETG substrate; sample desorption due to ablation of PETG is found to outweigh direct ablation of sample. Detection limits are given for several metal elements. Finally, a rapid (2.5-min), high-resolution separation of Cr^{III}/Cr^{VI} species injected in subpicomolar quantity is shown.

Microcolumn separation techniques, such as capillary electrophoresis (CE) or microliquid chromatography (LC), continue to mature as important analytical tools in separation science. Advantages of the techniques include rapid analysis, minute sample size requirements, high separation efficiency, low limits of detection, and economical operating costs. With mass spectrometric (MS) detection, both CE and LC belong to the most powerful techniques for the identification of unknown substances in complex matrixes.[1]

Most hyphenated techniques usually combine a separation module with an online spectrometric detection technique, such as electrospray ionization MS or inductively coupled plasma (ICP) optical emission spectrometry (OES) or MS, to obtain structural or quantitative information. For quantitative elemental analysis, ICPMS is preferred to electrospray or ion spray mass spectrometry, because the signal from these techniques does not neces-

sarily have to be related to the total elemental concentration of the metal, even if a bare metal peak is observed.[2]

An increasing demand for information about element speciation at trace levels leads to coupling microcolumn separation techniques to ICP.[3] The toxicity of most elements depends on their chemical form; in some cases, one form of the metal can be toxic whereas the same metal in a different form is nontoxic or even essential for proper functioning of living organisms. The determination of the concentration of specific chemical forms is vital for the interpretation of their biochemical behavior or assessment of the potential danger to organisms.

In the literature, all approaches considering online coupling of LC[4,5] or CE[6−8] with ICPMS assume the efficient introduction of analytes into the ICP. Furthermore, the run buffer, micellar agent, salt concentration, pH, complexing agents, and analyte should not interfere with the ICP measurement, and ICPMS interface should not influence the performance of the separation. In the case of CE, utilization of a proper enrichment preconcentration technique (such as sample stacking, on-column transient isotachophoresis, field amplitude sample injection, precolumn extraction, or concentration) will overcome the low concentration sensitivity and limited capacity of CE.[9]

There are three main requirements that a CE-ICP interface design has to satisfy.[10,11] First, the interface must provide an electrical connection and a stable electrical current for reproducible electrophoretic separations. Second, the interface must adapt the flow rate of the electroosmotic flow inside the CE capillary to the flow rate of the nebulizer, and finally, the interface should prevent the occurrence of laminar flow inside the CE capillary caused by the nebulizer.

* To whom correspondence should be addressed. E-mail:preisler@chemi.muni.cz. Tel.:+420 549 496 629. Fax: +420 549 492 494.

(1) Lehmann, R.; Liebich, H. M.; Voelter, W. *J. Capillary Electrophor.* **1996**, *3*, 89–110.

(2) Olesik, J. W.; Thaxton, K. K.; Olesik, S. V. *J. Anal. At. Spectrom.* **1997**, *12*, 507–515.

(3) Michalke, B. *Electrophoresis* **2005**, *26*, 1584–1597.

(4) Sutton, K.; Sutton, R. M. C.; Caruso, J. A. *J. Chromatogr., A* **1997**, *789*, 85–126.

(5) Montes-Bayon, M.; DeNicola, K.; Caruso, J. A. *J. Chromatogr., A* **2003**, *1000*, 457–476.

(6) Kannamkumarath, S. S.; Wrobel, K.; B'Hymer, C.; Caruso, J. A. *J. Chromatogr., A* **2002**, *975*, 245–266.

(7) Alvarez-Llamas, G.; de laCampa, M. D.; Sanz-Medel, A. *TrAC-Trends Anal. Chem.* **2005**, *24*, 28–36.

(8) Olesik, J. W.; Kinzer, J. A.; Olesik, S. V. *Anal. Chem.* **1995**, *67*, 1–12.

(9) Barnes, R. M. *Fresenius J. Anal. Chem.* **1998**, *361*, 246–251.

(10) Schaumloffel, D.; Prange, A. *Fresenius J. Anal. Chem.* **1999**, *364*, 452–456.

(11) Prange, A.; Schaumloffel, D. *J. Anal. At. Spectrom.* **1999**, *14*, 1329–1332.

Several interface constructions based on concentric,[12−16] microconcentric,[10,11,17−22] cross-flow,[14,17] or ultrasonic[23] nebulizers have been presented and widely used, but the pressure-induced laminar flow inside the capillary still has a negative influence on the overall performance of such interfaces, in terms of separation efficiency and precision of the CE−ICPMS system. The laminar flow is usually counterbalanced using a back pressure of the makeup liquid or by applying negative pressure to the inlet vial. The interface construction introduced by Schaumlöffel and Prange[10,11] addresses the issue of detrimental suction effects via optimization of the fluid mechanics in the interface. This leads to negligible laminar flow inside the CE capillary, and the migration times of the analytes are thus both stable and reproducible. This interface has been commercialized (CEI-100, CETAC Technologies, Omaha, NE). Finally, the electrophoretic resolution has usually been traded off for analysis speed since ions with similar mobilities do not have to be electrophoretically separated. A direct injection nebulizer, introduced in 1995 by Avila and co-workers,[24] is probably the most efficient liquid sample introduction method for CE; however, the exact amount of the injected sample was not reported.

In the case of off-line configuration, the analyte separated by CE could be collected in vials, and elements determined from separated fractions (after dilution to 100 μL) by electrothermal vaporization ICPMS.[25−27] Advantages include easier sample handling than in an online approach, with no special interface like a nebulizer required. Since the CE was run with online UV detection independently on the ICPMS detector, migration times and UV spectra were obtained prior to the element detection with ICPMS.

In another area of chemistry, proteomics, approaches dealing with fraction collection of CE effluent via a deposition interface have been presented,[28,29] and commercially available deposition devices, spotters, have been introduced by virtually all the major manufacturers and are widely used in LC−MS.[30] Fractions can be collected on a wide variety of substrates, such as matrix-assisted laser desorption/ionization (MALDI) targets,[31] poly(vinylidene difluoride) membranes,[32] or microchip structures. To enable off-line coupling to ICPMS, desorption of the spotted samples has to be involved to enable vaporizing and transferring the sample spots from the substrates to element detector.

In common laser ablation, introduced in 1985 by Gray et al.,[33] a short-pulsed, high-power laser beam is focused onto a sample surface. The laser beam converts a finite volume of the solid sample instantaneously into its vapor-phase constituents. The vapor is then analyzed by measuring atomic/ionic emissions in the induced plasma by laser-induced breakdown spectroscopy or by transporting the vapor to another measurement system, such as ICPMS. With ICP as an atomization source, laser ablation (LA) has proved to be one of the most powerful analytical tools that can serve for nearly nondestructive determination of numbers of elements with very low detection limits in solids. Applications of LA ICPMS cover a great range of academic and industrial fields that include environmental,[34−36] geological,[37−39] archeological,[40,41] forensic,[42] and semiconductor manufacturing sectors.[43] However, the primary role of LA is engaged in analysis of sample material itself, and the possibility of laser desorption of deposited samples has not been considered.

Off-line coupling of LA ICPMS has been reported for planar separation techniques, such as gel electrophoresis[44−46] and thin-layer chromatography,[47] where a laser was used to ablate bulk separation medium with incorporated analytes. Recently, effluent fractions from high-performance liquid chromatography were pipetted in replicates on a polystyrene substrate, dried, manually excised, and analyzed using LA ICPMS.[48] In all these cases, laser fluences reached units of GW·cm^{−2}

In this paper, laser desorption is used to vaporize sample spots or dried separation fractions that had been deposited on a

(12) Lu, Q. H.; Bird, S. M.; Barnes, R. M. *Anal. Chem.* **1995**, *67*, 2949–2956.
(13) B'Hymer, C.; Day, J. A.; Caruso, J. A. *Appl. Spectrosc.* **2000**, *54*, 1040–1046.
(14) Majidi, V.; Miller-Ihli, N. J. *Analyst* **1998**, *123*, 803–808.
(15) Majidi, V.; Miller-Ihli, N. J. *Analyst* **1998**, *123*, 809–813.
(16) Mounicou, S.; Polec, K.; Chassaigne, H.; Potin-Gautier, M.; Lobinski, R. *J. Anal. At. Spectrom.* **2000**, *15*, 635–642.
(17) Baker, S. A.; Miller-Ihli, N. J. *Appl. Spectrosc.* **1999**, *53*, 471–478.
(18) Polec, K.; Szpunar, J.; Palacios, O.; Gonzalez-Duarte, P.; Atrian, S.; Lobinski, R. *J. Anal. At. Spectrom.* **2001**, *16*, 567–574.
(19) Prange, A.; Schaumloffel, D.; Bratter, P.; Richarz, A. N.; Wolf, C. *Fresenius J. Anal. Chem.* **2001**, *371*, 764–774.
(20) Schaumloffel, D.; Prange, A.; Marx, G.; Heumann, K. G.; Bratter, P. *Anal. Bioanal. Chem.* **2002**, *372*, 155–163.
(21) Wang, Z. X.; Prange, A. *Anal. Chem.* **2002**, *74*, 626–631.
(22) Polec-Pawlak, K.; Schaumloffel, D.; Szpunar, J.; Prange, A.; Lobinski, R. *J. Anal. At. Spectrom.* **2002**, *17*, 908–912.
(23) Lu, Q. H.; Barnes, R. M. *Microchem. J.* **1996**, *54*, 129–143.
(24) Liu, Y.; Lopezavila, V.; Zhu, J. J.; Wiederin, D. R.; Beckert, W. F. *Anal. Chem.* **1995**, *67*, 2020–2025.
(25) Michalke, B.; Schramel, P. *J. Chromatogr., A* **1996**, *750*, 51–62.
(26) Michalke, B.; Schramel, P. *Fresenius J. Anal. Chem.* **1997**, *357*, 594–599.
(27) Michalke, B.; Lustig, S.; Schramel, P. *Electrophoresis* **1997**, *18*, 196–201.
(28) Foret, F.; Preisler, J. *Proteomics* **2002**, *2*, 360–372.
(29) Preisler, J.; Hu, P.; Rejtar, T.; Moskovets, E.; Karger, B. L. *Anal. Chem.* **2002**, *74*, 17–25.
(30) Zarei, M.; Kirsch, S.; Muthing, J.; Bindila, L.; Peter-Katalinic, J. *Anal. Bioanal. Chem.* **2008**, *391*, 289–297.
(31) Yeung, K. K. C.; Kiceniuk, A. G.; Li, L. *J. Chromatogr., A* **2001**, *931*, 153–162.
(32) Stevenson, T. I.; Loo, J. A.; Greis, K. D. *Anal. Biochem.* **1998**, *262*, 99–109.
(33) Gray, A. L. *Analyst* **1985**, *110*, 551–556.
(34) GarbeSchonberg, C. D.; Reimann, C.; Pavlov, V. A. *Environ. Geol.* **1997**, *32*, 9–16.
(35) Narewski, U.; Werner, G.; Schulz, H.; Vogt, C. *Fresenius J. Anal. Chem.* **2000**, *366*, 167–170.
(36) Raith, A.; Perkins, W. T.; Pearce, N. J. G.; Jeffries, T. E. *Fresenius J. Anal. Chem.* **1996**, *355*, 789–792.
(37) Yin, Q. Z.; Jacobsen, S. B.; McDonough, W. F.; Horn, I.; Petaev, M. I.; Zipfel, J. *Astrophys. J.* **2000**, *536*, L49–L53.
(38) Gunther, D.; Audetat, A.; Frischknecht, R.; Heinrich, C. A. *J. Anal. At. Spectrom.* **1998**, *13*, 263–270.
(39) Halliday, A. N.; Lee, D. C.; Christensen, J. N.; Rehkamper, M.; Yi, W.; Luo, X. Z.; Hall, C. M.; Ballentine, C. J.; Pettke, T.; Stirling, C. *Geochim. Cosmochim. Acta* **1998**, *62*, 919–940.
(40) Devos, W.; Moor, C.; Lienemann, P. *J. Anal. At. Spectrom.* **1999**, *14*, 621–626.
(41) Devos, W.; Senn-Luder, M.; Moor, C.; Salter, C. *Fresenius J. Anal. Chem.* **2000**, *366*, 873–880.
(42) Watling, R. J.; Lynch, B. F.; Herring, D. *J. Anal. At. Spectrom.* **1997**, *12*, 195–203.
(43) Li, F. H.; Balazs, M. K.; Pong, R. *J. Anal. At. Spectrom.* **2000**, *15*, 1139–1141.
(44) Schaumloffel, D. *J. Trace Elem. Med. Biol.* **2007**, *21*, 18–22.
(45) Garcia, J. S.; de Magalhaes, C. S.; Arruda, M. A. Z. *Talanta* **2006**, *69*, 1–15.
(46) Ballihaut, G.; Mounicou, S.; Lobinski, R. *Anal. Bioanal. Chem.* **2007**, *388*, 585–591.
(47) Resano, M.; Ruiz, E. G.; Mihucz, V. G.; Moricz, A. M.; Zaray, G.; Vanhaecke, F. *J. Anal. At. Spectrom.* **2007**, *22*, 1158–1162.
(48) Yang, L.; Sturgeon, R. E.; Mester, Z. *J. Anal. At. Spectrom.* **2005**, *20*, 431–435.

substrate−sample plate and to enable further transfer to ICPMS. The role of the substrate, absorbing additives, sample morphology, reproducibility, and limits of detection for five metal elements will be examined and discussed. Finally, automated off-line CE−ICPMS of Cr^{III}/Cr^{VI} speciation will be demonstrated. Cr^{III} is considered an essential trace element for the maintenance of an effective glucose, lipid, and protein metabolism in mammals.[49] On the other hand, Cr^{VI} can be toxic for biological systems,[50,51] and water-soluble Cr^{VI} is extremely irritating and toxic to human body tissue owing to its oxidizing potential and easy permeation of biological membranes.[52,53]

EXPERIMENTAL SECTION

Chemical Reagents. Solutions of NaOH (Merci), HCl (Lachema), and HCOOH (Riedel-de Haën) in water (Agilent, Waldbronn, Germany) were used for separation capillary treatment. EDTA (Lachema) was used as a complexing agent. Elements of Cr, Co, Ni, Sn, Cu, Fe, and Zn defined as certified reference materials in aqueous solutions (Analytika) were used as analytes for ICPMS. All chemicals were analytical-reagent grade.

Capillary Electrophoresis with Online UV Detection. Fused-silica capillaries (Polymicro Technologies) with an i.d. of 75 μm and an o.d. of 375 μm were washed with 10 mM solutions of NaOH and HCl (10 min each) and then filled with 10 mM solution of formic acid as the separation running buffer. The sample was injected from unbuffered solution by a pressure of 0.2 kPa for 5 s. Electrophoresis was driven at –480 V·cm^{-1} by a high-voltage power supply (model CZE1000R, Spellman, Hauppauge, NY). Platinum wires served as the electrodes in the electrolyte reservoirs. Electrophoretic current of 1.7 μA was measured with an ammeter placed within the circuit. For UV detection, the total length of the capillary was 26 cm and the effective length 20 cm. Absorbance at 214 nm was measured with a CE detector (model Spectra 100, Spectra Physics, Ontario, Canada).

Capillary Electrophoresis with Off-Line ICP Detection. To facilitate fraction collection, a liquid junction filled with 10 mM formic acid was employed as the joining component between the separation and the deposition capillaries. The same separation capillary was used as in the above case except that the total and effective length was 20 cm. The sample was injected again from an unbuffered solution at 0.2 kPa for 5 s, and the applied voltage was –480 V·cm^{-1}.

Subatmospheric Deposition Chamber. A laboratory-built subatmospheric chamber[28,29] served for deposition of precisely defined sample volumes or collection of separation effluent fractions similarly to commercial spotter devices (e.g., Probot, Dionex, Sunnyvale, CA). The deposition of solutions onto a sample plate (50 × 27 × 0.5 mm) fastened onto the XY-stage in the subatmospheric chamber was performed via a 29.6-cm-long, 51-μm-i.d., fused-silica capillary. The end of the deposition capillary

was silanized by immersing into tributylchlorosilane (Sigma-Aldrich) for 1 min to minimize potential memory effects. Dissimilar to commercial spotters, the flow in the deposition capillary was induced by lower pressure inside the subatmospheric chamber instead of pressurizing the separation capillary. For ∼20-kPa pressure inside the cylindrical chamber (45-cm diameter, 19-cm height) generated with a membrane pump (model N35AT18, KNF Neuberger, Freiburg, Germany), the aqueous solutions flow rate of ∼50 nL·s^{-1} was calculated from Poiseuille's equation. The capillary total volume was ∼610 nL and the dead time ∼12.1 s. The XY-stage and the probe for vertical movement, both operated by a laboratory-built controller running under a LabView (National Instruments, Austin, TX) program, were responsible for sample plate movement and droplet deposition. Four sample plates of different materials were tested; aluminum and copper plate, glass slide, and PETG sheet (Bayer sheet, Darmstadt, Germany).

Samples were spotted onto these plates as discrete fractions in a serpentine-like trail with 1.5-mm spacing in both directions. At the given flow rate, 2-s fractions of aqueous solutions corresponded to ∼100 nL of total volume in each fraction. Afterward, the sample plate was carried over to the ablation cell of the New Wave system described below.

LA ICPMS. Instrumentation for LA ICPMS consisted of a laser ablation system (model UP 213, New Wave, Fremont, CA) and an ICPMS spectrometer (model Agilent 7500 CE). The commercial Q-switched Nd:YAG laser ablation system works at the fifth harmonic frequency, 213 nm. The ablation device was equipped with programmable XYZ-stages to move the sample along a programmed trajectory during ablation/desorption. Visual target inspection, as well as photographic documentation was accomplished by means of a built-in microscope/CCD camera system. A sample was inserted in the SuperCell (New Wave) and was scanned by the laser beam, which was focused onto the sample surface through a quartz window. The ablation cell was flushed with a carrier gas (helium), which transported the laser-induced aerosol to the inductively coupled plasma, at a flow rate 1 L·min^{-1}. A sample gas flow of argon was admixed to the helium carrier gas flow subsequent to the laser ablation cell. Therefore, the total gas flow was 1.6 L·min^{-1}. To reduce possible polyatomic interference, a helium collision cell was used (gas flow 3 mL·min^{-1}). Optimization of LA ICPMS conditions (gas flow rates, sampling depth, electrostatic lens voltages of the MS) was performed with the glass reference material NIST SRM 612 regarding the maximum signal-to-noise (S/N) ratio and minimum oxide formation (ThO$^+$/Th$^+$ counts ratio 0.2%, U$^+$/Th$^+$ counts ratio 1.1%). Other ICPMS parameters were adjusted in compliance with the manufacturer's recommendations.

If not otherwise stated, the laser fluence was 71 MW·cm^{-2} and the repetition rate 10 Hz. The ions were measured with an integration time 0.1 s/isotope. The beam waist was set to a maximum of 300 μm to establish a large effective area for sample ablation/desorption. Dwell time 2 s, i.e., the time the sample was irradiated by the laser beam; ablation cell flush time 3 s and laser warm-up time 3 s were adjusted. With the 10-Hz laser repetition rate, dwell time 2 s corresponded to 20 laser shots/sample. In the case of laser raster scans, dwell times were adjusted according to the scan duration. Dynamic reaction cell was turned on during measurements.

(49) Barnowski, C.; Jakubowski, N.; Stuewer, D.; Broekaert, J. A. C. *J. Anal. At. Spectrom.* **1997**, *12*, 1155−1161.
(50) Prasad, A. S.; Ortega, J.; Brewer, G. J.; Oberleas, D.; Schoomaker, E. B. *JAMA-J. Am. Med. Assoc.* **1976**, *235*, 2396−2398.
(51) Gwizdala, A. B.; Johnson, S. K.; Mollah, S.; Houk, R. S. *J. Anal. At. Spectrom.* **1997**, *12*, 503−506.
(52) Andrle, C. M.; Jakubowski, N.; Broekaert, J. A. C. *Spectrochim. Acta, Part B: At. Spectrosc.* **1997**, *52*, 189−200.
(53) Mugo, R. K.; Orians, K. J. *Anal. Chim. Acta* **1993**, *271*, 1−9.

Pneumatic Nebulization ICPMS. The Babington nebulizer with Scott double-pass spray chamber (Agilent) was used. Optimization of ICPMS conditions was performed regarding the maximum S/N ratio for ^{52}Cr and ^{53}Cr and in compliance with the manufacturer's recommendations. Other ICPMS parameters were as follows: carrier gas (argon) flow, 0.90 L·min^{-1}; makeup gas (argon) flow, 0.19 L·min^{-1}; nebulizer pump flow, 0.022 mL·s^{-1}, and spray chamber temperature, 2 °C. Nebulization efficiency of, at most 5% was determined for this setup.

RESULTS AND DISCUSSION

While common LA ICP measurements rely on ablation processes upon the sample itself, in this case, the sample intended for analysis is deposited on a sample plate and a laser pulse is used to vaporize the sample. Principally, the transfer can be performed in three manners. Laser ablation, respectively laser desorption (LD) of sample itself, substrate-assisted laser desorption (SALD), or matrix-assisted laser desorption (MALD). In the two latter cases, a substrate or a supplementary additive with absorption of light greater than sample are employed, in an analogy to SELDI and MALDI processes. Initially, sample solutions were deposited onto different substrates to investigate the influence of experimental conditions, such as sample morphology, the nature of laser ablation/desorption processes, and data acquisition modes.

Model System Selection. For investigating the overall performance of LA(LD) ICPMS, chromium as an example element was selected. Chromium belongs to a group of elements, which can, without difficulty, be determined by ICPMS; Cr^{III} and Cr^{VI} differ in toxicity and CE may easily be used for Cr species separation. Chromium speciation using separation techniques has been addressed in the literature many times; therefore, the simple system of Cr^{III}/Cr^{VI} was selected to demonstrate the potential of the new coupling. The ion signal of two chromium isotopes, ^{52}Cr (83.8% natural abundance) and ^{53}Cr (9.5% natural abundance), was monitored.

Sample Plate Material Selection. The materials considered for sample plates were glass, PETG, copper, aluminum, and aluminum alloys (Al, AlMg, AlNi). Common stainless steel was regarded as an inappropriate plate material because of a perceptible content of Cr, which would have presumably increased the background level. First, LA ICPMS of each empty sample plate was performed to observe the background intensity of ^{52}Cr and ^{53}Cr; ion signals were integrated 0.1 s/isotope. The progress of the ion signals is shown for PETG and glass substrates on Figure 1A and B. The S/N ratio for ^{52}Cr and ^{53}Cr was obtained as the sum of the average ion intensities recorded with the laser on divided by the standard deviation obtained from 5 data points before and 25 points after turning the laser on. Copper and aluminum alloys were found to contain a significant level of chromium and therefore were avoided in further experiments. Mass of 52 amu in the PETG sheet showed major polyatomic interference as a result of the formation of a polyatomic molecule ^{40}Ar^{12}C. This interference occurred even if with the dynamic reaction cell switched on. Alternatively, ^{53}Cr could be monitored as the interference of ^{40}Ar^{13}C is less severe. Additionally, the transparency of glass and PETG was found to be beneficial as it allowed easy visual inspection of deposited droplets in the ablation cell. To avoid possible cross-contamination, a fresh PETG sample
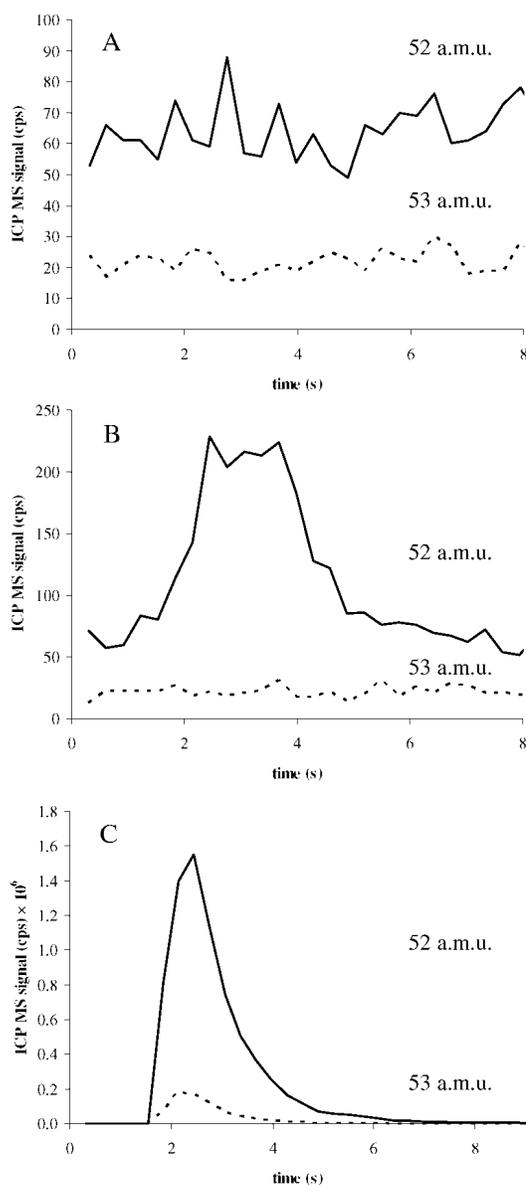

Figure 1. Time record of the ICPMS signal (amu = 52 and 53) of (A) bare glass substrate (B), PETG, and (C) 10 μM Cr^{III} solution deposited on a PETG plate (see text for details). The laser was turned on for 2.0 s at t = 1.0 s.

plate was always used. The glass slide was reused after cleaning in ethanol, deionized water, and acetone in an ultrasonic bath.

Sample Morphology. The sample size, shape, and appearance depended on the solution constitution, hydrophobic/hydrophilic character of the sample plate, sample plate batch in the case of PETG, and shape and treatment of the deposition capillary tip. This presumably influenced sample behavior during the deposition process, and the acquisition mode (a point or raster acquisition). As shown in Figure 2, the morphology of the same samples on various substrates is unique. While evenly spaced 100−500-μm-diameter dots were formed on the relatively hydrophobic surface of the PETG sheet, the spots on the glass sheet were spaced more randomly and spot diameter ranged from 500 to 1000 μm due to the more hydrophilic nature of glass surface. Sample-to-sample variations of spot diameter did not exceed 10% for given deposition conditions. For influencing the sample spot size, acetonitrile (ACN) was admixed to the Cr solution in 1:1 (v/v) ratio and the
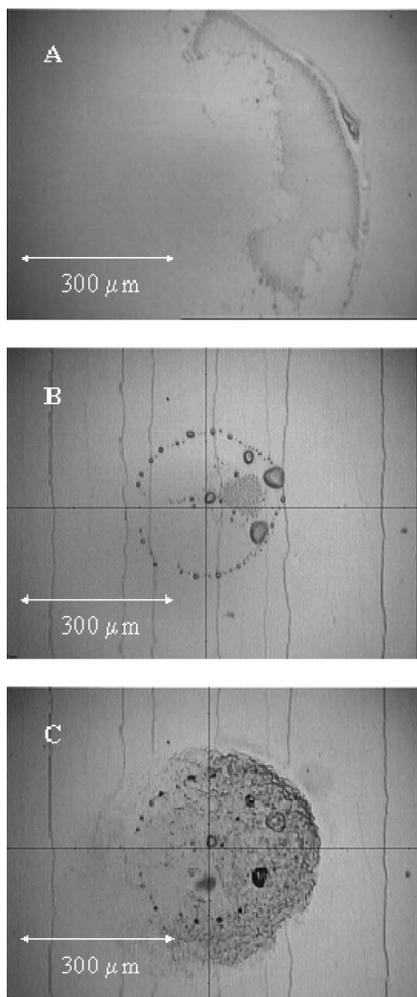
Figure 2. Photographs of 10 μM Cr^{III} solution deposited on (A) glass, (B) PETG, and (C) on PETG after laser desorption. Laser desorption of samples on glass is not shown due to a complete cleanup of deposited material. Slight vertical cracks on the photographs B and C were formed after unrolling PETG from a storage coil.

solution was deposited on glass and PETG plates. Nonetheless, fast evaporation of the organic solvent caused 2−3 times larger spots, and therefore, no ACN addition was further employed.

Laser Scan Pattern. A typical experiment performed on a chromium sample spot is shown in Figure 1C. Signal from ICPMS was continuously obtained at the noise level of ICP with the laser turned off. After the laser was turned on, the sample was ablated/desorbed, and the signal increased proportionally to the amount of Cr in the sample with ∼1-s delay, in the same manner as in the case of background measurements. After switching the laser off 2 s later (the dwell time), the signal decreased and tailed due to the delayed transfer from the ablation cell to ICP. The experiment also included the laser warm-up time (3 s) and the cell flush time (3 s). The reduction of the laser dwell time below 2 s was not imperative as it would not markedly decrease the overall analysis time.

According to the sample spot size, two different laser scan patterns were proposed. For sample spots with diameters of ≤300 μm (which was the maximum size of the adjustable laser beam waist), a point acquisition was selected; i.e., the laser beam was focused on the center of the sample spot and the ablation cell did not move during laser ablation. The entire sample was irradiated

for a certain time (typically 2 s, i.e., 20 laser pulses) and the desorbed aerosol continuously transferred to the ICP. For spot diameters larger than 300 μm, the laser beam was moved in an S-shaped raster (covering typically 700 μm × 700 μm area) to ablate/desorb the entire sample from the given sample spot. Three linear speeds of scan 50, 100, and 200 μm·s^{-1} were tested. The speed of 100 μm·s^{-1} was selected because the scanning of one spot ended in an acceptable time and transfer of the sample to ICP was still complete (data not shown). Both point and raster desorption yielded the same integrated ICPMS signal; i.e., the laser scan pattern did not affect the sample recovery as long as the entire sample was desorbed. Nevertheless, the raster acquisition resulted in a relatively time-consuming procedure (10−25 s/spot), which would have considerably increased the overall analysis time, compared to the point acquisition (2 s/spot). Hence, PETG was preferred to glass as the substrate because the small spot size allowed desorption from either a point or a raster of smaller size.

SALD Mechanism. To characterize the nature of the processes arising from the interaction of the laser radiation and the deposited sample, an experiment comparing vaporization of chromium from low-absorbing glass and highly absorbing PETG was performed. An aqueous solution of 10 μM Cr^{III} was deposited onto glass and PETG substrates in the form of 10-nL droplets. The size of the created spots was ∼400 μm on PETG substrate and ∼800 μm on the glass substrate. The samples were desorbed from both substrates by employing raster scan pattern in three replicates for each value of laser fluence in the range from 2.4 to 98 MW·cm^{-2}. As seen in Figure 3, the ICPMS signal reached a plateau at laser fluence ∼10 MW·cm^{-2} in the case of PETG substrate, while a gradual increase of the signal over the entire range of laser fluence can be observed for the glass substrate. Yet, the signal magnitude for the glass substrate obtained at the highest laser fluence is about a third of the value characteristic for the plateau in the case of the PETG substrate. Relative signal variation reflects an incomplete desorption and, in the case of glass substrate, less regular spot shapes. After the first scan was performed, a second scan within the same raster coordinates was performed to reveal any remaining analyte. With the exception of vaporization at laser fluence of 2.4 MW·cm^{-2}, the integrated ICPMS signal from the second scan did not exceed 3% of the signal from the first scan on both substrates, which points to a nearly complete removal of the sample. In the case of glass, no destruction of the slide was observed within the applied laser fluences, which means direct ablation of sample was responsible for chromium signal. Virtually all sample was removed from the glass slide even at low laser fluence. The increasing laser fluence resulted in higher signal probably due to formation of finer particles of sample. In the case of PETG, ablation of the substrate plays the key role as it sputters the deposited sample into the carrier gas. The SALD is the dominant mechanism, although the role of sample ablation increases at higher laser fluences. Consequently, laser fluence was set to ∼70 MW·cm^{-2} to ensure complete sample desorption and low signal variation for experiments on PETG. Under these conditions, more than 99% sample was removed and the relative standard deviation was below 3%.

Another idea of enhancement via supplementary desorption of another compound was tested with a glass slide as the target plate.
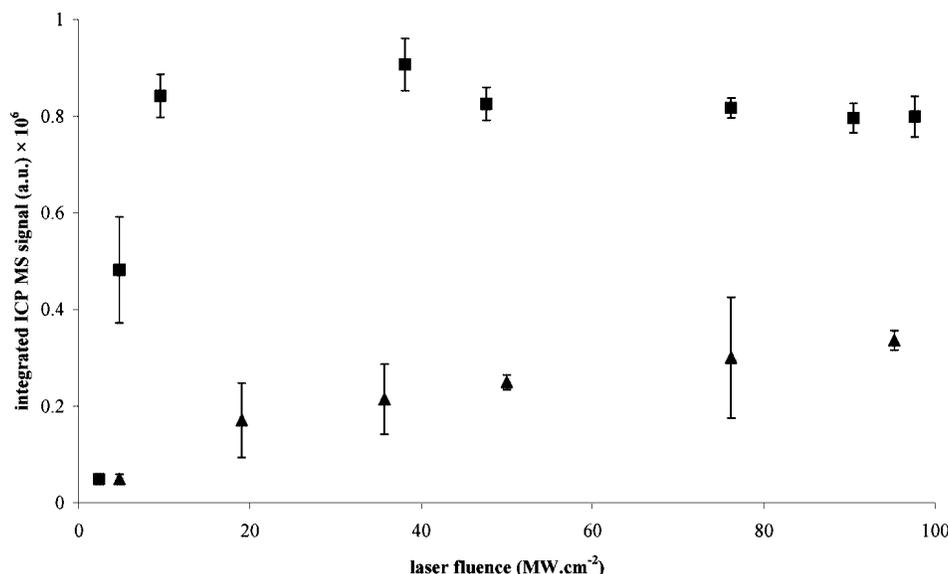
Figure 3. Dependence of integrated ICPMS signal (53 a.m.u.) on laser fluence for 10 μM Cr^{III} solution deposited on glass (▲) and PETG (■) plates.

Table 1. Limits of Detection of Sn, Cr, Cu, Ni, and Zn Estimated from Depositing 0.1 μM Solution (Deposited Volume ~100 nL)

metal isotope	LOD, peak area (fmol)	LOD, peak height (fmol)
^{118}Sn	0.8	0.2
^{120}Sn	0.1	0.3
^{52}Cr	1.1	0.4
^{53}Cr	7.7	1.7
^{63}Cu	1.9	1.1
^{65}Cu	2.8	1.1
^{58}Ni	2.1	0.7
^{60}Ni	3.5	1.5
^{64}Zn	13	9.7
^{66}Zn	14	9.8

The α-cyano-4-hydroxycinnamic acid, commonly used matrix in MALDI, was prepared as a 1 mg·mL^{-1} solution in 50% acetonitrile and added to the Cr sample. Desorption of such prepared samples was performed. Because a signal increase due to the addition of absorbing matrix was not reproducible, the use of the absorbing PETG substrate was preferred for sample vaporization.

Limits of Detection (LODs). For future speciation and determination of other metals by CE-SALD ICPMS, limits of detection (3σ) of deposited solutions Cr, Ni, Sn, Cu, and Zn were determined. Solutions containing all metals in concentrations of 1 and 0.1 μM were deposited onto a PETG plate, and 10 spots were analyzed separately for each metal. Three signals were acquired in ICPMS: signals for the two most abundant isotopes and ^{13}C as background level. Integration time was 0.1 s/isotope. Peak height and peak area (calculated as the sum of the rectangles between neighboring data points) estimations of LODs are summarized in Table 1. LODs were calculated from the 0.1 μM solution. For the LODs calculated from the peak height, the corresponding range of mass LODs is 20−650 fg, and the concentration LOD ranges are 2−100 nM or 0.2−6.5 μg·L^{-1}. The LODs expressed in amounts are 1 order of magnitude lower than in the case of the desorption from polystyrene,[54] probably due to a more quantitative desorption, different sample morphology, or

ablation system and ICPMS parameters. This, together with a smaller size of deposited droplets, facilitates coupling with a microcolumn separation.

In comparison to ICPMS limits of detection obtained with nebulizer and a quadrupole instrument,[55] the concentration LODs reported in this work are up to 2 orders of magnitude higher. The reason for such a difference is generally due to the fact that the nebulizer interface allows signal accumulation over time. It should be mentioned at this point that, for the intended analyte determination in CE fractions, low sample volume is also important in addition to low concentration detection limit. For a more direct comparison of detection limits, 2-s sample plugs of 0.1, 1.0, and 10 μg·L^{-1} chromium nitrate solution in 2% HNO$_3$ were delivered in five replicates into the stream of 2% HNO$_3$ at a flow rate 22 μL·s^{-1}. The length of the sample plugs matched the laser dwell time during the point desorption. The injected amounts of Cr were 0.084, 0.84, and 8.4 pmol. Based on the slope determined for the three Cr amounts, the LODs (3σ) calculated from peak area and height were 190 and 160 fmol for ^{52}Cr and 140 and 90 fmol for ^{53}Cr. In contrast to the concentration LODs, the LODs expressed in amounts are ~2 orders of magnitude higher for the nebulizer. This can be attributed mostly to the nebulization efficiency of the pneumatic nebulizer, which was at most 5% for this setup. Solvent vaporization might also contribute to further reduction of the overall ionization efficiency in the case of wet aerosol from the nebulizer.

Speciation Conditions. The optimal conditions for chromium speciation using CE-SALD ICPMS were selected according to the above results concerning the reproducibility of signal during ablation/desorption, spot size, and the laser energy. The PETG plate, the laser fluence 71 MW·cm^{-2}, and the dwell time, 2 s, were chosen as the optimized conditions for further CE-SALD ICPMS speciation.

CE Separation. Capillary zone electrophoresis separates on the basis of mobility in response to a voltage gradient along the capillary. The mobility of species is related to their charge and

(54) Yang, L.; Sturgeon, R. E.; Mester, Z. *Anal. Chem.* **2005**, *77*, 2971–2977.

(55) Becker, J. S.; Dietze, H. J. *Spectrochim. Acta, Part B: At. Spectrosc.* **1998**, *53*, 1475–1506.
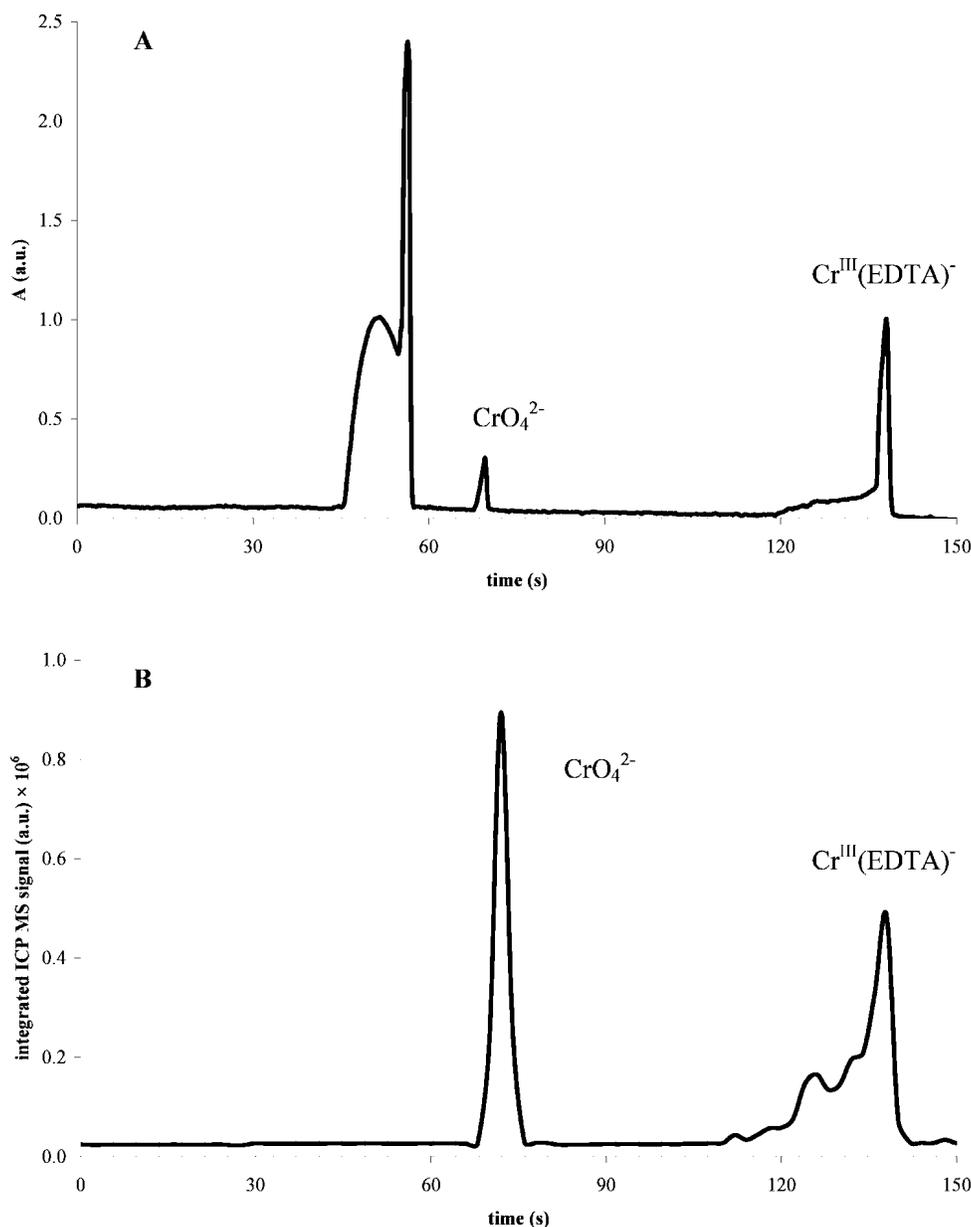
Figure 4. CE separation of Cr^{III}/Cr^{VI} species with (A) UV (214 nm) and (B) ICPMS (53 a.m.u.) detection. Injection from 100 μM $Cr^{III}(EDTA)^-$ and 100 μM CrO_4^{2-} solution; the injected amount was ~200 fmol.

size. A simple electrophoresis of Cr^{3+} species in a formic acid electrolyte, from chromium(VI) existing as $Cr_2O_7^{2-}$, CrO_4^{2-}, $HCrO_4^-$, or H_2CrO_4, cannot be accomplished. The mobility of highly charged species caused the loss of the Cr^{3+} signal in the electropherogram. Jung et al.[56] used EDTA as a complexing agent to create a negatively charged species $Cr^{III}(EDTA)^-$, which could be well separated from Cr^{VI} under the same conditions. CE with UV detection was used to optimize the separation of Cr species prior to deposition on a target. The 100 μM solution of chromium species in water prepared from $Cr^{III}(EDTA)^-$ and Cr^{VI} was used for hydrodynamic injection; ~200 fmol of each species was injected. A record of 2.5-min separation consisting of 75 fractions on PETG plate was desorbed in 12.5 min in the point acquisition mode at laser fluence 71 MW·cm^{-2}.

The UV detection of CE separation is shown in Figure 4A; ICPMS detection is in Figure 4B. The first peak in the UV electropherogram probably corresponds to NO_3^-, which is the anion of the initial Cr^{III} salt before complexation. The peak areas of the integrated ICPMS signal (53 a.m.u.), 11.7×10^6 and 13.2×10^6 a.u. for Cr^{VI} and Cr^{III}, respectively, are similar, as expected. It can be noted from comparison of the Cr^{VI} peak in both detection modes that the off-line coupling preserves high separation efficiency. When injecting sample, no sample stacking has been employed in order to determine the actual amount of the injected sample. With sample stacking, injection of similar amounts can be achieved from more diluted solutions.

CONCLUSIONS

This paper has presented a new approach in coupling a microcolumn separation technique, capillary electrophoresis, to

(56) Jung, G. Y.; Kim, Y. S.; Lim, H. B. *Anal. Sci.* **1997**, *13*, 463–467.

ICPMS. The coupling is performed via a fraction collection in a subatmospheric chamber, which has been used in previous works[28,29] to couple microcolumn separation techniques to MALDI TOF MS; similar commercial fraction collectors are available nowadays. The ICPMS analysis is enabled by laser ablation/ desorption of deposited samples on a substrate material; the process can be characterized as substrate-assisted laser desorption due to a significant contribution of the absorbing substrate. The suitability of materials, which can be used as the substrate, has been tested. The PETG plate showed to be the most appropriate material for Cr speciation analysis because of its properties, such as hydrophobicity, transparency, and commercial availability. The sample morphology, detection limits, and spot-to-spot reproducibility were examined. Due to submicroliter sample volumes used for analysis in SALD, concentration LODs were up to 2 orders of magnitude higher compared to conventional pneumatic nebulizer ICPMS. On the other hand, LODs expressed in analyte amount were ~2 orders of magnitude lower than those obtained with the pneumatic nebulizer as a result of enhanced overall sample transport efficiency. For most examined metals, the LODs lie around 1 fmol (~100 fg), 1 order of magnitude lower than previously published results,[48,54] which facilitate coupling to microcolumn separations. The spot-to-spot reproducibility was below 3%, which is adequate for the analysis of deposited separation fractions. The same solution is suitable for ICP OES detection.

The simple model system of Cr^{III}/Cr^{VI} has demonstrated the prospects of coupling a microcolumn separation to ICPMS in off-line mode. The separation efficiency has been conserved while the rapid analysis time has remained. The separation can be further optimized, e.g., by modification of separation conditions or increasing the capillary length. Alternatively, capillary liquid chromatography can be employed. Contrary to the use of nebulizers, low flow rate in the separation columns is advantageous as it leads to small sample spots, high sensitivity, and short analysis time. Furthermore, a single separation record on a sample plate can be analyzed in different detection modes. Thus, we expect the off-line coupling will be used e.g. for analysis of separated metalloproteins with complementary ICPMS and MALDI MS detection techniques to gain information on both metal content and protein mass or identity.

2.3 Substrate-assisted laser desorption inductively-coupled plasma mass spectrometry for the determination of copper in myeloid leukemia cells

SALD ICP MS has been characterized and utilized in model samples containing copper followed by an investigation of intracellular copper levels in disulfiram-treated myeloid leukemia cells. Disulfiram (DSF), as other thiocarbamates, is able to complex metals and permeate cell membranes while being more cytotoxic to leukemic cells than to cells of solid tumors. Hence, it may induce growth arrest and apoptosis of various cell types by increasing the intracellular level of copper up to several ng per 10^6 cells. Copper belongs to a group of essential trace metals and plays a key role in various biological processes. To be effective, many critical enzymes and transcription factors require copper; however, its amount in an organism is very tightly regulated. Analysis of Cu(II) model samples showed a constant signal over a wide range of laser power density, independence of signal on desorption modes and a wide linear dynamic range. Before treating the leukemic cells, several parameters were required to be optimized, *e.g.*, droplet deposition morphology, power density, cell lysis, or desorption raster as LOD and dynamic range depended upon these. Copper determined in DMSO-treated and untreated cells corresponded to natural intracellular concentration in leukemic cells. There was no statistically significant difference found in concentrations of naturally intracellular copper in untreated, DMSO-treated low density (LD, 50 000 cells per mL) and high density (HD, 200 000 cells per mL) cells. The intracellular concentration of copper in DSF-treated cells (both HD and LD) increased six times when 25 ng·mL^{-1} DSF was used and seven times when 50 ng·mL^{-1} DSF was used. Accuracy of copper determination by SALD ICP MS was verified by conventional Babington nebulizer ICP MS.

In conclusion, complete sample desorption could have been achieved using ten pulses with spot-to-spot reproducibility below 6%. With a linear dynamic range over six orders of magnitude and LOD of about 26 fg for copper, SALD ICP MS has proved to be a powerful tool for analyzing metals in real samples at micro-volume and trace concentrations, as demonstrated on the determination of copper in leukemia cells.

Substrate-assisted laser desorption inductively-coupled plasma mass spectrometry for determination of copper in myeloid leukemia cells

Pavla Jungová,[a] Jarmila Navrátilová,[b] Ondřej Peš,[a] Tomáš Vaculovič,[a] Viktor Kanický,[a] Jan Šmarda[b] and Jan Preisler*[ab]

This work presents a detailed characterization of substrate-assisted laser desorption inductively coupled plasma mass spectrometry (SALD ICP-MS), a new approach in the determination of trace elements in submicrolitre volumes. SALD ICP-MS allows quantitative analysis of metals in liquid samples with defined volumes deposited onto an absorbing substrate due to complete sample desorption at relatively low laser power density. Analysis of model samples of Cu(II) showed a constant signal over a wide range of laser power density, an independence of signal on desorption modes and a wide linear dynamic range. SALD ICP-MS with its limit of detection for copper below 26 fg in submicrolitre samples was successfully applied to investigate cytotoxic effects of disulfiram in human myeloid leukemia cells U937 depending on intracellular levels of copper.

Introduction

The development and application of laser ablation inductively coupled plasma mass spectrometry (LA ICP-MS) has rapidly advanced over the past years. The method is most frequently applied for local microanalysis[1,2] and for bulk analysis of steels, alloys, glasses, ceramics and/or powdered materials.[3] Additionally, focusing a laser beam on a specific spot or sample movement during ablation allows a local or spatial analysis of a sample surface, which is necessary for elemental distribution mapping, thin metal layer profiling,[4] elemental mapping in biological tissue sections[5] and elemental imaging in metalloprotein gel bands after electrophoretic separation.[6] Key benefits of LA ICP-MS include direct and fast characterization of solid or liquid materials with no or minimal sample preparation, small sample size requirement and nearly non-destructive analysis. The most common techniques used for the selective detection of metals in liquid samples include FAAS,[7–9] GF-AAS,[10] ETAAS,[11] ICP-AES,[12] ICP-MS,[13–17] ESI-MS.[18,19] However, conventional methods fail when analyzing biological and clinical samples with low analyte concentration, small sample volume or a complex matrix. The use of direct liquid ablation as a calibration technique for solid sample trace element determination has also been presented,[20,21] and more recently, a method based on the complete ablation of dried droplets[22] has been used for the quantification of Ni, Cd and Pb in drinking water and Se in yeast digest. In these studies, samples were mixed with a sodium acetate matrix, deposited on a polystyrene weighting boat and the maximum laser power density was applied to ensure complete sample ablation/desorption. Consequently, dried-droplet LA-ICP MS has been applied to determine SeMet in yeast after separation and fractionation by HPLC.[23] Dried residues of picolitre droplets generated by an inkjet printer were employed as calibration standards for LA ICP-MS.[24]

In our previous study[25] we presented a new substrate-assisted laser desorption (SALD) ICP-MS approach, applicable for the analysis of liquid samples deposited onto an absorbing substrate followed by complete sample desorption using a relatively low laser power density. Moreover, SALD ICP-MS has demonstrated full potential for coupling with microcolumn separation techniques, such as capillary electrophoresis (CE), and for the determination of trace elements in biological samples at submicrolitre level. Despite the fact that LA ICP-MS is currently one of the most employed methods for quantitative imaging of trace metals in biological samples,[26–28] it has been limited to the analysis of bulk samples where sample volume cannot be precisely defined. Herein SALD ICP-MS is presented as being able to analyze dried droplets with well-defined volumes from absorbing substrates.

In this work, we offer a detailed characterization of SALD ICP-MS on model samples (CuSO$_4$) followed by an investigation of intracellular copper levels in disulfiram-treated myeloid leukemia cells. Copper belongs to a group of essential trace metals and plays an important role in various biological processes. To be effective, many critical enzymes and transcription factors require copper;[29] however, its amount in an organism is very tightly regulated.[30,31] Disulfiram (DSF), an irreversible inhibitor of aldehyde dehydrogenase, is a drug approved for the treatment of alcoholism. Several studies have shown that DSF in safe concentrations possesses anticancer effects.[32–34] As other thiocarbamates, DSF is able to complex metals and permeate cell membranes[35] and is more cytotoxic to leukemic cells than to cells of solid tumors.[36] Next, DSF may induce growth arrest and apoptosis of various cell types by increasing the intracellular level of copper,[37] which was verified in our studies on human myeloid leukemia cells U937.[38] The regular amount of copper in 10^6 U937 cells reaches several nanograms.[39,40] A typical volume of such

[a]Department of Chemistry, Faculty of Science, Masaryk University, Kotlářská 2, 611 37 Brno, Czech Republic. E-mail: preisler@chemi.muni.cz; Fax: +420 549 492 494; Tel: +420 549 496 629
[b]Department of Experimental Biology, Faculty of Science, Masaryk University, Kotlářská 2, 611 37 Brno, Czech Republic

a sample amount corresponds to less than 100 μL, which does not allow dilution or using conventional techniques for copper determination. SALD ICP-MS with its limit of detection for copper ~180 fg in submicrolitre sample volume[25] will be successfully applied for analysis of these samples.

Experimental

Chemicals

Aqueous solutions of $CuSO_4$ by Lachema, Czech Republic, with concentrations 1.15×10^{-6}; 5.75×10^{-6}; 1.15×10^{-5}; 5.75×10^{-5} and 1.15×10^{-4} M were used as model samples for the characterization of SALD ICP-MS. For visualization, samples might have contained 10^{-5} M solution of rhodamine B by Sigma-Aldrich, Germany. Water was redistilled in a quartz apparatus from Heraeus (Hanau, Germany). All reagents were analytical-reagent grade.

Cell cultivation

U937 (ATCCT, cat. number CRL-1593.2) were seeded at low density (LD, 50 000 cells per mL) and high density (HD, 200 000 cells per mL) in Roswell Park Memorial Institute 1640 (RPMI 1640) medium purchased from Sigma-Aldrich, Czech Republic, containing 10% fetal calf serum by Invitrogen, UK, L-Glutamine in concentration 2×10^{-3} M, penicillin in concentration 100 U/mL and streptomycin in concentration 100 μg mL^{-1} (all Sigma-Aldrich) and cultured in humidified 5% CO_2 atmosphere at 37 °C. The cells were treated with tetraethylthiuram disulfide disulfiram (100 ng mL^{-1}, Sigma-Aldrich) dissolved in dimethylsulfoxide (DMSO, 100 ng mL^{-1}, Sigma-Aldrich) or left untreated for 5.5 h. As a control, the cells were treated with DMSO. Pelleted cells were washed twice with phosphate buffered saline (PBS), PBS was pumped out and the number of cells was counted using hemocytometer. The volume of ~10^6 cells was below 10 μL.

Cells lysis

Washed cells were lysed in 50 μL of deionized water for 10 min in an ultrasonic bath or in 100 μL of mixture of 3 M HCl (Lachema) and 10% trichloroacetic acid (TCA, Sigma-Aldrich) at laboratory temperature for 3 h followed by incubation at 70 °C for 5 h,[37] or in 100 μL of nitric acid (Lachema) and incubated at 37 °C overnight. The lysate was centrifuged (600 g/5 min) to remove cell debris.

Sample preparation

Supernatant or model $CuSO_4$ solution was, for easy visualization, mixed with an aqueous solution of rhodamine B. The total concentration of rhodamine B in any solution was 10^{-5} M. The addition of rhodamine B at applied concentration did not have any effect on the spot size. Sample solutions were spotted onto a polyethylene terephthalate glycol plate (PETG), brand name Vivak, as 200-nL droplets by a micropipette or in a laboratory-built sub-atmospheric chamber[41,42] providing deposition of precisely defined sample volumes. Lower pressure (~20 kPa) inside the cylindrical chamber (45-cm diameter, 19-cm height),

generated with a membrane pump, model N35AT18 (KNF Neuberger, Germany), ensured stable flow of a sample solution. The deposited sample volume was then calculated from the flow rate and the deposition time based on Poiseuille's equation.

SALD ICP MS

Sample plates were inserted into the laser ablation system, model UP 213 (New Wave, USA), with Q-switched Nd:YAG working at a wavelength of 213 nm and having a movable ablation cell, model SuperCell (New Wave), for sample movement during desorption. A built-in microscope/CCD camera system provided visual control of samples. Sample spots were scanned by a laser beam and the laser beamwaist was adjusted to the maximum size ~300 μm. The ablation cell was flushed with a carrier gas (helium) at flow rate 1.0 L min^{-1}, which transported the aerosol to an ICP mass spectrometer, model 7500CE (Agilent, Japan). A sample gas flow of argon was mixed with the helium carrier gas flow subsequent to the laser ablation cell (0.6 L min^{-1}). Optimization of LA ICP-MS conditions such as gas flow rates, sampling depth, electrostatic lens voltage of the MS was performed with the glass reference material NIST SRM 612 regarding the maximum signal-to-noise ratio of $^7Li^+$, $^{89}Y^+$ and $^{238}U^+$ for low, middle and high masses and minimum oxide formation (ThO$^+$/Th$^+$ counts ratio 0.2%, U$^+$/Th$^+$ counts ratio 1.1%). Other ICP MS parameters were adjusted in compliance with the manufacturer's recommendations. If not otherwise stated, sample spots were desorbed at the laser power density ~70 MW cm^{-2}, at a frequency of 10 Hz and a scan rate of 100 μm s^{-1} (raster desorption) or dwell time 2 s (point desorption). Size of the zigzag-shaped raster with spacing 200 μm was selected according to the spot diameter to cover the entire sample area. The ions were measured with an integration time 0.1 s/isotope. Cell flush time and laser warm-up time were set to 3 s. In the case that the helium collision cell was used, gas flow was 2.5 mL min^{-1}. The ^{13}C ion signal was monitored to indicate the ablation of the sample plate and to set the interval for integration of the copper ion signal accordingly. The ion signal of two copper isotopes, ^{63}Cu and ^{65}Cu, was recorded and the $^{65}Cu/^{63}Cu$ isotope ratio was observed to reveal possible polyatomic interferences ($^{40}Ar^{25}Mg^+$, $^{40}Ar^{23}Na^+$, etc). The signal of $^{65}Cu^+$ was used for all data evaluations further in the text.

Pneumatic nebulization ICP MS

A Babington nebulizer with Scott double-pass spray chamber (Agilent, Japan) was used. Optimization of ICP MS conditions was performed regarding the maximum S/N ratio for ^{63}Cu and ^{65}Cu and in compliance with the manufacturer's recommendations. The other ICP-MS parameters were: carrier gas (argon) flow, 0.90 L min^{-1}; makeup gas (argon) flow, 0.19 L min^{-1}; nebulizer pump flow, 0.022 mL s^{-1} and spray chamber temperature, 2 °C. A nebulization efficiency of 5% was determined for this setup.

Results and discussion

Substrate selection

Commercially available plastics, polyester polyethylene terephthalate glycol (PETG) brands Vivak and Axpet produced by

BayerSheet, Germany, polypropylene Evacast, foamed poly-vinylchloride Vikupor by Rochling, Germany, and polyvinyl-chloride Vikunyl by EVC, Great Britain, were selected as suitable substrates concerning availability, ease of plate fabrication and transparency. Initially, the presence of common metals in plastics, the deposited sample morphology and ablation crater formation were examined. The intensity of ICP MS signal of the two most abundant isotopes of Cr, Cu, Hg, Zn, Fe, Sn, Ni, Mo, Cd, Pt, Pb and one isotope of Al, Mn, Co were monitored with an integration time 0.1 s/isotope by point ablation with a dwell time 5 s to study which of the plastics is applicable to trace analysis of these common metals. Spot-to-spot reproducibility was given by a raster desorption of ten 100 nL spots of 10^{-4} M $CuSO_4$. Sample morphology and ablation crater formation was observed by microscope/CCD-camera system.

Carbon, a major element in plastics, raised formation of polyatomic molecules $^{40}Ar^{12}C$, with the same nominal mass as the major isotope of Cr. Other observed molecules $^{40}Ar^{16}O$ interfered with mass of Fe. Interferences might have been eliminated by switching on the dynamic reaction cell or other isotope monitoring. Polyatomic interferences with either of the copper isotopes were not observed. Polyvinylchloride Vikupor was excluded from further tests since a significant content of Al, Zn and Pb were discovered. Polypropylene Evacast was contaminated by Zn and spot borders were not recognizable on rough surface. Although polyvinylchloride Vikunyl contained none of the monitored metals, ablation formed irregular craters along the irradiated area of the polymer resulting in an incomplete sample desorption. Both PETG brands were found to be contaminated by cobalt. While poorly visible large sample spots (∼600 μm) and uneven size of spots on Axpet inflicted a low spot-to-spot reproducibility (RSD ∼34%). Samples deposited on PETG Vivak created uniform, clearly visible and bordered spots significantly increasing the reproducibility (RSD ∼9%). Desorption of both latter plastics from irradiated areas proceeded evenly.

In summary, all plastics except polyvinylchloride Vikunyl, which is not suitable due to forming irregular craters, were contaminated by at least one monitoring metal, but deposited samples were uniform and clearly bordered only on PETG Vivak. PETG Vivak was selected as the most suitable substrate among the tested plastics since it was not found to be contaminated by common metals but by cobalt, and deposited sample spots were identical and distinct. Moreover, the high absorption coefficient of PETG at the laser wavelength used (213 nm) extensively enhanced sample desorption (SALD mechanism) along the entire irradiated area.[25] PETG Vivak used for all further experiments will be referred to as PETG in the following text.

Sample morphology

A microscope/CCD-camera system allowing visual inspection was used to study sample morphology. Typical sample spots of $CuSO_4$, formed after depositing different volumes of its aqueous solution, are shown in Fig. 1. Visual observation predicated that copper, when the solvent evaporated, was concentrated in crystals at the spot border. Subsequently, this fact has been confirmed by analyzing a 100 nL spot of 10^{-4} M $CuSO_4$. Laser

beamwaist was adjusted to 30 μm and different sample spot sites were examined by point desorption as follows: desorption from three points in a spot border, where the highest concentration of crystals was noticed; three points in a spot center with no visible crystals; and three points in a number of visible crystals within the sample spot diameter. In the places with clearly visible
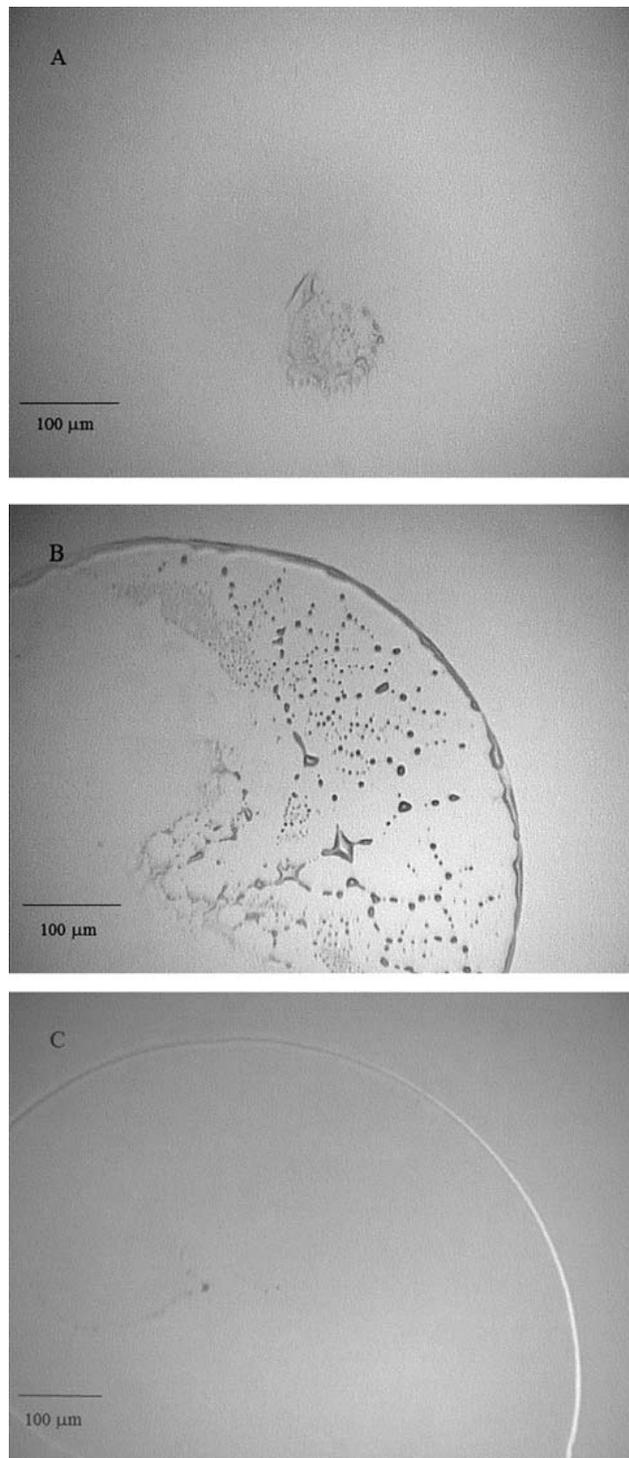

Fig. 1 Photographs of a $CuSO_4$ aqueous solution droplet deposited on PETG. Droplet volume and $CuSO_4$ concentration: A) 6 nL, 10^{-4} M; B) 100 nL, 10^{-4} M and C) 100 nL, 10^{-6} M with 10^{-5} M rhodamine B.

crystals the intensity of the $^{65}Cu^+$ signal was 15-fold to 50-fold higher than the signal intensity in the bare PETG surface.

Effect of laser power density on ICP MS signal

To investigate the optimal laser power density, a series of 100-nL droplets of 10^{-4} M $CuSO_4$ aqueous solution was deposited on PETG. Five spots were desorbed for each value of laser power density ranging from 2 to 129 MW cm^{-2}. To reduce possible polyatomic interference, a helium collision cell was used. While all sample spots were at least partially desorbed, a laser power density >10 MW cm^{-2} was sufficient to desorb more than 98% of the sample as evidenced by subsequent analysis of the same spot at 70 MW cm^{-2}. Moreover, further increase in laser power density had no effect on the integrated signal. Unfortunately, the stated laser power density values may be slightly inaccurate because the laser ablation system was not designed to be routinely used at these low values of laser power density. On the other hand, the higher the laser power density, the larger the polyatomic interferences were observed. As a compromise, a laser power density $\sim$70 MW cm^{-2} was selected for further experiments.

Raster desorption optimization

A series of 100-nL droplets of 10^{-4} M $CuSO_4$ aqueous solution was deposited onto PETG. Scan rates of 30; 70; 100; 200 and 500 μm s^{-1} and laser frequencies 5; 10 and 20 Hz were tested in all combinations. Natural ratio of copper isotopes ($^{65}Cu/^{63}Cu = 0.447$) was observed for scan rates up to 200 μm s^{-1} for all tested laser frequencies. An isotope ratio decrease was observed at higher scan rates because of a signal increase at mass 63. However, bare PETG surface ablation did not result in any signal change at any combination of laser frequency and scan rate. Presumably, the samples contained traces of sodium, which lead to polyatomic interference of $^{40}Ar^{23}Na$. In order to prove this hypothesis, an experiment with a dynamic reaction cell was carried out. The sample spots were desorbed by the same raster pattern at a scan rate of 100; 200; 300; 500 and 1000 μm s^{-1} at 20 Hz frequency. With the helium collision cell switched on, the $^{65}Cu/^{63}Cu$ isotope ratio was restored to its natural value and the integrated signal of both isotopes was consistent along all scan rates. It should be noted that the signal increase at mass 63 was not always observed at higher scan rates. Yet, to eliminate possible interferences, the dynamic reaction cell had to be employed or scan rates kept below 100 μm s^{-1}.

Point desorption optimization

Point desorption is particularly influenced by laser frequency, dwell time, and/or number of pulses. The integrated signal from desorption of 6-nL droplets of 10^{-4} M $CuSO_4$ in five replicates was monitored at 1, 2, 5, 10 and 20 Hz for 1 s, which corresponded to 1, 2, 5, 10 and 20 pulses. Second point desorption at 20 Hz for 1 s within the same coordinates was performed to reveal any remaining sample.

Usually one pulse was sufficient for desorption of more than 90% of the sample but the spot-to-spot reproducibility calculated from integrated signals of five copper spots exceeded 20%. To desorb more than 98% of a sample five pulses were needed

and the spot-to-spot reproducibility decreased to below 10% when using five or more pulses. Therefore ten pulses desorption was selected for further experiments. Variance of ten pulses was tested as a combination of frequency and time, *i.e.* 10 Hz for 1 s, 5 Hz for 2 s, 2 Hz for 5 s and 1 Hz for 10 s. Frequency 20 Hz was not included because the instrument setup allowed minimal dwell time 1 s. In any case, desorption of ten pulses yielded in identical ICP-MS signal; the RSD, however, increased from 6% at 10 Hz (dwell time 1 s) to 29% at 1 Hz (dwell time 10 s). Thus for further experiments, dwell time 1 s and laser frequency 10 Hz were set to ensure complete sample desorption and low signal variation.

Raster and point desorption comparison

As the maximum adjustable laser beamwaist is 300 μm, the desorption mode was selected according to the size of the dried-droplet spot. In order to investigate possible differences between point and raster desorption, a series of volumes of 3, 6, 10, 20 nL of 10^{-4} M $CuSO_4$ aqueous solution droplets were deposited on PETG. A typical spot diameter for volumes below 20 nL did not exceed 300 μm, and both desorption modes were applicable. Deposition of larger droplets might result in sample spot diameters exceeding 300 μm, which could have been entirely desorbed only by raster desorption. Thus, spots with a diameter below 300 μm (sample volume 3–20 nL, 0.3–2 pmol $CuSO_4$) were desorbed in five replicates by raster and point desorption. The helium collision cell was used. As seen in Fig. 2, integrated signals of $^{65}Cu^+$ reached similar values for both point and raster desorption, proportionally increasing with the deposited volume. Coefficients of determination were 0.9972 for point and 0.9954 for raster desorption. Total acquisition time for one sample spot (including laser warm-up and cell flush-out) were 7 s for point and $\sim$21 s for raster desorption. Therefore point desorption should be preferred in the case of sample spots with diameters lower than 300 μm. The lower integrated signal in the case of point desorption is probably related to incomplete desorption of the sample on the spot edges. Linearity of signal passed the F-test for both raster and point desorption.
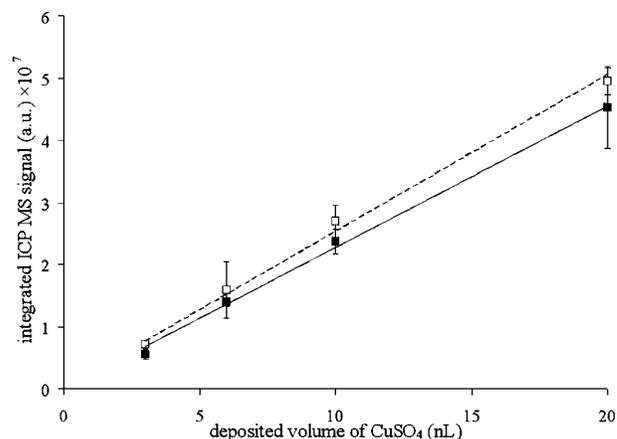

Fig. 2 Dependence of integrated ICP-MS signal (a.m.u. = 65) on droplet volume of 10^{-4} M $CuSO_4$ solution obtained by (–■–) point desorption; (–□–) raster desorption.

Dynamic range

One of the advantages of the ICP-MS instrument employed is its wide, linear dynamic range. In order to investigate the dynamic range of SALD ICP-MS, 100-nL droplets of aqueous mixture of 10^{-5} M rhodamine B and $CuSO_4$ at concentrations 10^{-7}; 10^{-6}; 10^{-5}; 10^{-4}; 10^{-3}; 10^{-2} and 10^{-1} M were deposited onto PETG and desorbed in five replicates for each concentration. The helium collision cell was used. Dynamic range proved to be linear within the examined scale and coefficient of determination was 0.9990.

Limit of detection (LOD)

In order to determine limit of detection (3σ) of Cu, 100-nL droplets of aqueous mixture of 10^{-7} M $CuSO_4$ and 10^{-5} M rhodamine B were deposited onto PETG and desorbed in five replicates. The helium collision cell was used. LOD was estimated from peak area (calculated as the sum of the rectangles between neighboring data points) was 0.4 fmol, *i.e.* 26 fg of Cu.

SALD ICP-MS of lysed cells

When cultivated, U937 cells were counted in a hemocytometer and PBS was pumped out. This left a certain amount of cells in a pellet without knowing sample volume. Thus, an addition of defined volume of lysis solution was required for direct quantitative analysis of cells. Three lysis solutions to LD cells were tested: water, HNO_3 and HCl/TCA, as in literature.[37] Natural intracellular concentration of copper in U937 cells is expected to be several nanograms per 10^6 cells.[40,43] An aqueous mixture of 10^{-5} M rhodamine B with various concentration of $CuSO_4$ was analyzed by SALD ICP-MS to produce a calibration curve. From the calibration curve, concentration of copper in the cells was determined.

First, analysis of a 200-nL water supernatant from cells containing 10^{-5} M rhodamine B showed the amount of copper to be below 1 ng per 10^6 cells. This suggested that copper was bound in an insoluble cell membrane, and for correct determination of the total copper concentration, the cell membrane required to be suitably disintegrated and re-dissolved.

Thus, lysis in 1.6 M HNO_3[43] was tested, but visual inspection showed that the cells were not completely lysed. More concentrated nitric acid; 3.7 M and 7.3 M, was prepared to ensure complete cell lysis. However, 200-nL supernatant droplets deposited on PETG caused etching of the PETG surface which resulted in a reduction of the integrated signal of Cu^+, probably because of the penetration of copper into the polymer grid. To avoid the etching, a cell lysate in 3.7 M HNO_3 was diluted with rhodamine B aqueous solution in volume ratio 1 : 4 and 1 : 7 so that the resulting concentration of HNO_3 was 0.9 M and 0.4 M. No etching was observed and the determined amount of copper was 1.7 and 3.5 ng per 10^6 cells. However, use of the diluted HNO_3 solutions was accompanied by a significant increase of relative standard deviation to 75%, respectively 88%.

Finally, a mixture of HCl/TCA was used as a lysis reagent. Completely lysed cells (visually examined) were deposited as 200-nL fractions showing minor etching of PETG and forming 2–3 times larger spots due to fast evaporation of the organic solvent. SALD ICP-MS analysis of 200-nL droplets (five replicates) resulted in 1.1 ± 0.3 ng of copper per 10^6 cells. To

Table 1 SALD ICP-MS analysis of copper in different lysates of cells U937

Lysis solution	Volume ratio with aqueous solution of rhodamine B	Amount of copper (ng per 10^6 cells)	RSD (%)
10^{-5} M rhodamine B	—	0.89 ± 0.36	41
7.3 M HNO_3	—	0.82 ± 0.93	113
1.6 M HNO_3	a		
3.7 M HNO_3	—	0.22 ± 0.32	150
3.7 M HNO_3	1 : 4	1.17 ± 0.88	75
3.7 M HNO_3	1 : 7	3.52 ± 3.08	88
3M HCl/10% TCA	—	1.09 ± 0.32	30
3M HCl/10% TCA	1 : 3	2.61 ± 0.12	5

a Cells were not completely lysed.

completely eliminate the PETG etching and minimize the spot size, the lysate was diluted with rhodamine B aqueous solution in volume ratio 1 : 3 so that the resulting concentration of rhodamine B was 10^{-6} M. The determined amount of copper was 2.6 ± 0.1 ng per 10^6 cells. To verify the visually established complete cell lysis, the cell debris from HCl/TCA lysate was deposited on the PETG covering an area of $\sim$1 mm^2. As the intensity of the ICP-MS signal from the debris and the blank PETG surface did not differ significantly, absence of copper in the cell debris with all the copper entirely in the cell lysate was confirmed.

As seen in Table 1, comparison of different sample preparation methods for SALD ICP-MS showed that lysis in the HCl/TCA mixture followed by dilution with rhodamine B was found to be the most suitable method for U937 cell preparation. The surface of the PETG was not etched, the sample spots size was $\sim$800 µm and the relative standard deviation reached 5%.

The effect of DSF on Cu content in U937 cells

With an accurate method for trace analysis of copper in cells, physiologically relevant levels of copper may be further studied. The effects of DSF on intracellular concentration of copper were determined for low (50 000 cell per mL) and high (200 000 cell per mL) densities of U937 cells. The cells were treated with DSF, DMSO as a control or left untreated for 5.5 h, lysed in a mixture of 3M HCl/10% TCA and analyzed by SALD ICP-MS. The cells were treated with DMSO to inspect possible effects of DMSO dissolvent. The intracellular concentration of copper was determined as ng per 10^6 cells. Data were obtained from three independent experiments over three days and processed using the Student's test; no data were excluded.

Copper determined in DMSO-treated and untreated cells corresponded to natural intracellular concentration in U937 cells. There was no statistically significant difference found in concentrations of naturally intracellular copper in untreated, DMSO-treated LD and HD cells, as seen in Table 2. The intracellular concentration of copper in DSF-treated cells (both HD and LD) increased six times when 25 ng mL^{-1} DSF was used, and seven times when 50 ng mL^{-1} DSF was used. The possible difference between LD and HD cells was examined by treating the cells with 100 ng mL^{-1} DSF; intracellular concentration of copper increased to 41.0 ± 1.7 ng per 10^6 cells in the case of LD

Table 2 SALD ICP-MS estimated copper amount in DSF-treated U937 cells

Cell density	DSF concentration/ng mL^{-1}	Amount of copper (ng per 10^6 cells)	RSD (%)
LD (50 000 cells per mL)	0	2.61 ± 0.12	5
	25	14.9 ± 2.6	17
	50	22.6 ± 4.5	20
	100	41.0 ± 1.7	4
HD (200 000 cells per mL)	0	2.4 ± 0.3	13
	25	18.4 ± 4.6	25
	50	22.1 ± 2.4	11
	100	23.8 ± 1.8	8

cells, while in the case of HD cells it did not increase considerably (to 23.8 ± 1.8 ng per 10^6 cells) compared to the addition of 50 ng mL^{-1} DSF.

These results confirmed that DSF causes accumulation of copper in U937 cells and that the process is significantly more efficient in LD U937 cells. The lower intracellular concentration of copper in the DSF-treated HD U937 cells was probably caused by a limited supply of copper in the cultivation medium. To verify this hypothesis, HD U937 cells were cultivated in 5 mL of media treated with DMSO (conditioned medium 1, CM1) and with DSF in concentration 100 ng mL^{-1} (conditioned medium 2, CM2). Concentrations of copper in the medium determined by SALD ICP-MS were 9.78 ± 0.04 ng mL^{-1} in CM1 and 5.06 ± 0.04 ng mL^{-1} in CM2. As expected, addition of DSF results in a decrease of copper in the medium due to copper transport into the cells. Furthermore, this documents that DSF, even at a concentration of 100 ng mL^{-1}, is not able to transport any more copper into the cells from the CM2 medium although this was not completely depleted from copper. The difference of amounts of extracellular copper between CM1 and CM2 was 23.60 ng for 5 mL media, which corresponds to the increase of intracellular copper in HD 100 ng mL^{-1} DSF-treated cells. Further information about Cu analysis in U937 cells is published elsewhere.[38]

Accuracy of copper determination in cells by SALD ICP MS

In order to examine the possible effect of HCl/TCA mixture on ICP MS response on copper, solutions of 1.15×10^{-4}; 5.75×10^{-5}; 1.15×10^{-5}; 5.75×10^{-6} and 1.15×10^{-6} M CuSO$_4$ in 3 M HCl/10% TCA, and in water, containing 10^{-5} M rhodamine B were prepared. A series of 200-nL droplets were deposited on PETG and analyzed by SALD ICP-MS. The slopes for calibration curves of CuSO$_4$ in HCl/TCA and in water were 1.61×10^8 with a coefficient of determination 0.998 and 1.57×10^8 with a coefficient of determination 0.997, respectively. Therefore it can be concluded that the ICP-MS signal is not affected by the lysis solution.

Furthermore, accuracy of copper determination by SALD ICP-MS was verified by conventional Babington nebulizer ICP-MS. Because of the larger consumption of sample, ten times larger volumes of media had to be used for cell culture preparation. HD cells treated with DMSO and DSF (100 ng mL^{-1}) were divided into two aliquots, each analyzed by SALD ICP-MS and nebulizer ICP MS. Both CM1 and CM2 media were analyzed by nebulizer ICP MS and the results were compared
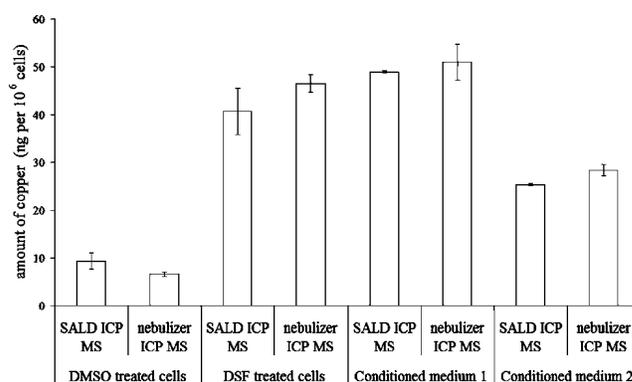

Fig. 3 Comparison of SALD ICP MS with conventional ICP MS using a Babington nebulizer. See text for details.

with the results obtained by the previous SALD ICP-MS experiment. As can be seen in Fig. 3, the results from SALD ICP-MS and nebulizer ICP-MS are comparable for all the cases, *i.e.* intracellular copper and extracellular copper in both media.

Conclusions

Detailed investigation and comprehensive characterization of a substrate-assisted laser desorption technique has been performed. Suitable commercially available substrates have been tested, and PETG has shown to be the most appropriate substrate especially due to absence of metal contaminants and transparency. SALD ICP-MS has shown large signal stability over a wide range of laser power density values. Moreover, the signal has not been affected when switching between the point and raster desorption modes. In the case of ^{63}Cu isotope determination, raster desorption is, however, limited to scan rates below 100 μm s^{-1}, if lacking dynamic reaction cell. Complete sample desorption can be achieved using ten pulses with spot-to-spot reproducibility below 6%. With linear dynamic range over six orders of magnitude and detection limits about 26 fg for copper, SALD ICP-MS has proved to be a powerful tool for the analysis of metals in real samples at micro volume and trace concentration, as demonstrated on the determination of copper in U937 cells. Moreover, the protocol for biological sample preparation has been optimized by the minimization of substrate etching, which was found to decrease the integrated ICP-MS signal.

Acknowledgements

Notes and references

1 C. A. Heinrich, T. Pettke, W. E. Halter, M. Aigner-Torres, A. Audetat, D. Günther, B. Hatentendorf, D. Bleiner, M. Guillong and I. Horn, *Geochim. Cosmochim. Acta*, 2003, **67**, 3473.

2 B. Stoffell, M. S. Appold, J. J. Wilkinson, N. A. McClean and T. E. Jeffries, *Econ. Geol.*, 2008, **103**, 1411.
3 D. Günther, S. E. Jackson and H. P. Longerich, *Spectrochim. Acta, Part B*, 1999, **54**, 381.
4 M. Bi, A. M. Ruiz, I. Gornushkin, B. W. Smith and J. D. Winefordner, *Appl. Surf. Sci.*, 2000, **158**, 197.
5 S. Wang, R. Brown and D. J. Gray, *Appl. Spectrosc.*, 1994, **48**, 1321.
6 M. R. B. Binet, R. Ma, C. W. Mcleod and R. K. Poole, *Anal. Biochem.*, 2003, **318**, 30.
7 V. A. Lemos, G. D. Novaes, A. L. de Carvalho, E. M. Gama and A. G. Santos, *Environ. Monit. Assess.*, 2009, **148**, 245.
8 J. S. Liu, H. W. Chen, X. Q. Mao and X. Jin, *Int. J. Environ. Anal. Chem.*, 2000, **76**, 267.
9 Q. Pasha, S. A. Malik and M. H. Shah, *J. Hazard. Mater.*, 2008, **153**, 1215.
10 C. S. Nomura, C. S. da Silva and P. V. Oliveira, *Quim. Nova*, 2008, **31**, 104.
11 K. Wróbel, E. B. Gonzales, K. Wrobel and A. Sanz-Mendel, *Analyst*, 1995, **120**, 809.
12 E. H. Evans, S. Chenery and A. Fisher, *J. Anal. At. Spectrom.*, 1999, **14**, 977.
13 M. Krachler, C. Heisel and P. Kretzer, *J. Anal. At. Spectrom.*, 2009, **24**, 605.
14 B. M. Wah Fong, T. S. Siu, J. S. K. Lee and S. Tam, *Clin. Chem. Lab. Med.*, 2009, **47**, 75.
15 V. K. Karandashev, A. N. Turanov, T. A. Orlova, A. E. Lazhnev, S. V. Nosenko, N. I. Zolotareva and I. R. Moskvitina, *Inorg. Mater.*, 2008, **44**, 1491.
16 J. Millos, M. Costas-Rodriguez, I. Lavilla and C. Bendicho, *Anal. Chim. Acta*, 2008, **622**, 77.
17 J. L. Rodrigues, J. A. Nunes, B. L. Batisat, S. S. De Souza and F. Barbosa, *J. Anal. At. Spectrom.*, 2008, **23**, 992.
18 K. Minakata, M. Suzuki and O. Suzuki, *Anal. Chim. Acta*, 2008, **614**, 161.
19 O. Schramel, B. Michalke and A. Kettrup, *J. Chromatogr., A*, 1998, **819**, 231.
20 D. Günther, R. Frischknecht, H. J. Muschenborn and C. A. Heinrich, *Fresenius J. Anal. Chem.*, 1997, **359**, 390.
21 F. Boué-Bigne, B. J. Masters, J. S. Crighton and B. L. Sharp, *J. Anal. At. Spectrom.*, 1999, **14**, 1665.
22 L. Yang, R. E. Sturgeon and Z. Mester, *Anal. Chem.*, 2005, **77**, 2971.
23 L. Yang, R. E. Sturgeon and Z. Mester, *J. Anal. At. Spectrom.*, 2005, **20**, 431.
24 U. E. A. Fittschen, N. H. Bings, S. Hauschild, S. Forster, A. F. Kiera, E. Karavani, A. Fromsdorf and J. Thiele, *Anal. Chem.*, 2008, **80**, 1967.
25 O. Peš, P. Jungová, R. Vyhnánek, T. Vaculovič, V. Kanický and J. Preisler, *Anal. Chem.*, 2008, **80**, 8725.
26 J. S. Becker, M. Zoriy and J. S. Becker, *J. Anal. At. Spectrom.*, 2007, **22**, 736.
27 J. Dobrowolska, M. Dehnhardt and A. Matusch, *Talanta*, 2008, **74**, 717.
28 M. V. Zoriy, M. Dehnhardt and A. Matusch, *Spectrochim. Acta, Part B*, 2008, **63**, 375.
29 M. L. Turski and D. J. Thiele, *J. Biol. Chem.*, 2009, **284**, 717.
30 P. J. Aggett and S. Fairweather-Tait, *Am. J. Clin. Nutr.*, 1998, **67**, 1061.
31 K. G. Daniel, R. H. Harbach, W. C. Guida and Q. P. Dou, *Front. Biosci.*, 2004, **9**, 2652.
32 D. Chen, Q. C. Cui, H. Yang and Q. P. Dou, *Cancer Res.*, 2006, **66**, 10425.
33 D. Z. Cen, D. Brayton, B. Shahandeh, F. L. Meyskens and P. J. Farmer, *J. Med. Chem.*, 2004, **47**, 6914.
34 D. Chen, F. Peng, Q. C. Cui, K. G. Daniel, S. Orlu, J. Liu and Q. P. Dou, *Front. Biosci.*, 2005, **10**, 2932.
35 C. S. I. Nobel, M. Kimland and B. Lind, *J. Biol. Chem.*, 1995, **270**, 26202.
36 M. Wickstrom, K. Danielsson, L. Rickardson, J. Gullbo, P. Nygren, A. Isaksson, R. Larsson and H. Lovborg, *Biochem. Pharmacol.*, 2007, **73**, 25.
37 S. S. Brar, C. Grigg, K. S. Wilson, W. D. Holder, Jr., D. Dreau and C. Austin, *Mol. Cancer Ther.*, 2004, **3**, 1049.
38 J. Navrátilová, P. Jungová, P. Vaňhara, J. Preisler, V. Kanický and J. Šmarda, *Int. J. Mol. Med.*, 2009, **24**, 661.
39 Z. L. Huang and M. L. Failla, *Faseb J.*, 2000, **14**, 794.
40 Z. X. L. Huang, M. L. Failla and P. G. Reeves, *Exp. Biol. Med.*, 2001, **226**, 222.
41 F. Foret and J. Preisler, *Proteomics*, 2002, **2**, 360.
42 J. Preisler, Hu, T. Rejtar, E. Moskovets and B. L. Karger, *Anal. Chem.*, 2002, **74**, 17.
43 Z. H. Huang and M. L. Failla, *J. Nutr.*, 2000, **130**, 1536.

3 Mass spectrometry as a tool in identification and characterization

In order to unambiguously identify and/or characterize a compound, MS is usually not sufficient and orthogonal information should be involved.[39] It has been proved that MS can provide maximum information when analyzing pure substances. Hence, reducing the sample mixture complexity is mandatory, whether through a separation technique or multiple-stage MS. The hybrid mass spectrometers capable of performing more than just measuring the mass-to-charge ratio of analytes are eligible. Furthermore, the utility of various other LC detectors and/or computational MS may help confirm identification, especially since collision-induced dissociation is not as reproducible as electron ionization fragmentation across different instruments or even instrument types.

When analyzing an unknown compound, one of the most basic — but fundamental — goals is assigning its molecular peak (if it exists) and retrieving its molecular formula. A few general principles could help in the task.

- *Isotopic pattern*

The isotopic pattern of the target molecular formula should be similar to the simulated one according to the binomial expansion.[40] Given the instrument resolving power, isotopic patterns are usually calculated for the most abundant elements (C, H, O, N, S, P). Other elements are usually included in specific cases of known heteroatoms, *e.g.*, analysis of metals, presence of M + n elements, isotope dilution methods, *etc.*

- *Molecular or ionic adducts*

Ions like Na^+, K^+, or Cl^- are commonplace and cannot be easily removed from the final mixture during the ionization process. They may easily replace the proton in ionization techniques producing even-electron ions. Hence, it is better to accommodate the adducts' specific mass shifts when searching for a molecular peak. Some classes of compounds are even better suited to be analyzed using artificially added ions such as Li^+ or Ag^+.[41]

- *Multiply-charged ions and n-mers*

Multiply-charged ions result from having more than a single site in a molecule where the charge could be located. They are typically seen in the ESI of biomolecules, and deconvolution of the charge state of two adjacent peaks in the positive mode can be calculated using a simple formula:

$$\text{Peak}_{m/z} = (M_w + z)/z$$

$$\text{Adjacent Peak}_{m/z} = (M_w + z + 1)/(z + 1)$$

Provided that the MS analyzer resolving power is sufficient, the isotopes of a multiply-charged ion will appear at fractional m/z values. Fragmentation of multiply-charged ions provide (typically) peaks of higher m/z than those of the precursor. The n-mers ions are considered merely gaseous phase-associated molecules, which happen to reach the detector with some probability. The intensity of n-mers is usually lower than that of the molecular peak and depends on the analyte concentration in the sample. The n-mers could easily form ionic adducts or lose neutral compounds and their fragmentation provides (typically) peaks of m-mers, where $m < n$.

- *Loss of a neutral molecule*

There is a plenty of so called good leaving groups, which could be cleaved off an analyte molecule during any stage of mass spectrum acquisition. A loss of molecules such as H_2O or CO_2 is often observed at certain compounds (aliphatic –OH or –COOH) even under soft ionization conditions. The specific shifts in m/z can help to determine the molecular composition.

- *Nitrogen rule*

Nitrogen has an even nominal mass (14) and odd valency (3). Neutral compounds, with all of the atoms in the molecule having a number of covalent bonds equal to their standard valency, have odd nominal mass if they contain an odd number of nitrogen atoms. Depending on the nature of the ionization process, either odd-electron or even-electron ions may be produced. The nitrogen rule is reversed in the case of even-electron ions, yet the principle is the same.

- *Hydrogen/Carbon ratio*

Another constraint for restricting formulas to those likely existing is including element ratios, especially the hydrogen/carbon ratio. In most cases, the hydrogen/carbon ratio does not exceed H/C > 3 and should not be less than 0.125 with typical ratios being found between 2.0 > H/C > 0.5.

- *Hydrogen/deuterium exchange*

Hydrogen/deuterium exchange (HDX) MS has been employed widely to determine the presence, the number and the position of exchangeable hydrogen atoms in small organic molecules, peptides, or proteins. The exchange of labile hydrogen with deuterium could happen in solution or gas phase of compounds containing groups such as –OH, –NH$_2$, –SH, –NH–, or COOH. Traditionally, deuterated solvents are used as mobile phase in liquid separation techniques; but, a cost-effective approach utilizes ND_3, CH_3OD or D_2O as sheath liquid in ESI or as an ionization gas in chemical ionization mode. HDX MS is typically employed in identification of isomeric compounds or in understanding the nature of chemical reactions formed via unpredictable pathways.

- *Mass defect*

The difference between the exact mass of an element (or a compound) and its closest integer value is called a mass defect. Chemical reactions will introduce a mass defect shift between the parent and its product molecule, which could be viewed using MS manufacturers algorithms when accurate mass is used. Typically, extracted ion chromatograms are generated in a fixed, narrow mass defect range, yielding peaks selectively for the parent-product compounds excluding majority of matrix components.
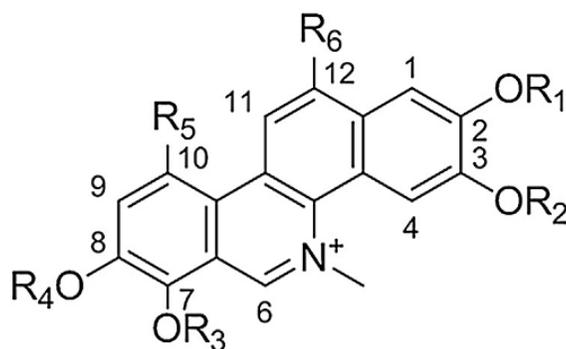
- *Chemical reactions*

A specific approach to identify a compound can involve a series of (bio)chemical reactions, *e.g.*, chemical reactions using a hemoprotein superfamily of cytochrome P450, in an *in vitro* or *in vivo* experimental design. *In vitro* designs are advantageous as the final mixture of metabolites and parent compounds contain merely phase I metabolites. *In silico* prediction software tools may help design the experiment in order to detect the prepared metabolites.

Additional approaches that complement the above-mentioned ones rely on utilizing chemical derivatization, different

ionization, instruments with high resolving power, fragmentation and a multiple-stage MS, retention-based characteristic, or orthogonal information from other detectors *e.g.* UV-Vis, fluorescence, electrochemical *etc.* These are, however, very situational and also depend on the available laboratory equipment.[42]

3.1 Identification of metabolites of selected benzophenanthridine alkaloids and their toxicity evaluation

Benzo[c]phenanthridine alkaloids (QBAs) belong to a group of isoquinoline alkaloids and were first discovered in the plant *Sanguinaria canadensis*, used in traditional medicine by Native Americans.[43] Sanguinarine (SA) was first isolated from the rhizome of the plant and bears its name. The plant contains other QBAs, such as chelerythrine (CHE), sanguilutine (SL), chelilutine (CL), sanguirubine (SR) and chelirubine (CR), see Figure 3. Hexasubstituted alkaloid macarpine (MA) was first isolated from *Macleaya microcarpa* in 1955.[44] Major QBAs, SA and CHE, have been produced commercially and belong to the best-investigated QBAs.

Alkaloid	R_1	R_2	R_3	R_4	R_5	R_6
Sanguinarine (SA)	-CH$_2$-		-CH$_2$-		-H	-H
Chelerythrine (CHE)	-CH$_2$-		-CH$_3$	-CH$_3$	-H	-H
Sanguilutine (SL)	-CH$_3$	-CH$_3$	-CH$_3$	-CH$_3$	-OCH$_3$	-H
Chelilutine (CL)	-CH$_2$-		-CH$_3$	-CH$_3$	-OCH$_3$	-H
Sanguirubine (SR)	-CH$_3$	-CH$_3$	-CH$_2$-		-OCH$_3$	-H
Chelirubine (CR)	-CH$_2$-		-CH$_2$-		-OCH$_3$	-H
Macarpine (MA)	-CH$_2$-		-CH$_2$-		-OCH$_3$	-OCH$_3$

Figure 3: Benzo[c]phenanthridine alkaloid structures.

Minor QBAs have never been produced in large amounts even though their recent research suggested they exhibit exclusively different properties despite their similarity with SA and CHE.[45] SL exhibited high anti-proliferation activity against specific melanoma cell lines, mediated by autophagy and and necroptosis.[46] QBAs cytotoxicity is predetermined by methylenedioxy rings at carbon positions C2–C3 and C7–C8. The most cytotoxic QBAs are CR, SA, and MA with IC$_{50}$ in a range of 0.5–6 · 10^{-6} M for THP-1 cell lines.[47,48] Synthetically modified QBAs or

de novo synthesized QBA analogs were prepared to increase the cytotoxic properties or alter the metabolism.[49,50] Another attempt to produce, isolate, characterize and assess the cytotoxicity of these minor QBAs metabolites have been made in the following article using rat liver microsomes (RLMs) and LC–MS/MS. Two major metabolites, O-demethylated CHE and O-demethylated SL, were successfully prepared, identified, isolated, and tested for cytotoxicity in comparison to the corresponding parent alkaloid. Biotransformation reactions varied significantly across all alkaloids despite the remarkable structural similarity of the studied QBAs. A few alkaloids were unable to undergo specific transformation reactions, which could potentially be associated with their elevated cytotoxicity. On top of that, by employing biotransformation reactions, it was possible to identify one of the metabolites of CHE. Two O-demethylation reactions in phase I metabolism may produce two isomers, which substantially differ in toxicity. When the prepared metabolite was purified, isolated, and tested for its cytotoxicity, the alkaloid fagaridine was ultimately unraveled as the CHE metabolite.

Author's contribution: 40 %

Identification of metabolites of selected benzophenanthridine alkaloids and their toxicity evaluation

Roman Sandor[a], Adam Midlik[a,b], Kristyna Sebrlova[a], Gabriela Dovrtelova[c], Kristyna Noskova[c], Jan Jurica[c,d], Iva Slaninova[e], Eva Taborska[a], Ondrej Pes[a,*]

[a] Department of Biochemistry, Faculty of Medicine, Masaryk University, Kamenice 5, 62500 Brno, Czech Republic
[b] Department of Chemistry, Faculty of Science, Masaryk University, Kamenice 5, 62500 Brno, Czech Republic
[c] Department of Pharmacology, Faculty of Medicine, Masaryk University, Kamenice 5, 62500 Brno, Czech Republic
[d] Central European Institute of Technology CEITEC MU, Kamenice 5, 62500 Brno, Czech Republic
[e] Department of Biology, Faculty of Medicine, Masaryk University, Kamenice 5, 62500 Brno, Czech Republic

ARTICLE INFO

ABSTRACT

Selected benzo[c]phenathridine alkaloids were biotransformed using rat liver microsomes and identified by liquid chromatography and mass spectrometry. While the metabolites of commercially available sanguinarine and chelerythrine have been studied in detail, data about the metabolism of the minor alkaloids remained unknown. Reactions involved in transformation include single and/or double *O*-demethylation, demethylenation, reduction, and hydroxylation. Two metabolites, when isolated, purified and tested for toxicity, were found to be less toxic than the original compounds.

© 2016 Elsevier B.V. All rights reserved.

1. Introduction

Quaternary benzo[c]phenanthridine alkaloids (QBAs) belong to a group of isoquinoline alkaloids widely distributed in the family Papaveraceae and, to a limited extent, in some species of the families Fumariaceae and Rutaceae. Sanguinarine (SA) and chelerythrine (CHE) are the best-known QBAs. In some plants, SA and CHE are accompanied by less-abundant pentasubstituted derivatives sanguilutine (SL), chelilutine (CL), sanguirubine (SR), chelirubine (CR), and hexasubstituted macarpine (MA) (Fig. 1).

The effects of QBAs on biological systems have been studied extensively, especially for commercially available SA and CHE. The results have been summarized in several reviews [1–4]. Research has primarily focused on antitumor effects of both alkaloids, but they also display antimicrobial, antifungal and anti-inflammatory activities. They may affect many targets on the molecular level and modify the activity and function of a wide variety of enzymes. The fractions rich in QBAs from *Sanguinaria canadensis* or *Macleaya cor-*

data have been used in toothpastes and mouthwashes as antiplaque agents [1,3].

While it seems that low concentrations of QBAs have no observable toxic effects [5–7], epidemiological case studies have shown an association between SA use and oral premalignant lesions [8,9] and a study with higher doses of SA discovered that SA displayed signs of significant liver damage in mice [10]. Further, it has been shown that SA creates complexes with DNA which could potentially lead to the changes in DNA structure and subsequently affect cell viability [11]. From a medical standpoint, the most interesting is the ability of QBAs to cause apoptosis. While SA causes apoptosis in cancer and normal cells alike, a few studies have shown that cancer cells are significantly more sensitive to the effects of SA than normal cells [12,13]. In contrast, Debiton et al. did not find any difference in effect of SA between cancer and normal cells [14]. Still, because of their medicinal potential, both SA and CHE have been substantially studied in this respect [15–18]. Nevertheless, the exact biological paths by which both substances affect cells are still not entirely known. Although the commercially available SA and CHE have been extensively studied, data about the effects of other minor QBAs on cells are still limited. For instance, it has been shown that MA and SR show a considerable fluorescence shift when bound to DNA, a property, which make them useful as fluorescent probes [19]. While

SL and CL exhibit antiproliferative and anti-microtubular activities [20], SR, CR, and MA are antiproliferative and pro-apoptotic, which has been well documented [21]. SL has been found to preferentially induce necroptosis over apoptosis in melanoma cells [22]. Their limited availability is the major challenge to be overcome when assessing their full potential and/or risks.

One of the reasons for inconsistent results of various studies could be the difference in metabolism of QBAs by different cells. There are substantial differences in the metabolism and enzymes present even between various healthy cell types and tissues, which can lead to different metabolite profiles. This could explain why some studies found a significant ROS production, leading to apoptosis [23–25] while others found no increase in ROS production when studying the pro-apoptic properties of QBAs [14,26]. The rapid apoptotic response induced by a glutathione depletion effect could be a part of a mechanism of SA cytotoxicity [14].

Plant cells producing QBAs are able to reabsorb SA and CHE reducing it to dihydro derivatives, thereby protecting themselves from their own product of synthesis [27]. It seems that also in animals and humans the first step in biotransformation of CHE and SA is their conversion to the respective dihydro derivatives. Psotova et al. identified in experiments with rats dihydro SA (DHSA) as the main metabolite in liver and plasma after the oral administration of SA [28]. Kosina et al. showed that formation of the dihydro-metabolites, which may be followed by specific O-demethylenation/O-demethylation processes, is probably the main route of biotransformation (detoxification) of the benzo[c]phenanthridines in human hepatocytes [29]. Deroussent et al. studied oxidative biotransformation of SA using eight human recombinant CYPs; however, only CYP1A1 and CYP1A2 displayed any metabolic activity. Up to six metabolites were detected. The main metabolite M2 (m/z 320) resulted from a ring-cleavage of SA followed by demethylation; 5,6-dihydrosanguinarine was the prominent derivative formed from SA in cells expressing no CYP [30].

The enzyme cofactors NADH and NADPH can participate in the reduction of SA to DHSA in cells, and this conversion has been demonstrated in vitro by several authors in the absence of any enzyme [29,31,32]. Wu et al. demonstrated that the SA iminium bond can be reduced 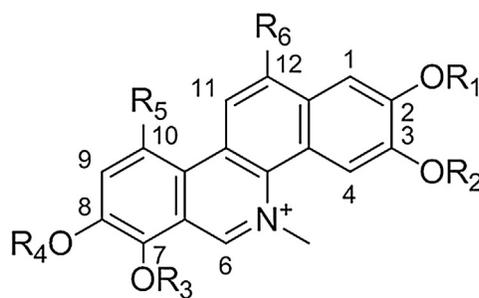by rat liver microsomes and cytosol in the absence of NAD(P)H. The reductase activity of both fractions was significantly enhanced in the presence of NADH. The amount of DHSA formed in liver cytosol was 4.6-fold higher in the presence of NADH. In this case, NADH was more effective than NADPH as an electron donor for the SA iminium bond reduction [33]. These observations indicated that cytosolic enzymes are highly likely to be involved in SA reduction in the rat liver. DHSA and dihydrochelerythrine (DHCHE) was proved in other animal cells, however; details of such processes have not yet been clarified [28–30,32,34].

While the metabolic biotransformation of SA has been well studied [35], the exact properties of many of its metabolites are not known. Without the knowledge of the metabolic fate of QBAs and properties of their metabolites, it is impossible to understand or predict the potential therapeutic options and side effects. Vacek et al. have performed a well-designed study where they have produced both phase I and II metabolites of CHE and DHCHE in vitro using human hepatocytes [36]. Authors tried testing cytotoxicity of DHCHE and O-demethylated CHE (DMCHE); however, both were prepared in vitro by reduction with NaBH$_4$. As enzymatic, stereoselective O-demethylation of CHE might provide two isomers, C8 DMCHE (fagaridine) and C7 DMCHE (NK 109 or isofagaridine), they could correspondingly differ in toxicity [37]. Metabolic studies of minor QBAs have not been yet performed and herein presented approach comprising of drug biotransformation, isolation of its metabolites, and (cyto-) toxicity assessment is required for their comprehensive study.

2. Materials and methods

2.1. Reagents and materials

Methanol (MeOH, p.a.) was obtained from Penta (Czech Republic). Phosphoric acid (p.a.), formic acid (LC MS), ammonium hydroxide (28–30% NH$_3$ in water), sodium formate (LC MS), Tris, KCl, sucrose, EDTA, NADP, glucose-6-phosphate, MgCl$_2$, glucose-6-phosphate dehydrogenase, fetal bovine serum, glutamine, penicillin, streptomycin, MeOH (LC MS), acetonitrile (ACN, HPLC grade, LC MS) and dimethylsulfoxide (DMSO, p.a.) were purchased from Sigma–Aldrich (Czech Republic). All water used was of

Alkaloid	R$_1$	R$_2$	R$_3$	R$_4$	R$_5$	R$_6$
Sanguinarine (SA)	-CH$_2$-		-CH$_2$-		-H	-H
Chelerythrine (CHE)	-CH$_2$-		-CH$_3$	-CH$_3$	-H	-H
Sanguilutine (SL)	-CH$_3$	-CH$_3$	-CH$_3$	-CH$_3$	-OCH$_3$	-H
Chelilutine (CL)	-CH$_2$-		-CH$_3$	-CH$_3$	-OCH$_3$	-H
Sanguirubine (SR)	-CH$_3$	-CH$_3$	-CH$_2$-		-OCH$_3$	-H
Chelirubine (CR)	-CH$_2$-		-CH$_2$-		-OCH$_3$	-H
Macarpine (MA)	-CH$_2$-		-CH$_2$-		-OCH$_3$	-OCH$_3$

Fig. 1. Benzo[c]phenanthridine alkaloid structures.

an ultra-pure grade supplied by an in-house Milli-Q system (Millipore, MA, USA).

2.2. Alkaloid isolation

The standards of the benzophenanthridine alkaloids originated from isolations during the systematic studies in the laboratories of the Department of Biochemistry from plant material of *Macleaya microcarpa* (Maxim.) Fedde, *Dicranostigma lactucoides* Hook. F. et Thomson, *S. canadensis* L., and *Stylophorum lasiocarpum* (Oliv.) Fedde. Briefly, SA, CHE, CR, CL, SL, SR and MA were prepared by extraction of dried, ground plant material with methanol in a FexIKA® apparatus (IKA, Germany). The extract was purified, concentrated and the last step of isolation was performed by means of semi-preparative reversed-phase (RP) chromatography [38,39]. The identity of the alkaloids was verified by EI-MS, ^{1}H NMR and ^{13}C NMR and their purities were at least 98% according to an HPLC analysis [40,41].

2.3. Isolation of rat liver microsomes

Male Wistar albino rats (280 ± 20 g), 8 weeks of age were used for the isolation of liver microsomal fraction. Animals were housed under standard laboratory conditions (22 ± 2 °C room temperature; 55 ± 5% room humidity; 12:12 h light/dark cycle) with free access to water and food. After 5 days of acclimatization, animals were sacrificed by decapitation and subjected to laparotomy.

A liver tissue from 10 animals (3 g) was homogenized, and rat liver microsomes (RLM) were isolated by differential ultracentrifugation ($19\,000 \times g$ and $105\,000 \times g$) in Tris/KCl buffer (pH 7.4; 20 mM) including washing with 0.15 M KCl and finally diluted in Tris/sucrose buffer (pH 7.4; 0.25 M). The total protein content in the microsomal preparations was assessed according to Lowry et al. using bovine serum albumin as a standard [42]. Aliquots of 250 μL were stored in −80 °C until needed. All experimental procedures were approved by both Local Committee for Animal Welfare and the Czech Central Committee for Animal Welfare, approval No. MSMT-158/2013-310 valid till 10/2017.

2.4. Incubation, extraction and analysis of samples

Each alkaloid (50 μg) was in two replicates incubated in a horizontal vortex mixer (120 min^{-1}) with water bath (37 °C) for 120 min at 37 °C with RLM and a NADPH generating system according to the previously described method of Wójcikowski et al. with a slight modification [43]. The incubation mixture of final volume of 1.0 mL contained phosphate buffer (pH 7.4; 50 mM), EDTA (1.1 mM), NADP (1.2 mM), glucose-6-phosphate (4.4 mM), MgCl$_2$ (3.2 mM), glucose-6-phosphate dehydrogenase (1 U mL^{-1}), RLM (50 μL, 20 mg mL^{-1}). The reaction was stopped by addition of 100 μL of ice-cold methanol and transferred to an ice bath.

Metabolites were purified by adding 1 mL of MeOH:ACN:formic acid (50:50:0.02, v/v/v) into a 100 μL aliquot of the incubation mixture, followed by vortex and centrifugation. A 50 μL portion of the supernatant was five times diluted with water and injected (20 μL) onto an LC column. Each alkaloid was designed for a set of incubations, where one sample contained the alkaloid, RLM and a NADPH generating system, the second one contained only RLM and the NADPH generating system (blank), and the third one tested the alkaloid in the NADPH generating system with no P450 enzymes. For isolation of selected metabolites, 200 μg of the alkaloid in two replicates was mixed with the same RLM system, incubated overnight (16 h) and purified accordingly.

2.5. LC MS

The LC MS method was developed using a Dionex Ultimate 3000RS (Thermo Scientific, CA, USA) module. Compound separation was achieved with a 3.0 mm × 150 mm, 5 μm Synergi RP-Max C18 (Phenomenex, CA, USA) column, thermostated at (23 ± 0.1) °C, and a flow-rate of 0.5 mL min^{-1}. The binary mobile phase system consisted of 0.1% (v/v) of formic acid and ACN. After a 20 μL injection, the volume of ACN was linearly increased from 20% to 40% over 10 min and then to 80% over the subsequent 10 min. ACN was held at 80% for 10 min, followed by equilibration under the initial conditions for 3.0 min. A complete HPLC run was 33 min. The HPLC system was connected to a Bruker MicrOTOF-Q II (Germany) mass spectrometer, operated in the positive electrospray ionization mode. The ionization conditions were determined by the software as follows: capillary voltage: 4500 V, end plate offset: −500 V, source temperature: 220 °C, desolvation gas (nitrogen) flow: 10 L min^{-1}, nebulizer (nitrogen) pressure: 300 kPa and collision cell voltage: 35 eV. The base-peak chromatogram (BPC) was acquired in MS mode by monitoring the m/z range of 50–3000 with a spectra sample time of 1 s. The mass spectrometer was calibrated using 10 mM sodium formate in 50% isopropyl alcohol on a daily basis and in the beginning of each LC run with a 20 μL loop flush. This step ensured the mass accuracy was below 5 ppm across the entire chromatogram. High-resolution MS and MS/MS spectra were first investigated to obtain the elemental formula of each compound. The final identification of target compounds relied on isotope pattern matching with a combination of MS/MS and retention behavior.

2.6. Metabolite isolation

An Agilent 1200 Series LC system (Agilent Technologies, CA, USA) equipped with a fraction collector employed in alkaloid isolation was used for purification and isolation of selected metabolites as well. It consisted of a ternary pump, a DAD, a syringe-loading sample injector (ECOM, Czech Republic) with a 5 mL external sample loop and a fraction collector. Alkaloids were separated on a C12 column (Synergi RP-Max, 4 μm, 150 mm × 10 mm ID, Phenomenex, CA, USA).

The mobile phase contained ammonium formate (0.1 M HCOOH titrated with NH$_4$OH to pH 3.75) and ACN with a following elution profile: ACN was linearly increased from 20% to 40% over 10 min and then to 80% over the subsequent 10 min. ACN was held at 80% for 10 min, followed by equilibration under the initial conditions for 3.0 min. The purified mixture of alkaloid and its metabolites was diluted five times with water and 5 mL of sample was injected onto a semi-preparative column. The flow-rate was set at 6 mL min^{-1} and fractions were collected on a peak basis using a diode array detector at 280 nm. Employment of ammonium formate provided similar retention times as in the case of LC–MS and enabled simple treatment of fractions, as it is readily volatile. Moreover, the peak tailing resulting from electrostatic interactions of charged benzophenanthridines with active silanol groups in the stationary phase was minimized by competing ammonium ions.

Both identity and purity of the fractions were determined by LC MS. The fractions from both replicates were joined and the solvent volume was reduced to ~500 μL. The final concentration of the purified metabolite was calculated based on the amount of the original alkaloid loaded into the RLM system and verified at 280 nm according to external calibration of the precursor alkaloid.

2.7. Antiproliferative activity

The antiproliferative activities of metabolites prepared by overnight incubation of CHE and SL were tested using the A-
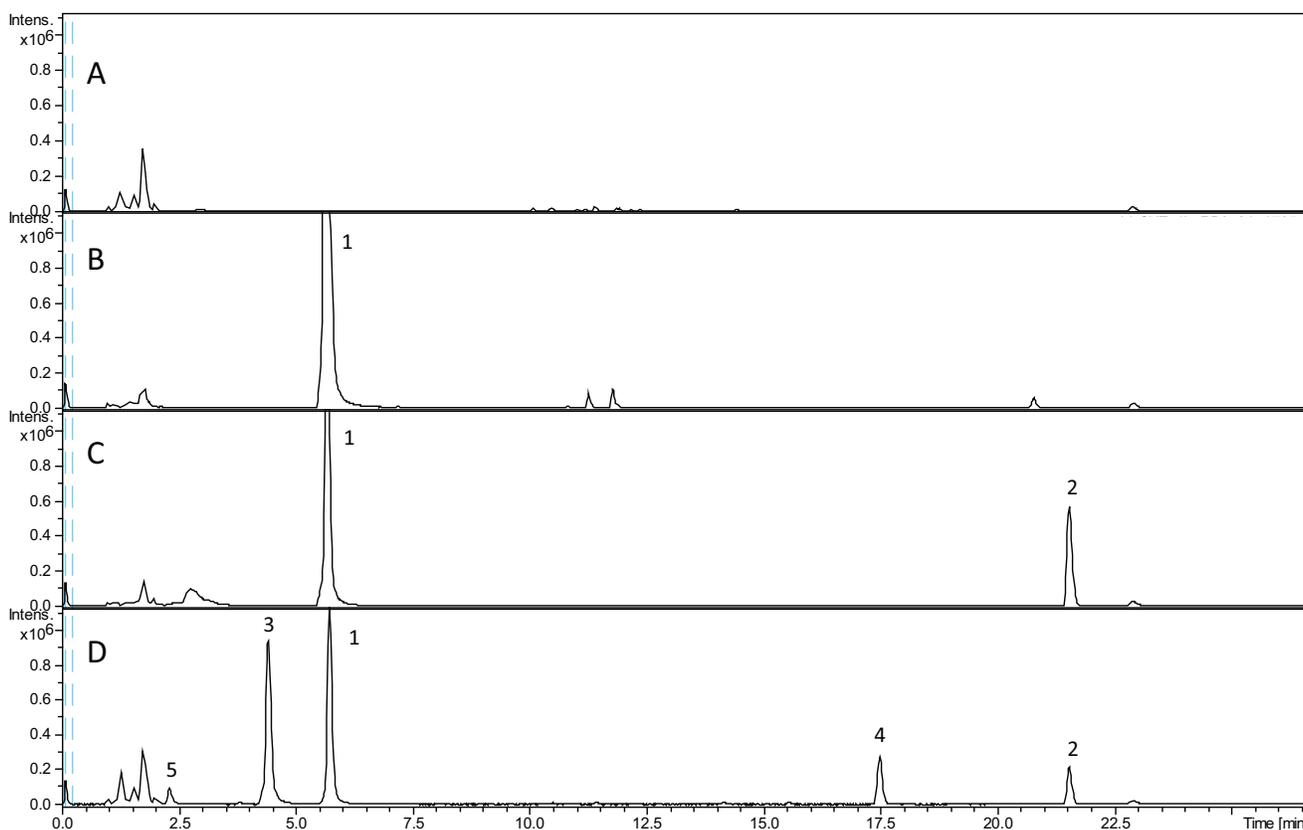
Fig. 2. Base peak chromatograms of a 4-h incubation mixture consisting of (A) RLM, (B) CHE, (C) CHE and NADPH, (D) CHE, NADPH, and RLM. Peaks are labeled as follows (1) CHE, (2) DHCHE, (3) *O*-demethyl CHE, (4) *O*-demethyl DHCHE, (5) demethylene *O*-demethyl CHE. For more details, see text.

375 human malignant melanoma cell line and a colorimetric MTT (3-(4,5-dimethylthiazol-2-yl)-2,5-diphenyl tetrazolium bromide) assay. The A-375 cell line was purchased from the European Collection of Animal Culture (ECACC, Salisbury, UK). The MTT assay was performed in a 96-well plate (Nunc A/S, Denmark). Individual wells were seeded with 200 μL of cells (1×10^4 per mL) and incubated in a RPMI 1640 medium supplemented with 10 mass% of fetal bovine serum, 2 mM of glutamine, 100 IU mL of penicillin and 100 μg mL^{-1} of streptomycin at 37 °C in a humidified atmosphere (5 vol.% CO$_2$). After 24 h of incubation, the medium was replaced with an alkaloid-containing medium at concentrations ranging from 0.3 mg L^{-1} to 10 mg L^{-1}. The MTT assay was performed 48 h after addition of the alkaloid: 20 μL of MTT (5 mg L^{-1} in PBS) was added to each well and incubated for 4 h under culture conditions. At the end of the incubation period, the medium was removed, the formazan crystals were dissolved in 200 μL of DMSO and the optical density was measured at 570 nm using a DTX 880 Multimode Detector (Beckman Coulter, CA, USA). The concentration of each compound was examined in four replicates.

3. Results and discussion

3.1. Metabolite identification

Products of biotransformation were identified by LC MS as result of a combination of MS, MS/MS, and retention behavior. Searching for metabolites was supported by a differential comparison of a series of chromatograms with and without RLM and in the NADPH system only, as seen in Fig. 2. Such a comprehensive approach with only protein precipitation as a purification step allowed for a maximum number of products. Selection of potential metabolites relied on accurate *m/z* and characteristic fragmentation patterns.

Benzophenanthridine alkaloids, unlike pavine or aporphine ones, strictly keep their nitrogen inside the highly aromatic ring during fragmentation even under conditions of high collision energy. If no nitrogen is lost during fragmentation then any change in parity in nominal mass resulted from a loss of a radical molecule. That is considered characteristic for methyl groups substituted on the nitrogen of the phenanthridine ring [30]. If a methoxy group was adjacent to a hydroxyl or another methoxy group, a loss of methane (−16 Da) followed by a loss of CO (−28 Da) was observed. Compounds in the chromatogram that experienced such fragmentation behavior were inspected as a possible product of enzymatic biotransformation. The last step in confident identification consisted in a relevant change in retention time of suggested structures. Generally, phase I metabolism aims to produce more polar compounds to increase their solubility and/or to make them available for conjugation reactions occurring during the phase II. The change corresponded with the chromatographic behavior with all identified compounds. The reduced dihydroderivatives, lacking the quaternary nitrogen, are known for their poor solubility in water, which was observable by a large increase in retention time on an RP column. Moreover, they can be distinguished in positive full scan MS, as they tend to be easily oxidized in the ion source providing characteristic peaks [M-2 + H]$^+$. This was especially important when identifying doubly *O*-demethylated or demethylenated dihydro derivatives, which eluted from the column even earlier than the original quaternary alkaloids. The dihydro derivatives are considered the major and probably the initial metabolites that are produced from any QBAs. It is reasonable to assume that the reductive transformation is the fastest process as their formation was accomplished even when they were subjected to a NADPH generating system with no RLM in the reaction mixture. While their toxicity was found to be rather low, they could serve as precursors for further metabolites whose

Table 1
Retention time, exact mass, elemental composition, a type of reaction, and metabolite content of QBAs after 120 min incubation with RLM.

Alkaloid	Detected compounds	tr (min)	Ion type	Observed m/z	Sum formula [M]	Nominal mass shift (Da)	Reaction(s) involved	[a]Peak area fraction (%)
SA		4.4	[M]$^+$	332.0927	$C_{20}H_{14}NO_4$			
	Demethylene SA	2.8	[M]$^+$	320.0923	$C_{19}H_{14}NO_4$	−12	Demethylenation	3.0
	Demethylene DHSA	12.2	[M+H]$^+$	322.1069	$C_{19}H_{15}NO_4$	−10	Reduction, demethylenation	0.2
	DHSA	22.1	[M+H]$^+$	334.1069	$C_{20}H_{15}NO_4$	+2	Reduction	96.8
CHE		5.7	[M]$^+$	348.1241	$C_{21}H_{18}NO_4$			
	Demethylene O-demethyl CHE	2.3	[M]$^+$	322.1079	$C_{19}H_{16}NO_4$	−26	O-demethylation, demethylenation	5.6
	Demethylene CHE	3.9	[M]$^+$	336.1210	$C_{20}H_{18}NO_4$	−12	Demethylenation	0.8
	Hydroxy O-demethyl CHE	4.3	[M]+	350.1028	$C_{20}H_{16}NO_5$	+2	O-demethylation, monooxygentaion	2.4
	O-demethyl CHE	4.4	[M]$^+$	334.1071	$C_{20}H_{16}NO_4$	−14	O-demethylation	62.4
	Demethylene O-demethyl DHCHE	5.8	[M+H]$^+$	324.1236	$C_{19}H_{17}NO_4$	−24	Reduction, O-demethylation, demethylenation	0.2
	Hydroxy DHCHE	15.6	[M+H]$^+$	366.1341	$C_{21}H_{19}NO_5$	+16	Reduction, monooxygenation	0.6
	O-demethyl DHCHE	17.5	[M+H]$^+$	336.1235	$C_{20}H_{17}NO_4$	−12	Reduction, O-demethylation	15.4
	DHCHE	21.5	[M+H]$^+$	350.1391	$C_{21}H_{19}NO_4$	+2	Reduction	12.6
CL		7.1	[M]$^+$	378.1351	$C_{22}H_{20}NO_5$			
	O-demethyl CL	5.7	[M]$^+$	364.1180	$C_{21}H_{18}NO_5$	−14	O-demethylation	22.1
	Bis (O-demethyl) DHCL	9,9	[M+H]$^+$	352.1176	$C_{20}H_{17}NO_5$	−26	Reduction, O-demethylation (2x)	2.0
	O-demethyl DHCL	16.2	[M+H]$^+$	366.1331	$C_{21}H_{19}NO_5$	−12	Reduction, O-demethylation	22.2
	DHCL	21.1	[M+H]$^+$	380.1483	$C_{22}H_{21}NO_5$	+2	Reduction	53.6
CR		6.1	[M]$^+$	362.1033	$C_{21}H_{16}NO_5$			
	O-demethyl CR	4.7	[M]$^+$	348.0865	$C_{20}H_{14}NO_5$	−14	O-demethylation	56.6
	O-demethyl DHCR	17.8	[M+H]$^+$	350.1027	$C_{20}H_{15}NO_5$	−12	Reduction, O-demethylation	2.3
	DHCR	21.9	[M+H]$^+$	364.1168	$C_{21}H_{17}NO_5$	+2	Reduction	41.1
SL		6.9	[M]$^+$	394.1654	$C_{23}H_{24}NO_5$			
	O-demethyl SL	5.6	[M]$^+$	380.1498	$C_{22}H_{22}NO_5$	−14	O-demethylation	2.7
	Hydroxy SL	6.1	[M]$^+$	410.1604	$C_{23}H_{24}NO_6$	+16	Monooxygenation	1.5
	Bis(O-demethyl) DHSL (A)	6.7	[M+H]$^+$	368.1499	$C_{21}H_{21}NO_5$	−26	Reduction, O-demethylation (2×)	2.5
	Bis(O-demethyl) DHSL (B)	8.5	[M+H]$^+$	368.1487	$C_{21}H_{21}NO_5$	−26	Reduction, O-demethylation (2×)	0.9
	O-demethyl DHSL (A)	12.5	[M+H]$^+$	382.1668	$C_{22}H_{23}NO_5$	−12	Reduction, O-demethylation	24.0
	O-demethyl DHSL (B)	13.1	[M+H]$^+$	382.1639	$C_{22}H_{23}NO_5$	−12	Reduction, O-demethylation	0.4
	O-demethyl DHSL (C)	14.1	[M+H]$^+$	382.1639	$C_{22}H_{23}NO_5$	−12	Reduction, O-demethylation	0.6
	Hydroxy DHSL	17.0	[M+H]$^+$	412.1759	$C_{23}H_{25}NO_6$	+18	Reduction, monooxygenation	0.3
	DHSL	18.5	[M+H]$^+$	396.1853	$C_{23}H_{25}NO_5$	+2	Reduction	67.0
SR		6.0	[M]$^+$	378.1341	$C_{22}H_{20}NO_5$			
	O-demethyl SR	4.6	[M]$^+$	364.1185	$C_{21}H_{18}NO_5$	−14	O-demethylation	22.8
	O-demethyl DHSR	15.7	[M+H]$^+$	366.1330	$C_{21}H_{19}NO_5$	−12	Reduction, O-demethylation	1.1
	DHSR	19.9	[M+H]$^+$	380.1498	$C_{22}H_{21}NO_5$	+2	Reduction	76.0
MA		7.8	[M]$^+$	392.1169	$C_{22}H_{18}NO_6$			
	Demethylene MA	5.1	[M]$^+$	380.1122	$C_{21}H_{18}NO_6$	−12	Demethylenation	9.9
	Demethylene DHMA	11.2	[M+H]$^+$	382.1283	$C_{21}H_{19}NO_6$	−10	Reduction, demethylenation	1.5
	DHMA	22.3	[M+H]$^+$	394.1319	$C_{22}H_{19}NO_6$	+2	Reduction	88.5

[a] Peak area fraction roughly represents a portion of a metabolite from the sum of all metabolites.

presence, structure, and formation rate might be the determining factors of the initial compound toxicity.

Biotransformation of seven QBAs with major and minor metabolites is summarized in Table 1. Products of biotransformation that contributed with their peak area to the mixture from more than 50% in the chromatogram (excluding the original alkaloid) were assigned as major metabolites. It is important to note that the purpose of representing metabolite distribution solely from the peak area fraction was only to approximate the real situation, as their true response might be different. The reason for such a semi-quantitative comparison is the fact that standards of metabolites are not available.

3.2. Metabolite isolation

The purified mixture of alkaloids and their metabolites were separated by a semi-preparative HPLC. The fractions containing transformed dihydro compounds (*e.g.*, O-demethylated DHCHE)

were kept for several days in dark and cold to let them re-oxidize to the respective quaternary compound. The initial large difference in retention times between oxidized, charged molecules and reduced, less polar dihydro derivatives allowed for obtaining the purest quaternary metabolites in the end. This was especially important when assessing the toxicity, as even low amount of the original alkaloid could have influenced the outcome of the tested metabolite. The final concentrations of isolated compounds were $32\,mg\,L^{-1}$ and $29\,mg\,L^{-1}$ for O-demethylated CHE and O-demethylated SL, respectively. None of the dihydro-metabolites was tested for toxicity, as it was impossible to keep them in the reduced form without affecting the toxicity itself, *i.e.*, addition of NADH or NaBH$_4$.

3.3. Metabolite structure to toxicity relationship

Despite the similar structures of studied QBAs, different QBAs underwent slightly different reactions during metabolism and the resulting distribution of metabolites for each alkaloid was unique.
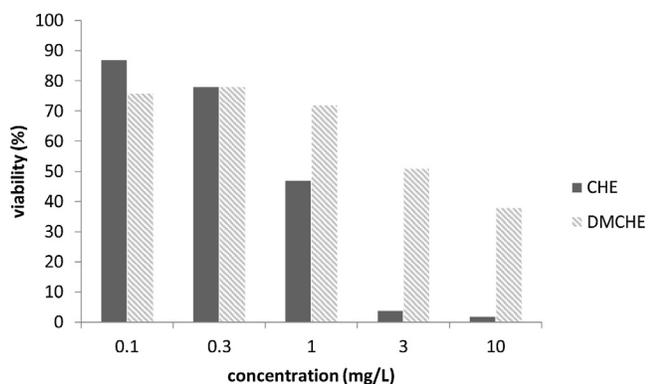
Fig. 3. An MTT assay of CHE and *O*-demethyl CHE in a range of concentrations 0.1–10 mg/L.
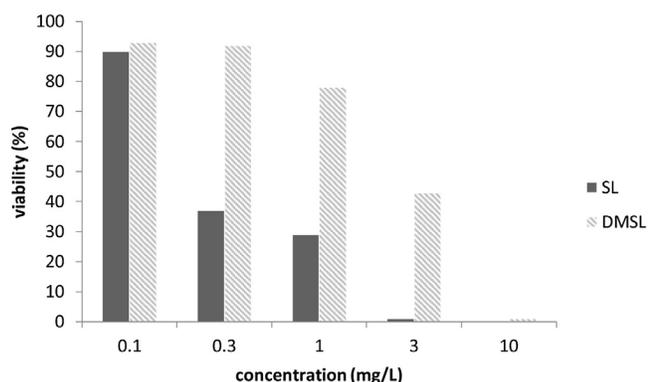

Fig. 4. An MTT assay of SL and *O*-demethyl SL in a range of concentrations 0.1–10 mg/L.

The biosynthetic pathway and known data about toxicity seems to be related to the metabolic fate of the compounds. In most plants, the biosynthetic pathway ends with the creation of SA, but a few plant species, such as *M. microcarpa* or *S. lasiocarpum*, may induce two stepwise hydroxylation and methylation reactions resulting in production of CR and then MA [44]. When SA, CR, and MA were subjected to RLM the *O*-demethylation reaction was observed in CR only. Sanguinarine obviously could have not undergone *O*-demethylation, having no methoxy groups, and underwent demethylenation instead; MA favored the same ring opening reaction over *O*-demethylation, despite the additional methoxy group when compared to CR. The rate of *O*-demethylation seems to be associated with the cytotoxicity of each alkaloid, as SA and MA have proved substantially more toxic than CR when assessed using a standard MTT assay [45].

The major metabolite of CHE, *O*-demethylated CHE, was formed by a stereospecific enzymatic reaction providing demethylation of a methoxy group attached either to the carbon C8 (fagaridine) or C7 (NK-109) of the ring. The products substantially differ in toxicity; fagaridine is non-toxic but NK-109 was found to be as toxic as SA or nitidine [37]. The toxicity of the *O*-demethylated product was lower when compared to the original CHE as seen in Fig. 3. This fact, while strengthening the confidence in fagaridine formation, also indicated that the relatively low toxicity of CHE might be caused by its straightforward detoxification to a relatively high number of metabolites through the P450 enzyme family.

CL with three and SL with five methoxy groups favored single and double *O*-demethylation as a major type of reaction, respectively. We did not observe a fully demethylated product from CL or SL under any conditions, which could imply that the methoxy group at C10 of the benzophenanthridine ring at these two alkaloids was

kept intact in all cases. However, this requires to be confirmed, *e.g.*, by NMR spectrometry. The *O*-demethylated SL, when subjected to an MTT assay, was found to be less toxic than the original SL as seen in Fig. 4. It is worth noting that while this fact has been assumed since the first oral administration of SA and/or CHE, experimental data about the toxicity of their major metabolites have not yet been shown.

4. Conclusions

Biotransformation of five minor QBAs was investigated using *in vitro* incubations with RLM. The manner of biotransformation of alkaloids varied significantly although the original alkaloids are of a very similar structure and the incubation conditions were identical. Typical transformation reactions included *O*-demethylation, *O*-demethylenation, hydroxylation, and/or their combination. The inability to undergo specific transformation reactions may explain high retention of MA in the organism and thus high toxicity. Toxicity of *O*-demethylated metabolites, which were successfully isolated and their structure was confirmed by MS or MS/MS, was in general lower in comparison to the original alkaloids.

References

[1] V. Šimánek, R. Vespalec, A. Šedo, J. Ulrichová, J. Vičar, Quaternary benzo[C]phenanthridine alkaloids—biological activities, in: M. Schneider (Ed.), Chemical Probes in Biology, Springer, Netherlands, 2003, pp. 245–254.
[2] Z. Dvorak, V. Kuban, B. Klejdus, J. Hlavac, J. Vicar, J. Ulrichova, V. Simanek, Heterocycles 68 (2006) 2403–2422.
[3] A. Zdarilova, J. Malikova, Z. Dvorak, J. Ulrichova, V. Simanek, Chem. Listy 100 (2006) 30–41.
[4] I. Slaninova, K. Pencikova, J. Urbanova, J. Slanina, E. Taborska, Phytochem. Rev. 13 (2014) 51–68.
[5] P. Kosina, D. Walterova, J. Ulrichova, V. Lichnovsky, M. Stiborova, H. Rydlova, J. Vicar, V. Krecman, M.J. Brabec, V. Simanek, Food Chem. Toxicol. 42 (2004) 85–91.
[6] J. Psotova, R. Vecera, A. Zdarilova, E. Anzenbacherova, P. Kosina, A. Svobodova, J. Hrbac, D. Jirovsky, M. Stiborova, V. Lichnovsky, J. Vicar, V. Simanek, J. Ulrichova, Vet. Med. (Praha) 51 (2006) 145–155.
[7] F. Pica, E. Balestrieri, A. Serafino, R. Sorrentino, R. Gaziano, G. Moroni, N. Moroni, G. Palmieri, M. Mattei, E. Garaci, P. Sinibaldi-Vallebona, Anticancer Drugs 23 (2012) 32–42.
[8] D.D. Damm, A. Curran, D.K. White, J.E. Drummond, Oral Surg. Oral Med. Oral Pathol. Oral Radiol. Endod. 87 (1999) 61–66.
[9] L.R. Eversole, G.M. Eversole, J. Kopcik, Oral Surg. Oral Med. Oral Pathol. Oral Radiol. Endod. 89 (2000) 455–464.
[10] C.-S. Choy, K.-P. Cheah, H.-Y. Chiou, J.-S. Li, Y.-H. Liu, S.-F. Yong, W.-T. Chiu, J.-W. Liao, C.-M. Hu, J. Appl. Toxicol. 28 (2008) 945–956.
[11] M. Maiti, R. Nandi, K. Chaudhuri, FEBS Lett. 142 (1982) 280–284.
[12] N. Ahmad, S. Gupta, M.M. Husain, K.M. Heiskanen, H. Mukhtar, Clin. Cancer Res. 6 (2000) 1524–1528.
[13] Z. Slunska, E. Gelnarova, J. Hammerova, E. Taborska, I. Slaninova, Toxicol. In Vitro 24 (2010) 697–706.
[14] E. Debiton, J.C. Madelmont, J. Legault, C. Barthomeuf, Cancer Chemother. Pharmacol. 51 (2003) 474–482.
[15] F.-J. Cao, R. Yang, C. Lv, Q. Ma, M. Lei, H.-L. Geng, L. Zhou, Eur. J. Pharm. Sci. 67 (2015) 45–54.
[16] S. Kumar, P. Deepak, P.K. Gautam, A. Acharya, J. Cancer Res. Therap. 9 (2013) 693–700.
[17] S. Kumar, M.S. Tomar, A. Acharya, Leuk. Lymphoma 56 (2015) 1846–1855.
[18] S. Kumar, A. Acharya, Tumor Biol. 35 (2014) 129–140.
[19] J. Urbanova, P. Lubal, I. Slaninova, E. Taborska, P. Taborsky, Anal. Bioanal. Chem. 394 (2009) 997–1002.
[20] I. Slaninova, E. Taborska, H. Bochorakova, J. Slanina, Cell Biol. Toxicol. 17 (2001) 51–63.
[21] I. Slaninova, Z. Slunska, J. Sinkora, M. Vlkova, E. Taborska, Pharm. Biol. 45 (2007) 131–139.

[22] J. Hammerova, S. Uldrijan, E. Taborska, A.H. Vaculova, I. Slaninova, Biol. Chem. 393 (2012) 647–658.

[23] S. Yamamoto, K. Seta, C. Morisco, S.F. Vatner, J. Sadoshima, J. Mol. Cell. Cardiol. 33 (2001) 1829–1848.

[24] H.Q. Yin, Y.H. Kim, C.K. Moon, B.H. Lee, Biochem. Pharmacol. 70 (2005) 242–248.

[25] B.-C. Jang, J.-G. Park, D.-K. Song, W.-K. Baek, S.K. Yoo, K.-H. Jung, G.-Y. Park, T.-Y. Lee, S.-I. Suh, Toxicol. In Vitro 23 (2009) 281–287.

[26] J. Vrba, P. Kosina, J. Ulrichova, M. Modriansky, Toxicol. Lett. 151 (2004) 375–387.

[27] D. Weiss, A. Baumert, M. Vogel, W. Roos, Plant Cell Environ. 29 (2006) 291–302.

[28] J. Psotova, B. Klejdus, R. Vecera, P. Kosina, V. Kuban, J. Vicar, V. Simanek, J. Ulrichova, J. Chromatogr. B: Anal. Technol. Biomed. Life Sci. 830 (2006) 165–172.

[29] P. Kosina, J. Vacek, B. Papouskova, M. Stiborova, J. Styskala, P. Cankar, E. Vrublova, J. Vostalova, V. Simanek, J. Ulrichova, J. Chromatogr. B: Anal. Technol. Biomed. Life Sci. 879 (2011) 1077–1085.

[30] A. Deroussent, M. Re, H. Hoellinger, T. Cresteil, J. Pharm. Biomed. Anal. 52 (2010) 391–397.

[31] J. Kovar, J. Stejskal, H. Paulova, J. Slavik, Collect. Czech. Chem. Commun. 51 (1986) 2626–2634.

[32] S.S. Matkar, L.A. Wrischnik, U. Hellmann-Blumberg, Arch. Biochem. Biophys. 477 (2008) 43–52.

[33] Y. Wu, Z.-Y. Liu, Y. Cao, X.-J. Chen, J.-G. Zeng, Z.-L. Sun, Pharmacol. Rep. 65 (2013) 1391–1400.

[34] H.-H. Zhang, Y. Wu, Z.-L. Sun, Z.-Y. Liu, Rapid Commun. Mass Spectrom. 27 (2013) 979–984.

[35] Z. Dvorak, V. Simanek, Curr. Drug Metab. 8 (2007) 173–176.

[36] J. Vacek, B. Papouskova, P. Kosina, A. Galandakova, J. Ulrichova, J. Chromatogr. B: Anal. Technol. Biomed. Life Sci. 941 (2013) 17–24.

[37] T. Nakanishi, M. Suzuki, A. Saimoto, T. Kabasawa, J. Nat. Prod. 62 (1999) 864–867.

[38] E. Taborska, F. Veznik, L. Slavikova, J. Slavik, Collect. Czech. Chem. Commun. 43 (1978) 1108–1112.

[39] J. Dostal, E. Taborska, J. Slavik, Fitoterapia 63 (1992) 67–69.

[40] R. Marek, J. Tousek, J. Dostal, J. Slavik, R. Dommisse, V. Sklenar, Magn. Reson. Chem. 37 (1999) 781–787.

[41] J. Suchomelova, H. Bochorakova, H. Paulova, P. Musil, E. Taborska, J. Pharm. Biomed. Anal. 44 (2007) 283–287.

[42] O.H. Lowry, N.J. Rosebrough, A.L. Farr, R.J. Randall, J. Biol. Chem. 193 (1951) 265–275.

[43] J. Wojcikowski, K. Golembiowska, W.A. Daniel, Biochem. Pharmacol. 76 (2008) 258–267.

[44] M.H. Zenk, Pure Appl. Chem. 66 (1994) 2023–2028.

[45] K. Sebrlova, O. Pes, I. Slaninova, O. Vymazal, J. Kantorova, E. Taborska, Chem. Pap. 69 (2015) 698–708.

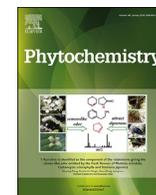## 3.2 Sanguinarine is reduced by NADH through a covalent adduct

QBAs have been known for several biological properties, which were empirically verified but not elucidated. The ability of SA to deplete the reducing potential of a cell has been one of them. Elucidation of SA properties would unlikely have started if another publication by Matkar et al. had not come first.[51] The authors claimed to discover a new, negatively-charged(!) species of SA, which they identified by electrophoresis. Since the authors provided no sufficient reasoning about the proper existence of such a species, we decided to replicate the experiment, and attempted to identify the species in a more sensible way. A careful investigation and examination of several TLC bands revealed that the novel SA species is extremely polar and converts to SA after some time. This implied a thought of a covalently bound adduct of SA and NADH, which could even be an intermediate product in a reaction of SA with cell reducing equivalents NADH or NADPH. Both coenzymes have been well-known for the following features:

1. High resistance to effective oxidation by air oxygen.
2. Net transfer of a hydride ion as the formal mechanism of their oxidation/reduction.

SA was able to covalently attach NADH and act as a mediator of NADH oxidation by air oxygen. In other words, SA exhibited enzyme-like activity; it was not consumed during the reaction and accelerated the NAD(P)H reaction with oxygen. From the other point of view, many researchers have been looking for a compound, which could elucidate (reject) the theory of a net hydride transfer, and SA (and possibly other QBAs) could serve as candidate molecules. If a hydride ion had really been formed inside the cell it would have been extremely unstable and immediately reacted with protons in its surroundings, especially those originating from dissociation/ionization of water molecules. The existence of the covalent adduct was identified using LC–MS and its reaction kinetics was characterized using LC with UV-Vis detection. The presence of the adduct contributed to explaining the mechanism of depletion of reducing equivalents in a cell while supporting an alternative theory of their electrochemical behavior beyond simple hydride transfer.

Sanguinarine is reduced by NADH through a covalent adduct

Roman Sandor [a], Jiri Slanina [a], Adam Midlik [b, c], Kristyna Sebrlova [a], Lucie Novotna [a], Martina Carnecka [a], Iva Slaninova [d], Petr Taborsky [e], Eva Taborska [a], Ondrej Pes [a, *]

[a] Department of Biochemistry, Faculty of Medicine, Masaryk University, Kamenice 5, 62500 Brno, Czech Republic
[b] National Centre for Biomolecular Research, Faculty of Science, Masaryk University Brno, Kamenice 5, 62500 Brno, Czech Republic
[c] Central European Institute of Technology CEITEC MU, Kamenice 5, 62500 Brno, Czech Republic
[d] Department of Biology, Faculty of Medicine, Masaryk University, Kamenice 5, 62500 Brno, Czech Republic
[e] Department of Chemistry, Faculty of Science, Masaryk University, Kamenice 5, 62500 Brno, Czech Republic

ARTICLE INFO

ABSTRACT

Sanguinarine is a benzo[c]phenanthridine alkaloid with interesting cytotoxic properties, such as induction of oxidative DNA damage and very rapid apoptosis, which is not mediated by p53-dependent signaling. It has been previously documented that sanguinarine is reduced with NADH even in absence of any enzymes while being converted to its dihydro form. We found that the dark blue fluorescent species, observed during sanguinarine reduction with NADH and misinterpreted by Matkar et al. (Arch. Biochem. Biophys. 2008, 477, 43–52) as an anionic form of the alkaloid, is a covalent adduct formed by the interaction of NADH and sanguinarine. The covalent adduct is then converted slowly to the products, dihydrosanguinarine and NAD$^+$, in the second step of reduction. The product of the reduction, dihydrosanguinarine, was continually re-oxidized by the atmospheric oxygen back to sanguinarine, resulting in further reacting with NADH and eventually depleting all NADH molecules. The ability of sanguinarine to diminish the pool of NADH and NADPH is further considered when explaining the sanguinarine-induced apoptosis in living cells.

© 2017 Elsevier Ltd. All rights reserved.

1. Introduction

Sanguinarine (SA) belongs to a family of plant secondary metabolites called quaternary benzo[c]phenanthridine alkaloids (QBAs). These compounds have been extensively studied for their numerous biological activities, such as antitumor, antimicrobial, antifungal, and anti-inflammatory. While the results have been summarized in several works, the greatest attention is given to the anticancer activity of QBAs (Slaninova et al., 2014; Gaziano et al., 2016). It has been reported that SA is *in vitro* cytotoxic preferentially toward cancer cells than normal cells at concentrations that are comparable to those of the current clinically used anticancer agents (Ahmad et al., 2000). Under physiological conditions, a hydroxide anion (OH$^-$) is reversibly attached to the iminium bond of SA to give a 6-hydroxy product called an alkanolamine or a pseudo-base (Fig. 1). The alkanolamine form, which is a nonpolar uncharged molecule, can easily enter a cell to establish a new, pH-dependent equilibrium between the iminium and alkanolamine form inside the cell. The alkaloid toxicity depends on the ability of the planar, charged quaternary form of SA to produce a stable complex with DNA, which subsequently could affect the cell viability (Slaninova et al., 2001; Vacek et al., 2011). Treatment of cells with SA led to a rapid production of reactive oxygen species (ROS) (Burgeiro et al., 2013), fast and severe glutathione depletion (Debiton et al., 2003), oxidative DNA damage and very rapid apoptosis that was not mediated by p53-dependent DNA damage signaling (Matkar et al., 2008a; Hammerova et al., 2011). The first step in the metabolism of SA in rat liver is the reduction of the quaternary form to dihydrosanguinarine (DHSA) (Fig. 1). The conversion might be mediated by several NAD(P)H dependent oxidoreductases (Deroussent et al., 2010; Wu et al., 2013). In cell cultures of *Eschscholzia californica*, SA is reabsorbed and reduced to DHSA by sanguinarine reductase, which was isolated (Weiss et al., 2006) and characterized (Vogel et al., 2010). Additionally, it has been observed that SA underwent the conversion to its inactive reduced form even when incubated with NADH in the absence of any enzyme (Kovar et al., 1986; Matkar et al., 2008b), however; physiologically important reducing agents, such as glutathione and L-ascorbic acid,

* Corresponding author.
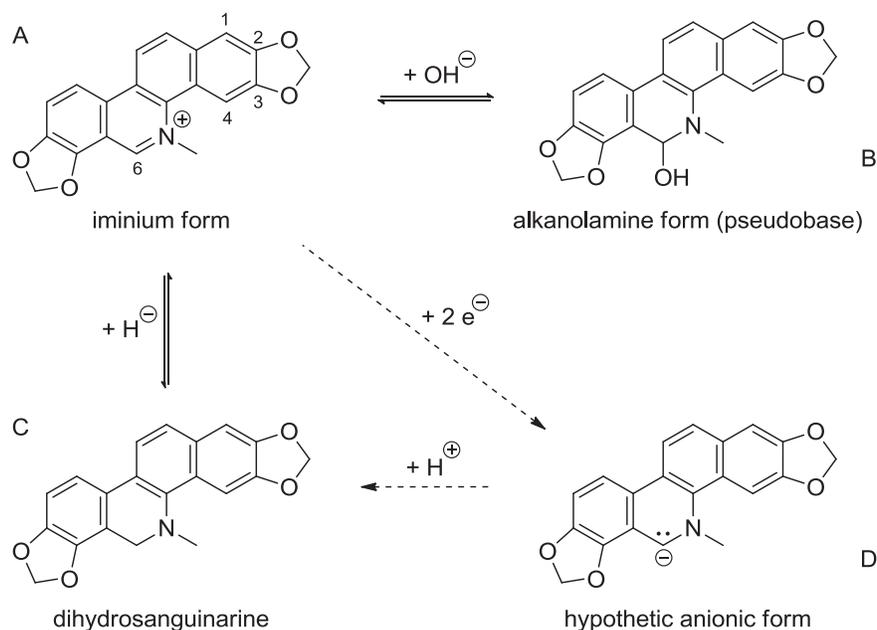*E-mail address:* ondramayl@gmail.com (O. Pes).

Fig. 1. A molecule of sanguinarine in A) an iminium (a quaternary) form, B) an alkanolamine form, C) dihydrosanguinarine, and D) a hypothetic anionic form suggested by Matkar et al. (2008b). The iminium form exhibits yellow fluorescence while the forms B and C glow dark blue under the UV light.

were unable to effectively reduce SA (Kosina et al., 2011). On top of that, SA, as well as other QBAs, may undergo a complex series of metabolic changes, some of which may contribute to their biological effects (Sandor et al., 2016).

When studying a relationship between the cell death and the ability of SA to deplete the cellular antioxidant capacity Matkar et al. (2008b) observed a novel, dark blue fluorescent, anionic form of SA formed by the reduction with NADH in the absence of any enzyme. The authors detected a new form of SA by reversed phase thin layer chromatography (RP-TLC) and determined the negative charge of species by gel electrophoresis. While a new form of SA would be somewhat fascinating, an alternative explanation of these findings could be presented and interpreted.

In this study, we have employed chromatographic and spectrometric techniques to give a novel interpretation of SA being reduced with NADH to DHSA. We found that the dark blue fluorescent anion produced during SA reduction with NADH, originally observed by Matkar et al. (2008b), is a covalent adduct formed by the reaction of NADH and SA. The adduct is then converted slowly to products, DHSA and NAD^+, in the second step of reduction. DHSA is continuously re-oxidized back to SA by the atmospheric oxygen resulting in eventual NADH depletion.

2. Results

2.1. Reduction of SA with NADH forms an unexpected spot on thin-layer chromatography

First, we have aimed to reproduce the RP-TLC performed by Matkar et al. (2008b). Resulting chromatograms might be seen in Fig. 2. The retention factor (Rf) for NADH was one as it traveled along with the polar mobile phase with no retention on the non-polar solid phase. Visualization under UV light (340 nm) showed a fluorescence band of NADH broadened over the entire chromatogram concentrating at the head. The same band at the head of the chromatogram was clearly visible in the line where NADH was mixed with SA. This was in accordance with our expectations as the NADH molecule was negatively charged and thus highly polar. Dark

blue fluorescence was clearly visible in the lines where SA was mixed with NADH (Rf ~ 0.75) and with $NaBH_4$ (Rf ~ 0.35). After four hours in dark, both dark blue spots turned their fluorescence to the same orange-yellow color as it has been observed in the sole SA line (Fig. 2B). A lower Rf of the dark blue spot in the SA + $NaBH_4$ line allowed for identification as DHSA as it was characterized by blue fluorescence and a decrease in polarity, which had resulted from a loss of the charged quaternary form. The same DHSA band would have been observed in the SA + NADH line if the mixture had been applied onto a TLC plate after a longer time (data not shown). A spot between SA and DHSA (Rf ~ 0.45) observed at lines of pure SA and SA + NADH probably represented an alkanolamine form of SA. Another dark blue fluorescent spot in the SA + NADH line with Rf ~0.75 could not have been attributed to any known species of SA and was then studied comprehensively by liquid chromatography with mass spectrometric detection (LC-MS).

2.2. Sanguinarine forms a covalent adduct with NADH

LC-MS was employed as a next step in revealing the origin of the interaction between SA and the NADH molecule. A representative chromatogram of an LC-MS method at very similar conditions to those used for RP-TLC might be seen in Fig. 3. The product, formed from the reaction between SA and NADH, was then expected to elute around the tenth minute. Detection at 280 nm and by MS showed a few distinct peaks around that retention time. In order to be able to identify the product, positive mode MS and MS/MS spectra were acquired (Fig. 4). Peaks observed in Fig. 4 might be accordingly assigned to the pure reactants (SA at 332 Da and NADH at 666 Da) as well as to the product of their reaction (997 Da for a singly charged and 499 Da for a doubly charged ion). The MS/MS spectrum of the doubly charged ion produces only SA as a major fragment. This fragmentation might be explained by a favorable formation of an aromatic quaternary form of SA and a neutral residue of NADH. In other words, SA is a good leaving fragment while retaining its charge as it contains quaternary nitrogen. In negative mode, the adduct was observed at 995 Da (data not shown) indicating that the mass of the neutral species was 996 Da.
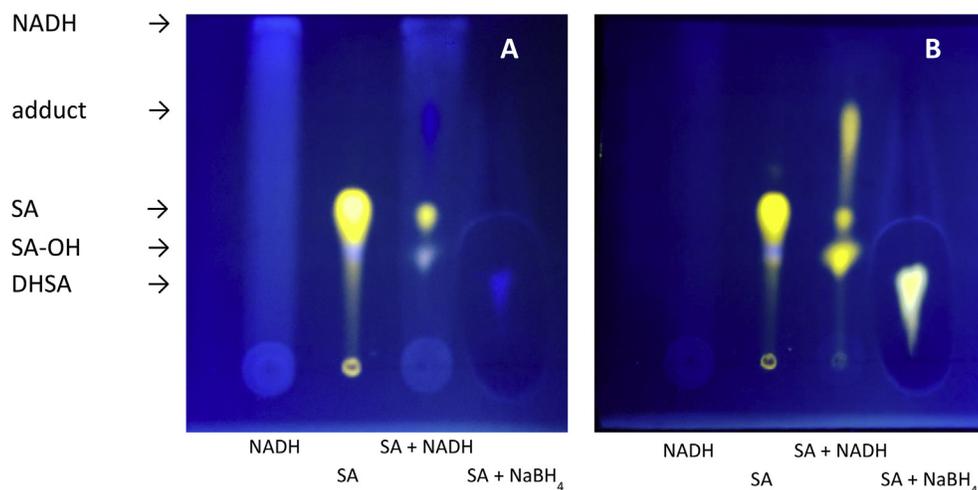
Fig. 2. RP-TLC of NADH, SA, an equimolar mixture SA + NADH, and a mixture of SA with NaBH$_4$ after A) 15 min, B) 240 min. SA-OH − an alkanolamine form of SA. For details, please see text.
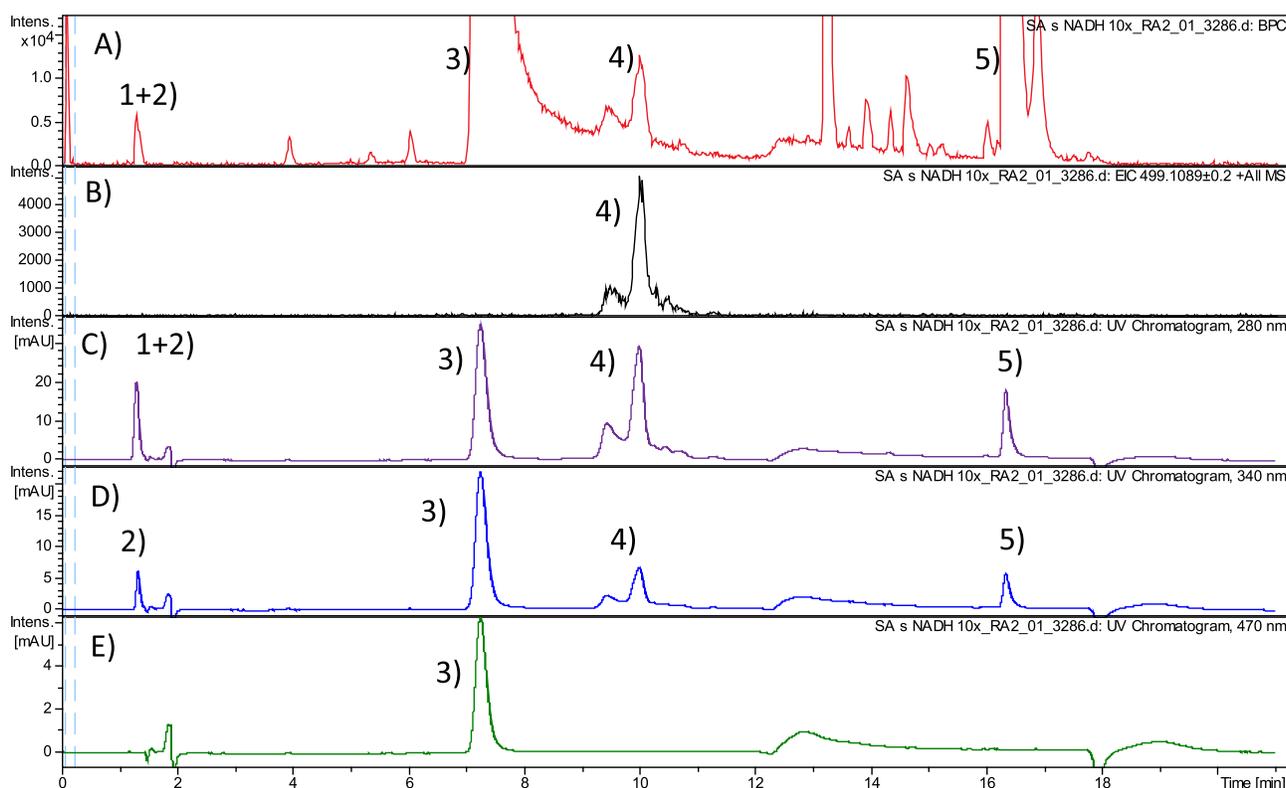

Fig. 3. Liquid chromatography of SA mixed with NADH after 2 h of reaction with detection A) MS of a base peak, B) MS of an extracted ion m/z 499.1089 ± 0.2 C) at 280 nm, D) at 340 nm, E) at 470 nm. Peaks are labeled as follows: 1) NAD$^+$, 2) NADH, 3) SA, 4) a group of adducts of SA with NADH, 5) DHSA. SA is the only colorful compound as it absorbs visible light. For details, please see text. (For interpretation of the references to colour in this figure legend, the reader is referred to the web version of this article.)

To confirm that the 997 Da ion is a covalent adduct and not just an association of SA and NADH (332 Da + 665 Da = 997 Da) in a liquid or gas phase, the diode-array spectra of the substrates and products were evaluated, see Fig. 5. All chromatographic peaks of the adduct absorbed at 280 and 340 nm which were also the absorption maxima of NADH. However, the characteristic absorption maximum of the SA quaternary form (470 nm) was not found in the peaks of the adducts. Since the formation of the adduct led to discoloration of SA, the 997 Da adduct should not be considered a mass spectrometry gas phase species and a covalent bond was

likely to be formed. The existence of more than one peak around the 10th minute evoked the product existed in several isomeric forms; please see Discussion for more details.

The adduct is likely to be the same substance observed by Matkar et al. (2008b) in their experiments due to the similar properties (such as negative charge, polarity, and dark-blue fluorescence changing with time). At neutral pH, the net charge of the adduct is (−1), because the negative charge of phosphate groups (−2) is only partially weakened by the positively charged nitrogen atom of pyridine (+1). The net negative charge of the product was
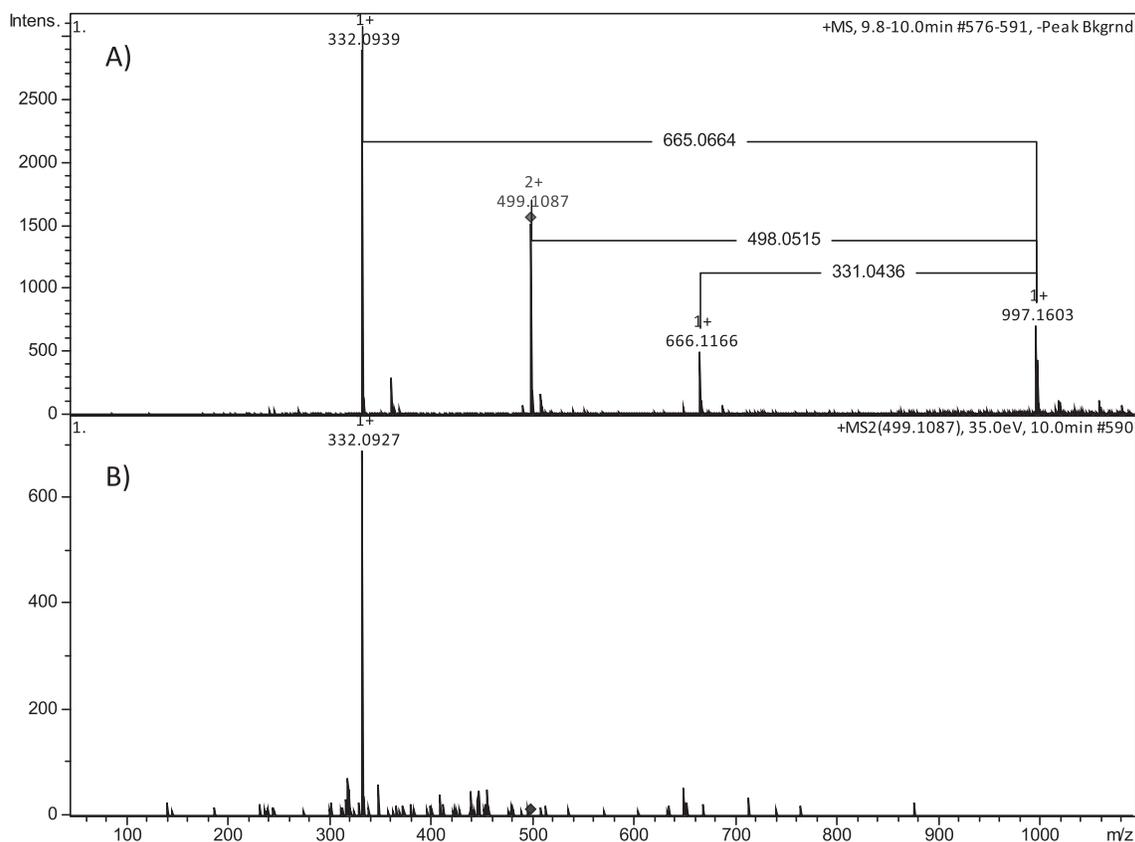
Fig. 4. A positive ESI A) MS spectrum of the SA + NADH adduct from the 10th min (Fig. 3) and B) MS/MS spectrum of the doubly charged, monoisotopic adduct ion 499.1087 Da (theoretical 499.1119 Da). Other monoisotopic signals belong to a singly charged adduct 997.1603 Da (theoretical 997.2165 Da), an ion of NADH 666.1166 Da (theoretical 666.1320 Da), and an ion of SA 332.0939 Da (theoretical 332.0917 Da).
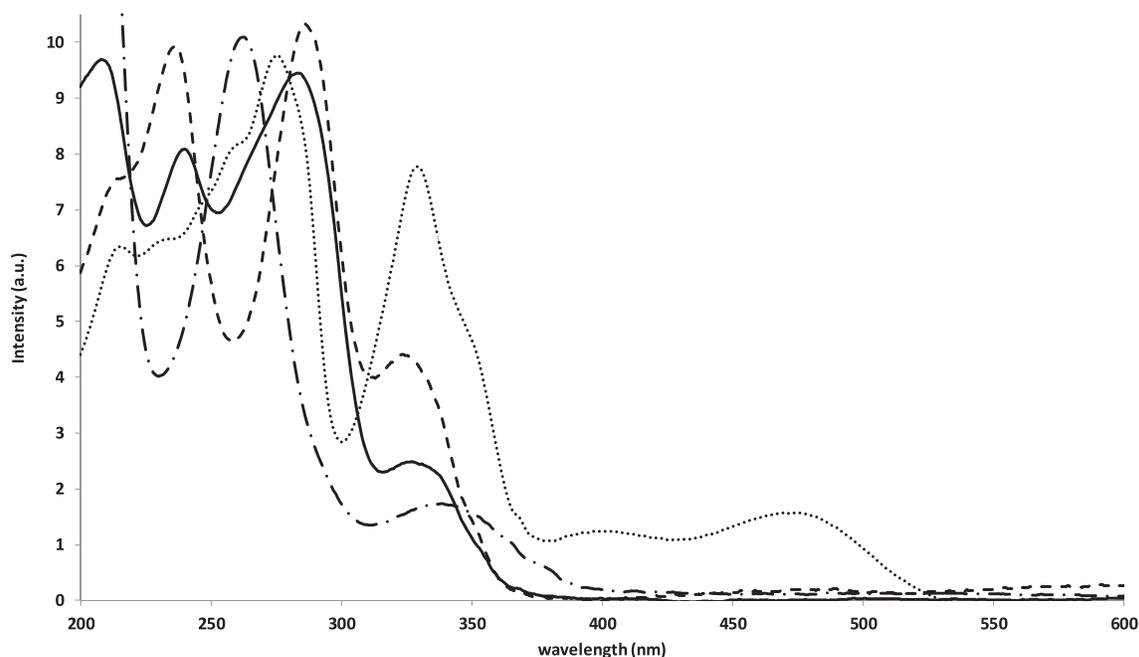
Fig. 5. Diode-array spectrum of the NADH-SA adduct (solid), NAD$^+$/NADH (dash-dotted) SA (dotted), and DHSA (dashed). The spectra have been normalized to the adduct maximum intensity at 280 nm.

originally incorrectly interpreted as a new form of SA, which was not supported by any evidence (Matkar et al., 2008b). Furthermore, if the anionic species had truly existed, it should have been a highly

unstable, as it would have immediately accepted a proton from water (Fig. 1).
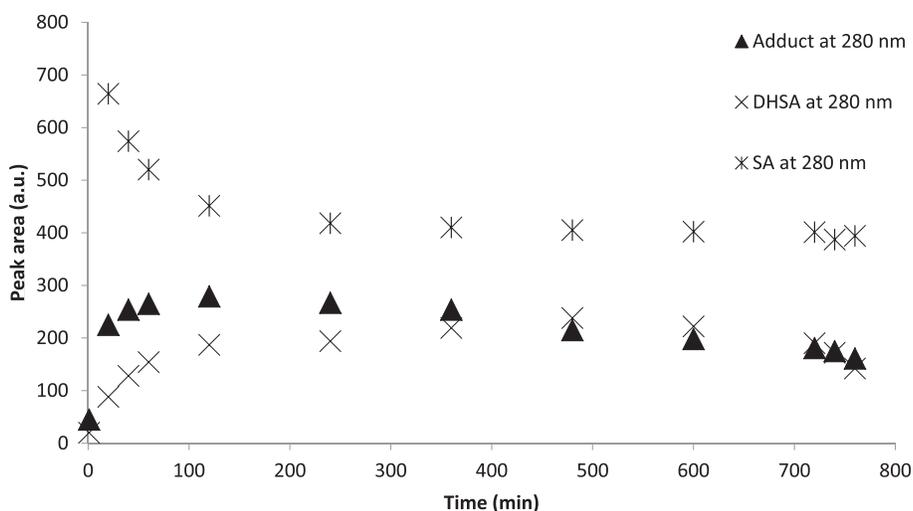
Fig. 6. NADH and SA were mixed as described in section 5.3, sealed under Ar and twelve consecutive LC-MS runs were performed. The initial rates expressed as a slope of a linear regression from the first three points were −11.0, +5.3, and +2.8 peak area/minute for SA, the adduct, and DHSA respectively.
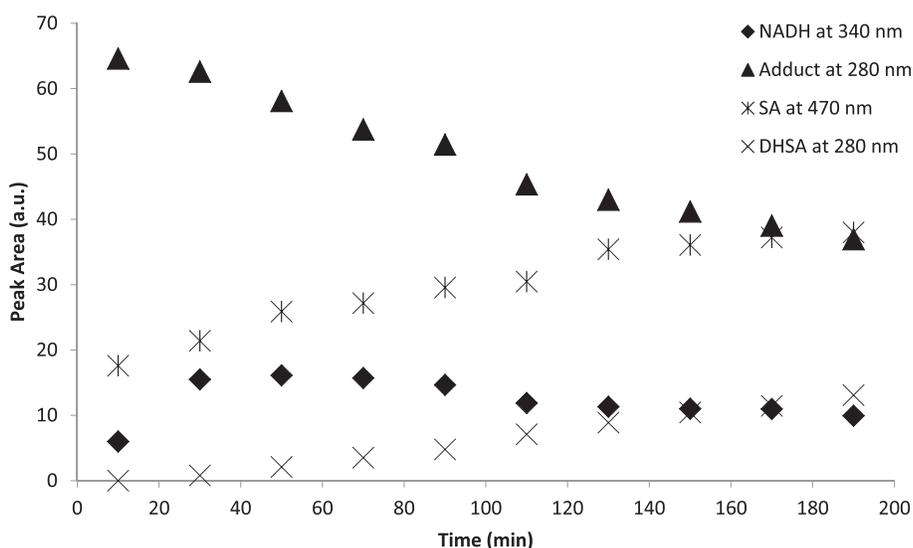
Fig. 7. Ten consecutive LC-MS runs from a vial with the adduct transferred from the fraction collected by semi-preparative chromatography. NADH peak area is kept at a constant level while the peak area of DHSA increases.

2.3. The covalent adduct is an intermediate in the reduction of SA with NADH

Kinetics of the reaction was measured to explore if the covalent adduct was involved in the final reduction of SA to DHSA. It is worth noting, that the same reduction reaction was described by Kovar et al. (1986); however, the authors did not attempt to clarify the mechanism of the reduction, although they suggested a rather complex transition state, which must have been formed between the target molecules. The formation kinetics at 280 nm might be seen in Fig. 6, which clearly showed an increased concentration of the adduct and DHSA over time. While the maximum concentration of the adduct was observed in 120 min, DHSA reached its peak concentration in about 480 min. In other words, the higher rate of the adduct formation than the rate of its decomposition to DHSA suggested that the adduct was truly necessary for the reaction to be completed. The decline in SA concentration was biphasic with the fast decrease occurring in the first 120 min followed by a slow

Fig. 8. Representation of the NAD(P)H depletion effect caused by continual re-oxidation of DHSA. SA^+ - a quaternary form, SA-NAD(P)H - the adduct of SA^+ with NADH.

Fig. 9. The proposed Ene mechanism for NADH dehydrogenases, the upper figure shows NADH oxidation, the lower figure shows NAD$^+$reduction, according to Hamilton (1971); Libby and Mehl (2012).

sanguinarine + NADH

dihydrosanguinarine
+ NAD$^+$

Fig. 10. Reduction of SA with NADH based on the proposed Ene adduct mechanism.

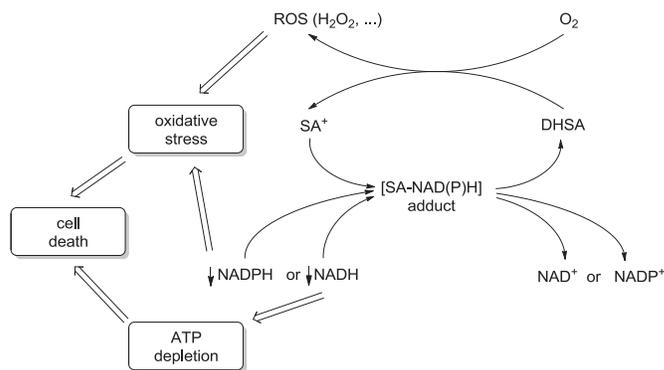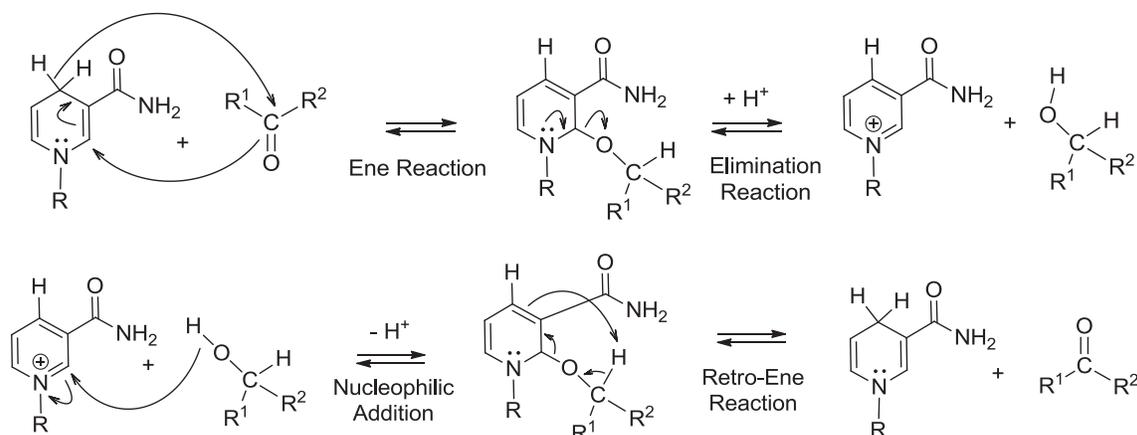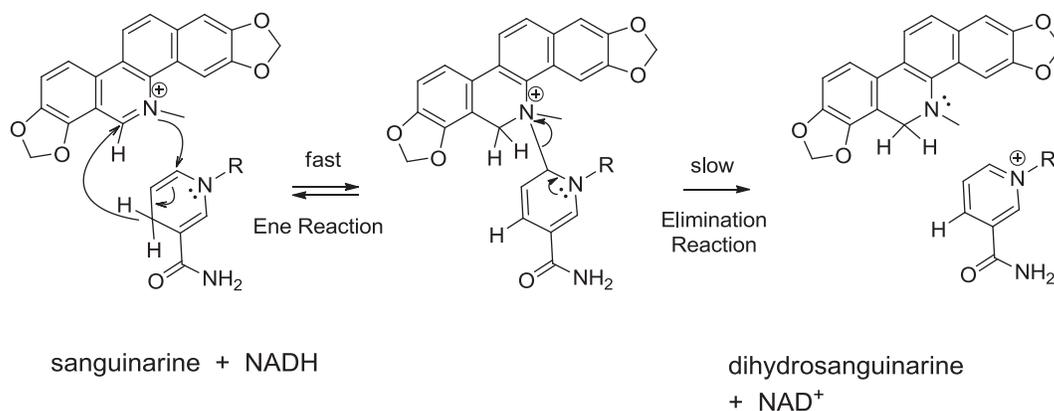decrease. It corresponds to the rapid formation and a slow decomposition of the adduct. The additional decrease in DHSA after the 480th minute is caused by re-oxidation of the entire mixture by the atmospheric oxygen. If the vials had not been sealed under argon atmosphere, the re-oxidation would have appeared around the 400th minute and the resulting DHSA would have been subsequently converted to SA (data not shown).

In order to support our hypothesis that the adduct was a real intermediate in the reduction of SA with NADH, the adduct has been isolated by semi-preparative LC and its further conversion was immediately analyzed by LC-UV-MS, as seen in Fig. 7. Initially, the adduct was partially converted back to reactants, SA and NADH, indicating that the formation of the covalent adduct was reversible. The NADH concentration had peaked around 50 min and then declined very slowly. This decrease in NADH concentration indicated the presence of additional reaction. At the same time, the concentration of the adduct and DHSA kept decreasing and slowly increasing, respectively. This suggested that the additional reaction was the conversion of the adduct to DHSA and that the adduct was indeed a true intermediate of the reaction. The continuous increase in the SA concentration could be explained as a sum of a velocity of the initial reversed reaction and a velocity of DHSA oxidation caused by the atmospheric oxygen.

It is worth to note that the equilibrium conditions in the vial from the fraction collector were substantially different from those when the mixture was fresh. When SA and NADH were freshly mixed the excess of NADH made sure the reaction would progress,

up to some point, in a reducing environment. On the other hand, when a fraction containing the adduct was removed from the collector and transferred to the LC-MS vial, the equilibrium was shifted to the left i.e., the adduct partially decomposed to reactants (NADH and SA) and a part was converted to products (NAD$^+$ and DHSA).

When the reaction was left overnight to proceed completely, SA and NAD$^+$ were the only compounds observed in the reaction mixture. SA catalyzed the oxidation of NADH by the air oxygen, in other words, sanguinarine showed an oxygen-NADH oxidoreductase-like activity. This effect of SA is probably the reason why SA and other QBAs could deplete NAD(P)H in the cells and induce rapid cell death (Fig. 8).

3. Discussion

3.1. NADH is oxidized by SA in a two-step process involving the covalent adduct formation

In our study, we observed a formation of a covalent adduct during the reduction of SA with NADH. Although we have observed the formation of several isomeric adducts between SA and NADH with similar chromatographic properties, we expect solely a single species was converted to the products — DHSA and NAD$^+$.

The existence of the covalent intermediate as a result of an attack of NADH to the reactive iminium bond of SA is supported by two facts:

1) The molecular mass of the adduct and its respective fragmentation to SA and NADH.
2) Discoloration (a lack of 470 nm absorption band) and dark blue fluorescence of the adduct.

The originally postulated one-step hydride transfer to NAD^+ has been still a prevailing mechanism of enzymatic NAD^+ reduction especially due to an inability to detect any reaction intermediates. Here, we try to suggest another option to explain the net hydride transfer.

Hamilton (1971) proposed the formation of the covalent intermediate between an alcohol substrate and a pyridine coenzyme during oxidation catalyzed by dehydrogenases (Fig. 9, the lower panel). The first step was an electrocyclic Ene reaction, which was facilitated by transition states with aromatic character. In the second step, the adduct was decomposed to the products by an elimination reaction triggered by a proton. The Ene mechanism for hydride transfer did not receive much attention especially due to an inability to detect any reaction intermediates. Libby and Mehl (2012) found covalent Ene adduct intermediates in a dihydropyridine model for NADH reduction reactions and Rosenthal et al. (2014) detected a covalent Ene adduct intermediate in an enzymatic hydride transfer from NADPH to the corresponding substrate. The results suggested that Ene reaction mechanism could be shared by more NAD(P)H dehydrogenases.

Since we have not characterized the exact structure of the adduct, the mechanism of the SA reduction discussed here is only tentative. One possibility suggests that the reduction of SA with NADH should proceed via the Ene reaction mechanism, which is in line with previous reports (Libby and Mehl, 2012; Rosenthal et al., 2014), and the proposed reaction is given in Fig. 10. The net hydride transfer then involves transition states with aromatic character, as well as lowering activation energy.

The existence of several isomeric forms of the adduct observed in the LC chromatogram around the 10th minute (Fig. 3B) might be explained by a creation of two new adjacent stereogenic centers in the molecule of the Ene adduct − the quaternary nitrogen of SA and C-6 of the nicotinamide ring (Fig. 10). The Ene adduct then comprises two pairs of enantiomers providing two peaks on the chromatogram monitored at m/z 499. If we take into account the possibility of using C-2 instead of C-6 for the formation of the Ene adduct, we could obtain even four enantiomeric pairs. Such explanation is in accordance with the previous findings (Libby and Mehl, 2012), where the isomers of Ene adducts formed between a model molecule of NADH and the substrates. Both SA and NAD^+ in the oxidized form have a pyridinium ring containing a reactive iminium bond, which plays a key role in the covalent adduct formation in the proposed Ene reaction. Considering a substrate oxidation with NAD^+ (Fig. 9, the lower panel), the iminium bond of NAD^+ is attacked by a nucleophilic oxygen of a hydroxylic group. Correspondingly, during the SA reduction with NADH, the reactive iminium bond of SA might have been attacked by any of the nucleophilic atoms of NADH. This would also explain the reversible formation of the isomeric adducts seen in LC-MS (Fig. 3).

4. Conclusions

In this work, we observed a novel species of a covalent adduct, which was capable of acting as an intermediate in the facilitation of the SA reduction by NADH. The idea of such an intermediate existence was postulated by Kovar et al. (1986); nevertheless, there have been no later attempts to characterize the intermediate. The species is likely to be the same molecule Matkar et al. (2008b) observed in their experiments; however, they misinterpreted the intermediate as a negatively charged species of SA.

We have shown that the process of reduction went through a stable covalent intermediate, which is contradictory to the accepted model of a one-step hydride transfer. Our data supported the covalent intermediate hypothesis, but we managed to form such an intermediate with a native molecule of NADH, instead of a hard-to-design synthetic model molecule.

The product of the reduction, DHSA, was continually re-oxidized back to SA by the atmospheric oxygen to generate a new portion of SA available for a further reaction with NADH. This fact guaranteed that the concentration of the adduct remained constant and we suppose this happens also in living cells, in which SA is quickly reduced by NAD(P)H-dependent enzymes. This idea is supported by other authors, who observed an induced apoptosis due to the rapid depletion of a reducing potential of the cell (Debiton et al., 2003; Hammerova et al., 2012; Pallichankandy et al., 2015). Inhibition of NAD(P)H-dependent enzymes by SA previously observed (Kalogris et al., 2014) could be caused by the covalent adduct due to its structural similarity with NAD(P)H.

5. Experimental

5.1. Reagents and materials

Methanol (MeOH, *p.a.*) was obtained from Penta (Czech Republic). Acetic acid (LC-MS), ammonium hydroxide (28–30% NH_3 in water), sodium formate (LC-MS), NADH disodium salt (Grade I), MeOH (LC-MS), and acetonitrile (ACN, HPLC grade, LC-MS) were purchased from Sigma−Aldrich (Czech Republic). All water used was of an ultra-pure grade supplied by an in-house Milli-Q system (Millipore, MA, USA).

5.2. Alkaloid isolation

The standards of the benzophenanthridine alkaloids originated from isolation during the systematic studies in the laboratories of the Department of Biochemistry from plant material of *Macleaya microcarpa* (Maxim.) Fedde, *Dicranostigma lactucoides* Hook. F. et Thomson, *Sanguinaria canadensis* L., and *Stylophorum lasiocarpum* (Oliv.) Fedde. Briefly, SA was prepared by extraction of dried, ground plant material with methanol in a FexIKA® apparatus (IKA, Germany). The extract was purified, concentrated and the last step of isolation was performed by means of semi-preparative reversed-phase (RP) chromatography. The identity of the alkaloid was verified by the LC-MS analysis.

5.3. Reaction conditions

SA was incubated with NADH in an equimolar ratio at room temperature under argon atmosphere in a sealed vial for 5 min, if not stated otherwise. For an LC-MS analysis (Fig. 6), the mixture of 0.5 ml of 1 mmol/L of alkaloid and 0.5 ml 1 mmol/L NADH was diluted ten times, sealed in an LC-MS vial under argon atmosphere, and immediately injected onto the LC-MS system. For a semi-preparative analysis, the mixture of 0.5 ml of 1 mmol/L of alkaloid and 0.5 ml of 1 mmol/L NADH was sealed under argon atmosphere, left for 60 min, and then 1 ml was injected onto the semi-preparative column specified in the section 5.4.

5.4. Adduct isolation and purification

An Agilent 1200 Series LC system (Agilent Technologies, CA, USA) equipped with a fraction collector was used for purification and isolation of the adduct. It consisted of a ternary pump, a diode array detector (DAD), a syringe loading sample injector (ECOM, Czech Republic) with a 5 ml external sample loop and a fraction

collector. The alkaloid-NADH complex was separated on a C12 column (Synergi RP-Max, 4 μm, 250 mm × 10 mm ID, Phenomenex, CA, USA). The mobile phase consisted of ammonium formate buffer (0.05 M HCOOH titrated with NH_3 to pH = 4.50) and ACN with the following elution profile: ACN was linearly increased from 25% to 27.5% over first 5 min, then to 41.5% over the subsequent 5 min, next to 47% at the 15th minute and finally to 80% at 20 min, where it was held for 10 min before equilibration under the initial conditions for 3.0 min. The flow rate was set at 4 mL min^{-1} and fractions were collected on a peak basis using a DAD at 280 nm. Fraction identified as the adduct was transferred into an LC-MS vial and ten LC-MS runs (Fig. 7) were performed.

5.5. Liquid chromatography — mass spectrometry

The LC-MS method was developed using a Dionex Ultimate 3000RS (Thermo Scientific, CA, USA) module. Compound separation was achieved with a 3.0 mm × 150 mm, 5 μm Synergi RP-Max C18 (Phenomenex, CA, USA) column, set at $(23 \pm 0.1)\,°C$, and a flow-rate of 0.5 mL min^{-1}. The binary mobile phase system consisted of ammonium acetate buffer (10 mM, pH = 4.4) and ACN. After a 10-μL injection, the percentage of ACN was linearly increased from 20% to 40% over 10 min and then to 80% over the subsequent 1 min. ACN was held at 80% for 5 min, followed by equilibration under the initial conditions for another 5 min. A complete LC run was 21 min. The LC system was equipped with a DAD detector and at the same time, it was connected to a Bruker MicrOTOF-Q II (Germany) mass spectrometer operated in the positive electrospray ionization mode. The ionization conditions were determined by the software as follows: capillary voltage: 4500 V, end plate offset: −500 V, source temperature: 220 °C, desolvation gas (nitrogen) flow: 8 L min^{-1}, nebulizer (nitrogen) pressure: 300 kPa, and collision cell voltage: 6 eV. The base peak chromatogram (BPC) was acquired in MS mode by monitoring the m/z range of 50–3000 with a spectra sample time of 1 s and MS/MS spectra were collected in a data-dependent mode. The mass spectrometer was calibrated using 10 mM sodium formate in 50% isopropyl alcohol on a daily basis and in the beginning of each LC run with a 20-μL loop flush. High-resolution MS and MS/MS spectra were first investigated to obtain the elemental formula of each compound. The final identification of target compounds relied on isotope pattern matching with a combination of MS/MS and retention behavior.

5.6. Thin-layer chromatography

Thin-layer chromatography was performed on aluminum plates (6 × 12 cm) covered by Silica gel 18 F_{254s} (Merck, Germany) and a mobile phase consisting of ammonium formate 0.1 M and MeOH (92:8 v/v). The chamber with the mobile phase was left covered for 20 min to saturate before any separation. Samples were immediately after mixing applied to the plate, which was after drying (2–3 min) inserted into the chamber with the mobile phase. The separation took approximately ten minutes. After the experiment, the TLC plate was removed, allowed to dry for 15 min, visually inspected and photographed under UV light at 340 nm.

Acknowledgement

References

Ahmad, N., Gupta, S., Husain, M.M., Heiskanen, K.M., Mukhtar, H., 2000. Differential antiproliferative and apoptotic response of sanguinarine for cancer cells versus normal cells. Clin. Cancer Res. 6, 1524–1528.

Burgeiro, A., Bento, A.C., Gajate, C., Oliveira, P.J., Mollinedo, F., 2013. Rapid human melanoma cell death induced by sanguinarine through oxidative stress. Eur. J. Pharmacol. 705, 109–118. https://doi.org/10.1016/j.ejphar.2013.02.035.

Debiton, E., Madelmont, J.C., Legault, J., Barthomeuf, C., 2003. Sanguinarine-induced apoptosis is associated with an early and severe cellular glutathione depletion. Cancer Chemother. Pharmacol. 51, 474–482.

Deroussent, A., Re, M., Hoellinger, H., Cresteil, T., 2010. Metabolism of sanguinarine in human and in rat: characterization of oxidative metabolites produced by human CYP1A1 and CYP1A2 and rat liver microsomes using liquid chromatography-tandem mass spectrometry. J. Pharm. Biomed. Anal. 52, 391–397. https://doi.org/10.1016/j.jpba.2009.09.014.

Gaziano, R., Moroni, G., Buè, C., Miele, M.T., Sinibaldi-Vallebona, P., Pica, F., 2016. Antitumor effects of the benzophenanthridine alkaloid sanguinarine: evidence and perspectives. World J. Gastrointest. Oncol. 8, 30–39. https://doi.org/10.4251/wjgo.v8.i1.30e v8.i1.30.

Hamilton, G.A., 1971. Proton in biological redox reactions. Prog. Bioorg. Chem. 1, 83–157.

Hammerova, J., Uldrijan, S., Taborska, E., Slaninova, I., 2011. Benzo[c]phenanthridine alkaloids exhibit strong anti-proliferative activity in malignant melanoma cells regardless of their p53 status. J. Dermatol. Sci. 62, 22–35. https://doi.org/10.1016/j.jdermsci.2011.01.006.

Hammerova, J., Uldrijan, S., Taborska, E., Vaculova, A.H., Slaninova, I., 2012. Necroptosis modulated by autophagy is a predominant form of melanoma cell death induced by sanguilutine. Biol. Chem. 393, 647–658. https://doi.org/10.1515/hsz-2011-0279.

Kalogris, C., Garulli, C., Pietrella, L., Gambini, V., Pucciarelli, S., Lucci, C., Tilio, M., Zabaleta, M.E., Bartolacci, C., Andreani, C., Giangrossi, M., Iezzi, M., Belletti, B., Marchini, C., Amici, A., 2014. Sanguinarine suppresses basal-like breast cancer growth through dihydrofolate reductase inhibition. Biochem. Pharmacol. 90, 226–234. https://doi.org/10.1016/j.bcp.2014.05.014.

Kosina, P., Vacek, J., Papouskova, B., Stiborova, M., Styskala, J., Cankar, P., Vrublova, E., Vostalova, J., Simanek, V., Ulrichova, J., 2011. Identification of benzo[c]phenanthridine metabolites in human hepatocytes by liquid chromatography with electrospray ion-trap and quadrupole time-of-flight mass spectrometry. J. Chromatogr. B Anal. Technol. Biomed. Life Sci. 879, 1077–1085. https://doi.org/10.1016/j.jchromb.2011.03.023.

Kovar, J., Stejskal, J., Paulova, H., Slavik, J., 1986. Reduction of quaternary benzo-phenanthridine alkaloids by NADH and NADPH. Collect. Czech. Chem. Commun. 51, 2626–2634.

Libby, R.D., Mehl, R.A., 2012. Characterization of covalent Ene adduct intermediates in "hydride equivalent" transfers in a dihydropyridine model for NADH reduction reactions. Bioorg. Chem. 40, 57–66. https://doi.org/10.1016/j.bioorg.2011.10.002.

Matkar, S.S., Wrischnik, L.A., Hellmann-Blumberg, U., 2008a. Sanguinarine causes DNA damage and p53-independent cell death in human colon cancer cell lines. Chem. Biol. Interact. 172, 63–71. https://doi.org/10.1016/j.cbi.2007.12.006.

Matkar, S.S., Wrischnik, L.A., Hellmann-Blumberg, U., 2008b. Production of hydrogen peroxide and redox cycling can explain how sanguinarine and chelerythrine induce rapid apoptosis. Arch. Biochem. Biophys. 477, 43–52. https://doi.org/10.1016/j.abb.2008.05.019.

Pallichankandy, S., Rahman, A., Thayyullathil, F., Galadari, S., 2015. ROS-dependent activation of autophagy is a critical mechanism for the induction of anti-glioma effect of sanguinarine. Free Radic. Biol. Med. 89, 708–720. https://doi.org/10.1016/j.freeradbiomed.2015.10.404.

Rosenthal, R.G., Ebert, M.O., Kiefer, P., Peter, D.M., Vorholt, J.A., Erb, T.J., 2014. Direct evidence for a covalent ene adduct intermediate in NAD(P)H-dependent enzymes. Nat. Chem. Biol. 10, 50–55. https://doi.org/10.1038/NCHEMBIO.1385.

Sandor, R., Midlik, A., Sebrlova, K., Dovrtelova, G., Noskova, K., Jurica, J., Slaninova, I., Taborska, E., Pes, O., 2016. Identification of metabolites of selected benzophenanthridine alkaloids and their toxicity evaluation. J. Pharm. Biomed. Anal. 121, 174–180. https://doi.org/10.1016/j.jpba.2016.01.024.

Slaninova, I., Taborska, E., Bochorakova, H., Slanina, J., 2001. Interaction of benzo[c] phenanthridine and protoberberine alkaloids with animal and yeast cells. Cell Biol. Toxicol. 17, 51–63. https://doi.org/10.1023/A:1010907231602.

Slaninova, I., Pencikova, K., Urbanova, J., Slanina, J., Taborska, E., 2014. Antitumour activities of sanguinarine and related alkaloids. Phytochem. Rev. 13, 51–68. https://doi.org/10.1007/s11101-013-9290-8.

Vacek, J., Vrublova, E., Kubala, M., Janovska, M., Fojta, M., Simkova, E., Styskala, J., Skopalova, J., Hrbac, J., Ulrichova, J., 2011. Oxidation of sanguinarine and its dihydro-derivative at a pyrolytic graphite electrode using ex situ voltammetry. Study of the interactions of the alkaloids with DNA. Electroanalysis 23, 1671–1680. https://doi.org/10.1002/elan.201100028.

Vogel, M., Lawson, M., Sippl, W., Conrad, U., Roos, W., 2010. Structure and mechanism of sanguinarine reductase, an enzyme of alkaloid detoxification. J. Biol. Chem. 285, 18397–18406. https://doi.org/10.1074/jbc.M109.088989.

Weiss, D., Baumerkt, A., Vogel, M., Roos, W., 2006. Sanguinarine reductase, a key enzyme of benzophenanthridine detoxification. Plant, Cell & Environ. 29, 291–302. https://doi.org/10.1111/j.1365-3040.2005.01421.x.

Wu, Y., Liu, Z.Y., Cao, Y., Chen, X.J., Zeng, J.G., Sun, Z.L., 2013. Reductive metabolism of the sanguinarine iminium bond by rat liver preparations. Pharmacol. Rep. 65, 1391–1400.

3.3 Seasonal variation in alkaloid composition and antiproliferative activity of Stylophorum lasiocarpum (Oliv.) Fedde

Since many QBAs cannot be efficiently synthesized, the major way for their obtaining is isolation and purification from plant material. Minor QBAs, especially MA and CR, can be isolated from a plant *Stylophorum lasiocarpum*, which is considered an essential source of minor QBAs. LC–MS was used to identify and characterize the alkaloids found in roots and aerial parts of the plant. A combination of retention time, precise mass-to-charge ratio, isotopic patterns, and fragmentation behavior allowed for identifying seventeen compounds produced in the benzo[c]phenanthridine pathway starting from (S)-reticuline. In most plants, the end product is SA; however, *S. lasiocarpum* belongs to a few plant species producing MA by involving two hydroxylation and methylation steps. The seasonal variation of QBAs production was established to maximize the isolation efficiency for cultivation and harvesting of the plant material.

Author's contribution: 20 %

ORIGINAL PAPER

Seasonal variation in alkaloid composition and antiproliferative activity of *Stylophorum lasiocarpum* (Oliv.) Fedde

[a]**Kristýna Šebrlová***, [a]**Ondřej Peš**, [b]**Iva Slaninová**, [b]**Ondřej Vymazal**,
[a]**Jana Kantorová**, [a]**Eva Táborská**

[a]*Department of Biochemistry,* [b]*Department of Biology, Faculty of Medicine, Masaryk University,*
Kamenice 5, 62500, Brno, Czech Republic

Stylophorum lasiocarpum (Oliv.) Fedde (Papaveraceae) belongs to traditional Chinese medicine herbs but there was minimal information on the content of alkaloids in this plant. Extracts from the aerial part and roots were examined by liquid chromatography with UV and mass spectrometric detection, with nineteen alkaloids identified. Changes in alkaloid content over the entire vegetation period of a one- and two-year old plant were studied. The protoberberine alkaloids, coptisine and stylopine, were found to be the main substances in extracts of the aerial part irrespective of the plant's age and time of harvest. Variable amounts of protopine, sanguinarine, chelerythrine, chelirubine, macarpine, chelilutine and berberine were also recorded in the aerial part. The roots contained significantly larger quantities of all alkaloids than the aerial part with the levels of most alkaloids varying from May to October, peaking in the middle of the vegetation period. Coptisine was the dominant alkaloid in all samples. The antiproliferative activities of the root extract and of seven individual alkaloids were tested on A375 human malignant melanoma cells. The significant dose-dependent toxicity of the root extract was attributed largely to the quaternary benzo[*c*]phenanthridine alkaloids, macarpine and sanguinarine.
© 2014 Institute of Chemistry, Slovak Academy of Sciences

Introduction

Stylophorum lasiocarpum (Oliv.) Fedde is a biennial or short-lived perennial herb native to Central and Eastern China. *S. lasiocarpum* is one of the 23 species of the tribe Chelidonieae (Papaveraceae family). Due to its close similarity to the species *Chelidonium majus*, the plant is also known as Chinese celandine poppy or human bloodwort. Although the dried whole herb of *S. lasiocarpum* is included among traditional Chinese medicine (TCM) herbs, to the best of our knowledge, information on its medicinal effects is minimal (Lei et al., 2014). *S. lasiocarpum* is generally applicable when treating injuries, controlling bleeding, relieving pain or alleviating swelling (Feng et al., 1985).

Stylophorum lasiocarpum is permeated by a well-developed duct system of laticifers producing orange-red latex. The stems are erect, usually simple and glabrous with basal leaves forming a rosette. Two or three cauline leaves are borne from the upper stem, almost opposite or whorled, similar to the lower leaves but subpetiolate. Four to seven yellow flowers bloom in an umbel-like cluster, opening in succession. The fruits are narrow (approx. 60 mm × 5 mm) terete capsules covered in short hairs; they bear numerous seeds that are oval (approx. 1 mm), tessellate and cristately carunculate (Zhang et al., 2008). The main secondary metabolites are isoquinoline alkaloids (Table 1).

The alkaloids of the plant were first characterised by Slavík et al. (1991). Stylopine (STY) and coptisine (COP) were the principal alkaloids identified in the

**Corresponding author, e-mail: k.pencikova@mail.muni.cz

Table 1. *Stylophorum lasiocarpum* alkaloids

Ring type	Alkaloid	R^1	R^2	R^3	R^3	R^4	R^5
	Sanguinarine (SA)	—CH₂—		—CH₂—		—H	—H
	Chelerythrine (CHE)	—CH₂—		—CH₃	—CH₃	—H	—H
	Sanguilutine (SL)	—CH₃	—CH₃	—CH₃	—CH₃	—H	—H
	Chelilutine (CL)	—CH₂—		—CH₃	—CH₃	—OCH₃	—H
	Sanguirubine (SR)	—CH₃	—CH₃	—CH₂—		—OCH₃	—H
	Chelirubine (CR)	—CH₂—		—CH₂—		—OCH₃	—H
	Macarpine (MA)	—CH₂—		—CH₂—		—OCH₃	—OCH₃
	Berberine (BER)	—CH₃	—CH₃	–		–	–
	Coptisine (COP)	—CH₂—		–		–	–
	Canadine (CAN)	—CH₃	—CH₃	–		–	–
	Stylopine (STY)	—CH₂—		–		–	–
	Protopine (PRO)	–		–		–	–
	Chelidonine	–		–		–	–
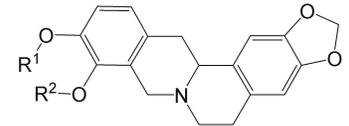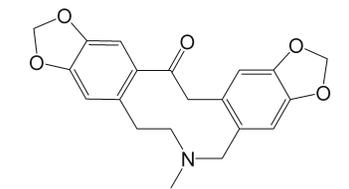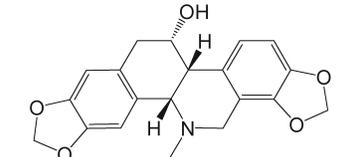
roots, while smaller quantities of sanguinarine (SA), macarpine (MA), chelerythrine (CHE), chelirubine (CR), chelilutine (CL), protopine (PRO), corysamine, berberine (BER) and *N*-methylstylopinium hydroxide were also isolated. Thin-layer chromatography (TLC) detected trace amounts of chelidonine, allocryptopine, cryptopine, scoulerine, isoboldine and magnoflorine. The aerial part of the plant yielded STY, COP and chelidonine as the dominant alkaloids and lower amounts of PRO and *N*-methylstylopinium hydroxide. Trace amounts of SA, CR, cryptopine, scoulerine, isoboldine, corytuberine, corysamine, BER and magnoflorine were detected by TLC in the aerial part of the plant.

Suchomelová et al. (2007) subsequently studied the roots of the plant species as a potential source of quaternary benzo[*c*]phenanthridine alkaloids (QBAs) and confirmed that the major alkaloids were COP and STY and, in addition, found benzo[*c*]phenanthridine (SA, CHE, CR, CL, MA) and protoberberine (BER) alkaloids. Accordingly, *S. lasiocarpum* belongs to a small group of plant species that, in addition to SA

and CHE, contain less common QBAs such as CR, CL or MA. SA and CHE are present in relatively high amounts in these plants, may be isolated, and have been commercially available for years. They have been the subjects of a number of biological studies that have been summarised in recent reviews (Dvořák et al., 2006; Slaninová et al., 2014). By contrast, the content of other QBAs is significantly lower in these plants and their availability is very limited, hence they have long evaded attention. The first biological studies recently described the effects of these alkaloids on human cancer cells. Strong anti-proliferative and pro-apoptotic properties were observed upon treatment with MA, CHR, SR (Slaninová et al., 2007a), SL and CHL (Slunská et al., 2010). The effects of SL and CHL were independent of the activity of p53 (Hammerová et al., 2011) and SL effectively killed cells overexpressing the anti-apoptotic protein Bcl2 (Hammerová et al., 2012). Despite the close similarity of the QBAs' molecular structures, the cell death mechanism was different for each alkaloid (Hammerová et al., 2011). SL induced the caspase-independent cell death, necrop-

tosis (Hammerová et al., 2012). These properties of QBAs indicate their prospective applications in the treatment of resistant tumours. In addition to these biological effects on cells, QBAs in the quaternary form have been reported as interacting with dsDNA and G-quadruplexes (Rybáková et al., 2013). Currently, the targeting of quadruplexes by small molecules seeks to elucidate the biological effects and plays an interesting role in the development of new potential anti-cancer drugs (Galezowska et al., 2012).

Among the rare QBAs, MA is particularly distinguished by its unusual properties, being reported as a promising fluorescent probe for cell nuclei-labelling as well as for cell cycle visualisation in fluorescence microscopy and flow cytometry. Slaninová (2007b) described the ability of MA to act as a supravital DNA dye on various living human cells (HL60, HeLa and LEP). On the addition of MA to cells, the instantly appearing bright red nuclear fluorescence revealed the nuclear architecture at various stages of the cell cycle not only in living cells but also in yeasts and bacteria. In addition, MA is highly antiproliferative in vitro, predominantly by apoptosis, and is significantly more cytotoxic than any other QBAs (Ishikawa et al., 1995; Slaninová et al., 2007a).

The above information will undoubtedly advance the research and application of minor QBAs in cancer biology and therapy. However, an essential requirement of any further research is to obtain the QBAs in sufficient quantities. As they are not commercially available and their synthesis is somewhat unsatisfactory (Ishikawa et al., 1995), the best approach for their large-scale production appears to be isolation from the plant material. *S. lasiocarpum* is regarded as a core source of minor QBAs, albeit that no comprehensive data on the production, accumulation and distribution of QBAs in this plant have ever been published. Such data, as well as descriptions of the antiproliferative activities of the plant extract and its individual alkaloids, are provided in the present study.

Experimental

Plant material

Stylophorum lasiocarpum Oliv. Fedde was cultivated in the Medicinal Herbs Centre of the Faculty of Medicine of Masaryk University (Brno, Czech Republic). A voucher specimen of *S. lasiocarpum* (Oliv.) Fedde (BRNU, ID number 620684) is deposited in the herbarium of Masaryk University (Brno, Czech Republic). Three individual plants of one- and two-year old cultures were randomly harvested during the vegetation period from May to October. The plant material was wiped, dried in the dark at ambient temperature for 10 days and ground to a fine powder.

Reagents and materials

Methanol (p.a.) was obtained from Penta (Czech Republic), phosphoric acid (p.a.), formic acid (p.a.), sodium 1-heptanesulphonate (p.a.), fetal bovine serum, glutamine, penicillin, streptomycin, acetonitrile (ACN) (HPLC grade, LC MS) and dimethylsulphoxide (p.a.) (DMSO) were purchased from Sigma–Aldrich (Czech Republic).

The standards of the alkaloids originated from isolations during the systematic studies of Papaveraceae in the laboratories of the Department of Biochemistry: allocryptopine, berberine, canadine, coptisine, chelerythrine, chelilutine chelirubine, macarpine, magnoflorine, protopine, sanguinarine (Táborská et al., 1978; Dostál et al., 1992), dihydrochelerythrine, dihydrochelilutine, dihydrochelirubine, dihydrosanguinarine, chelidonine, *N*-methylstylopinium, stylopine, norsanguinarine, stylopine (Slavík & Slavíková, 1977). The identity of the alkaloids was verified by EI-MS, ^{1}H NMR and ^{13}C NMR and their purities were at least 98 % according to HPLC analysis (Marek et al., 1999; Suchomelová et al., 2007).

Extraction and isolation

Dried, ground plant material (0.5 g) was extracted with 100 mL of methanol in a FexIKA® apparatus (IKA, Germany), which is based on fluidised bed extraction. The extraction protocol was optimised on the basis of a comparison with Soxhlet extraction with methanol (Urbanová et al., 2012). Extraction times of 4×15 min for the aerial part and 6×15 min for the roots were used. The recoveries of both methods were comparable. The solvent from the extract was then evaporated to 25 mL. Prior to LC UV, the extract was diluted $3 \times$ and filtered through a 0.45-μm nylon syringe filter. For LC MS, the extract was diluted $20 \times$ and filtered through a 0.22-μm PTFE syringe filter.

LC MS

The LC MS method was developed using a Dionex Ultimate 3000RS (Thermo Scientific, CA, USA) module. Compound separation was achieved with a 3.0 mm $\times$ 150 mm, 5 μm Synergi RP-Max C18 (Phenomenex, CA, USA) column, thermostated at (23 ± 0.1) °C, and a flow-rate of 0.5 mL min^{-1}. The binary mobile phase system consisted of 0.1 mass % of formic acid and ACN. After 20-μL injection, the volume of ACN was linearly increased from 20 % to 40 % over 10 min and then to 80 % over the subsequent 10 min. ACN was held at 80 % for 10 min, followed by equilibration under the initial conditions for 3.0 min. A complete HPLC run was 33 min. The HPLC system was connected to a Bruker MicrOTOF-QII (Germany) mass spectrometer, operated in the positive

electrospray ionisation mode. The ionisation conditions were determined by the software as follows: capillary voltage: 4500 V, end plate offset: –0.5 V, source temperature: 220 ℃, desolvation gas (nitrogen) flow: 10 L min^{-1}, nebuliser (nitrogen) pressure: 300 kPa and collision cell voltage: 35 eV. The base-peak chromatogram (BPC) was acquired in MS mode by monitoring the m/z range of 50–3000 with a spectra sample time of 1 s. The identification of target compounds relied on isotope pattern matching with a combination of MS/MS and retention behaviour. High-resolution MS and MS/MS spectra were first investigated to obtain the elemental formula of each compound. A compound was identified unambiguously if the fragmentation patterns of the unknown and the standard were identical.

LC UV

The HPLC apparatus consisted of a LC-20 AD high-pressure gradient pump LC-20 AD, an SPD M20A diode-array detector (Shimadzu, Japan) and a syringe-loading sample injector (ECOM, Czech Republic) with a 20-μL external sample loop. Alkaloids were separated on a C12 column (Synergi RP-Max, 4 μm, 150 mm × 4.60 mm ID, Phenomenex, CA, USA).

The method used was detailed in our previous study (Suchomelová et al., 2007). Briefly, the mobile phase was prepared from a stock solution of 0.01 M sodium 1-heptanesulphonate and 0.1 M triethylamine in Milli-Q water (Millipore, MA, USA), adjusted to pH 2.5 with phosphoric acid. Mobile phase A consisted of 75 : 25 (vol.) stock solution : ACN. Mobile phase B was 40 : 60 (vol.) stock solution : ACN.

The following elution profile was employed: 0–1 min 100 % A; 1–10 min 0–20 % B; 10–22 min 20–50 % B; 22–28 min 50–100 % B; 28–40 min 100 % B; 40–48 min 100 % A. The flow-rate was set at 0.5 mL min^{-1}, the injection volume was 20 μL and detection was performed using a diode array detector at 280 nm. The identification of the separated alkaloids was based on comparisons of their retention times with those of authentic standards. Quantitative analysis was performed using external standards and was validated previously (Suchomelová et al., 2007).

Antiproliferative activity

The antiproliferative activities of the whole extract and of the individual alkaloids COP, MA, CR, SA, CHE, BER and CL were tested using the A-375 human malignant melanoma cell line and a colorimetric MTT (3-(4,5-dimethylthiazol-2-yl)-2,5-diphenyl tetrazolium bromide) assay. The extract was standardised ($n = 2$) and contained: CL (0.76 ± 0.11) mg L^{-1}, BER: (1.48 ± 0.22) mg L^{-1}, CHE (3.11 ± 0.58) mg L^{-1}, MA (10.2 ± 1.1) mg L^{-1}, PRO (4.09 ± 0.38) mg L^{-1}, CR

(7.62 ± 0.85) mg L^{-1}, SA (6.04 ± 0.49) mg L^{-1}, STY (10.6 ± 1.0) mg L^{-1} and COP (22.5 ± 1.9) mg L^{-1}. The A-375 cell line was purchased from the European Collection of Animal Culture (ECACC, Salisbury, UK). The MTT assay was performed in a 96-well plate (Nunc A/S, Denmark). Individual wells were seeded with 200 μL of cells (1×10^4 per mL) and incubated in a RPMI 1640 medium supplemented with 10 mass % of fetal bovine serum, 2 mM of glutamine, 100 IU mL of penicillin and 100 μg mL^{-1} of streptomycin at 37 ℃ in a humidified atmosphere (5 vol. % CO$_2$). After 24 h of incubation, the medium was replaced with an extract- or alkaloid-containing medium at concentrations ranging from 0.3 mg L^{-1} to 10 mg L^{-1}. The MTT assay was performed 48 h after addition of the extract: 20 μL of MTT (5 mg L^{-1} in PBS) was added to each well and incubated for 4 h under culture conditions. At the end of the incubation period, the medium was removed, the formazan crystals were dissolved in 200 μL of DMSO and the optical density was measured at 570 nm using a DTX 880 multimode detector (Beckman Coulter, CA, USA). The concentration of each compound was examined in four replicates.

Results and discussion

Identification of S. lasiocarpum alkaloids

The extracts were first analysed by mass spectrometry to confirm the identity of the alkaloids intended for quantitation. The base peak chromatogram of the root extract is shown in Fig. 1, and the retention times, elemental composition and major fragments of the root and aerial-part extracts are summarised in Table 2. Seventeen compounds were identified by comparing the fragmentation and retention behaviours of the alkaloid peaks in the extracts obtained from *S. lasiocarpum* roots with those of standard samples. All, with the exception of COP, are components of a benzo[c]phenanthridine pathway that starts from (S)-reticuline and involves eleven highly specific enzymes (Zenk, 1994). COP is regarded as a side-product of the pathway because it is formed by the oxidation of STY. Pathway intermediates, such as N-methylstylopinium, PRO or dihydro-SA, were also detected. In most plants, the biosynthetic pathway ends with the creation of SA but a few plant species, including *S. lasiocarpum,* may induce two subsequent hydroxylation and methylation steps resulting in MA production (Zenk, 1994). The presence of dihydro-CL, dihydro-CHE, nor-SA, dihydro-CR, dihydro-SA and canadine (CAN) was observed for the first time. The detection of QBA dihydroderivatives is not surprising as they are typically found in all plants producing QBAs; however, they are often neglected due to their non-polar character. The presence of chelidonine and N-methylstylopinium in the extract of the aerial part

Table 2. Retention time, exact mass of molecular ion or protonated ions and major fragment ions ([M]) of compounds found in extracts of root (1–17) and aerial part (1–19) of *S. lasiocarpum*

Peak	t_R/min	m/z	Ion	Observed mass	Calculated mass	Difference in ppm	Formula	Major fragment ions, m/z	Compound name
1	2.0	342.1694	$[M]^+$	342.1694	342.1705	−3.2	$C_{20}H_{24}NO_4$	175.0763; 191.0931; 207.0828; 209.0953; 219.0795; 222.0675; 233.0606; 235.0762; 237.0899; 247.0749; 265.0854; 282.0895; 297.1126	Magnoflorine
2	3.3	354.1351	$[M + H]^+$	353.1278	353.1263	4.2	$C_{20}H_{19}NO_5$	149.0597; 165.0546; 188.0703; 189.0779; 206.0799; 235.0762; 247.0762; 265.0856; 267.0658; 275.0711; 293.0801; 295.0968; 305.0909; 336.1232	Protopine
3	3.7	370.1648	$[M + H]^+$	369.1575	369.1576	−0.3	$C_{21}H_{23}NO_5$	165.0903; 181.0865; 188.0725; 206.0808; 275.0702; 281.1112; 290.0935; 306.0895; 308.1057; 311.1266; 321.1191; 336.1234; 339.1238; 352.1535	Allocryptopine
4	3.8	320.0942	$[M]^+$	320.0942	320.0923	5.9	$C_{19}H_{14}NO_4$	233.0824; 234.0918; 247.0646; 248.0711; 249.0786; 260.0696; 262.0864; 264.1018; 275.0601; 277.0736; 290.0820; 292.0980; 305.0685; 318.0763	Coptisine
5	4.1	324.1251	$[M + H]^+$	323.1178	323.1158	6.2	$C_{19}H_{17}NO_4$	149.0596; 174.0556; 176.0706; 188.0711; 219.0797; 249.0888; 262.0824; 265.0887; 277.0820; 290.0815; 292.0963; 307.0976	Stylopine
6	4.4	340.1535	$[M + H]^+$	339.1462	339.1471	−2.7	$C_{20}H_{21}NO_4$	149.0593; 165.0877; 174.0562; 176.0703; 324.1214	Canadine
7	4.6	332.0935	$[M]^+$	332.0935	332.0923	3.6	$C_{20}H_{14}NO_4$	216.0808; 218.0960; 244.0757; 246.0921; 261.0752; 272.0697; 274.0871; 287.0576; 289.0737; 302.0810; 304.0961; 316.0611; 317.0686	Sanguinarine
8	5.0	336.1226	$[M]^+$	336.1226	336.1236	−3.0	$C_{20}H_{18}NO_4$	246.0897; 263.0921; 274.0854; 275.0928; 278.0814; 291.0870; 292.0967; 302.0805; 304.0962; 306.0761; 317.0695; 320.0932	Berberine

Table 2. (continued)

Peak	t_R/min	m/z	Ion	Observed mass	Calculated mass	Difference in ppm	Formula	Major fragment ions, m/z	Compound name
9	5.8	348.1248	$[M]^+$	348.1248	348.1236	3.4	$C_{21}H_{18}NO_4$	275.0895; 276.0919; 286.0881; 287.0928; 290.0809; 302.0775; 303.0886; 304.0961; 314.0803; 315.0881; 316.0956; 318.0765; 330.0742; 332.0939	Chelerythrine
10	6.2	362.1033	$[M]^+$	362.1033	362.1028	1.4	$C_{21}H_{16}NO_5$	261.0793; 289.0745; 291.0869; 302.0490; 303.0825; 304.0753; 317.0683; 318.0771; 331.0829; 332.0563; 334.1058; 346.0700; 347.0782	Chelirubine
11	7.3	348.0861	$[M]^+$	378.1340	378.1341	−0.3	$C_{22}H_{20}NO_5$	305.0702; 320.0906; 321.0938; 332.0910; 334.1101; 347.1166; 348.0860; 362.1014; 363.1090	Chelilutine
12	7.8	392.1145	$[M]^+$	392.1145	392.1134	2.8	$C_{22}H_{18}NO_6$	291.0891; 319.0846; 330.0753; 331.0800; 334.0915; 346.0694; 347.0782; 348.0868; 360.0842; 361.0929; 362.0672; 364.1142; 376.0818; 377.0903	Macarpine
13	21.1	380.1495	$[M + H]^+$	379.1422	379.1420	0.5	$C_{22}H_{21}NO_5$	319.0907; 320.0848; 332.0938; 334.0868; 335.0889; 348.1084; 350.1062; 363.1106; 364.1186; 378.1338	Dihydrochelilutine
14	21.6	350.1382	$[M + H]^+$	349.1309	349.1314	−1.4	$C_{21}H_{19}NO_4$	288.0992; 289.0912; 290.0836; 302.0798; 303.0897; 304.0900; 315.0858; 316.0970; 317.1035; 318.0964; 332.0936; 334.1082; 348.1234	Didhydrochelerythrine
15	21.6	318.0752	$[M + H]^+$	317.0679	317.0688	−2.8	$C_{19}H_{11}NO_4$	232.0756; 260.0704; 288.0643; 290.0807	Norsanguinarine
16	22.0	364.1185	$[M + H]^+$	363.1112	363.1107	1.4	$C_{21}H_{17}NO_5$	290.0785; 291.0854; 304.0714; 305.0778; 306.0982; 317.0688; 318.0752; 319.0700; 332.0893; 334.0772; 346.0694; 347.0774; 348.0855; 349.0933; 362.1040	Dihydrochelirubine
17	22.2	334.1089	$[M + H]^+$	333.1016	333.1001	4.5	$C_{20}H_{15}NO_4$	246.0882; 260.0752; 261.0772; 262.0828; 274.0817; 276.1009; 288.0747; 289.0750; 302.0791; 303.0835; 304.0927; 317.0717; 318.0779; 330.0748; 332.0926	Dihydrosanguinarine

Table 2. (continued)

Peak	t_R/min	m/z	Ion	Observed mass	Calculated mass	Difference in ppm	Formula	Major fragment ions, m/z	Compound name
18	3.8	354.1335	$[M + H]^+$	353.1258	353.1263	−1.4	$C_{20}H_{19}NO_5$	163.0396; 188.0681; 217.0640; 235.0771; 237.0906; 245.0609; 247.0755; 265.0837; 275.0699; 293.0802; 295.0969; 305.0785; 323.0920; 336.1226	Chelidonine[a]
19	3.9	338.1404	$[M]^+$	338.1404	338.1392	3.5	$C_{20}H_{20}NO_4$	149.0593; 176.0697; 188.0717; 190.0871; 207.0799; 219.0800; 235.0751; 237.0890; 247.0756; 249.0902; 265.0848; 277.0873; 295.0964; 307.1016	N-Methylstylopinium[a]

a) Found only in the aerial part.
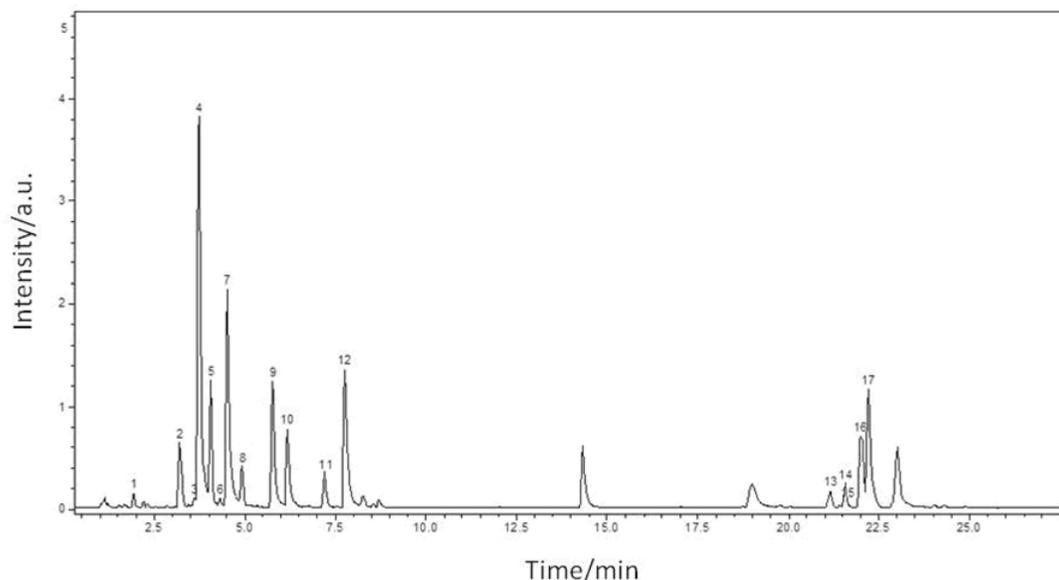
Fig. 1. LC MS base-peak chromatogram of 20 × diluted *S. lasiocarpum* root extract. Peaks labelled 1–17 were identified and are summarised in Table 2. Unlabelled peaks contain compounds of no interest as their MS/MS provided different, non-alkaloid structure patterns.

portions of *S. lasiocarpum* was observed in addition to the alkaloids found in the root extract.

Seasonal analysis of *S. lasiocarpum* alkaloids

Aerial part

The QBA content in the aerial part of one- and two-year plants was determined and is summarised in Table 3. The protoberberine alkaloids COP and STY were found to be the main substances in extracts of the aerial part irrespective of plant age; SA and CR were the major QBA portions. While the SA content increased at the culmination of the first year of vegetation, the CR content was relatively constant throughout the first year of vegetation. In the second year, both SA and CR displayed two maxima: in June and at the end of the vegetation period. PRO exhibited exactly the opposite trend, as it is a biosynthetic precursor of SA and CR (Tanahashi & Zenk, 1990). Similar behaviours were reported in the analysis of the aerial parts of *Macleaya microcarpa* Fedde (Pěnčíková et al., 2011).

Although the contents of CL and CHE were negligible in both years, the production of MA was higher toward the end of the second year. In the system-

Table 3. Content of isoquinoline alkaloids from aerial part of *S. lasiocarpum* during vegetation periods of one- and two-year old cultures; year of harvest: 2012; the amount of alkaloid is of dry mass (mean ± standard deviation, $n = 2$)

Plant age/year	Month	Amount/(mg g^{-1})								
		CL	BER	CHE	MA	PRO	CR	SA	STY	COP
One	May	0.012 ± 0.003	0.040 ± 0.003	0.023 ± 0.008	0.093 ± 0.019	0.394 ± 0.059	0.188 ± 0.039	0.091 ± 0.020	1.61 ± 0.26	3.92 ± 0.64
	June	0.007 ± 0.002	0.018 ± 0.006	0.010 ± 0.004	0.037 ± 0.013	0.150 ± 0.027	0.199 ± 0.047	0.0640 ± 0.0070	1.01 ± 0.12	3.63 ± 0.29
	July	0.002 ± 0.001	0.016 ± 0.002	0.026 ± 0.002	0.019 ± 0.005	0.215 ± 0.015	0.223 ± 0.019	0.304 ± 0.029	2.010 ± 0.067	4.47 ± 0.24
	August	0.005 ± 0.001	0.021 ± 0.001	0.008 ± 0.002	0.005 ± 0.001	0.122 ± 0.017	0.262 ± 0.028	0.434 ± 0.055	1.985 ± 0.071	5.21 ± 0.21
	September	0.006 ± 0.001	0.024 ± 0.004	0.039 ± 0.008	0.011 ± 0.004	0.104 ± 0.009	0.233 ± 0.010	1.30 ± 0.27	1.787 ± 0.084	4.58 ± 0.31
	October	0.023 ± 0.002	0.016 ± 0.002	0.018 ± 0.003	0.033 ± 0.009	0.152 ± 0.018	0.269 ± 0.016	1.70 ± 0.17	2.475 ± 0.054	5.31 ± 0.26
Two	May	0.011 ± 0.001	0.017 ± 0.003	0.013 ± 0.001	0.032 ± 0.007	0.516 ± 0.004	0.185 ± 0.025	0.081 ± 0.011	1.769 ± 0.067	3.88 ± 0.22
	June	0.022 ± 0.009	0.020 ± 0.005	0.055 ± 0.003	0.125 ± 0.005	0.172 ± 0.028	1.332 ± 0.034	0.766 ± 0.030	1.826 ± 0.092	6.89 ± 0.15
	July	0.023 ± 0.013	0.010 ± 0.001	0.018 ± 0.002	0.026 ± 0.005	0.501 ± 0.014	0.250 ± 0.031	0.204 ± 0.019	1.328 ± 0.077	3.82 ± 0.24
	August	0.070 ± 0.011	0.021 ± 0.003	0.023 ± 0.004	0.114 ± 0.024	0.189 ± 0.021	0.67 ± 0.20	1.00 ± 0.14	2.01 ± 0.17	3.93 ± 0.19
	September	0.014 ± 0.003	0.021 ± 0.010	0.020 ± 0.008	0.054 ± 0.003	0.264 ± 0.021	0.392 ± 0.048	0.92 ± 0.22	1.88 ± 0.22	4.09 ± 0.23
	October	0.008 ± 0.002	0.036 ± 0.006	0.030 ± 0.005	0.222 ± 0.023	0.144 ± 0.029	1.22 ± 0.33	1.46 ± 0.30	1.81 ± 0.15	4.60 ± 0.24

Table 4. Content of isoquinoline alkaloids from roots of *S. lasiocarpum* during vegetation periods of one- and two-year old cultures; year of harvest: 2012; the amount of alkaloid is of dry mass (mean ± standard deviation, $n = 2$)

| Plant age/year	Month	Amount/(mg g^{-1})								
		CL	BER	CHE	MA	PRO	CR	SA	STY	COP
One	May	0.044 ± 0.007	0.92 ± 0.22	0.54 ± 0.11	2.45 ± 0.21	1.55 ± 0.20	1.552 ± 0.032	2.07 ± 0.32	9.4 ± 1.3	13.9 ± 2.1
	June	0.183 ± 0.017	0.485 ± 0.055	0.930 ± 0.059	2.146 ± 0.040	0.1150 ± 0.0050	1.588 ± 0.037	1.685 ± 0.081	3.77 ± 0.20	9.50 ± 0.41
	July	0.275 ± 0.021	0.585 ± 0.041	1.33 ± 0.16	4.28 ± 0.43	0.516 ± 0.098	2.76 ± 0.27	4.07 ± 0.62	7.16 ± 0.67	9.6 ± 1.1
	August	0.108 ± 0.012	0.746 ± 0.010	0.107 ± 0.012	1.79 ± 0.25	0.354 ± 0.013	1.41 ± 0.20	1.17 ± 0.12	7.35 ± 0.13	14.96 ± 0.25
	September	0.078 ± 0.010	1.95 ± 0.10	0.126 ± 0.012	1.88 ± 0.26	0.44 ± 0.14	1.440 ± 0.076	1.735 ± 0.089	7.69 ± 0.40	18.32 ± 0.96
	October	0.041 ± 0.004	0.857 ± 0.056	0.041 ± 0.011	1.21 ± 0.19	0.063 ± 0.021	1.057 ± 0.033	0.872 ± 0.029	5.40 ± 0.18	13.15 ± 0.70
Two	May	0.100 ± 0.008	0.585 ± 0.084	0.396 ± 0.042	3.92 ± 0.48	0.151 ± 0.023	1.54 ± 0.15	1.41 ± 0.13	4.76 ± 0.48	9.94 ± 0.76
	June	0.148 ± 0.048	0.607 ± 0.079	0.68 ± 0.15	7.05 ± 0.68	0.939 ± 0.051	3.77 ± 0.97	3.13 ± 0.45	3.46 ± 0.22	13.91 ± 0.57
	July	0.304 ± 0.016	0.649 ± 0.072	1.40 ± 0.11	5.8 ± 1.1	1.10 ± 0.22	5.99 ± 0.39	4.61 ± 0.12	3.45 ± 0.19	11.05 ± 0.63
	August	0.160 ± 0.026	1.159 ± 0.089	0.306 ± 0.052	2.96 ± 0.14	0.214 ± 0.025	4.12 ± 0.16	2.46 ± 0.16	5.23 ± 0.40	13.06 ± 0.67
	September	0.135 ± 0.045	0.695 ± 0.054	0.139 ± 0.031	2.37 ± 0.22	0.548 ± 0.027	3.63 ± 0.65	1.96 ± 0.31	5.21 ± 0.38	14.2 ± 1.2
	October	0.061 ± 0.008	0.738 ± 0.069	0.155 ± 0.026	2.02 ± 0.38	0.238 ± 0.098	2.67 ± 0.18	1.898 ± 0.052	5.00 ± 0.31	15.37 ± 0.88
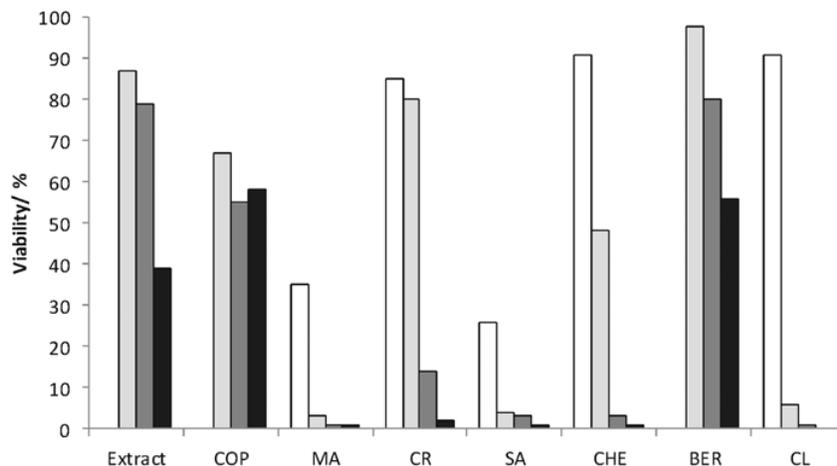
Fig. 2. Mean ($n = 4$) percentage of viable cells after treatment with root extract or individual alkaloids (0.3–10 mg L^{-1}). Established by MTT assay. Legend: 0.3 mg mL^{-1} ( ), 1 mg mL^{-1} ( ), 3 mg mL^{-1} ( ), 10 mg mL^{-1} ( ).

atic analysis of QBA-containing plants, only *S. lasio-carpum* included considerable amounts of MA and CR in the aerial part (Pěnčíková et al., 2012).

Roots

Roots, in comparison with leaves, were found to contain analogous alkaloids and the seasonal levels of major alkaloids are summarised in Table 4. The levels of most alkaloids varied from May to October, peaking in the middle of the vegetation period. The roots clearly contained larger quantities of all alkaloids, whereas COP and STY were the major substances in all samples. Although the levels of COP did not differ in individual cultures, the concentrations of STY were slightly lower in the two-year old plant.

Notably, the rarely occurring MA was found in amounts readily comparable to SA, irrespective of the age of the plant. An inter-species comparison shows that the amount of MA in a one-year old plant was equivalent to that found in the roots of *M. microcarpa* 13 years old (Pěnčíková et al., 2011). The levels of MA in the roots of both cultures indicated a maximum at the midpoint of the vegetation cycle, unlike in the aerial part where few maxima were observed. Furthermore, in the two-year old culture, the concentrations of both MA and CR exceeded those of SA over the entire vegetation period. The amount of CR in the roots of a second-year *S. lasiocarpum* was also equivalent to that in the roots of a 13-year old *M. microcarpa*, i.e. approximately 5 mg g^{-1} of dry mass.

The changes in alkaloid content and their relative proportion in the entire herb suggest that such seasonal variations could be the result of long-distance transport from leaves to roots and vice versa or local de novo biosynthesis of the full range of alkaloids. The localisation of isoquinoline alkaloid biosynthesis has only been sporadically studied in a few species, sug-

gesting local de novo biosynthesis of isoquinoline alkaloids in various organs (Weid et al., 2004; Samanani et al., 2005, 2006; Khodorova et al., 2013).

Antiproliferative activity of standardised root extract and pure alkaloids

The antiproliferative activities of the root extract and of seven individual alkaloids were tested on A375 human malignant melanoma cells after 48-hours' incubation using a colorimetric MTT assay. Extracts at concentrations of 1 mg L^{-1}, 3 mg L^{-1} and 10 mg L^{-1} and pure alkaloids over a concentration range of 0.3–10 mg L^{-1} resulted in a dose-dependent decrease in cell metabolic activity (Fig. 2). The QBAs generally exhibited higher toxicity than other alkaloids, with MA and SA being the most toxic. Several groups have previously described the antiproliferative activity of SA on various cancer cell types (Slaninová et al., 2014). We previously described the strong antiproliferative effects of MA and CR on several cancer cell lines (Slaninová et al., 2001, 2007a), but this is the first documentation of their effect on malignant melanoma cells. The fact that these alkaloids exhibit a high antiproliferative activity even against melanoma cells suggests that they are strong candidates for further cancer biology and therapy studies.

The toxicity of COP, the main alkaloid of *S. lasiocarpum* extracts, on melanoma cells is much lower than that of SA and MA. It was not possible to determine the toxicity of PRO and STY due to their low solubility in water. In an attempt to improve the solubility, DMSO and/or hydrochloric acid were added, but insoluble residues appeared each time. In respect of the toxicity of the solvents (DMSO or HCl) at higher concentrations, no definitive and accurate conclusion was drawn (data not shown). The absence of derivatives with higher solubility could be the reason for the

ongoing lack of information regarding the cytotoxicity of PRO and STY.

Conclusions

This study provides the first comprehensive qualitative and quantitative set of data on alkaloids found in *S. lasiocarpum* throughout the vegetation period of a one- and two-year old plant. Although the content of individual alkaloids varied during vegetation, the major alkaloids were COP, STY, MA, CR and SA.

While the protoberberine alkaloid content was not dependent on plant age, the amount of QBAs was particularly high when isolated from the second-year roots in July. Variations in the alkaloid content should be taken into consideration when assessing the safety and effectiveness of herbal remedies based on this plant, especially due to the high cytotoxicity of QBAs.

S. lasiocarpum requires shade, abundant irrigation and has relatively small roots; these factors might preclude routine cultivation. However, the isolation of MA and CR from plant material remains the best approach for their large-scale production, with the older roots being the prospective source.

References

Dostál, J., Táborská, E., & Slavík, J. (1992). Preparative column chromatography of quaternary benzophenanthridine alkaloids of *Dicranostigma lactucoides. Fitoterapia, 63,* 67–69.

Dvořák, Z., Kubáň, V., Klejdus, B., Hlavac, J., Vicar, J., Ulrichová, J., & Simánek, V. (2006). Quaternary benzo[*c*]phenanthridines sanguinarine and chelerythrine: A review of investigations from chemical and biological studies. *Heterocycles, 68,* 2403–2422. DOI: 10.3987/rev-06-610.

Feng, R. Z., Lian, W. Y., Fu, G. X., & Xiao, P. G. (1985). Chemotaxonomy and resource utilization of tribe *Chelidonieae* (Pavaveraceae). *Acta Phytotaxonomica Sinica, 23,* 36–42.

Galezowska, E., Kosman, J., Stepien, A., Rubis, B., Rybczynska, M., & Juskowiak, B. (2012). Bioactive papaverine derivatives bind G-quadruplexes selectively. *Chemical Papers, 66,* 79–84. DOI: 10.2478/s11696-011-0092-4.

Hammerová, J., Uldrijan, S., Táborská, E., & Slaninová, I. (2011). Benzo[*c*]phenanthridine alkaloids exhibit strong antiproliferative activity in malignant melanoma cells regardless of their p53 status. *Journal of Dermatological Science, 62,* 22–35. DOI: 10.1016/j.jdermsci.2011.01.006.

Hammerová, J., Uldrijan, S., Táborská, E., Vaculová, A. H., & Slaninová, I. (2012). Necroptosis modulated by autophagy is a predominant form of melanoma cell death induced by sanguilutine. *Biological Chemistry, 393,* 647–658. DOI: 10.1515/hsz-2011-0279.

Ishikawa, T., Saito, T., & Ishii, H. (1995). Synthesis of macarpine and its cytotoxicity: Toward a synthetic route for 12-alkoxybenzo[*c*]phenanthridine alkaloids through aromatic

nitrosation under basic condition. *Tetrahedron, 51,* 8447–8458. DOI: 10.1016/0040-4020(95)00460-p.

Khodorova, N. V., Shavarda, A. L., Lequart-Pillon, M., Laberche, J. C., Voitsekhovskaja, O. V., & Boitel-Conti, M. (2013). Biosynthesis of benzylisoquinoline alkaloids in *Corydalis bracteata*: Compartmentation and seasonal dynamics. *Phytochemistry, 92,* 60–70. DOI: 10.1016/j.phytochem.2013.04.008.

Lei, Q. F., Zhao, X. L., Xu, L. J., Peng, Y., & Xiao, P. G. (2014). Chemical constituents of plants from tribe chelidonieae and their bioactivities. *Chinese Herbal Medicines, 6,* 1–21. DOI: 10.1016/s1674-6384(14)60001-0.

Marek, R., Toušek, J., Dostál, J., Slavík, J., Dommisse, R., & Sklenář, V. (1999). ^{1}H and ^{13}C NMR study of quaternary benzo[*c*]phenanthridine alkaloids. *Magnetic Resonance in Chemistry, 37,* 781–787. DOI: 10.1002/(sici)1097-458x(199911)37:11<781::aid-mrc556>3.3.co;2-8.

Pěnčíková, K., Urbanová, J., Musil, P., Táborská, E., & Gregorová, J. (2011). Seasonal variation of bioactive alkaloid contents in *Macleaya microcarpa* (Maxim.) Fedde. *Molecules, 16,* 3391–3401. DOI: 10.3390/molecules16043391.

Pěnčíková, K., Urbanová, J., & Táborská, E. (2012). Occurrence of quaternary benzo[*c*]phenanthridine alkaloids in *Stylophorum lasiocarpum* (Oliv.) fedde. In *Proceedings of the International Congress Natural Anticancer Drugs*, June 30–July 4, 2012. Olomouc, Czech Republic: Palacký University Olomouc.

Rybáková, S., Rájecký, M., Urbanová, J., Pěnčíková, K., Táborská, E., Gargallo, R., & Táborský, P. (2013). Interaction of oligonucleotides with benzo[*c*]phenanthridine alkaloid sanguilutine. *Chemical Papers, 67,* 568–572. DOI: 10.2478/s11696-013-0340-x.

Samanani, N., Park, S. U., & Facchini, P. J. (2005). Cell type-specific localization of transcripts encoding nine consecutive enzymes involved in protoberberine alkaloid biosynthesis. *Plant Cell, 17,* 915–926. DOI: 10.1105/tpc.104.028654.

Samanani, N., Alcantara, J., Bourgault, R., Zulak, K. G., & Facchini, P. J. (2006). The role of phloem sieve elements and laticifers in the biosynthesis and accumulation of alkaloids in opium poppy. *The Plant Journal, 47,* 547–563. DOI: 10.1111/j.1365-313x.2006.02801.x.

Slaninová, I., Táborská, E., Bochořáková, H., & Slanina, J. (2001). Interaction of benzo[*c*]phenanthridine and protoberbine alkaloids with animal and yeast cells. *Cell Biology and Toxicology, 17,* 51–63. DOI: 10.1023/a:1010907231602.

Slaninová, I., Slunská, Z., Šinkora, J., Vlková, M., & Táborská, E. (2007a). Screening of minor benzo[*c*]phenanthridine alkaloids for antiproliferative and apoptotic activities. *Pharmaceutical Biology, 45,* 131–139. DOI: 10.1080/13880200601113099.

Slaninová, I., Slanina, J., & Táborská, E. (2007b). Quaternary benzo[*c*]phenanthridine alkaloids – novel cell permeant and red fluorescing DNA probes. *Cytometry Part A, 71,* 700–708. DOI: 10.1002/cyto.a.20423.

Slaninová, I., Pěnčíková, K., Urbanová, J., Slanina, J., & Táborská, E. (2014). Antitumour activities of sanguinarine and related alkaloids. *Phytochemistry Reviews, 13,* 51–68. DOI: 10.1007/s11101-013-9290-8.

Slavík, J., & Slavíková, L. (1977). Minor alkaloids from *Chelidonium-majus* L. *Collection of Czechoslovak Chemical Communications, 42,* 2686–2693. DOI: 10.1135/cccc19772686.

Slavík, J., Hanuš, V., & Slavíková, L. (1991). Alkaloids from *Stylophorum lasiocarpum* (OLIV.) FEDDE. *Collection of Czechoslovak Chemical Communications, 56,* 1116–1122. DOI: 10.1135/cccc19911116.

Slunská, Z., Gelnarová, E., Hammerová, J., Táborská, E., & Slaninová, I. (2010). Effect of quaternary benzo[*c*]phenanthridine alkaloids sanguilutine and chelilutine on normal

and cancer cells. *Toxicology in Vitro*, *24*, 697–706. DOI: 10.1016/j.tiv.2010.01.012.

Suchomelová, J., Bochořáková, H., Paulová, H., Musil, P., & Táborská, E. (2007). HPLC quantification of seven quaternary benzo[*c*]phenanthridine alkaloids in six species of the family Papaveraceae. *Journal of Pharmaceutical and Biomedical Analysis*, *44*, 283–287. DOI: 10.1016/j.jpba.2007.02.005.

Táborská, E., Věžník, F., Slavíková, L., & Slavík, J. (1978). Quaternary alkaloids of 3 species of dicranostigma HOOK-f et THOMS. *Collection of Czechoslovak Chemical Communications*, *43*, 1108–1112. DOI: 10.1135/cccc19781108.

Tanahashi, T., & Zenk, M. H. (1990). Elicitor induction and characterization of microsomal protopine-6-hydroxylase, the central enzyme in benzophenanthridine alkaloid biosynthesis. *Phytochemistry*, *29*, 1113–1122. DOI: 10.1016/0031-9422(90)85414-b.

Urbanová, J., Pěnčíková, K., Gregorová, J., Hohnová, B., Šťavíková, L., Karásek, P., Roth, M., & Táborská, E. (2012). Isolation of quaternary benzo[*c*]phenanthridine alkaloids from *Macleaya microcarpa* (maxim.) FEDDE: Comparison of maceration, soxhlet extraction and pressurised liquid extraction. *Phytochemical Analysis*, *23*, 477–482. DOI: 10.1002/pca.2344.

Weid, M., Ziegler, J., & Kutchan, T. M. (2004). The roles of latex and the vascular bundle in morphine biosynthesis in the opium poppy, *Papaver somniferum*. *Proceedings of the National Academy of Sciences of the United States of America*, *101*, 13957–13962. DOI: 10.1073/pnas.0405704101.

Zenk, M. H. (1994). The formation of benzophenanthridine alkaloids. *Pure and Applied Chemistry*, *66*, 2023–2028. DOI: 10.1351/pac199466102023.

Zhang, M. L., Su, Z. Y., Lidén, M., & Grey-Wilson, C. (2008). Stylophorum. *Flora of China*, *7*, 284–285.

3.4 Heavy water enhancement of fluorescence signal in reversed-phase liquid chromatography

MS could prove essential even in fields and applications, which seem quite different such as fluorescence spectrometry. It has been known that fluorescence intensity and lifetime heavily depend on the fluorophore's surroundings. Dynamic quenching is a process that enables dissipating the excitation energy in non-radiative pathways. In a water environment, dynamic quenching is mediated mainly by –OH oscillators. To effectively decrease the quenching, solutions with alkaline pH are used since many of those –OH groups become charged, and the quenching process via non-radiative pathways is minimized. Sometimes however, the pH value cannot be efficiently increased, for example, in chromatography using silica-based columns. Another approach to decrease dynamic quenching could be the employment of deuterated solvents – specifically employing heavy water as a mobile phase in reversed-phase chromatography. The labile (acidic) hydrogens in the fluorescent compound are dynamically exchanged for deuterium atoms, which are heavier and oscillate with lower frequency. The overall fluorescence intensity could be thus increased up to hundreds of percent. Although heavy water is relatively expensive to use as a common solvent in high flow-rate chromatography, it may be easily included in microflow LC, cLC, or CE. Vitamin B, doxorubicin, and fluorescein were selected, and the effect of fluorescence enhancement by substituting light water in the mobile phase with heavy water was examined. The number of exchanged hydrogens was monitored by MS to provide a better understanding of the structure-to-enhancement relationship. The overall process of fluorescence enhancement by deuterated solvents is rather complex and was recently studied more comprehensively.[52]

Heavy water enhancement of fluorescence signal in reversed-phase liquid chromatography

Petr Taborsky[a], Josef Kucera[a], Jan Jurica[b], Ondrej Pes[c],*

[a] Department of Chemistry, Faculty of Science, Masaryk University, Kotlářská 2, 611 37 Brno, Czech Republic
[b] Department of Pharmacology, Faculty of Medicine, Masaryk University, Kamenice 5, 62500 Brno, Czech Republic
[c] Department of Biochemistry, Faculty of Medicine, Masaryk University, Kamenice 5, 62500 Brno, Czech Republic

ARTICLE INFO

ABSTRACT

Liquid chromatography with fluorescence detection has been used in analyses demanding high sensitivity and selectivity. As majority systems rely on reversed-phase columns with water being the main component of the mobile phase, fluorescent compounds with emission maxima higher than 500 nm might be dynamically quenched. A simple replacement of H_2O with D_2O enhanced the sensitivity for selected compounds by 10–200%. Affected compounds included an anti-cancer drug doxorubicin, a luminescent probe fluorescein, and naturally occurring forms of vitamin B_2. Similar levels of enhancement were obtained by fluorescence spectrometry. Such simple yet effective approach may greatly improve HPLC analyses coupled to fluorescence detection.

1. Introduction

Fluorescence detection in liquid chromatography (LC) has been widely spread due to a number of key features, such as high sensitivity, high selectivity, and repeatability. Reversed-phase high-performance LC (RP HPLC) with the C_{18} modified silica has become the most frequent type of an HPLC column since the market introduction. There might be some drawbacks when using light water in RP HPLC with fluorescence detection as water molecules can cause numerous collisions with the excited fluorophore molecules, which result in a non-radiative relaxation. The process was described as luminescence dynamic quenching and the energy is dissipated as heat *via* the −OH oscillation [1]. Dynamic quenching is typical for luminophores with emission maxima higher than 500 nm as it is accompanied by relatively high absorbance of H_2O above 500 nm [2].

When the water is replaced with another solvent the fluorescence intensity, lifetime, as well as fluorescence quantum yield might change. For example, luminescence lifetime of ethidium bromide was 1.8 ns in H_2O but increased to 5.0 ns in DMSO, 6.9 in ethanol, 5.9 ns in glycerol, or to 6.3 ns in D_2O [3]. The shorter fluorescence lifetime of ethidium bromide in light water was attributed to the non-radiative deactivation process described above. The quantum yield of the fluorescent dye ATTO 655 (0.23 in H_2O) was increased to 0.39 in methanol, 0.55 in acetone, 0.56 in DMSO, and to 0.48 in D_2O [1].

Dynamic fluorescence quenching induced by deuterated water was

found minimal in comparison to H_2O. One of the explanations relies on low absorbance of D_2O in a region above 500 nm [2]. Hence, if H_2O is replaced by D_2O in the mobile phase, the fluorescence signal-to-noise response may increase without any further modification of the compound separation. Although the enhancement induced by D_2O replacement is neither uniform nor known beforehand, an increase of fluorescence intensity and lifetime between units and hundreds of per cent might be observed.

We have selected a couple of compounds to demonstrate the aforementioned behavior of fluorophores surrounded by D_2O instead of H_2O. In order to enlighten the relationship between fluorescence intensity in light and heavy water, mass spectrometry was used as well.

Doxorubicin, which has been used as an anticancer agent, has been analyzed with satisfactory sensitivity in various biological fluids by chromatography [4–6] or targeted by fluorescence probes [7]. Fluorescein, which is heavily employed as a fluorescence labeling agent [8], has been used in imaging [9], chromatography [10,11], in cell targeting [12], or sensing [13]. Trace amounts of vitamin B_2 has been commonly determined by fluorescence techniques [14–17]. The mentioned applications may greatly benefit from the employment of heavy water into the methodology even as the overall impact and utilization still remain to be answered in future. In other words, we do not expect all researchers immediately exchanging their mobile phases, however; it may help in specialized types of applications or analyses where the limits of detection need to be pushed even further. It includes micro- or nano-HPLC to maintain the costs reasonable.

* Corresponding author.
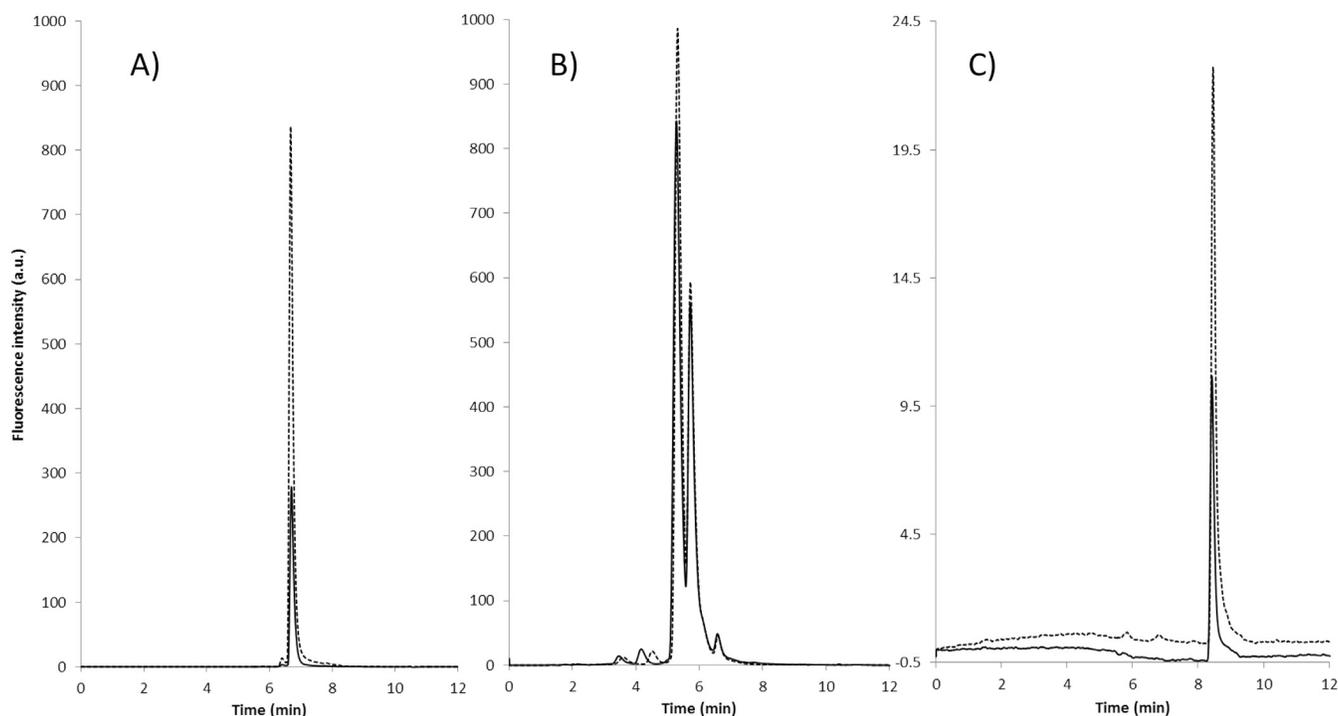 *E-mail address:* ondramayl@gmail.com (O. Pes).

Fig. 1. Liquid chromatography with fluorescence detection of A) doxorubicin (26 µM, λ_{ex} = 480 nm, λ_{em} = 590 nm), B) vitamin B_2 species (15 µM each, (λ_{ex} = 377 nm, λ_{em} = 530 nm), and C) fluorscein (542 nM, λ_{ex} = 490 nm, λ_{em} = 518 nm) in H_2O (solid line) and D_2O (dashed line).

2. Experimental

2.1. Reagents and materials

Formic acid (LC MS), acetic acid (LC MS), ammonium hydroxide (28–30% NH_3 in water), sodium formate (LC-MS), acetonitrile (ACN, LC-MS), heavy water, fluorescein, doxorubicin, riboflavin, flavin mononucleotide (FMN), and flavin adenine dinucleotide (FAD) were purchased from Sigma-Aldrich (Czech Republic). Light water was of an ultra-pure grade supplied by an in-house Milli-Q system (Millipore, MA, USA).

2.2. Fluorescence spectrometry

Stock solutions were prepared by dilution of solid chemicals in H_2O. The concentration of all stock solutions was 0.1 mM. Samples were prepared by dilution of the stock solutions in D_2O and H_2O. Final concentrations were 0.22 µM for fluorescein, 0.01 µM for doxorubicin, and 1.4 µM for FAD, FMN, and riboflavin. The pH (pD) value of sample solutions was checked to be 7 ± 0.05 and was not further adjusted.

A spectrofluorometer Aminco-Bowman Series 2 (Thermo Fisher Scientific, MA, USA) equipped with a 150 W Xe lamp was used for steady state measurements. Excitation and emission wavelengths were set at 445 nm and 525 nm for riboflavin, FMN, and FAD; 490 nm and 590 nm for doxorubicin; and 480 nm and 515 nm for fluorescein. The spectra were acquired with 1 nm resolution and a scanning speed of 1 nm/s.

Time-domain measurements were performed using TCSPC SPC-130EM (Becker and Hickl GmbH, Germany) instrumentation equipped with a 408 nm diode laser (picosecond resolution, repeating frequency 150 MHz). The emission monochromator was set at same values as in steady-state measurements. The quartz cuvettes were used in all experiments.

2.3. Liquid chromatography with fluorescence or mass spectrometric detection

Samples were measured on an LC system Shimadzu LC-10 ADVp (Shimadzu, Japan) consisting of a manual injector, low pressure gradient ternary pump, and a fluorescence detector RF 10AXL and a Dionex UltiMate 3000RS (Thermo Fisher Scientific, CA, USA) equipped with a high-pressure gradient binary pump, an autosampler, and a heated column compartment. The latter was connected to a Bruker MicrOTOF-Q II (Germany) mass spectrometer.

Compound separation was achieved with a 2.1 mm × 150 mm, 5 µm Acclaim 120 C_{18} (Thermo Fisher Scientific, CA, USA) column, and a flow-rate of 0.4 mL min^{-1}. The binary mobile phase system consisted of ACN and 0.1% formic acid for doxorubicin, ACN and 0.1% formic acid with 0.1% ammonia for B_2 vitamins, and pure H_2O without any additives for fluorescein analysis. H_2O or D_2O was used as a solvent for the mobile phase preparation. After a 20-µL injection, the percentage of ACN was linearly increased from 10% to 60% over 7 min where it was held for 2 min, followed by equilibration under the initial conditions for another 5 min. A complete LC run was 14 min.

Fluorescence detector was set at 480 nm excitation and 590 nm emission wavelengths for doxorubicin, at 377 nm excitation and 530 nm emission wavelengths for B_2 vitamins, and at 489 nm excitation and 512 nm emission wavelengths for fluorescein analysis.

MS was operated in the positive electrospray ionization mode and the ionization conditions were determined by the software as follows: capillary voltage: 4500 V, end plate offset: −500 V, source temperature: 220 °C, desolvation gas (nitrogen) flow: 8 L min^{-1}, nebulizer (nitrogen) pressure: 300 kPa, and collision cell voltage: 6 eV. The base peak chromatogram (BPC) was acquired in MS mode by monitoring the m/z range of 50–1500 with a spectra sample time of 1 s and MS/MS spectra were collected in a data-dependent mode. The mass spectrometer was calibrated using 10 mM sodium formate in 50% isopropyl alcohol on a daily basis and at the beginning of each LC run with an external 20-µL loop flush. High-resolution MS and MS/MS spectra were
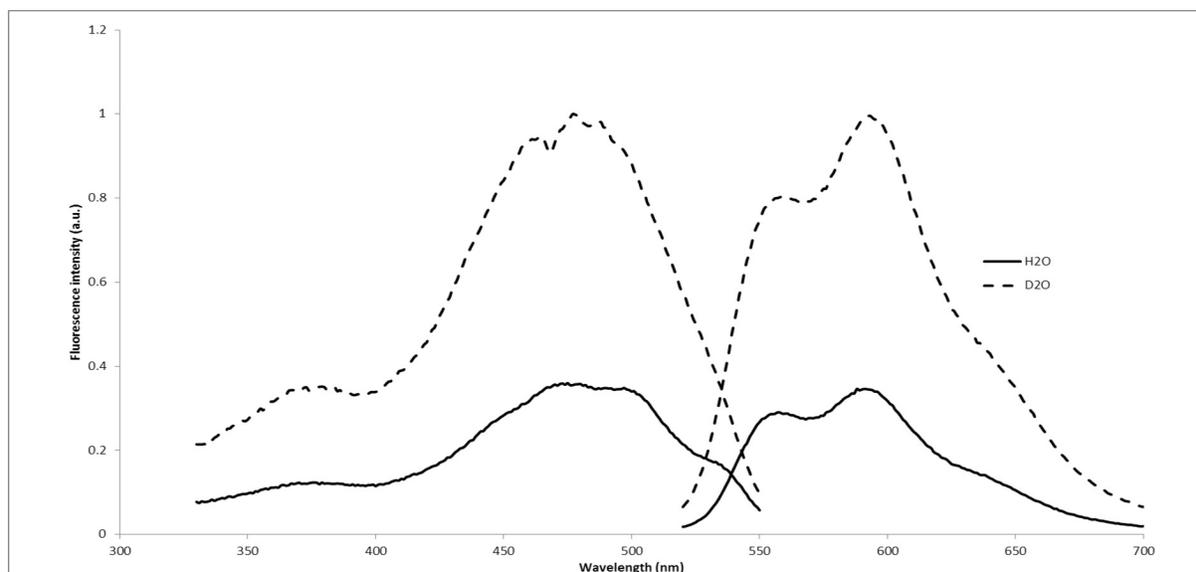
Fig. 2. Emission and excitation spectra of doxorubicin in H_2O and D_2O (λ_{exc} = 490 nm, λ_{em} = 590 nm, T = 293.15 K).

first investigated to obtain the elemental formula of each compound. The final identification of target compounds relied on isotope pattern matching with a combination of MS/MS and retention behavior.

3. Results and discussion

Chromatograms of doxorubicin, B_2 vitamin forms, and fluorescein in H_2O and D_2O with fluorescence detection might be seen in Fig. 1A. At doxorubicin, the fluorescence intensity is 2.98 times higher when heavy water was used as a solvent in the mobile phase. Fluorescence excitation and emission spectra of doxorubicin in H_2O and D_2O can be seen in Fig. 2. Fluorescence spectrometry at pH = 7 showed an increase in intensity (I_{D2O}/I_{H2O} = 2.87) as well as in lifetime (τ_{D2O}/τ_{H2O} = 4.04) of doxorubicin (Table 1).

B_2 vitamin forms provided 1.16 and 1.06 times higher fluorescence intensity for FAD and FMN, respectively. Fluorescence intensity of riboflavin in heavy water mobile phase was 0.95 times lower. Fluorescence excitation and emission spectra of riboflavin, FMN, and FAD in H_2O and D_2O can be seen in Fig. 3. Fluorescence spectrometry at pH = 7 showed an average 10% increase in intensity as well as in the lifetime of all vitamin B_2 forms (Table 1).

Fluorescein is well known to greatly increase its fluorescence intensity when ionized under high pH values (pH > 8) [18]. However, the chromatography columns based on silica particles are prone to degradation at high pH due to attack by excess hydroxide ions at the silica surface [19]. Hence, only water without any additives was used in a gradient elution of fluorescein from a column (Fig. 1C). The fluorescence intensity increased 2.19 times when pure D_2O was used in the mobile phase. Fluorescence spectrometry in pure H_2O or D_2O showed an increase in intensity (I_{D2O}/I_{H2O} = 2.22) as well as in lifetime

(τ_{D2O}/τ_{H2O} = 1.43) (Fig. 4, Table 1).

However, it has been reported that deuterated solvents might modify the separation between deuterated and non-deuterated analytes [20]. Even the relative response for unlabeled and deuterated forms of analyte was found to vary significantly from one batch of matrix to the other [21–23]. The exact cause of this deviation is unknown, but it may be related to the phenomenon that the properties of deuterated compounds somewhat differ from those of their unlabeled analogues.

When light water was used as a mobile phase solvent, all MS and MS spectra were unambiguously attributed to doxorubicin, FAD, FMN, riboflavin, and fluorescein. When heavy water was used, the MS and MS/MS spectra were searched for peaks with a mass increase corresponding to the number of hydrogens, which had been replaced by deuterium. The exchangeable hydrogen atoms are usually bound to N, O, or S atoms in functional groups such as −OH, −NH−, −NH₂, and −COOH. Accurate measurements of exchangeable hydrogen atoms in a molecule commonly assist in structural elucidation [24–30].

Consistently, all acidic hydrogens in the structure of doxorubicin, riboflavin, FMN, and fluorescein were replaced with deuterium as seen from Figs. 5, 6, 7, and 8. In the case of the FAD molecule, the number of replaced hydrogen was determined from MS[1] (data not shown) as no MS/MS spectra were acquired due to poor ionization efficiency in the positive mode. It is worth mentioning, that the consistency of the H/D exchange might differ in gaseous and liquid phase and the conditions for reliable quantitation should be confirmed *e.g.*, by an overnight experiment.

The question when the fluorescence intensity may increase due to the heavy water employment might be answered by dynamic quenching, which is caused by a difference in the −OH and −OD oscillator ability to efficiently quench a fluorophore molecule. In other words, when a fluorophore is heavily surrounded by −OH groups (either intra- or intermolecularly) the effect of quenching was observed. When the oscillator groups were replaced by −OD groups the quenching effect was lower. However, the −OD groups had to be in a direct contact with the fluorophore. Hence, doxorubicin and fluorescein with the highest amount of −OH oscillators surrounding the fluorophore showed the highest increase of fluorescence intensity when the −OH groups were replaced by −OD (Table 1). The increase of fluorescence intensity was higher than in the case of B_2 vitamins even as the number of totally exchanged atoms was lower since both deuterium atoms have replaced the hydrogen atoms in the −OH oscillator directly connected to a fluorophore part of the molecule. When fluorescein was

Table 1
Fluorescence properties of selected compounds in H_2O and D_2O. *Total number of hydrogens replaced by deuterium atoms.

	λ_{ex} (nm)	λ_{em} (nm)	I_D (a.u.)	I_H (a.u.)	I_D/I_H	τ_D (ns)	τ_H (ns)	τ_D/τ_H	$n_{D/H}$*
Doxorubicin	478	593	63.7	22.2	2.87	4.20	1.04	4.04	7
Fluorescein	489	512	58.9	26.6	2.22	4.85	3.40	1.43	2
FAD	370	525	45.8	41.5	1.10	3.66	3.19	1.15	10
FMN	370	525	75.1	64.9	1.16	5.11	4.58	1.11	6
Riboflavin	370	525	110	93.0	1.18	5.06	4.58	1.11	5
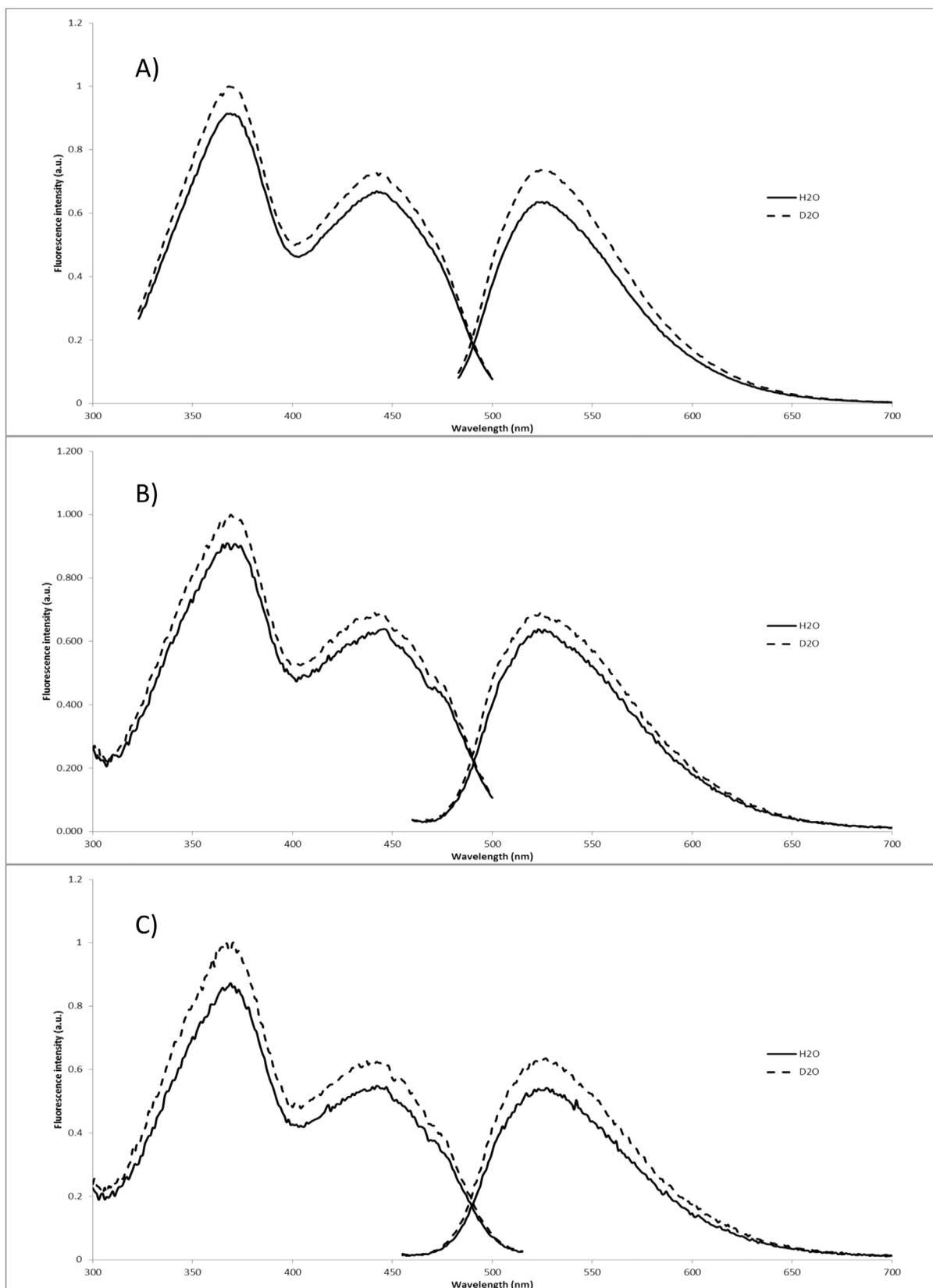
Fig. 3. Emission and excitation spectra of A) riboflavin, B) FMN, and C) FAD in H_2O and D_2O ($\lambda_{exc} = 445$ nm, $\lambda_{em} = 525$ nm, T = 293.15 K).

put in the H_2O/D_2O adjusted to pH $\geq$ 10, the fluorescence intensity did not differ as both −OH/−OD groups were ionized (data not shown).

In the case of the vitamin B_2 species, the ability of heavy water to enhance the fluorescence intensity and lifetime was observed at FAD and FMN only, a riboflavin molecule showed no overall increase in fluorescence intensity. Most likely, the size of the molecules needs to be
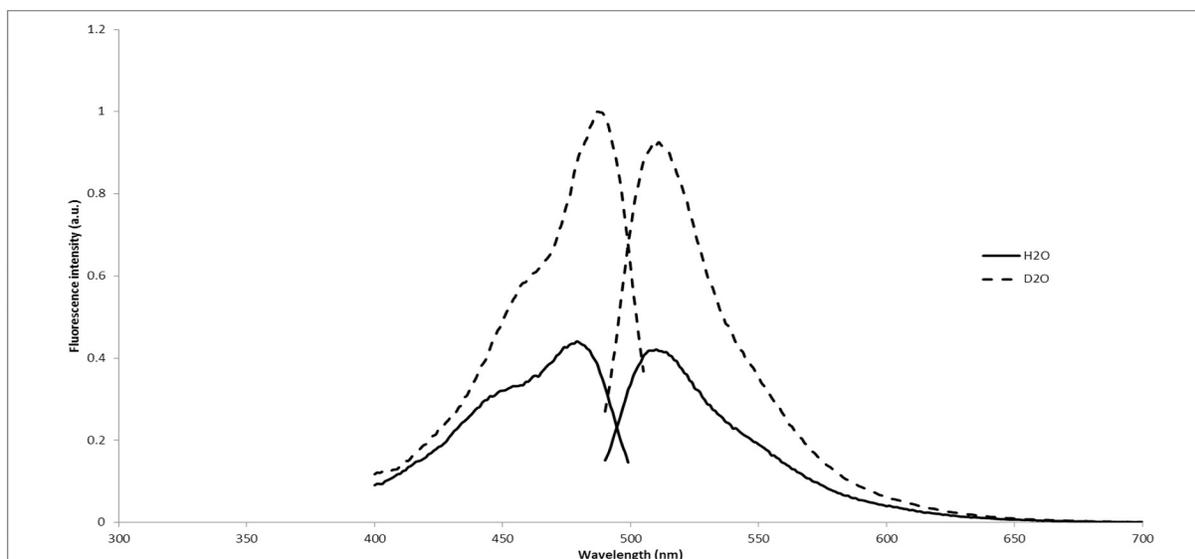
Fig. 4. Emission and excitation spectra of fluorescein in H_2O and D_2O (λ_{exc} = 480 nm, λ_{em} = 515 nm, T = 293.15 K).
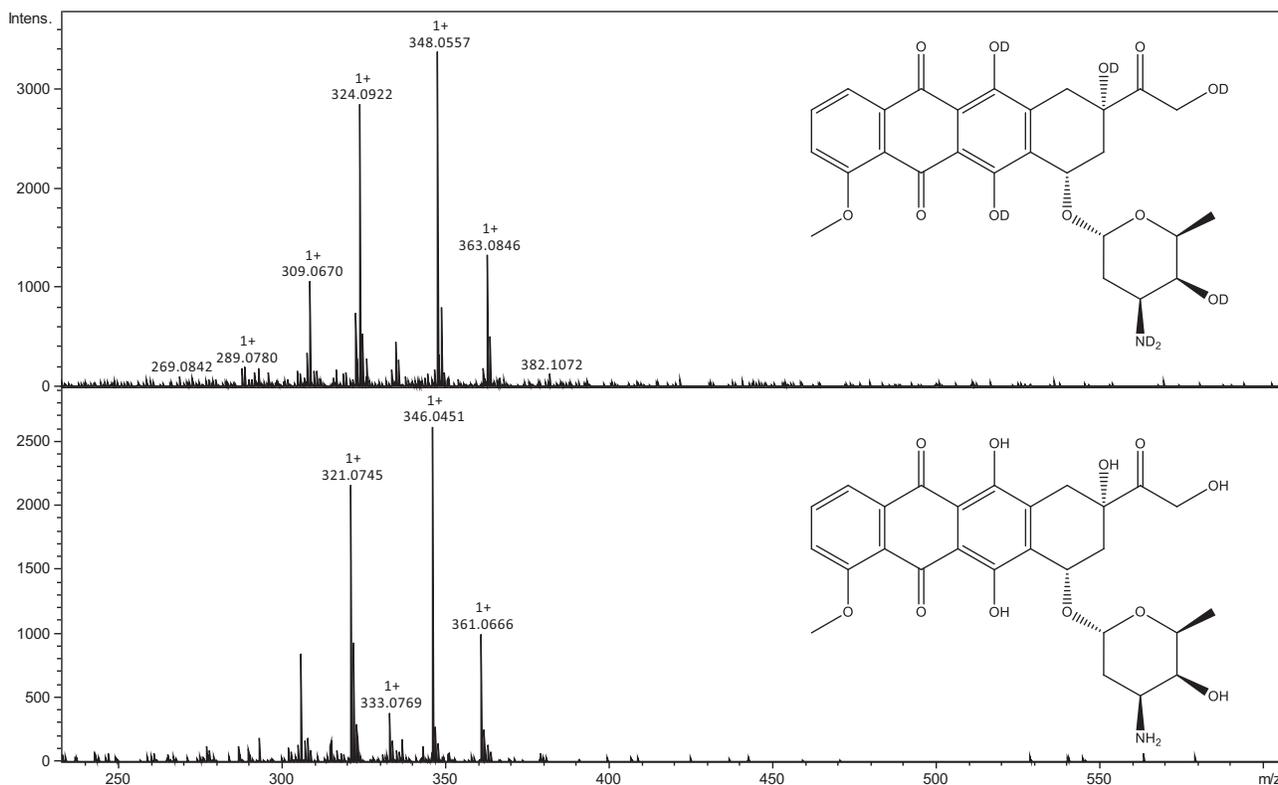
Fig. 5. MS/MS of doxorubicin ions $[M + H]^+$ (lower pane) and $[M + D]^+$ (upper pane). The difference between M is 7 Da.

taken into account, as well as the absence of −OH groups in a close proximity to the fluorophore. The effect of the =NH− to =ND− replacement may have contributed too. Nevertheless, the employment of heavy water enhanced the fluorescence intensity of FMN and FAD, when compared to doxorubicin, only by approximately 10%. Certainly, other conditions, such as pH or ionic strength need to be taken into account, as many molecules are known to be fluorescent in a specific, usually alkaline range of pH; outside this range, they are heavily quenched.

4. Conclusions

Replacement of light water in the mobile phase with heavy water was found a simple yet effective approach to enhance the sensitivity of selected fluorescent compounds. The increase of the fluorescence intensity, as well as the lifetime was affected by the presence of −OH/−OD groups in the nearest vicinity of the fluorophore. More molecules have to be studied in order to clarify the structure-to-enhancement relationship as there may be additional factors influencing the overall change in fluorescence.
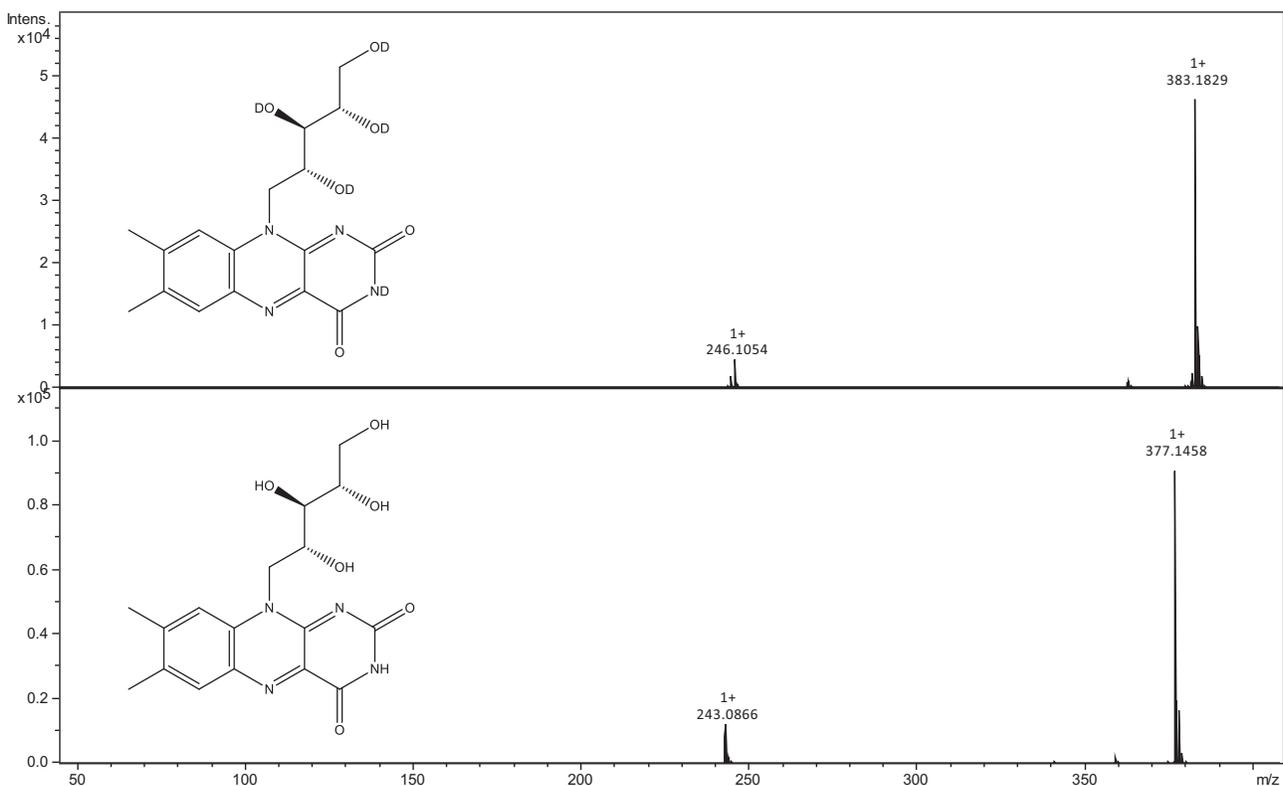
Fig. 6. MS/MS of riboflavin ions [M + H]$^+$ (lower pane) and [M + D]$^+$ (upper pane). The difference between M is 5 Da.
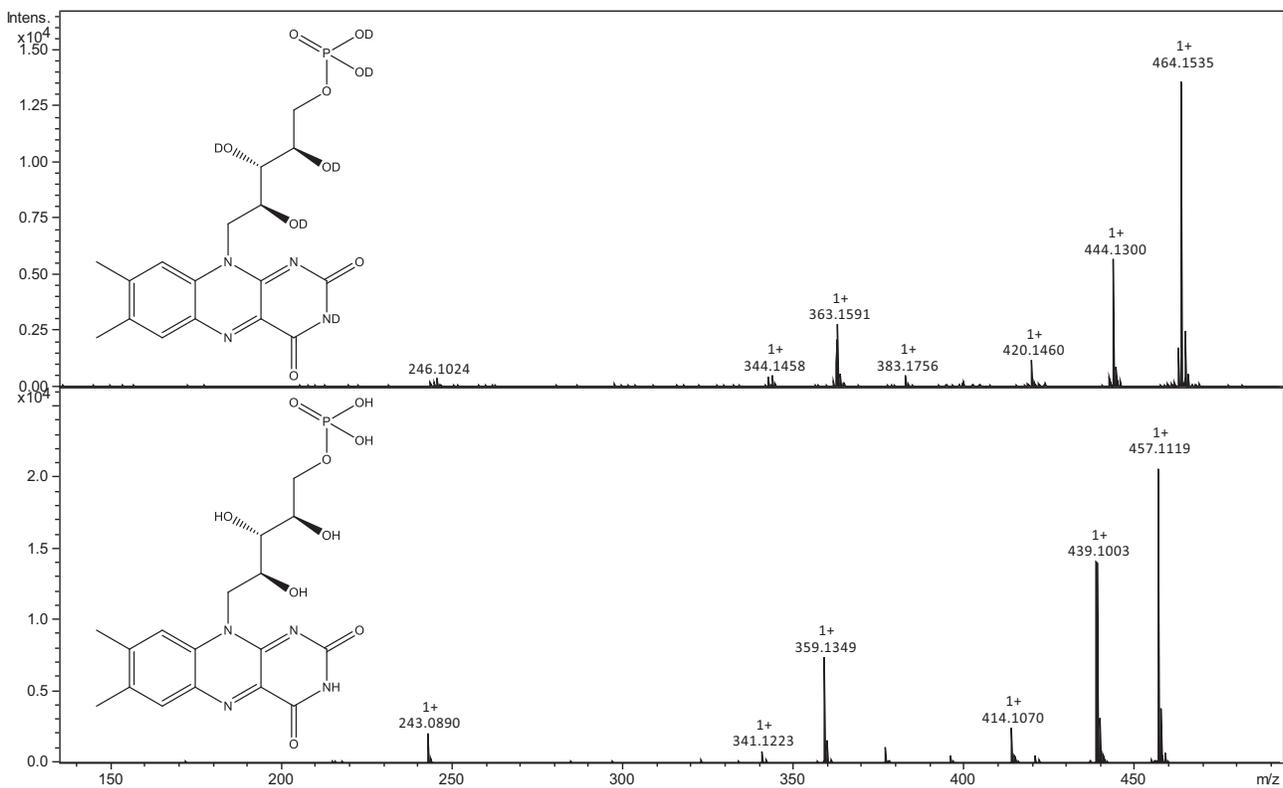
Fig. 7. MS/MS of FMN ions [M + H]$^+$ (lower pane) and [M + D]$^+$ (upper pane). The difference between M is 6 Da.
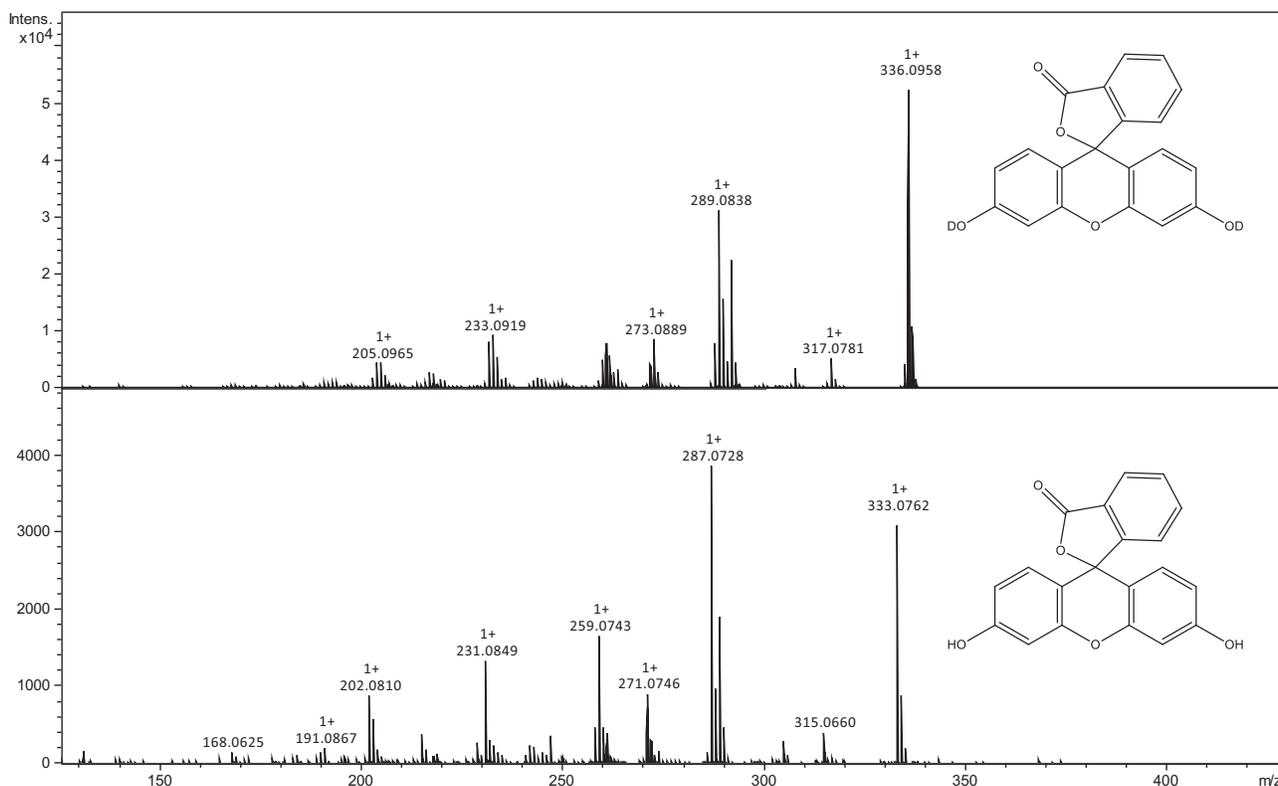
Fig. 8. MS/MS of fluorescein ions $[M + H]^+$ (lower pane) and $[M + D]^+$ (upper pane). The difference between M is 2 Da.

Acknowledgements

References

[1] S.F. Lee, Q. Verolet, A. Furstenberg, Improved super-resolution microscopy with Oxazine fluorophores in heavy water, Angew. Chem. Int. Ed. 52 (2013) 8948–8951.

[2] K. Klehs, C. Spahn, U. Endesfelder, S.F. Lee, A. Furstenberg, M. Heilemann, Increasing the brightness of cyanine fluorophores for single-molecule and super-resolution imaging, ChemPhysChem 15 (2014) 637–641.

[3] J. Olmsted, D.R. Kearns, Mechanism of ethidium-bromide fluorescence enhancement on binding to nucleic-acids, Biochemistry-Us 16 (1977) 3647–3654.

[4] M.L. Soriano, C. Carrillo-Carrion, C. Ruiz-Palomero, M. Valcarcel, Cyclodextrin-modified nanodiamond for the sensitive fluorometric determination of doxorubicin in urine based on its differential affinity towards beta/gamma-cyclodextrins, Microchim. Acta 185 (2018).

[5] J. Han, Z. Zhang, H.Y. Zhao, Y. Li, Z.L. Chen, Simultaneous determination of doxorubicin and its dipeptide prodrug in mice plasma by HPLC with fluorescence detection, J. Pharm. Anal. 6 (2016) 199–202.

[6] A.T. Lucas, S.K. O'Neal, C.M. Santos, T.F. White, W.C. Zamboni, A sensitive high performance liquid chromatography assay for the quantification of doxorubicin associated with DNA in tumor and tissues, J. Pharm. Biomed. 119 (2016) 122–129.

[7] Z.F. Xu, P.H. Deng, J.H. Li, L. Xu, S.P. Tang, Molecularly imprinted fluorescent probe based on FRET for selective and sensitive detection of doxorubicin, Mater. Sci. Eng. B-Adv. 218 (2017) 31–39.

[8] P. Moghaddam-Taaheri, A.J. Karlsson, Protein labeling in live cells for immunological applications, Bioconjug. Chem. 29 (2018) 680–685.

[9] S. Jiao, X.C. Wang, Y.H. Sun, L.J. Zhang, W.H. Sun, Y. Sun, X.H. Wang, P.Y. Ma, D.Q. Song, A novel fluorescein-coumarin-based fluorescent probe for fluoride ions and its applications in imaging of living cells and zebrafish in vivo, Sensors Actuators B Chem. 262 (2018) 188–194.

[10] Y.Y. He, L.J. Zhao, H.Y. Yuan, Z.M. Xu, Y. Tang, D. Xiao, M.M.F. Choi, HPLC with in-capillary optical fiber laser-induced fluorescence detection of picomolar amounts of amino acids by precolumn fluorescence derivatization with fluorescein isothiocyanate, Chromatographia 74 (2011) 541–547.

[11] M. Mashata, H. Chrystyn, B.J. Clark, K.H. Assi, Development and validation of HPLC method for the determination of tobramycin in urine samples post-inhalation using pre-column derivatisation with fluorescein isothiocyanate, J. Chromatogr. B 869 (2008) 59–66.

[12] X.N. Liu, J.J. Kang, H. Wang, T. Huang, C. Li, Construction of fluorescein

isothiocyanate-labeled MSNs/PEG/lycorine/antibody as drug carrier for targeting prostate cancer cells, J. Nanosci. Nanotechnol. 18 (2018) 4471–4477.

[13] Y. Jiao, X. Liu, L. Zhou, H.Y. He, P. Zhou, C.Y. Duan, X.J. Peng, A fluorescein derivative-based fluorescent sensor for selective recognition of copper(II) ions, J. Photochem. Photobiol., A 355 (2018) 67–71.

[14] Y. Tang, J. Zhang, L.M. Teng, Y.Y. He, D. Xiao, Rapid determination of vitamin B2 in foods by HPLC with in capillary optical Fiber laser-induced fluorescence detection technique, Asian J. Chem. 26 (2014) 4968–4970.

[15] C.C. Hardwick, T.R. Herivel, S.C. Hernandez, P.H. Ruane, R.P. Goodrich, Separation, identification and quantification of riboflavin and its photoproducts in blood products using high-performance liquid chromatography with fluorescence detection: a method to support pathogen reduction technology, Photochem. Photobiol. 80 (2004) 609–615.

[16] M.L. Privitera, V.A. Lozano, Development of a second-order standard addition fluorescence method for the direct determination of riboflavin in human urine samples without previous clean up and separation steps, Microchem. J. 133 (2017) 60–66.

[17] M. Voicescu, G. Neacsu, A. Beteringhe, O. Craciunescu, R. Tatia, L. Moldovan, Antioxidant and cytotoxic properties of riboflavin in PEG/BSA systems, Chem. Pap. 71 (2017) 1107–1117.

[18] M.M. Martin, L. Lindqvist, The pH dependence of fluorescein fluorescence, J. Lumin. 10 (1975) 381–390.

[19] R. Puryear, P. Macech, D. Austin, I. Yazawa, First silanol-free high pH silica-based C18 column, Lc Gc N Am. 36 (2018) 15.

[20] K. Jinno, Chromatographic performance of deuterated solvents in reversed phase micro high-performance liquid-chromatography, J. High Resolut. Chromatogr. 5 (1982) 364–367.

[21] N.C. van de Merbel, Quantitative determination of endogenous compounds in biological samples using chromatographic techniques, Trac-Trend Anal. Chem. 27 (2008) 924–933.

[22] T.M. Binz, U. Braun, M.R. Baumgartner, T. Kraemer, Development of an LC-MS/MS method for the determination of endogenous cortisol in hair using C-13(3)-labeled cortisol as surrogate analyte, J. Chromatogr. B 1033 (2016) 65–72.

[23] M. Jemal, A. Schuster, D.B. Whigan, Liquid chromatography/tandem mass spectrometry methods for quantitation of mevalonic acid in human plasma and urine: method validation, demonstration of using a surrogate analyte, and demonstration of unacceptable matrix effect in spite of use of a stable isotope analog internal standard, Rapid Commun. Mass Spectrom. 17 (2003) 1723–1734.

[24] A. Deroussent, M. Re, H. Hoellinger, E. Vanquelef, O. Duval, M. Sonnier, T. Cresteil, In vitro metabolism of ethoxidine by human CYP1A1 and rat microsomes: identification of metabolites by high-performance liquid chromatography combined with electrospray tandem mass spectrometry and accurate mass measurements by time-of-flight mass spectrometry, Rapid Commun. Mass Spectrom. 18 (2004) 474–482.

[25] W. Lam, R. Ramanathan, In electrospray ionization source hydrogen/deuterium exchange LC-MS and LC-MS/MS for characterization of metabolites, J. Am. Soc.

Mass Spectrom. 13 (2002) 345–353.

[26] A.E.F. Nassar, Online hydrogen-deuterium exchange and a tandem-quadrupole time-of-flight mass spectrometer coupled with liquid chromatography for metabolite identification in drug metabolism, J. Chromatogr. Sci. 41 (2003) 398–404.

[27] T.J. Novak, R. Helmy, I. Santos, Liquid chromatography-mass spectrometry using the hydrogen/deuterium exchange reaction as a tool for impurity identification in pharmaceutical process development, J. Chromatogr. B 825 (2005) 161–168.

[28] D.Q. Liu, C.E.C.A. Hop, Strategies for characterization of drug metabolites using liquid chromatography-tandem mass spectrometry in conjunction with chemical derivatization and on-line H/D exchange approaches, J. Pharm. Biomed. 37 (2005) 1–18.

[29] G.D. Chen, A. Khusid, I. Daaro, P. Irish, B.N. Pramanik, Structural identification of trace level enol tautomer impurity by on-line hydrogen/deuterium exchange HR-LC/MS in a LTQ-Orbitrap hybrid mass spectrometer, J. Mass Spectrom. 42 (2007) 967–970.

[30] R.M. Smith, O. Chienthavorn, I.D. Wilson, B. Wright, S.D. Taylor, Superheated heavy water as the eluent for HPLC-NMR and HPLC-NMR-MS of model drugs, Anal. Chem. 71 (1999) 4493–4497.

3.5 A study on bioluminescence and photoluminescence in the earthworm *Eisenia lucens*

Bioluminescence is explained by a chemical reaction of two substances – luciferin and luciferase. The luciferin molecule is typically a low-molecular weight substance, which is combined with a high-molecular weight compound (typically a protein molecule), oxidized, and the light is emitted. Several well-known luciferin-luciferase systems have been employed in chemiluminescence immunoassays.[53] Bioluminescent segmented earthworms (Annelida) have been reported predominantly from marine species; however, terrestrial bioluminescent species belonging to clitellates, *e.g.*, *Diplocardia longa*, *Microscolex phoshoreus*, or *Fridericia heliota* have been studied as well. *Eisenia lucens* (also known as *Eisenia submontana*) lives under wet bark in the central European region and its bioluminescent luciferin-luciferase system has yet not been studied in detail. Fluorescence spectroscopy, fluorescence lifetime microscopy (FLIM), and LC–MS with ESI and APCI were employed to uncover the culprit of the bioluminescence chemistry. Riboflavin was assumed to play a key role as it was found to be in high concentrations in these earthworms and was fluorescent. When the earthworm was irritated (mechanically, chemically, or electrically) it expelled bioluminescence coelomic fluid from its dorsal pores. The emitted blue-green light faded away after a few seconds, and the composition of the coelomic fluid was examined by several spectrometric techniques. An LC analysis with UV-Vis and MS detection confirmed the presence of riboflavin in the coelomic fluid at a concentration of 23 μM. Photoluminescence of *E. lucens* could be explained by the high content of riboflavin; however, bioluminescence exhibited a different emission maximum. Since FLIM revealed no other emitting species being present inside the eleocytes, the bioluminescent emitted light might have been mediated by riboflavin, but another luciferin molecule was likely involved. A few luciferin molecules from other species, *e.g.*, N-isovaleryl-3-aminopropanal, long-chain aldehydyc hydrogencarbons, or their oxidized products, have been sought inside the coelomic fluid by ESI and APCI LC–MS. Nonetheless, no particular evidence of a different luciferin molecule was found. Hence, the question about the common origin of the earthworm and bacterial bioluminescence, which is based on luminescence of a riboflavin derivative molecule FMN, was only suggested and left to be answered in future research.

Photochemical & Photobiological Sciences

COMMUNICATION

A study on bioluminescence and photoluminescence in the earthworm *Eisenia lucens*†

O. Pes,[a] A. Midlik,[a,b] J. Schlaghamersky,[c] M. Zitnan[d] and P. Taborsky*[b,e]

Eisenia lucens is an earthworm living in the organic soil layer of decomposing wood. When irritated, the worm expels coelomic fluid through pores in its body wall, exhibiting blue-green bioluminescence. The mechanism of the bioluminescence, which seems to be different from other bioluminescence systems of terrestrial animals, has been studied in this work. Many lines of evidence indicate that riboflavin stored in coelomycetes plays an important role in this glowing reaction.

Introduction

Bioluminescence has been reported from a considerable number of species of segmented worms (Annelida). Many belong to predominant marine polychaetes with several bioluminescent representatives of the taxon Clitellata, specifically of earthworms (Megadrili), from the families Lumbricidae and Megascolecidae, and of the related but substantially smaller potworms (Enchytraeidae).[1] Except for a few species of the megascolecid genus *Pontodrilus*,[2,3] all bioluminescent clitellates (at least 33 species) are terrestrial.[4] Bioluminescence in clitellates has been mostly studied in the earthworms *Diplocardia longa*,[5,6] *Microscolex phosphoreus*,[4] and the enchytraeid *Fridericia heliota*.[7–11] *Diplocardia longa*, which has been studied in detail by Wampler and colleagues,[5,6,12,13] expels a bioluminescent fluid from its pores with bioluminescence originating from discrete subcellular loci within free chloragogen cells sus-

pended in the coelomic fluid.[12] Wampler *et al.* proved that *N*-isovaleryl-3-aminopropanal was the luciferin molecule.[4,6] They also suggested that all bioluminescent earthworms used the *N*-isovaleryl-3-aminopropanal/hydrogen peroxide reaction, although they admitted that the colour of bioluminescence varied among species (from 490 nm to over 600 nm).[4] The Siberian potworm *Fridericia heliota* (Enchytraeidae) exhibits blue bioluminescence (maximum at 478 nm) with the light being emitted from epidermal cells. The bioluminescent system included a luciferin combined with CompX, lysine, GABA, and oxalate. Apart from that, the reaction required atmospheric oxygen, ATP, Mg^{2+} and *Fridericia* luciferase.[7–11,14]

Eisenia lucens (Waga, 1857) from Lumbricidae is an earthworm found in Central and Eastern Europe. Its bioluminescence has been firstly reported by the Polish scientist Antoni S. Waga in 1854, who described it and named it as *Lumbricus lucens*. Later, the species was re-discovered by F. Vejdovský and described as *Eisenia submontana*, which is now considered a junior synonym of *E. lucens*. The constitution and shape of an *Eisenia lucens* body is similar to other *Eisenia* species such as *Eisenia fetida* (erroneously given as *E. foetida*) and *Eisenia andrei*. Adults have 60–130 segments and reach 4.5–18 cm in length and 5–6.5 mm in width. The body coloration is conspicuous: each segment has a transverse band of red-brown to red-violet colour in its middle, whereas the parts towards the intersegmental grooves are of lighter yellowish to greyish colour (this colour also prevails ventrally). The prostomium is epilobic, the clitellum being saddle-shaped. Typical montane forest habitats are in the Carpathian arch but might also be found in other parts of Europe, west to northern Spain; completely missing in Northern Europe. The earthworm commonly lives under the bark and in wet decomposing wood of downed tree trunks and stumps, but has been reported in the organic soil, in particular under moist to wet conditions. The bioluminescence reaction might be inspected after a mechanical, chemical, or electrical irritation of the earthworm when the coelomic fluid is expelled from its dorsal pores. An attempt to describe the bioluminescence reaction of *E. lucens* was made in the work of Bačkovský *et al.* from 1939;

a Department of Biochemistry, Faculty of Medicine, Masaryk University, Kamenice 753/5, Brno, CZ 62500, Czech Republic

b Department of Chemistry, Faculty of Science, Masaryk University, Kamenice 753/5, Brno, CZ 62500, Czech Republic. E-mail: taborak@email.cz

c Department of Botany and Zoology, Faculty of Science, Masaryk University, Kamenice 753/5, Brno, CZ 62500, Czech Republic

d Material Research Centre, Faculty of Chemistry, Brno Technical University of Technology, Purkyňova 464/118, Brno, CZ 61200, Czech Republic

e Central European Institute of Technology (CEITEC), Masaryk University, Czech Republic, Kamenice 753/5, Brno, CZ 62500, Czech Republic

†Electronic supplementary information (ESI) available. See DOI: 10.1039/c5pp00412h

This journal is © The Royal Society of Chemistry and Owner Societies 2016

Photochem. Photobiol. Sci., 2016, **15**, 175–180 | 175

however, the authors studied merely the photoluminescence reaction by comparing the fluorescence spectra of riboflavin and *E. lucens* extract. Although they reported an increased amount of riboflavin in the earthworm, they did not examine the chemical form of the emitting species (riboflavin, FAD, FMN), and concluded that riboflavin acted as a luciferase.[15]

In this paper, we attempted to characterize the bioluminescence system using a combination of techniques such as fluorescence microscopy, fluorescence lifetime imaging (FLIM), luminescence spectrometry, and mass spectrometry (LC MS).

Materials and methods

Riboflavin, FMN, FAD, palmitic acid, *cis*-11-hexadecenal, spectroscopy ethanol, ammonium formate (LC MS), methanol (MeOH) (LC MS) and acetonitrile (ACN) (LC MS) were purchased from Sigma Aldrich (Czech Republic). Specimens of *Eisenia lucens* were collected in two areas within the Czech Republic: the Bohemian-Moravian Highlands (49°39′18.9″N 15°59′34.2″E) and the Moravian-Silesian Beskids (49°32′14.0″N 18°39′13.4″E). Earthworms were stored in plastic containers filled with decaying wood and soil at a constant temperature of 20 °C. Earthworms were chemically stimulated by 50% ethanol. The expelled fluid was collected, centrifuged, diluted 10 times with water and filtered through a 0.22 μm PTFE syringe filter.

Luminescence

All spectra (photoluminescence and bioluminescence) were measured on a spectroluminometer Aminco-Bowman Series 2 (Thermospectronic, USA), equipped with a Xe lamp (for excitation between 200 and 900 nm). An Olympus BX60 fluorescence microscope (blue light excitation) with a digital image analysis system (Stream Motion 1.9.2) was employed in the study of native photoluminescence. FLIM (Fluorescence LifeTime Imaging) measurements were done using the confocal microscope Leica TCS SP8 X, equipped with a tuneable pulse white laser. A pulse laser of 405 nm was used as an excitation source.

Mass spectrometry

The LC MS method was developed using a Dionex Ultimate 3000RS (Thermo Scientific, CA) module. Compound separation was achieved with a 3.0 × 100 mm, 2.6 μm Kinetex C18 (Phenomenex, CA) column equipped with a guard column at 23 °C, and a flow rate of 0.3 mL min^{-1}. The binary mobile phase system consisted of 0.1% ammonium formate (pH = 6.2) and MeOH or ACN. The injection volume was 10 μL. For separation of isoalloxazines (method A), MeOH was linearly increased from 15% to 75% over 20 min, kept constant at 75% over the next 2 min and followed by equilibration under the initial conditions for 3.0 min. For separation of fatty compounds (method B), ACN was held at initial 50% for 2 min and then linearly increased to 95% over 10 min, kept constant at 95% over the next 10 min and followed by equilibration under the initial conditions for 3.0 min. A complete LC run in each

method took 25 min. The isoalloxazine ring was detected by monitoring absorbance at 448 nm. The HPLC system was connected to a MicrOTOF-QII (Bruker, Germany) mass spectrometer operated in positive electrospray (ESI+) mode with method A, negative electrospray (ESI−) mode and positive atmospheric pressure chemical ionization (APCI+) mode with method B. The ionization conditions were set by the software according to the mode used; nebulizing and desolvation gas was nitrogen. ESI+: capillary voltage +4500 V, end plate offset −500 V, source temperature 250 °C, desolvation gas flow 5 L min^{-1}, nebulizer pressure 2 bar, and collision cell voltage 35 eV. ESI−: capillary voltage −4500 V, end plate offset +500 V, source temperature 250 °C, desolvation gas flow 5 L min^{-1}, nebulizer pressure 2 bar, and collision cell voltage 35 eV. APCI+: capillary voltage +4500 V, end plate offset −500 V, corona needle 4000 nA, source temperature 210 °C, vaporizer temperature 250 °C, desolvation gas flow 2 L min^{-1}, nebulizer pressure 1 bar, and collision cell voltage 35 eV. A base-peak chromatogram (BPC) was acquired in the MS mode by monitoring in a range of 50 to 2000 *m/z* with a spectra sample time of 1 s. Identification of target compounds relied on a combination of accurate *m/z*, isotopic pattern, MS/MS and retention behaviour. High-resolution MS and MS/MS spectra were first investigated to obtain the elemental formula of each compound. A compound was unambiguously identified if the fragmentation patterns of the unknown and the standard compound were identical. Due to the lack of fragmentation spectra of non-polar compounds obtained by method B, compounds were identified by comparing accurate *m/z* and retention time with those of a standard compound.

Results and discussion

After irradiation by violet or blue light, several parts of the earthworm bodies showed bright green photoluminescence (occasionally reported as autofluorescence). The main centres of photoluminescence emission were rows of bristles protruding through the body wall and granules inside eleocytes (Fig. 1). Eleocytes, a type of coelomocytes (cells floating in the coelomic fluid), are detached chloragocytes, *i.e.* cells that originally covered the outer wall of the intestine forming the chloragogen tissue. Similar fluorescent coelomocytes were observed also in other, non-bioluminescent species of earthworms *e.g.*, *E. fetida*.[16–18]

To obtain coelomic fluid a few earthworms were irritated with a 50% solution of ethanol on a glass plate. The expelled fluid, when collected and diluted by re-distilled water, showed two bands (370 and 440 nm) in the luminescence excitation and absorption spectra, which were typical for tricyclic isoalloxazine rings. If excited at 370 nm the sample emitted green fluorescence with a maximum at 523 nm. By comparing such spectra with those of biogenic isoalloxazines, riboflavin and its derivatives flavinadenindinucleotide (FAD) and flavinmononucleotide (FMN) were found as the best match. In order to identify which of the three compounds is the emitting species
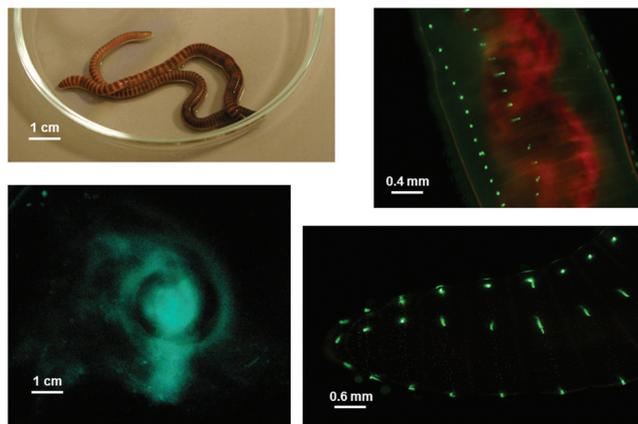
Fig. 1 Visualisation of the earthworm *Eisenia lucens* by photography – under daylight (upper-left) and in the dark after irritation (lower-left), and by fluorescence microscopy – native green photoluminescence of bristles (lower-right) and detached chloragocytes (upper-right). The red fluorescence originates inside the intestinal tract.

in the earthworm, an LC analysis with UV-Vis and MS detection was performed (Fig. 2). By comparing chromatograms of a standard mixture of riboflavin, FMN, and FAD with a coelomic fluid sample, we noticed that a single compound of riboflavin appears in the system. To confirm this, a peak (m/z 377.1612) at 9.4 min was subjected to MS/MS analysis and fragmentation to lumichrome (m/z 243.0977), as in pure riboflavin, was observed. This unambiguously confirmed the presence of riboflavin in the earthworm, however; there were no signs of FMN or FAD. Other peaks in the base peak chromatogram (BPC)
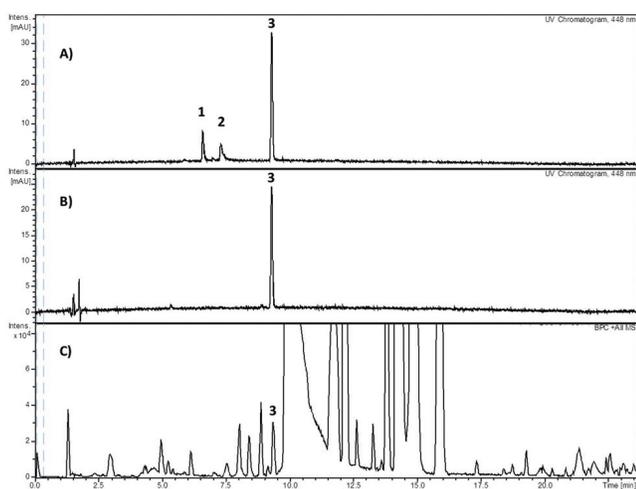
Fig. 2 LC with detection at 448 nm of (A) a model solution containing (1) FAD (6.6 min), (2) FMN (7.3 min), and (3) riboflavin (9.4 min), and the expelled coelomic fluid of *Eisenia lucens* detected (B) at 448 nm and (C) by MS of a base peak (BPC) in positive ESI mode. The injection volume was 10 μL and the concentration of each analyte was 3 μg mL^{-1} except for riboflavin (10 μg mL^{-1}). The retention time of riboflavin in BPC is slightly increased (~3.6 s) due to the sequential design of used detectors.

were not characterized in detail, nevertheless; they might be attributable to phospholipids, peptides and other low-molecular compounds commonly found in living organisms. UV-Vis detection with external standard calibration provided the content of riboflavin in the expelled coelomic fluid to equal a concentration of 23×10^{-6} mol l^{-1}.

Photoluminescence of *Eisenia lucens* can be assigned to the presence of such a high quantity of riboflavin. This essential vitamin plays a key role in the immune potency of animals including earthworms and its presence at high concentrations was described for other earthworms as well *e.g.*, the non-luminescent *E. andrei* and *E. fetida*.[19,20]

While the expelled coelomic fluid containing coelomocytes was of yellow colour in daylight, blue-green bioluminescence was observed when earthworms were irritated in the dark (see Fig. 1 and a video in the ESI†). When a freshly expelled portion of the coelomic fluid was subsequently placed into a cuvette and bioluminescent emission spectra were recorded, the emission maximum observed immediately after irritation was 493 nm, and the dependence of intensity at 493 nm on time was found to be exponential with a bioluminescence half-life of about 6 s (Fig. 3). The measured bioluminescence emission spectra of *Eisenia lucens* are clearly different from those obtained when excited by light. On the other hand, they are in a close match with the bioluminescence of bacteria from the genera *Photobacterium*, *Beneckea*, *Vibrio*, and *Xenorhabdus*.[21,22] Bacterial luminescence is generally based on a high molecular weight flavoprotein (luciferase) catalyzing the oxidation of FMNH$_2$ by oxygen in the presence of a long-chain aldehyde.[23] Emitted light maximum is ~495 nm, which indicates the FMN to be the emitting species. LC MS analysis confirmed that although the expelled coelomic fluid of *Eisenia lucens* did not contain any FMN/FAD, a precursor of FMN – riboflavin was present in great excess. This may indicate that the bioluminescence mechanisms of bacteria and *E. lucens* are similar (Fig. 3) except for riboflavin being the emitting species. We suggest that riboflavin is *in vivo* converted to the reduced,
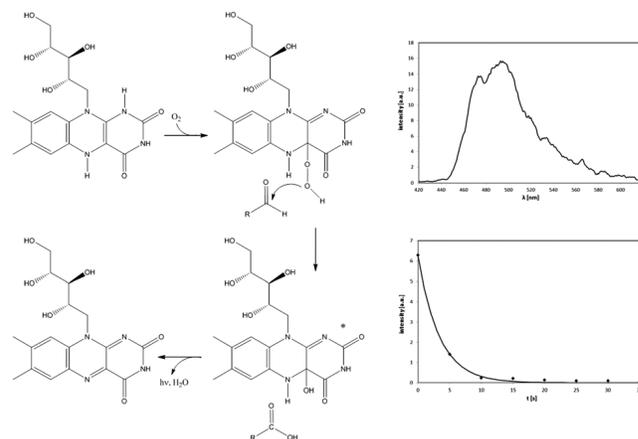
Fig. 3 A suggested mechanism of *Eisenia lucens* bioluminescence, maximum emission (493 nm) and bioluminescence half-life (6.2 s).

This journal is © The Royal Society of Chemistry and Owner Societies 2016

Photochem. Photobiol. Sci., 2016, **15**, 175–180 | **177**

highly-energetic, non-aromatic form by NAD(P)H as in the case of FAD to $FADH_2$ conversion in higher organisms. Such oxidation of flavines (including the oxidation of the reduced riboflavin), was simulated *in vitro* by several groups. Zeng *et al.* prepared an experiment where riboflavin was converted to the reduced form by Fe^{2+} ions in a pyrophosphate buffer.[24] Chemiluminescence with emission maximum at ~490 nm was induced by an addition of hydrogen peroxide. Similarly, Towner *et al.* demonstrated in their report (Towner, Technical manuscript, 1969) another experiment. Os(III) was used instead of Fe(II) to reduce riboflavin in a phosphate or borate buffer. All these experiments showed that the riboflavin chemiluminescence/bioluminescence reaction is plausible.

When the coelomic fluid was studied by fluorescence microscopy, it contained glowing granules inside the eleocytes, which were identified as the apparent source of bioluminescence (Fig. 4). FLIM revealed a uniform distribution of fluorescence lifetimes (~2 ns) along the entire cell strengthening the fact that riboflavin is the only emitting species in the earthworm. As a small organic molecule, its lifetime is accepted to be in units of nanoseconds. Prior to any bioluminescence, an oxidation step is required. Generally, two oxidation agents – oxygen and hydrogen peroxide are associated with a glowing reaction. A simple experiment confirmed that bioluminescence of *Eisenia lucens* is caused by atmospheric oxygen: a specimen, irritated under a N_2 atmosphere, was expelling coelomic fluid in the flask. The expelled fluid was not bioluminescent until the flask was opened and aerial oxygen was allowed for the reaction. By combining this observation with microscopy, we suggest that riboflavin molecules from the expelled eleocytes are oxidized by aerial oxygen.

The question whether any luciferin molecule was involved in the reaction mechanism was again pursued using LC MS. It is worth noting that the term "luciferin" has never been strictly defined. Originally, it meant an essential ingredient needed

for emission of bioluminescence. Now it seems appropriate to define it as the general term of an organic compound that exists in a luminous organism and provides the energy for light emission by being oxidized, normally in the presence of a specific luciferase.[21] We have included already known luciferin molecules, such as *N*-isovaleryl-3-aminopropanal suggested by Wampler in *Diplocardia longa* or long chain aldehydes (or related products of oxidation carboxylic acids) typical for luminous bacteria, in the search. Under conditions of analysis of isoalloxazines, there were no signs of *N*-isovaleryl-3-aminopropanal or fatty compounds being present. In order to bring attention towards more non-polar compounds, the elution strength of the mobile phase was increased and the MS was operated in negative ESI and positive APCI modes. This allowed for the detection of fatty acids or fatty aldehydes, respectively, and palmitic and palmitoleic acids as well as three isomers of hexadecenal were found. However, no structural data on the location or conformation of the double bond were acquired. While all these 16-C compounds may naturally be present in living organisms and are required for specific purposes (fuel, signalling, building blocks, *etc.*), they might also be involved in the *E. lucens* bioluminescence reaction as a potential luciferin molecule. Bioluminescence reactions are also catalysed by compounds called luciferase enzymes. Identification of the luciferase proteins is considered in further research.

The use and adaptive value of bioluminescence in earthworms are still not well understood. It is often mentioned that it might deter predators when earthworms are attacked.[25] Bioluminescence is possibly a part of a complex defence strategy of earthworms. We observed that after irritation, the earthworms attempted to change their position quickly by convulsive movements, leaving a glowing spot in the place of their previous position, which should keep the predator confused about the worm's true location. Similar strategies are used by some marine luminous organisms such as squids. Another approach to deflect predators is used by a few species of terrestrial earthworms *e.g.*, *Megascolides australis* that expel non-luminescent coelomic fluid, which is believed to be toxic or repellent.[25] The obvious resemblance of the bioluminescence mechanism of luminous bacteria and earthworms could indicate a similar origin of this ability. However, the adaptive value of bacterial bioluminescence has not yet been uncovered.

Conclusions

The present work reports about novel findings in photoluminescence and bioluminescence of the earthworm *Eisenia lucens*. As its body contains a vast amount of riboflavin, there is a high probability that among other functions in the organism, riboflavin stored in the eleocytes plays a key role in the bioluminescence of this species. We propose that the mechanism of bioluminescence in *E. lucens* is analogous to the mechanism described in bioluminescent bacteria except for the emitting species to be riboflavin molecules oxidized by atmos-
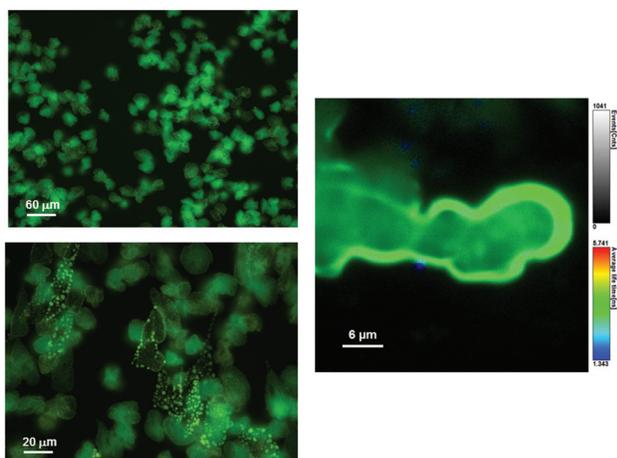

Fig. 4 *Eisenia lucens* coelomocytes (eleocytes) subjected to fluorescence microscopy (left) and FLIM (right) – green colour here represents a lifetime of about 2 ns.

178 | *Photochem. Photobiol. Sci.*, 2016, **15**, 175–180

This journal is © The Royal Society of Chemistry and Owner Societies 2016

pheric oxygen. The relationship is deepened by the existence of possible luciferins/oxoluciferins as derivatives of the 16-C aldehyde/carboxylic acid redox pairs.

Acknowledgements

References

1 O. Shimomura, Bioluminescence, *Photochem. Photobiol.*, 1983, **38**, 773–779.

2 B. G. M. Jamieson and J. E. Wampler, Bioluminescent Australian earthworms 2. taxonomy and preliminary-report of bioluminescence in the genera spenceriella, fletcherodrilus and pontodrilus (megascolecidae, oligochaeta), *Aust. J. Zool.*, 1979, **27**, 637–669.

3 J. E. Wampler and B. G. M. Jamieson, Cell bound bioluminescence from pontodrilus-bermudensis, and its similarities to other earthworm bioluminescence, *Comp. Biochem. Physiol., Part A: Mol. Integr. Physiol.*, 1986, **84**, 81–87.

4 J. E. Wampler, The bioluminescence system of microscolex-phosphoreus and its similarities to those of other bioluminescent earthworms (oligochaeta), *Comp. Biochem. Physiol., Part A: Mol. Integr. Physiol.*, 1982, **71**, 599–604.

5 H. Ohtsuka, N. G. Rudie and J. E. Wampler, Structural identification and synthesis of luciferin from bioluminescent earthworm, diplocardia-longa, *Biochemistry*, 1976, **15**, 1001–1004.

6 N. G. Rudie, H. Ohtsuka and J. E. Wampler, Purification and properties of luciferin from bioluminescent earthworm, diplocardia-longa, *Photochem. Photobiol.*, 1976, **23**, 71–73.

7 S. M. Marques, V. N. Petushkov, N. S. Rodionova and J. C. G. Esteves da Silva, LC-MS and microscale NMR analysis of luciferin-related compounds from the bioluminescent earthworm Fridericia heliota, *J. Photochem. Photobiol., B*, 2011, **102**, 218–223.

8 V. Petushkov, M. Dubinnyi, A. Tsarkova, N. Rodionova, M. Baranov, O. Shimomura and I. Yampolsky, A novel ATP-dependent bioluminescent system from the Siberian earthworm Fridericia heliota: structure elucidation of luciferin and its analogs, *Luminescence*, 2014, **29**, 54–55.

9 V. N. Petushkov, M. A. Dubinnyi, A. S. Tsarkova, N. S. Rodionova, M. S. Baranov, V. S. Kublitski, O. Shimomura and I. V. Yampolsky, A Novel Type of Luciferin from the Siberian Luminous Earthworm Fridericia heliota: Structure Elucidation by Spectral Studies and Total Synthesis, *Angew. Chem., Int. Ed.*, 2014, **53**, 5566–5568.

10 V. N. Petushkov, M. A. Dubinnyi, N. S. Rodionova, K. D. Nadezhdin, S. M. Marques, J. C. G. Esteves da Silva, O. Shimomura and I. V. Yampolsky, AsLn2, a luciferin-related modified tripeptide from the bioluminescent earthworm Fridericia heliota, *Tetrahedron Lett.*, 2014, **55**, 463–465.

11 V. N. Petushkov, A. S. Tsarkova, M. A. Dubinnyi, N. S. Rodionova, S. M. Marques, J. C. G. Esteves da Silva, O. Shimomura and I. V. Yampolsky, CompX, a luciferin-related tyrosine derivative from the bioluminescent earthworm Fridericia heliota. Structure elucidation and total synthesis, *Tetrahedron Lett.*, 2014, **55**, 460–462.

12 N. G. Rudie and J. E. Wampler, Earthworm bioluminescence - characterization of luminescent cell from diplocardia-longa, *Comp. Biochem. Physiol., Part A: Mol. Integr. Physiol.*, 1978, **59**, 1–8.

13 N. G. Rudie, M. G. Mulkerrin and J. E. Wampler, Earthworm bioluminescence - characterization of high specific activity diplocardia-longa luciferase and the reaction it catalyzes, *Biochemistry*, 1981, **20**, 344–350.

14 R. Bellisar and M. J. Cormier, Peroxide-linked bioluminescence catalyzed by a copper-containing, non-heme luciferase isolated from a bioluminescent earthworm, *Biochem. Biophys. Res. Commun.*, 1971, **43**, 800–805.

15 J. M. Bačkovský, J. Komárek and K. Wenig, Attempt to explain the mechanism of luminescence in Vejdovský's earthworm., *Věstník ČS. Zoologické Společnosti v Praze*, 1939, **7**, 1–10.

16 R. B. Heredia, S. Duenas, L. Castillo, J. J. Ventura, M. Silva Briano, F. Posadas del Rio and M. G. Rodriguez, Autofluorescence as a tool to study mucus secretion in Eisenia foetida, *Comp. Biochem. Physiol., Part A: Mol. Integr. Physiol.*, 2008, **151**, 407–414.

17 A. I. Mazur, M. Klimek, A. J. Morgan and B. Plytycz, Riboflavin storage in earthworm chloragocytes and chloragocyte-derived eleocytes and its putative role as chemoattractant for immunocompetent cells, *Pedobiologia*, 2011, **54**, S37–S42.

18 B. Plytycz and A. J. Morgan, Riboflavin storage in earthworm chloragocytes/eleocytes in an eco-immunology perspective, *Invertebr. Survival J.*, 2011, **8**, 199–209.

19 P. Sulik, M. Klimek, P. Talik, J. Kruk, A. J. Morgan and B. Plytycz, Searching for external sources of the riboflavin stored in earthworm eleocytes, *Invertebr. Survival J.*, 2012, **9**, 169–177.

20 A. Rorat, N. Kachamakova-Trojanowska, A. Jozkowicz, J. Kruk, C. Cocquerelle, F. Vandenbulcke, M. Santocki and B. Plytycz, Coelomocyte- Derived Fluorescence and DNA Markers of Composting Earthworm Species, *J. Exp. Zool., Part A*, 2014, **321**, 28–40.

This journal is © The Royal Society of Chemistry and Owner Societies 2016

Photochem. Photobiol. Sci., 2016, **15**, 175–180 | 179

21 O. Shimomura, *Bioluminescence: Chemical Principles and Methods*, World Scientific, 2006.

22 S. C. Tu and H. I. X. Mager, Biochemistry of bacterial bioluminescence, *Photochem. Photobiol.*, 1995, **62**, 615–624.

23 A. A. Green and W. D. McElroy, Bacterial luciferase, *Methods Enzymol.*, 1955, **2**, 857–861.

24 J. Zeng and R. A. Jewsbury, Chemiluminescence of flavins in the presence of Fe(II), *J. Photochem. Photobiol., A*, 1995, **91**, 117–120.

25 E. Rota, Lights on the ground: A historical survey of light production in the Oligochaeta, in *Bioluminescence in Focus – A Collection of Illuminating Essays*, ed. V. B. Meyer-Rochow, Research Signpost, India, 2009, pp. 105–138.

4 Mass spectrometry as a sensitive and selective detector

Although triple quadrupole (QqQ) mass analyzers may sometimes be called "just" detectors, they are very specific and sensitive at the same time. The ability to tune several compound-specific fragmentation patterns, accounting for a constant difference in mass (x-axis) and, at the same time, a constant intensity ratio (y-axis) of target fragments, results in invaluable hyphenation options with separation techniques. Manufactured QqQ mass analyzers share the vast majority of the worldwide market in analysis of low molecular (< 3000 Da) compounds. In an overstating way, it may be said that QqQ mass analyzers are rarely used in other modes of operation beyond selective reaction monitoring (SRM). As any compound could be detected in concentrations as low as the signal-to-noise ratio allows, the option to selectively decrease the noise is entirely valid and perfectly approachable by including two ion filtration steps in the first and the third quadrupole. Quantitation guidelines using SRM recommend including one transition (usually the most intensive) for quantitation and an additional one for confirmation of the target compound's identity. If the intensity ratio of the chosen transitions does not equal that of the authentic standards, the identity of the target compound cannot be assured. Approximately 3,000 to 4,000 QqQ instruments per year are installed worldwide, making them readily available and reducing the cost per sample. There are many clinical applications of LC–MS, and the reasons for choosing LC–MS over LC with conventional detectors are high specificity, high sensitivity and the ability to employ isotopically labeled internal standards.[54,55] It is worth noting that other types of analytical instruments that rely on chemical or spectrometric detection cannot profit from isotopically labeled compounds.

Quantitative determination in MS is usually assessed by one of the following calibration models:

- *An authentic analyte without a sample matrix*

It is a classical example of an external calibration curve using an analyte in calibration solutions differing in composition from the authentic matrix used in samples. Sometimes it may provide reliable results in terms of validation, *e.g.*, for urine or saliva specimen.

- *An authentic analyte in a surrogate matrix*

The surrogate matrix is intentionally selected to mimic the authentic matrix yet containing no analyte. Such design restricts the model for determining exogenous compounds not found in the sample matrix. The calibration samples could be prepared in an analyte-free matrix such as animal, or human blank matrices. This approach is commonplace across a majority of LC–MS analyses nowadays.

- *A surrogate analyte in an authentic matrix*

The analyte requires to be distinguishable in a different domain than chemistry. Stable isotopes are chemically non-distinguishable but differ in physical properties such as mass. Generally, isotopic analogs involving stable isotopes but deuterium are preferable as the extreme ratio of size to mass in hydrogen/deuterium negatively impacts their chemical properties, such as retention times.[56]

- *An authentic analyte in an authentic matrix*

The most demanding and practically inconvenient approach restricts the calibration model to the addition of the

standard prior to or during the analysis. It immensely increases the number of analyses required to be performed to obtain a reliable result from each sample.

Absolute MS responses are generally not used as they are subject to significant day-to-day variation because of a lot of difficult-to-control factors influencing the absolute MS response, *e.g.*, the cleanliness of ion source and ion optics, collision cell pressure, the MS vacuum, or ion suppression. Ion suppression may be defined as a simultaneous presence of more than one component in the ion source resulting in compounds competing during the ionization process for a charge. The charge is always finite and redistributed to the competing species based on their concentrations and their tendencies to ionize in the gaseous phase.[57] Buffers and other mobile phase additives are also sources of ion suppression (matrix effects). Although matrix effects cannot be avoided entirely, they can be minimized or compensated for by optimizing sample preparation procedures, manipulating LC and MS conditions, and using internal standards. One of the requirements for internal standard calibration is that the internal standard and the analyte behave similarly during the entire analytical process including sample extraction and cleanup steps. Isotopically labeled analogs of the analyte behave in all ways identically to the analyte except for the molecular weight being shifted to higher mass-to-charge ratios. Synthesizing isotopically labeled chemicals can be expensive and time-consuming; however, employing such internal standards circumvents many problems, and testing is more rapid with significantly lower costs per test and fewer reanalyses. To avoid the natural occurrence of analyte isotopes interfering with the labeled internal standard, the mass difference between the analyte and the corresponding isotopically labeled analog should be at least 3 Da.[58] Under certain circumstances, deuterated analogs do not co-elute with their native analytes and cause inaccuracies in quantification. The deuterium isotope effect induces this phenomenon due to a slight change in lipophilicity, and other, more expensive ^{13}C-, ^{15}N- or ^{17}O-labeled analogs are considered more appropriate. Any validation procedure should assess the matrix effects by either postextraction or postcolumn infusion strategies.[59–61] Should the slopes of calibration curves obtained with and without matrix differ, the matrix effects are present.

The process of quantifying and data collection inevitably leads to classification, prediction, and attempting to quantify and understand the uncertainty inherent in phenomena underlying data – statistical modeling. Even calculation of a mean value can be considered a statistical model. Such a model should optimally enable distinguishing between noise and a true effect for generalization from the sample to the population. However, for more than a decade, academic research has been mired in a "replication crisis," in which the findings of thousands of published studies have proven to be difficult if not impossible to reproduce. One of the reasons is definitely the tendency of journals to prioritize papers that have surprising results, or that upset conventional wisdom. In other words, the publication bias could prompt even well-intentioned researchers to engage in parsing data until statistically significant (and therefore publishable) results come up. A term of *p*-hacking encompasses factors influencing the statistical significance by manipulating *p* values (intentionally or not) *e.g.*, by altering the sample size, removing outlying results, or multiple testing without any corrections. Because *p* values are a frequency probability, if enough *p* values are calculated, then one is bound to be statistically significant.[62] And all statistically significant findings tend to overestimate the size of effects.[63]

Null hypothesis significance testing (NHST) in its hybrid form, considered the golden standard in biological, medical,

social, or economical science, can be viewed as a collective work of Ronald Fisher, Jerzy Neyman, Egon Pearson, and Everet Franklin Lindquist.[64–66]

Basically, there are two major flaws in NHST.

- *Null hypothesis*

Null hypotheses rarely can be true. Just about every treatment one might consider will have some effect, and no comparisons or regression coefficient of interest will be exactly zero.[67] It is then meaningless to formulate and test null hypotheses that we know ahead of time cannot be true. With sufficient sample size, any hypothesis can be rejected, and there is no real point in gathering a mountain of data just to reject a hypothesis that we did not believe in the first place.[63] Next, the research questions used to construct null and alternative hypotheses require to be falsifiable while the null hypothesis is only the complement of the alternative hypothesis and contradicts the researchers' expectations. In other words, as NHST dichotomizes any question to reject/fail to reject, null hypotheses are formulated only to be disproved.

- *The p value*

If the null hypothesis is true in the population, what is the probability of encountering a space of outcomes that are as extreme as (or more extreme than) the actually observed outcome? Such probability is called a p value, and could be viewed as a conditional probability of observing the current data given a true null hypothesis: $\Pr(\text{Data}|\text{H}_0 = \text{True})$. The space of all possible outcomes under the true null hypothesis is however based on the intentions how the data will be collected.[68] Although p values are helpful in assessing how incompatible the data are with a specified statistical model, contextual factors must also be considered, such as the design of a study, the quality of the measurements, the external evidence for the phenomenon under study, and the validity of assumptions that underlie the data analysis. The p values do not say anything about the effect size, the probability of replicating the result, or if the result is of major theoretical, clinical or practical importance. Thus not all p values are equal and equal p values may be interpreted very differently. For instance, a p value of 0.01 from a small underpowered study is more likely to be a false positive that the same p value from a large, well-powered study.

The p value is often misunderstood as being the probability that the null hypothesis is true given the observed data: $\Pr(\text{H}_0 = \text{True}|\text{Data})$.[69] To turn p values into such probabilities requires Bayes' theorem and is therefore not defined in classical (frequentist) statistics. In other words, the probability that the null hypothesis is true given the data depends indeed on the p value, but also on the power of the study to detect an effect and the prior probability that the null hypothesis is true. For instance, the performance of a diagnostic test depends on its sensitivity, specificity, disease prevalence, and positive predictive value. Test sensitivity is equivalent to statistical power. Test specificity is equivalent to the p value. Disease prevalence in the population being tested is equivalent to the prior that the null hypothesis is false. What the clinician wants to know is the probability that the subject has the disease given the test is positive. This is the positive predictive value and, in hypothesis testing, is equivalent to the probability that the alternative hypothesis is true given the data.[70] If a p value is determining whether a particular null value of a parameter can be rejected, the confidence interval (CI) provides a range of parameter values not being rejected. Particularly, the 95% CI consists of all parameter values that would not be rejected by a two-tailed significance

test that allows 5% false alarms (type I errors). Since CIs are defined by p values, for every misconception of p values, there can be a corresponding misconception of CIs.[68] Such a common misconception is that CI represents some sort of probability distribution over the parameter values. No, the 95% CI consists of merely two end points covering (approximately) two standard errors (SE) from both sides of the parameter mean value. For a treatment effect to be statistically significant, the CI cannot include zero. A CI that contains zero is uncertain whether there is a treatment effect. In noisy studies when SE is large, a high effect requires to be observed for achieving the desirable level of significance. Unrealistically high effects are then published and the same inherent problem of attempting to do inference based only on sample probability for the data commits Bernoulli's Fallacy.[71] The way out of this trap could be more and more accumulated evidence within subjective confines of the assumptions we make about the world, *i.e.*, criteria for publication should be determined not on the statistical significance of the findings but on the extent to which those findings can move existing beliefs and shape new policies – the culprit of Bayesian statistics.

Bayesian statistics is named after Thomas Bayes (1702–1761), a British Presbyterian minister and amateur mathematician who was interested in the notion of inverse probability, now referred to as posterior probability.[72,73] Bayes' rule was independently discovered by Pierre-Simon Laplace in 1774 who actually used the rule in practice.[74] Over the next forty years he developed it into the form we use today.[75] Bayesian inference could be seen as a principled incremental process of scientific discovery encoded in the generic expression of Bayes theorem formally given as

$$Pr(A|B) = \frac{Pr(B|A) \cdot Pr(A)}{Pr(B)}$$

where A, B are the specified events represented by conditional Pr(A|B), Pr(B|A) and unconditional Pr(A), Pr(B) probabilities.[76] In contrast to frequentist statistics, where parameters are treated as unknown constants, Bayesian statistics is distinguished by a broad view of probability, *i.e.*, parameters are treated as random variables with specified prior distributions that reflect prior knowledge about the parameters before the observation of data. Bayes' theorem can then be reformulated using a single parameter model consisting of a continuous response y, and a parameter θ.

$$p(\theta|y) = \frac{p(y|\theta) \cdot p(\theta)}{\int p(y|\theta) \cdot p(\theta) \, d\theta}$$

The denominator term is called the total or marginal probability of data and acts as a normalizing constant for the posterior probability to lie within the unit interval. As statistical models grow parametrically larger the analytical solution for the denominator begins to be impossible to compute, and it needs to be estimated numerically – usually by some form of Markov chain Monte Carlo (MCMC) simulation. Hence, drawing inferences from data is represented by the posterior distribution $p(\theta|y)$, which is proportional to the product of the likelihood $p(y|\theta)$ of data and the prior $p(\theta)$ information.

$$p(\theta|y) \propto p(y|\theta) \cdot p(\theta)$$

Such diachronic inference can generally be described by the following procedure:

1. Encode the initial beliefs (expert knowledge, previous results, similar studies performed, base rate, *etc.*) in the form of a prior distribution.

2. Collect data via experimentation, observation, querying, *etc.*

3. Update the beliefs using Bayes' theorem to the posterior distribution, which can be seen as a weighted compromise between the prior and the observed data.

4. Repeat the entire process as more data become available.

Statistical modeling based on Bayesian inference has the ability to propagate uncertainty through the joint posterior distribution of parameters conditioned on the data. A Bayesian credible interval says where the true parameter value likely is (a frequentist confidence interval says where the true parameter value likely is not). A diachronic nature of Bayesian updating enables to change hypotheses over time as new data become available – today's posterior can be used as tomorrow's prior. Robust models originating from relaxing the assumptions are straightforwardly specified using full Bayesian generative approach, *e.g.*, instead of testing, transforming, or removing outlying data points, it is easier to keep them all but use for example Student's t-distribution with finite variance (degrees of freedom $\nu > 2$) to increase the likelihood that central tendency estimators are compatible with the observed data including outliers. Any model may be easily generalized, any assumptions might be relaxed (heterogeneity, overdispersion, inflation, normality, *etc.*), and any of the shape or scale distribution parameters might be conditioned on data in the same fashion as the central tendency parameters. Bayesian models are able to test multiple hypotheses without increasing the false alarm rate, or can even answer questions that cannot be answered using NHST, *e.g.*, what is the probability that the coefficient is zero under the null hypothesis? The process of learning inside a human brain is based on Bayesian updating – credibility is reallocated across plausible events in everyday reasoning.[77]

The former diagnostic test could now be formulated more intuitively using Bayes' theorem.

$$Pr(Disease|Test^+) = \frac{Pr(Test^+|Disease) \cdot Pr(Disease)}{Pr(Test^+)}$$

where $Pr(Test^+)$ is the average probability of a positive test result given as

$$Pr(Test^+) = Pr(Test^+|Disease) \cdot Pr(Disease) + Pr(Test^+|Healthy) \cdot (1 - Pr(Disease))$$

The important message here is the counterintuitive result obtained in rare events, *e.g.*, in diseases with low prevalence. If the prevalence (prior probability) is extremely low ($< 1\%$) then even very high diagnostic sensitivity and specificity ($> 99\%$) will not dramatically raise the conditional probability of having the disease given being tested positive (positive predicted value) because a great number of subjects would have been tested as false positives. Based on that, any scientific inference could be framed in the following terms: (1) A hypothesis is either true or false; (2) a statistical procedure is used to get an imperfect cue of the hypothesis' falsity; (3) Bayes' theorem should be used to logically deduce the impact of the cue on the status of the hypothesis. The third term is hardly ever done.[78] Suppose the probability of positive finding when a hypothesis is true, is $Pr(Significant \mid True) = 0.95$. This is sensitivity

or statistical power of the test. Suppose that the probability of a positive finding, when a hypothesis is false, is Pr(Significant | False) = 0.05. That is the false positive rate or 1 - Specificity, and it represents the 5% level (p value = 0.05) of conventional significance testing. Finally, the base rate (the prior probability) at which hypotheses are true could be given as 1 in every 100 hypotheses turns out to be true (Pr(True) = 0.01). The real value is unknown, but the history of science suggests it is small. To compute the posterior, the appropriate values are plugged in Bayes' theorem:

$$\text{Pr(True | Significant)} = \frac{0.95 \cdot 0.01}{0.95 \cdot 0.01 + 0.05 \cdot 0.99}$$

$$\text{Pr(True | Significant)} \approx 0.16$$

So a significant finding corresponds to a 16% chance that the hypothesis is true. Even if the false positive rate goes down to 1% (Specificity = 99%) the posterior probability (positive predicted value) reaches ~ 0.5, which is as good as a coin toss. The most important thing is to improve the base rate (the prior probability Pr(True)), and that requires thinking, not testing.[79] For example, if the same hypothesis was independently studied with the same statistical power (95%) and a false alarm rate (5%), the base rate (the prior probability) could be specified as the former posterior probability Pr(True) ~ 0.16. In that case, the second significant finding would result in the new ~ 78% chance that the hypothesis was true, which is in concordance with the diachronic inference *i.e.*, the initial beliefs are being updated by incremental knowledge.

4.1 Determination of lansoprazole, 5-hydroxylansoprazole, and lansoprazole sulfone in human plasma for CYP2C19 and CYP3A4 phenotyping

LC–MS is an ideal tool for metabolite prediction, detection, identification, and quantitation in phenotyping studies. Typically, the administered parent compound is metabolized to major and minor metabolites at a given rate, which is essentially dependent on the activity of the cytochrome P450 (CYP) system – the subject's phenotype. It has shown advantageous to determine the CYP activity before drug administration to adjust the pharmacotherapy accordingly. The CYP metabolic activity is assessed by a specific substrate selectively biotransformed by distinct CYP isoenzymes. The reaction rate or the metabolic ratio could then determine the metabolic phenotype. Lansoprazole (LAN) is used as a proton pump inhibitor in duodenal ulcers, reflux esophagitis, Zollinger-Ellison syndrome, *H. pylori* eradication, and gastroesophageal reflux disease in patients requiring therapy. Metabolites of LAN, 5-hydroxylansoprazole (OHL) and lansoprazole sulfone (LS) were determined by LC–UV and LC–MS to assess the CYP2C19 and CYP3A4 metabolic activity. Although LC–MS provided low LOD, the linear dynamic range was insufficient to quantify the parent compound (LAN) for the metabolic ratio assessment. Combining both detection techniques can provide overlap in linear dynamic ranges of both methods and thus increase the reliability of the entire determination. In conclusion, CYP2C19 and CYP3A4 phenotyping using combined LC–UV and LC–MS allowed reliable identification of poor metabolizers of either CYP isoform.

KOSTOLANSKA, Katarina, Ondrej PES, Ondrej ZENDULKA, Jan MACHAL and Jan JURICA. Determination

of lansoprazole, 5-hydroxylansoprazole, and lansoprazole sulfone in human plasma for CYP2C19 and CYP3A4 phenotyping. Chemical Papers. 2019, 73(12), 2955–2963. ISSN 2585-7290. doi:10.1007/s11696-019-00682-4 Document Type: Article, IF = 1.680; JCR Category + Category Quartile: CHEMISTRY, MULTIDISCIPLINARY Q3; AIS = 0.222

Author's contribution: 20 %

ORIGINAL PAPER

CrossMark

Determination of lansoprazole, 5-hydroxylansoprazole, and lansoprazole sulfone in human plasma for CYP2C19 and CYP3A4 phenotyping

Katarína Kostolanská[1] · Ondřej Peš[1] · Ondřej Zendulka[2] · Jan Máchal[3] · Jan Juřica[2,4,5]

Abstract

A simple and sensitive liquid chromatography method with absorbance or mass spectrometry detection was developed and validated for the determination of lansoprazole, lansoprazole sulfone, and 5-hydroxylansorpazole in human serum with omeprazole as an internal standard. Analytes were, after an extraction step with a mixture of isopropyl alcohol: dichloromethane (2:8, v/v), separated in a gradient elution (acetonitrile: 20 mM ammonium formate) and detected at 280 and 300 nm or by monitoring selective reactions in a triple quadrupole mass analyzer. The limits of detection were, for all analytes, below 2 ng/mL and 3 pg/mL in the LC UV and LC MS method, respectively. The combined linear dynamic range exceeded 5 orders of magnitude. The method was successfully applied in the assessment of CYP2C19 and CYP3A4 metabolic phenotypes in ST-elevated myocardial infarction patients receiving novel anticoagulant treatment.

Keywords Cytochrome P450 · Phenotype · Lansoprazole · 5-Hydroxylansoprazole · Lansoprazole sulfone · Liquid chromatography · Mass spectrometry · Metabolites

Introduction

Cytochromes P450 (CYP) plays a pivot role in the metabolism of most clinically used drugs and affects effective drug concentrations in plasma. In some drugs, it is useful

✉ Jan Juřica
jurica@med.muni.cz

[1] Department of Biochemistry, Faculty of Medicine, Masaryk University, Kamenice 5, 62500 Brno, Czech Republic

[2] Department of Pharmacology, Faculty of Medicine, Masaryk University, Kamenice 5, 62500 Brno, Czech Republic

[3] Department of Pathological Physiology, Faculty of Medicine, Masaryk University, Kamenice 5, 62500 Brno, Czech Republic

[4] Department of Human Pharmacology and Toxicology, University of Veterinary and Pharmaceutical Sciences Brno, Palackeho tr. 1946/1, 61242 Brno, Czech Republic

[5] Department of Biochemistry, Faculty of Science, Masaryk University, Kamenice 5, 62500 Brno, Czech Republic

to assess the CYP metabolic activity prior to or during the pharmacotherapy to adjust the individual dosage according to the patient's phenotype. To determine the CYP metabolic activity, a specific substrate, also known as a marker of metabolic activity, which is metabolized selectively by a distinct CYP isoenzyme, is used. The velocity of the reaction or the ratio of the substrate to its metabolite concentrations in plasma (metabolic ratio, MR) is then defining the metabolic phenotype. (Fuhr and Rost 1994; Turjap et al. 2016). With regard to the phenotype (or MR), metabolizers can be classified as up to 4 different classes—poor metabolizers (PM), intermediate metabolizers (IM), extensive metabolizers (EM) and ultrarapid metabolizers (Zanger et al. 2004). Poor metabolizers are prone to drug overdose, toxicity and adverse drug reactions of CYP substrates and thus, knowledge of metabolic phenotype is useful for the drugs with low therapeutic index. Lansoprazole (LAN) belongs to proton pump inhibitors used in the treatment of duodenal ulcers, reflux esophagitis, Zollinger–Ellison syndrome, *H. pylori* eradication, gastroesophageal reflux disease, or nonsteroidal antiinflammatory drugs-associated benign ulcers in patients requiring therapy (MHRA 2017). It is administered at the dose of 15 or 30 mg orally as a racemic mixture of *R*- and *S*-isomers. LAN is rapidly absorbed from

the gastrointestinal tract after oral administration, reaching maximal plasma concentrations in 1.7 h. The therapeutic effect is observed within 1–3 h after oral dosing with the bioavailability of about 80%. LAN is extensively (97%) bound on plasma proteins (Dynamed American Society of Health System Pharmacists 2018). Due to the irreversible inhibition of H^+/K^+ ATPase in the parietal cells, the effect persists for 2–4 days. Lansoprazole is metabolized via CYP3A4 and CYP2C19 enzymes. CYP2C19 is responsible for low-capacity but highly selective hydroxylation and CYP3A4 for high-capacity sulfoxidation. The velocity of both reactions is greater from its S-enantiomer than from R-enantiomer (Kim et al. 2003). There have been some mentions to use LAN as a measure of CYP2C19 (Gumus et al. 2012; Sohn et al. 1997; Xu et al. 2010; Zhang et al. 2011) and CYP3A4 (Yanagida et al. 2009) metabolic activity, although no clear MR cutoff value for distinguishing extensive and poor metabolizers of CYP2C19 or CYP3A4 was established. However, poor metabolizers had significantly higher molar ratio of LAN to 5-hydroxylansoprazole (OHL) than extensive metabolizers (Gumus et al. 2012) and, based on in vitro data, LAN was also suggested as a probe substrate for CYP3A4 phenotyping.(Yanagida et al. 2009).

Essentially, LAN may be administered for determination of both CYP2C19 and CYP3A4 metabolic activity in a single, low dose. To distinguish between a poor and extensive metabolizer, a visual inspection of MR histograms, probit plot analysis, or receiver operator characteristics analysis is performed (Jackson et al. 1989; Swar et al. 2016). Omeprazole (OME) is used as CYP-specific probe for CYP2C19 phenotyping as a single probe substrate as well as a part of several "cocktail" approaches for phenotyping CYP enzymes. For this purpose, several different cocktails of markers have been used (Asimus et al. 2007; Dierks et al. 2001; Sharma et al. 2004). Due to a variety of clinical reasons, LAN is preferred over OME in many countries and therefore, LAN may be a useful alternative for CYP phenotyping without the necessity to use another drug probe substrate.

The aim of this work was to develop a simple and sensitive method for the determination of LAN, lansoprazole sulfone (LS) and OHL using absorbance or mass spectrometry (MS) detection. The validated method was then applied to real plasma samples of ST-elevated myocardial infarction (STEMI) patients receiving medication metabolized via CYP2C19 or CYP3A4.

LAN can be determined by a variety of analytical methods including chromatography, capillary electrophoresis, or polarography (Dogrukol-Ak et al. 2001; Elkady et al. 2018; Chung et al. 2017; Nassar et al. 2017; Uno et al. 2005b; Yeniceli et al. 2004). Most of the methods deal with the determination of LAN or impurities in pharmacy products, such as capsules and tablets (Belal et al. 2004; Dogrukol-Ak

et al. 2001; Chung et al. 2017; Nassar et al. 2017; Yeniceli et al. 2004). MS detection has been used to report LAN in biological fluids (Bharathi et al. 2009; Elkady et al. 2018; Ganesh et al. 2011; Luo et al. 2018; Oliveira et al. 2003; Song et al. 2009; Sun et al. 2015; Wang et al. 2015; Wu et al. 2008; Zhang et al. 2014). Some LC–UV methods for the determination of solely LAN were also published (Yang et al. 2011). (Bharathi et al. 2009). However, a few publications are detecting LAN and its CYP-specific metabolites simultaneously (Aoki et al. 1991; Gumus et al. 2012; Song et al. 2008; Uno et al. 2005b).

While LC UV methods have a limit of quantification (LOQ) in the range of 2–10 ng/mL for all analytes (Aoki et al. 1991; Gumus et al. 2012; Landes et al. 1992; Uno et al. 2005a; Yanagida et al. 2009), which does not have to be sufficient to evaluate a poor metabolizer profile, high-sensitive LC MS methods usually suffer from a shifted working range, which does not have to cover the levels of the drug and its metabolites in a single, preferably linear, calibration curve.

A simple LC method employing either an absorbance or MS detector might be used to provide reliable levels of LAN and its metabolites over a broad dynamic range originating from the overlap of dynamic ranges of both detection techniques. It is a common situation in clinical practice when a drug administered at rather high doses (~ 1–100 mg) is metabolized to rather low-concentration products demanding more sensitive methods to quantify them reliably. However, the plasma level of the drug itself is usually extrapolated, estimated, or even ignored, as it was found outside the calibration range, or suffered from the detector saturation. The aim of the presented approach is to simultaneously determine plasma concentrations of LAN, LS, and OHL in a very broad range of analyte concentrations. Another step towards convenient determination of CYP2C19 and CYP3A4 metabolic activity from a single dose of LAN would be to arrange both detectors in a series.

Experimental

Chemicals

LAN, OHL, LS and internal standard OME were purchased from Santa Cruz Biotechnology (Dallas, Texas, USA). Acetonitrile (ACN), methanol (MeOH), acetic acid, sodium hydroxide, and ammonium hydroxide were purchased from Sigma-Aldrich (Prague, Czech Republic). Isopropanol and dichloromethane were purchased from Merck (Darmstadt, Germany). All reagents used were of an analytical grade except for methanol and acetonitrile, which were of an LC MS grade. All water used was of an ultra-pure grade supplied by an in-house Milli-Q system (Millipore, MA, USA).

Standard stock solutions, calibration standards, and quality controls

LAN, LS, OHL, and OME were dissolved in ACN to prepare stock solutions (2.20, 1.30, 1.20, and 2.20 mg/mL, respectively). The stock solutions were stored at − 80 °C. Working standard solutions were made by diluting the stock solutions with water–acetonitrile (1:1, v/v). A working internal standard solution was prepared at a final concentration of 3.0 µg/mL for LC UV and 150 ng/mL for LC MS method. The calibration standards (Table 1) were prepared by spiking pooled blank human plasma obtained from 8 healthy volunteers. The serum was verified to be free of LAN, LS, and OHL by using LC MS.

Quality control (QC) samples for both LC UV and LC MS were prepared in three levels (low, medium, and high) and are given in Table 1. The final concentration of OME was 300 ng/mL in the LC UV method and 15.0 ng/mL in the LC MS method.

LC UV

The liquid chromatographic system Dionex UltiMate 3000RS (Thermo Fisher Scientific, CA, USA) equipped with a binary high-pressure gradient pump, an autosampler, a heated column compartment, and a DAD detector was employed in the LC–UV method. Data from the detector were collected and analyzed using Chromeleon™ 6.8 software (Thermo Fisher Scientific, CA, USA). An Ascentis Express C18 reversed-phase chromatographic column (100 × 3.0 mm I.D.; 2.7 µm) with Ascentis® Express C18 (5 mm × 3 mm; 2.7 µm) security guard (both Sigma-Aldrich, Czech Republic) were used for the gradient separation. The mobile phase consisted of (A) 20 mM acetic acid adjusted to pH 4.5 with 25% ammonium hydroxide solution and (B) acetonitrile. The LC UV initial composition of 75% A and 25% B was linearly increased to 60% A and 40% B over the next 6 min. It was held for 1.5 min, followed by equilibration under the initial conditions for another 2.5 min. The flow rate was 0.6 mL/min and the column was operated at 40 ± 0.1 °C. The absorbance of the eluent was monitored at 300 nm (OHL, OME) and 280 nm (LAN, LS).

LC MS

The LC MS method was developed using a Dionex Ultimate 3000RS (ThermoScientific, CA, USA) module, equipped with a binary high-pressure gradient pump, an autosampler, and a column oven. The same column, pre-column, and mobile phase were used as in the LC UV method.

The LC MS initial composition of 80% A and 20% B was linearly increased to 80% A and 20% B over the next 6 min. It was held for 0.5 min, followed by equilibration under the initial conditions for another 1.5 min. The flow rate was 0.6 mL/min and the column was operated at 23 ± 0.1 °C. The parameters were slightly modified to lower the retention times as the MS detection usually does not demand chromatographically resolved peaks all the time.

A Bruker EVOQ Qube triple quadrupole mass spectrometer (Germany) operated in the positive heated electrospray ionization mode was used in LC MS. The parameters of operation were set as the following: Spray voltage + 4000 V, cone temperature 350 °C, cone gas flow 20 psi, heated probe temperature 300 °C, probe gas flow 40 psi (nitrogen), and nebulizer gas flow 45 psi (nitrogen). Argon was used as collision gas. All other parameters were set at default values provided by the manufacturer. The flow from LC was diverted to waste in the range of 0–2 min and 5.5–8 min. Target compounds were scanned in the selected reaction monitoring mode (SRM) as fragments of $[M + H]^+$ ions: LAN 370.1–252.0 (8 eV) and 370.1–119.1 (13 eV); LS 386.1–119.1 (26 eV) and 386.1–322.1 (18 eV); OHL 386.1–251.9 (10 eV) and 386.1–135.0 (26 eV); OME 346.0–198.0 (8 eV) and 346.0–151.1 (19 eV). Dwell time for each transition was 50 ms.

Patients' samples

Real plasma samples were obtained from 101 STEMI patients treated by percutaneous coronary intervention and subsequently with novel anticoagulants prasugrel or ticagrelor; both have been ascertained as CYP2C19 and/or CYP3A4 substrates. The patients received the dose of 30 mg of lansoprazole and the blood samples were drawn 3 h after the administration. The study was approved by the

Table 1 Concentration levels of the calibration standards for the LC UV and LC MS method

Level		1	2	3	4	5	6
QC		Low		Medium			High
LC UV (ng/mL)	OHL	34.4	68.8	138	275	550	1100
	LAN	68.8	138	275	550	1100	2200
	LS	40.6	81.3	163	325	650	1300
LC MS (pg/mL)	OHL	22.0	55.0	550	1100	2200	11,000
	LAN	22.0	55.0	550	1100	2200	11,000
	LS	26.0	65.0	650	1300	2600	13,000

local Ethical committee (an Ethical committee of St. Anne's faculty hospital).

Sample preparation

Aliquots (250 µL) of human blank plasma sample or spiked human plasma were transferred into a screw-capped glass tubes. 25 µL of the internal standard solution, 50 µL of 0.1 M NaOH and 5 mL of extraction mixture (isopropanol:dichloromethane 2:8, v/v) were added and the tubes were vortexed 10 min at 2000 rpm at the horizontal vortex and centrifuged for 5 min at 4000 g at room temperature. 4 mL of organic layer was decanted into conical glass centrifuge tubes and the aqueous phase discarded. The organic phase in the conical tube was evaporated at 36 °C under a gentle stream of nitrogen. The residues, after evaporation, were redissolved in either 250 µL (LC UV) or 1000 µL (LC MS) of 20% ACN and 20 µL (LC UV) or 10 µL (LC MS) was injected onto an analytical column.

Method validation

The method was validated for its selectivity, linearity, limit of detection, limit of quantitation, accuracy, precision, matrix effects, extraction recovery, and stability according to the principles of the relevant Food and Drug Administration guidance (FDA 2018).

LOD, LOQ, and linearity

Calibration curves were constructed using six non-zero levels. Calibration standards were prepared by spiking 250 µL blank plasma with 12.5–25 µL of standard stock solutions to prepare calibration standards as indicated in Table 1. The analyte to internal standard peak area ratios was plotted against the corresponding concentrations. The calibration curve was estimated by the least-squares regression procedure. LOD and LOQ were determined for each analyte by analyzing the lowest calibration point of calibration and calculating a theoretical signal–noise ratio of 3:1 for LOD and 10:1 for LOQ. The values were verified by measuring samples containing each analyte using the calculated concentrations.

Accuracy and precision

To determine the intra- and inter-day precision and accuracy of the assay, five replicates of each analyte in blank plasma at three concentration levels (low, medium, high) within the calibration range were analyzed for five consecutive days. Precision was calculated as intra- and inter-day relative standard deviation (RSD) values and accuracy was expressed

as a mean relative error [(measured concentration − nominal concentration) × 100/(nominal concentration)].

Matrix effect and extraction recovery

Matrix effect was measured by comparing the calculated concentrations of LAN, LS, and OHL in spiked plasma samples after extraction (A) to the spiked solvent at the same concentration (B) (Matrix effect $= A/B \times 100$). Recovery was measured by comparing the calculated concentrations of LAN, LS, and OHL from spiked plasma samples before extraction (C) to concentrations obtained when spiked after extraction (D) (Recovery $= C/D \times 100$). Five replicates at low, medium, and high concentration levels were used for both parameters.

Stability of extracted samples

The stability of the samples extracted at low, medium, and high concentration levels samples reconstituted in 20% ACN was evaluated by LC UV as a percentage of the zero-day concentration after 7 days of storing at 4 °C in the dark. The stability of the dried extracts was evaluated by preparation of seven replicates at the same concentration levels, which were reconstituted directly before an LC UV analysis.

Results and discussion

LC UV

A representative LC UV chromatogram can be seen in Fig. 1. Peaks were chromatographically resolved ($R > 2$) with retention times under 7 min. Base peak widths were about 0.2 min. The LC UV method, despite its simplicity, can be straightforwardly applied to determine a ratio of a concentration of LAN metabolites over that of LAN. When the concentration of metabolites was below of LOQ, the LC MS method was employed.

LC MS

Representative LC MS chromatograms are shown in Fig. 2. Generally, the LC MS method was used in cases when the OHL and LS concentrations were not approachable by LC UV. On the other hand, LC UV was used to determine the LAN concentration in most cases as the LC MS dynamic range could not have covered the levels in the vast majority of real samples. As both methods were spatially and temporally uncoupled, slightly different conditions could have been applied. Since MS usually does not require the peaks to be chromatographically resolved, a modification of the

Fig. 1 LC UV chromatograms of a blank plasma sample spiked with OHL (2.9 min; 68.8 ng/mL), LAN (5.1 min; 138 ng/mL), LS (5.9 min; 81.3 ng/mL), and IS OME (3.4 min; 150 ng/mL). Detection at 302 nm (OHL, OME—solid line) and 282 nm (LAN, LS—dashed line) were used in calculations
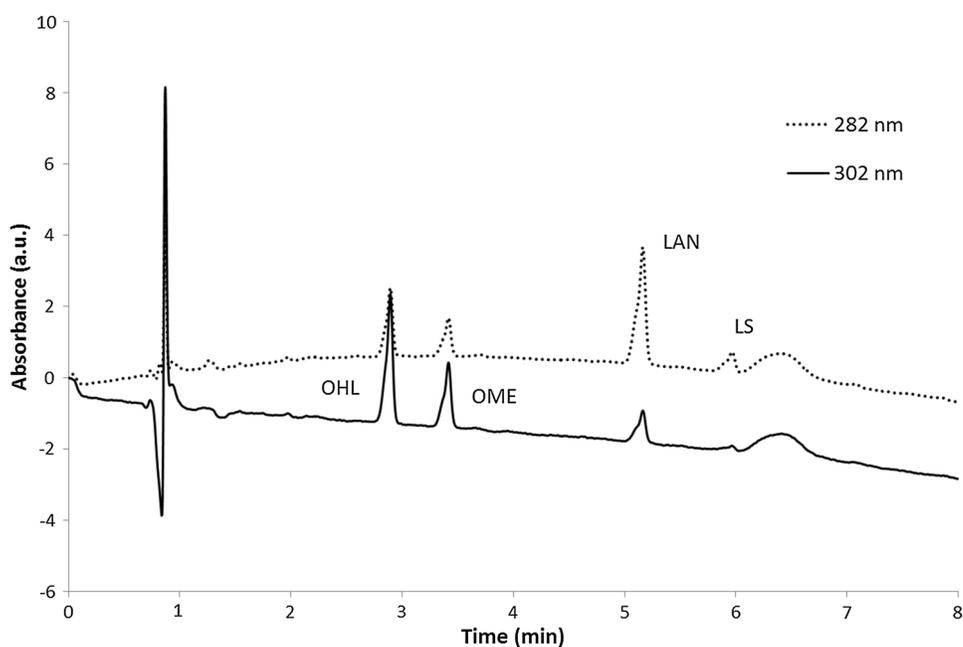
separation gradient and temperature was done to favor faster retention times with base peak widths of around 0.1 min.

LOD, LOQ, and linearity

The calibration curve in the LC UV method was linear in the employed calibration range of each analyte. The coefficient of determination (R^2) was higher than 0.999 for all three analytes.

The LC MS method operated primarily in a range of sub-ng/mL concentrations and was linear in the range of 22–11,000 pg/mL with $R^2 > 0.989$. The LOD and LOQ obtained by the LC UV method were 0.85 and 2.8 ng/mL for OHL, 1.5 and 5.0 ng/mL for LAN, and 1.7 and 5.8 ng/mL for LS, respectively. These were comparable with formerly published LC UV methods. The LC MS provided LOD and LOQ to be 1.2 and 4.1 pg/mL for OHL, 0.73 and 2.5 pg/mL for LAN, and 2.2 and 7.1 pg/ml for LS, respectively, which allowed to phenotype of poor metabolizers. To the best of our knowledge, no sub-ng/mL detection limits have been published to date for any of the compounds.

Accuracy and precision

The intra- and inter-day variations for the measured analytes in the LC UV method were lower than 4.23% and 14.6%, respectively. The LC MS method provided intra- and inter-day variations lower than 7.82% and 14.2%, respectively (Tables 2, 3). A series of five replicates with concentrations overlapping dynamic ranges of both methods was calculated using both calibration curves to verify the unbiased accuracy (data not shown).

Matrix effect and extraction recovery

Extraction recovery was calculated using the LC UV method only and the results for all analytes are summarized in Table 4. The matrix effect was calculated only by the LC MS method and was not observed ($\geq 75\%$ and $\leq 125\%$; Table 4).

Stability of extracted samples

A substantial change ($> 20\%$) in the concentration of all analytes was verified by LC UV three days after extraction and reconstitution when stored at 4 °C in dark (Table 5). Since all compounds showed poor stability, it was not continued to obtain a 7-day profile. Instead, the dried sample extracts, when stored at 4 °C in dark and reconstituted prior to the N-th day analysis, were evaluated in the same manner. No significant change ($< 15\%$) in the concentration of the analytes was observed during the consecutive 7 days (Table 5). Although it involved a combined error originating from the preparation of replicates, it allowed for bulk processing of a great number of patient samples without the necessity to analyze them immediately after extraction.

Experimental data obtained from the experimental samples

The LC UV and LC MS methods were successfully applied in the evaluation of CYP2C19 and CYP3A4 metabolic phenotype of 101 ST-elevated myocardial infarction patients receiving novel anticoagulant treatment (Table 6). The patients were phenotyped with the use of a single dose lansoprazole (30 mg) and 3-h-postdose levels of LAN,
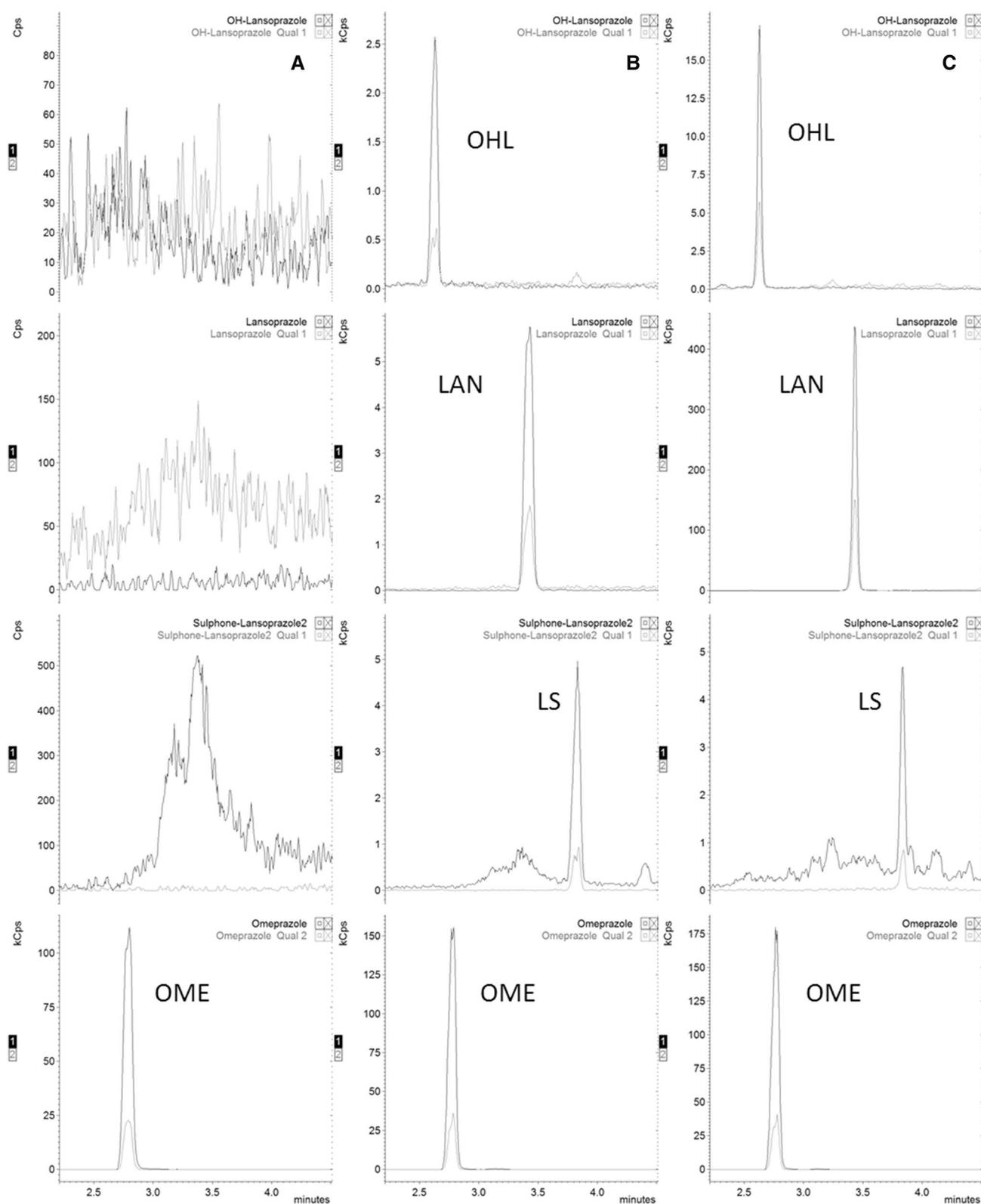
Fig. 2 LC MS chromatograms of **a** a blank plasma sample, **b** a blank plasma sample spiked with OHL (22 pg/mL), LAN (22 pg/mL), and LS (26 pg/mL), and **c** a real plasma sample from a poor metabolizer. Two SRM transitions for OHL ($t_R = 2.6$ min), LAN ($t_R = 3.4$ min), LS ($t_R = 3.8$ min), and IS OME ($t_R = 2.7$ min) are represented by the top to bottom frames, respectively

Table 2 Intra- and inter-day accuracy and precision of the LC UV method

	Nominal concentration (ng/mL)	Intra-day ($N=5$)		Inter-day ($N=5$)	
		Accuracy (%)	Precision RSD (%)	Accuracy (%)	Precision RSD (%)
OHL	1100	0.89	0.102	− 5.08	14.6
	138	3.40	0.821	− 5.44	6.71
	34.4	13.8	3.22	3.35	7.92
LAN	2200	1.50	0.121	− 7.73	7.37
	275	6.17	1.18	− 5.94	10.9
	68.8	23.1	3.40	16.2	5.19
LS	1300	0.587	0.0989	2.82	6.93
	163	3.86	1.22	6.37	7.40
	40.6	8.35	4.23	− 0.831	9.00

Table 3 Intra- and inter-day precision and accuracy of the LC MS method

	Nominal concentration (pg/mL)	Intra-day ($N=5$)		Inter-day ($N=5$)	
		Accuracy (%)	Precision RSD (%)	Accuracy (%)	Precision RSD (%)
OHL	11,000	1.21	5.43	− 3.71	8.43
	550	− 2.31	5.30	7.13	8.30
	5.50	4.30	2.83	− 12.7	11.8
LAN	11,000	− 2.50	2.33	− 8.45	8.88
	550	4.34	3.17	7.59	11.0
	5.50	− 6.24	6.56	− 5.98	14.2
LS	13,000	1.78	4.55	4.65	10.9
	650	11.9	7.82	− 6.37	9.50
	6.50	− 13.5	6.88	15.7	10.1

Table 4 Extraction recovery and matrix effect ($N=5$)

	OHL	LAN	LS		OHL	LAN	LS
Recovery (%)				RSD (%)			
Low	95.6	97.6	99.9	Low	13.7	11.7	10.9
Medium	88.3	89.8	92.1	Medium	11.8	9.93	10.3
High	82.2	87.0	88.5	High	9.02	12.8	9.65
Matrix effect (%)				RSD (%)			
Low	115	104	118	Low	9.89	4.27	12.3
Medium	111	96.7	98.2	Medium	11.2	10.3	7.65
High	104	95.9	117	High	14.0	9.81	8.88

OHL and LS were determined. 12 out of 101 patients had levels of LS lower than 3 ng/mL, which are below the LOQ of the LC UV method and thus, these samples were subjected to the LC MS analysis. On the other hand, 76 out of 101 patients had levels of LAN greater than 100 ng/mL, which are greater than the highest point of calibration in the LC–MS method. Thus, poor metabolizers need to be phenotypized with the use of LC–MS method and majority of the samples should be measured with LC–UV method, so as to avoid imprecision at higher concentrations of LAN

by LC–MS method. The combination of methods is useful for the whole spectrum of metabolizers.

In the real patient samples, a clear cut-off in the histogram distribution of the LAN/LS molar concentration ratio was observed (a gap in the continuous distribution between 20 and 23). Ten subjects had LAN/LS greater than 23 and were, thus, suspected as poor metabolizers of CYP3A4. Accordingly, another two patients were suspected as poor metabolizers of CYP2C19 due to a clear cut-off observed in the histogram of LAN/OHL molar concentration ratio; a

Table 5 Percentage of the zero-day concentration of OHL, LAN, and LS at low, medium, and high concentration levels determined by LC UV when reconstituted and stored at 4 °C in the dark, and when stored at 4 °C in dark and reconstituted prior to the N-th day injection (numbers in parentheses)

		Day 1	Day 2	Day 3	Day 4	Day 5	Day 6	Day 7
Low	OHL	98.7 (100)	69.0 (103)	37.4 (101)	ND (100)	NA (95.4)	NA (96.1)	NA (94.3)
	LAN	82.5 (98.6)	54.1 (96.1)	41.0 (101)	ND (104)	NA (98.9)	NA (97.2)	NA (103)
	LS	80.3 (108)	77.5 (89.4)	101 (86.9)	238.1 (104)	NA (108)	NA (105)	NA (90.1)
Medium	OHL	99.6 (101)	108 (91.6)	53.2 (103)	40.7 (101)	NA (104)	NA (101)	NA (99.2)
	LAN	94.4 (106)	81.6 (86.4)	20.5 (114)	ND (94.6)	NA (111)	NA (102)	NA (103)
	LS	99.1 (102)	167 (89.1)	176 (94.1)	202 (114)	NA (105)	NA (102)	NA (98.2)
High	OHL	99.2 (101)	73.1 (105)	48.0 (92.0)	34.3 (104)	NA (98.9)	NA (96.7)	NA (98.8)
	LAN	98.5 (113)	63.7 (93.1)	33.1 (91.4)	15.5 (103)	NA (101)	NA (105)	NA (100)
	LS	99.5 (107)	93.3 (90.8)	115 (89.2)	144 (115)	NA (103)	NA (104)	NA (96.5)

ND not detected, *NA* not acquired

Table 6 Distribution of measured concentration levels of OHL, LAN, and LS among real samples ($N = 101$)

	OHL	LAN	LS
$c < 3$ ng/mL	6	4	12
$c > 100$ ng/mL	1	76	19

gap started with 52 and the two subjects had MR of 85.8 and 90.5. Hence, both LC UV and LC MS methods were necessary to reliably identify non-compliant patients ($N = 4$), who could not have been identified without using the combined dynamic range of both methods. It is worth noting that the poor metabolizers often suffer from adverse drug reactions and their phenotype should ideally be known beforehand.

Conclusion

To determine the CYP2C19 and CYP3A4 metabolic phenotype, a simple and rapid method relying on either UV or MS detection was developed and validated. The idea of an involvement of two detectors allowed for an increased linear dynamic range, which has proved essential for accurate quantitation of the ratio of a low metabolite (LS, OHL) over a high LAN concentration. The LOD and LOQ obtained by LC MS considerably (two orders of magnitude) exceeded the ones published so far. Utilization of both methods provided a reliable identification of non-compliant patients and poor metabolizers of either CYP isoform. A single system equipped with both detectors could be employed as an ultimate platform in routine CYP2C19 and CYP3A4 metabolic phenotype determination from a single dose of LAN.

Compliance with ethical standards

Conflict of interest Authors declare there are no potential conflicts of interest to disclose.

References

Aoki I, Okumura M, Yashiki T (1991) High-performance liquid-chromatographic determination of lansoprazole and its metabolites in human serum and urine. J Chromatogr Biomed Appl 571:283–290

Asimus S, Elsherbiny D, Hai TN, Jansson B, Huong NV, Petzold MG, Simonsson USH, Ashton M (2007) Artemisinin antimalarials moderately affect cytochrome P450 enzyme activity in healthy subjects. Fundam Clin Pharmacol 21:307–316

Belal F, El-Enany N, Rizk M (2004) Anodic polarographic determination of lansoprazole and omeprazole in pure form and in pharmaceutical dosage forms. J Food Drug Anal 12:102–109

Bharathi DV, Hotha KK, Jagadeesh B, Chatki PK, Thriveni K, Mullangi R, Naidu A (2009) Simultaneous estimation of four proton pump inhibitors–lansoprazole, omeprazole, pantoprazole and rabeprazole: development of a novel generic HPLC-UV method and its application to clinical pharmacokinetic study. Biomed Chromatogr 23:732–739

Chung H, Truong Q, Mai X, Choi Y, Kang J, Mar W, Kim K (2017) Determination of S-(-)-lansoprazole in dexlansoprazole preparation by capillary zone electrophoresis. Arch Pharm Res 40:962–971

Dierks EA, Stams KR, Lim HK, Cornelius G, Zhang HL, Ball SE (2001) A method for the simultaneous evaluation of the activities of seven major human drug-metabolizing cytochrome P450 s using an in vitro cocktail of probe substrates and fast gradient liquid chromatography tandem mass spectrometry. Drug Metab Dispos 29:23–29

Dogrukol-Ak D, Tuncel M, Aboul-Enein H (2001) The determination of lansoprazole in pharmaceutical preparation by capillary electrophoresis. Chromatographia 54:527–530

Dynamed American Society of Health System Pharmacists, I, 1995–2018 (2018) Dynamed. EBSCO Information Services, Ipswich

Elkady EF, Fouad MA, Jaadan BM (2018) LC-MS/MS bioassay of four proton pump inhibitors. J Chromatogr B Analyt Technol Biomed Life Sci 1076:61–69

FDA (2018) Bioanalytical method validation, guidance for industry. In: U.S. Department of Health and Human Services, F. A. D. A., Center for Drug Evaluation and Research (CDER) (Ed.). FDA, p 44

Fuhr U, Rost KL (1994) Simple and reliable CYP1A2 phenotyping by the paraxanthine/caffeine ratio in plasma and in saliva. Pharmacogenetics 4:109–116

Ganesh M, BhagiyaLakshmi M, Hemalatha P, Patil R, Sakthimanigandan K, Jang HT, Rajasekar K (2011) Liquid chromatography-electrospray tandem mass spectrometry (LC-MS/MS) determination of lansoprazole in human plasma. J Liq Chromatogr Relat Technol 34:129–142

Gumus E, Karaca O, Babaoglu M, Baysoy G, Balamtekin N, Demir H, Uslu N, Bozkurt A, Yuce A, Yasar U (2012) Evaluation of lansoprazole as a probe for assessing cytochrome P450 2C19 activity and genotype-phenotype correlation in childhood. Eur J Clin Pharmacol 68:629–636

Jackson PR, Tucker GT, Woods HF (1989) Testing for bimodality in frequency distributions of data suggesting polymorphisms of drug metabolism–histograms and probit plots. Br J Clin Pharmacol 28:647–653

Kim K, Kim M, Park J, Shon J, Yoon Y, Lee S, Liu K, Chun J, Hyun M, Shin J (2003) Stereoselective metabolism of lansoprazole by human liver cytochrome P450 enzymes. Drug Metab Dispos 31:1227–1234

Landes B, Miscoria G, Flouvat B (1992) Determination of lansoprazole and its metabolites in plasma by high-performance liquid-chromatography using a loop column. J Chromatogr Biomed Appl 577:117–122

Luo L, Wen X, Du Y, Jiang Z, Guo X (2018) Enantioselective analysis of lansoprazole in rat plasma by LC–MS/MS: application to a stereoselective pharmacokinetic study. Biomed Chromatogr 32:4345

Medicines and Healthcare Regulatory Agency (MHRA) (2017) SmPC, Zoton FasTab. In: MHRA (ed), pp 1–14

Nassar MY, El-Shahat MF, Khalil SM, El-Moety EA (2017) Optimization and validation of spectrophotometric and potentiometric methods for determination of lansoprazole and omeprazole in pure and capsules. Indian J Pharm Sci 79:420–430

Oliveira CH, Barrientos-Astigarraga RE, Abib E, Mendes GD, da Silva DR, de Nucci G (2003) Lansoprazole quantification in human plasma by liquid chromatography-electrospray tandem mass spectrometry. J Chromatogr B Analyt Technol Biomed Life Sci 783:453–459

Sharma A, Pilote S, Belanger PM, Arsenault M, Hamelin BA (2004) A convenient five-drug cocktail for the assessment of major drug metabolizing enzymes: a pilot study. Br J Clin Pharmacol 58:288–297

Sohn D, Kwon J, Kim H, Ishizaki T (1997) Metabolic disposition of lansoprazole in relation to the S-mephenytoin 4′-hydroxylation phenotype status. Clin Pharmacol Ther 61:574–582

Song M, Gao X, Hang T, Wen A (2008) Simultaneous determination of lansoprazole and its metabolites 5′-hydroxy lansoprazole and lansoprazole sulphone in human plasma by LC-MS/MS: application to a pharmacokinetic study in healthy volunteers. J Pharm Biomed Anal 48:1181–1186

Song M, Gao X, Hang TJ, Wen AD (2009) Pharmacokinetic properties of lansoprazole (30-mg enteric-coated capsules) and its metabolites: a single-dose, open-label study in healthy Chinese male subjects. Curr Ther Res Clin Exp 70:228–239

Sun L, Cao Y, Jiao H, Fang Y, Yang Z, Bian M, Zhang H, Gong X, Wang Y (2015) Enantioselective determination of (R)- and (S)-lansoprazole in human plasma by chiral liquid chromatography with mass spectrometry and its application to a stereoselective pharmacokinetic study. J Sep Sci 38:3696–3703

Swar BD, Bendkhale SR, Rupawala A, Sridharan K, Gogtay NJ, Thatte UM, Kshirsagar NA (2016) Evaluation of cytochrome P450 2C9 activity in normal, healthy, adult Western Indian population by both phenotyping and genotyping. Indian J Pharmacol 48:248–251

Turjap M, Zendulka O, Glatz Z, Brejcha S, Madr A, Jurica J (2016) Determination of caffeine and its metabolites in saliva and urine as a measure of CYP1A2 metabolic activity. Curr Pharm Anal 12:325–332

Uno T, Yasui-Furukori N, Takahata T, Sugawara K, Tateishi T (2005a) Determination of lansoprazole and two of its metabolites by liquid-liquid extraction and automated column-switching high-performance liquid chromatography: application to measuring CYP2C19 activity. J Chromatogr B Anal Technol Biomed Life Sci 816:309–314

Uno T, Yasui-Furukori N, Takahata T, Sugawara K, Tateishi T (2005b) Determination of lansoprazole and two of its metabolites by liquid-liquid extraction and automated column-switching high-performance liquid chromatography: application to measuring CYP2C19 activity. J Chromatogr B Analyt Technol Biomed Life Sci 816:309–314

Wang H, Sun Y, Meng X, Yang B, Wang J, Yang Y, Gu J (2015) Determination of lansoprazole enantiomers in dog plasma by column-switching liquid chromatography with tandem mass spectrometry and its application to a preclinical pharmacokinetic study. J Sep Sci 38:2960–2967

Wu GL, Zhou HL, Shentu JZ, He QJ, Yang B (2008) Determination of lansoprazole in human plasma by rapid resolution liquid chromatography-electrospray tandem mass spectrometry: application to a bioequivalence study on Chinese volunteers. J Pharm Biomed Anal 48:1485–1489

Xu HR, Chen WL, Li XN, Chu NN (2010) The effect of CYP2C19 activity on pharmacokinetics of lansoprazole and its active metabolites in healthy subjects. Pharm Biol 48:947–952

Yanagida Y, Watanabe M, Takeba Y, Kumai T, Matsumoto N, Hayashi M, Suzuki S, Kinoshita Y, Kobayashi S (2009) Potential of lansoprazole as a novel probe for cytochrome P450 3A activity by measuring lansoprazole sulfone in human liver microsomes. Biol Pharm Bull 32:1422–1426

Yang DZ, Gao YY, Jiang XL, Dong WF, Tang DQ (2011) Pharmacokinetics of Lansoprazole Injection in Peptic Ulcer and Healthy Volunteers. Lat Am J Pharm 30:1016–1020

Yeniceli D, Dogrukol-Ak D, Tuncel M (2004) Determination of lansoprazole in pharmaceutical capsules by flow injection analysis using UV-detection. J Pharm Biomed Anal 36:145–148

Zanger UM, Raimundo S, Eichelbaum M (2004) Cytochrome P450 2D6: overview and update on pharmacology, genetics, biochemistry. Naunyn Schmiedebergs Arch Pharmacol 369:23–37

Zhang D, Wang XL, Yang M, Wang GC, Liu HC (2011) Effects of CYP2C19 polymorphism on the pharmacokinetics of lansoprazole and its main metabolites in healthy Chinese subjects. Xenobiotica 41:511–517

Zhang H, Xia CH, Huang SB, Liu MY, Xiong YQ (2014) Determination of Lansoprazole in Human Plasma Using LC-MS and Pharmacokinetic Study in Chinese Healthy Volunteers. Lat Am J Pharm 33:624–630

4.2 Online solid-phase extraction liquid chromatography-mass spectrometry of hair cortisol using a surrogate analyte

Hair cortisol has been widely analyzed since its introduction in 2000.[80,81] Commonly used methods include immunoassays and LC–MS. The specificity of immunoassays is somewhat questionable,[82] and the LC–MS approaches asses the baseline levels by the most distal hair segment pretending it contains no endogenous cortisol. Binz *et al.* first proved that the most distal segment may contain as much cortisol as anywhere along the hair strand,[83] and suggested a more reliable approach of a surrogate analyte in the authentic matrix. We decided to follow the same approach to cope with the bias at baseline levels of blank samples. Even though hair cortisol analysis has been performed for twenty years, the physiological ranges were scarcely been agreed on. The lower limit (~ 1 pg/mg) of the reference interval was established consistently; however, the upper limit dramatically differed due to extreme intraindividual variability. We have found out that the hair cortisol concentration (HCC) thresholds were not sharp; quite oppositely, HCC might be classified along with the following guidelines:

1. Healthy individuals > 1 pg/mg.
2. Cortisol metabolism impairment > 100 pg/mg.
3. Topically applied corticosteroids > 1000 pg/mg.

Unsharp borders exist due to stress contributions, the onset of impairment, and other factors that could not have been addressed solely by HCC determination.

Stress, which many scientists try to objectively quantify using HCC, could be viewed as a confounder (or a latent variable), which could not be directly conditioned on. In other words, it is impossible to divide subjects into stressed and non-stressed groups. Thus, the contribution of physical stress to HCC could be relatively high per hair segment. On the other hand, hair cortisol analysis could be especially helpful in corticosteroid substitution therapy monitoring, establishing ectopic ACTH production, diagnosing a cyclic version of Cushing's syndrome, or psychiatric disorders. The longitudinal measurement using hair segmentation could provide HCC values unaffected by diurnal rhythms and momentary cortisol levels in the organism. Topically applied corticosteroids were easily distinguishable as HCC reached values over 1000 pg/mg, which could have not originated from steroid therapy or impairment. In a linkup article, plasma urine and hair cortisol levels of 22 patients subjected to substitution therapies were longitudinally measured between Q2/2018 and Q4/2019. Hierarchical Bayesian modeling was applied to compare the effectiveness of the therapy. Individual hair cortisol levels better reflected the optimal therapeutic state than routinely measured plasma and urine cortisol. The discontinuation of the substitution therapy *e.g.*, after adrenalectomy, could have been suggested by HCC monitored retroactively via a segmentation process.[84]

ORIGINAL PAPER

CrossMark

Online solid-phase extraction liquid chromatography–mass spectrometry of hair cortisol using a surrogate analyte

Katarina Kostolanska[1] · Lucie Novotna[1] · Eva Taborska[1] · Ondrej Pes[1] 📷

Abstract

Online SPE LC–MS with $^{13}C_3$-cortisol as a surrogate analyte was developed, validated and applied for obtaining hair cortisol levels of 114 healthy volunteers. The first 3 cm from a posterior vertex position were analyzed as three individual segments resulting in 310 hair cortisol levels, which were used, after log transformation, to predict a range of values observed in future. The median value of hair cortisol was 4.76 pg/mg. The employed method allowed simple processing, high throughput and may be readily expanded to analyze additional steroid compounds in hair.

Keywords Endogenous cortisol · Long-term hair concentration · Surrogate analyte · LC–MS · Online SPE

Introduction

Cortisol is a glucocorticoid hormone with major effect upon a range of physiological homeostatic mechanisms. It plays an important role in stressful situations when stressors activate the hypothalamic–pituitary–adrenocortical (HPA) system.

Cortisol has been routinely analyzed in the laboratory from saliva, serum/plasma, and/or urine. However, the HPA axis represents a highly dynamic system influenced by several factors and expose circadian rhythmicity. The most widely analyzed saliva or plasma reflect only acutely circulating cortisol levels, urine provides usually 24-h assessments of levels through the day. Measurements in the above-mentioned body fluids are limited in the temporal range of assessment. Cirimele et al. were first who detected cortisol and other glucocorticoids in hair (Cirimele et al. 2000). Cortisol is being constantly incorporated into a growing hair shaft and, accordingly, can allow the unique possibility to assess the long-term systemic levels and obtain a retrospective index of long-term hormone secretion. Based on an average hair growth rate of 1 cm per month (Wennig 2000), it is possible to distribute the hair along the length of individual segments and determine the concentration of cortisol reflecting secretion in the monitored period. But due to a rapid decrease of cortisol in hair, the measure may be limited to the past 6 months (Kirschbaum et al. 2009).

Concerning the diagnostic value, differences in cortisol levels can be used to evaluate disturbances of the HPA axis. It may serve in the diagnosis of Cushing's syndrome disease but it may also be useful as a marker of successful therapy. Changes in cortisol levels have been observed in mental diseases, e.g., depression, general anxiety disorder or post-traumatic stress disorder as well as physical diseases where it could serve as a marker for diagnosis or risk stratification (Russell et al. 2012).

Commonly used methods for a hair steroid analysis are immunoassays; principally enzyme-linked immunosorbent assays (ELISA). The major disadvantage of immunoassays is low specificity. Given to high structural similarity of steroid compounds, there is a risk of cross-reactions inside the immuno-complex that may overestimate the target concentration. In this context, cortisone especially has been observed as a major source of interference in immunoassays research of salivary cortisol (Miller et al. 2013). These approaches are often unsuitable for clinical applications that require a low detection limit (Taieb et al. 2002). Much higher specificity is provided by liquid chromatography–mass spectrometry (LC–MS). Compared to immunoassays with specificity to only a single analyte, LC–MS proves to measure a panel of multiple steroid hormones simultaneously, currently 28 steroids (Dong et al. 2017). LC–MS offers other advantages, such as high sensitivity,

✉ Ondrej Pes
   ondramayl@gmail.com

1   Department of Biochemistry, Faculty of Medicine, Masaryk University, Kamenice 5, 62500 Brno, Czech Republic

wide dynamic range, high throughput, and an option for automated sample preparation (Gao et al. 2016) Current and potential future applications of hair cortisol analysis have been summarized in a review by Wester and Rossum (Wester and van Rossum 2015), however; the exact physiological range of hair cortisol concentration has not yet been established.

In general, cortisol content in hair is very low. Raul et al. reported cortisol concentration ranged from 5.2 to 91 pg/mg with a mean value of 19 pg/mg. LC–MS/MS with electrospray ionization (ESI) in the positive mode was used for quantification; limit of detection (LOD) and limit of quantitation (LOQ) was 1 and 5 pg/mg, respectively (Raul et al. 2004). Another study reported a median cortisol level of 8.8 pg/mg for elementary school girls with a range of 5–1330.5 pg/mg (Vanaelst et al. 2013). Though, only 39 of 168 samples were higher than LOQ (5 pg/mg). Hair cortisol levels 12.7 ± 14 pg/mg in hair samples of healthy volunteers with an age range of 4–63 years were obtained by LC–MS/MS/MS (Quinete et al. 2015). The broad range of physiological values is likely affected by the fact that the mechanism of cortisol incorporation into the hair shaft has yet not been fully revealed.

As cortisol is normally present in hair, it is difficult to achieve a high throughput methodology using an authentic matrix calibration curve. A method of the standard addition should be used instead (Tsakelidou et al. 2017). Some authors have considered a distal segment of hair as an analyte-free matrix even that ascertained cortisol concentration (1.2 pg/mg) was found in the 4 cm segment of the distal end of 20 cm long human hair (Binz et al. 2016). In such cases, the matrix varies from sample to sample and a lack of a reference material made all the validation studies ambiguous. Cortisol added to the solution of "blank hair" might behave differently and may significantly contribute to the high variation of hair cortisol, especially at low concentration levels. Hence, spiking with known amounts of reference standards should be avoided if the method of standard addition is not used for each sample. Alternatively, the results should be associated with the synthetic matrix only (Doroschuk et al. 2016).

The only approach using an authentic matrix and a surrogate analyte was demonstrated by Binz et al. (Binz et al. 2016) even as using a surrogate analyte might prove very advantageous in the analysis of endogenous compounds in challenging matrices and allows for facile method development when there is no analyte-free matrix available. The response of the isotopically labeled $^{13}C_3$-cortisol as a surrogate analyte was consistent and nearly identical with that of cortisol. Moreover, a method of a calibration curve in the authentic matrix could have been employed without the risk of deteriorating the results. The authors compared both approaches and validated the surrogate analyte method to

unambiguously determine the lowest cortisol levels in all hair samples.

In the present study, we aimed to assess a prediction interval based on data of hair cortisol in the local adult population using an approach based on online SPE LC–MS/MS with ^{13}C-labeled cortisol as a surrogate analyte.

Results and discussion

Online SPE LC–MS

An automated on-line SPE LC–MS provided high throughput of samples and minimized the retention time fluctuation as the autosampler loop (void volume > 100 μl) was excluded from the separation pathway. Moreover, we have, to our best knowledge, presented an inexpensive approach of utilizing a guard column cartridge (2 pcs) as a trapping column for the SPE purification/enrichment for the first time. The first 2 min of a chromatogram served for trapping and washing of the sample, which was done by a continuous flow of 2 mL of 10% MeOH from the secondary pump. When detection at 260 nm was used instead of MS the compounds originating from the washing step of SPE were eluted during the first milliliter of 10% MeOH (data not shown).

Representative LC/MS chromatograms are shown in Fig. 1. Figure 1a shows a hair sample from the hair pool; Fig. 1b, c show a hair pool sample spiked with $^{13}C_3$-cortisol and D_8-cortisone, and Fig. 1d shows a representative hair sample of a participant with spiked D_8-cortisone. In most cases, the endogenous cortisol levels in hair pool were below limits of detection, however; as the sample matrix was not homogenous there were cases when the quantitation would have been ruined if the surrogate cortisol calibration had not been used. The response factor for $^{13}C_3$-cortisol/cortisol was 0.94. Peaks of cortisol and cortisone were chromatographically resolved to eliminate errors resulting from very similar mass-to-charge ratios of target compounds. This was achieved by employing > 50% MeOH in the mobile phase during a single gradient run. On the other hand, the system backpressure was relatively high (~ 300 bar), which may shorten the analytical column lifetime. The separation conditions were chosen to allow the simple introduction of additional steroid compounds into the method in future. Due to the high MeOH content in the mobile phase, it might be advantageous to employ a heating gradient inside the ESI chamber (Şener et al. 2017).
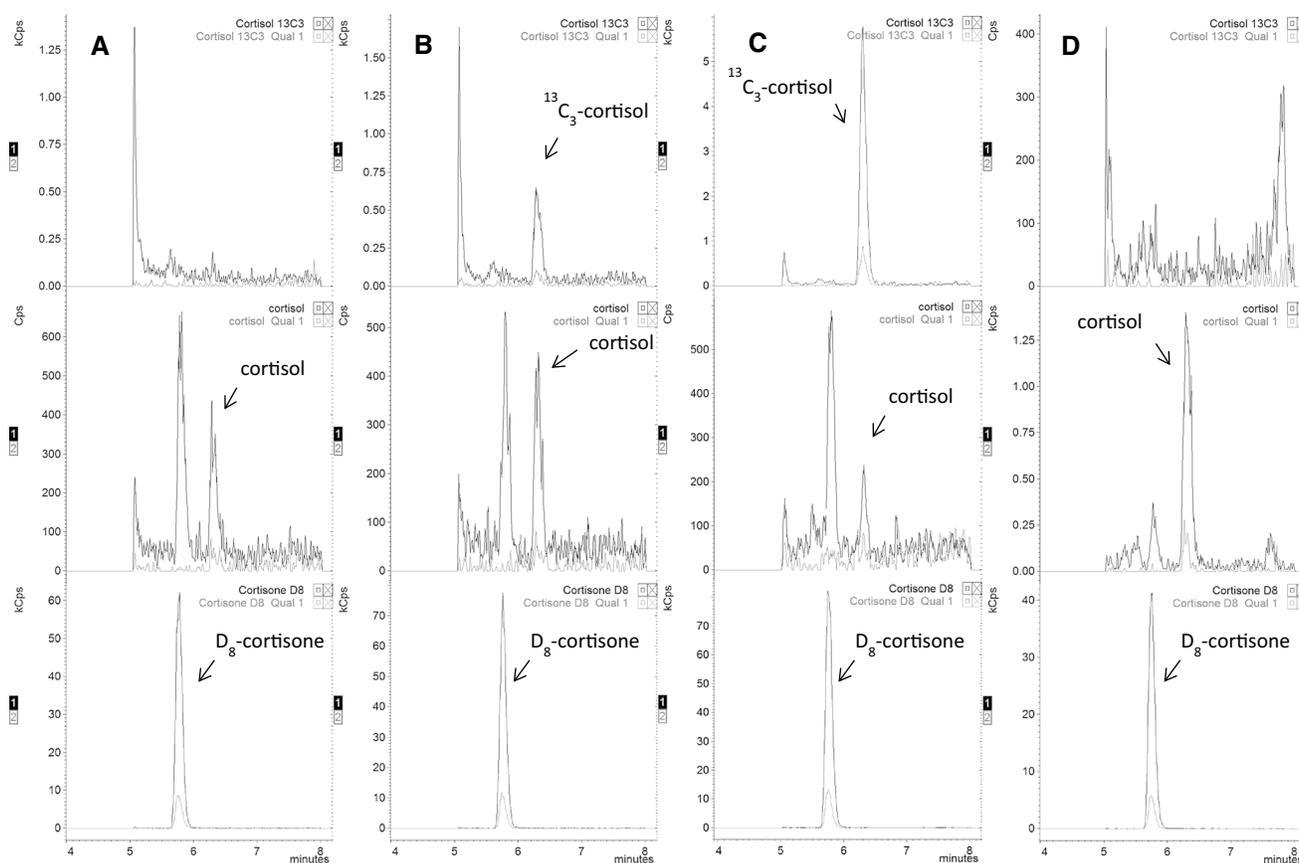
Fig. 1 Online SPE LC–MS chromatograms of **a** a hair pool sample, **b** a hair pool sample spiked with $^{13}C_3$-labeled cortisol (1.25 pg/mg), **c** a hair pool sample spiked with $^{13}C_3$-labeled cortisol (12.5 pg/mg), and **d** a real hair sample (8 mg). Two SRM transitions for $^{13}C_3$-cortisol ($t_R = 6.3$ min), cortisol ($t_R = 6.3$ min), and IS D_8-cortisone ($t_R = 5.8$ min) are represented by the upper, middle, and lower frames, respectively. Please notice, that the endogenous cortisol was found in the hair pool sample at rather low, however, detectable levels

Linearity, LOD, and LOQ

Calibration was carried out using a $^{13}C_3$-labeled cortisol. The calibration curve showed linearity in the entire range 1–100 pg/mg. The square of the correlation coefficient (R^2) of the calibration curve was 0.9995. The intercept was tested by regression analysis and found insignificant (p value 0.076, $\alpha = 0.05$). The LOD and LOQ were found 0.3 and 0.8 pg/mg for $^{13}C_3$-cortisol with a signal–noise ratio of 3:1 (LOD) and 10:1 (LOQ), respectively. The LOD and LOQ were in a similar range than previously published methods with LC–MS. A calibration curve from 1 to 100 pg/mg was used to determine cortisol levels in authentic hair samples as the cortisol concentrations in hair normally exceed 1 pg/mg.

Recovery and matrix effect

The data for recovery and matrix effects are summarized in Table 1. Recovery was 91.4, 100.2 and 90.1% for the low,

Table 1 Recovery and matrix effect, ($N = 5$)

	$^{13}C_3$-cortisol		
	Low (5 pg/mg)	Medium (20 pg/mg)	High (100 pg/mg)
Recovery (%)	91.4	100	90.1
RSD (%)	11	8.8	9.0
Matrix effect (%)	116	97.4	106
RSD (%)	6.2	9.6	5.8

medium and high concentration, respectively, with the relative standard deviation (RSD) below 12%. Matrix effects were not observed for $^{13}C_3$-cortisol (≥ 75 and $\leq 125\%$).

Precision and accuracy

The results for accuracy and precision for $^{13}C_3$-cortisol as an analyte are summarized in Table 2. In this case, all the data met the required criteria (RSD < 15%).

Table 2 Accuracy and precision, on 5 consecutive days

$^{13}C_3$-cortisol	Low (5 pg/mg)	Medium (20 pg/mg)	High (100 pg/mg)
Characteristics ($N = 25$)			
Mean (pg/mg)	5.09	20.2	102
SD (pg/mg)	0.307	1.46	6.01
Accuracy			
Variance (pg/mg)	0.090	0.20	2.0
Bias (%)	1.7	1.0	2.0
Intraday precision ($N = 5$)			
RSD (%)	3.5	6.2	4.9
Interday precision ($N = 25$)			
RSD (%)	6.0	7.2	5.9

Clinical application

To indicate a range of hair cortisol values, which might be applicable as a reference range, a series of 114 volunteers (40 men, 74 women, age 19–27 years) has been analyzed for hair cortisol levels, see Table 3. Such effort was already made by other groups, however; a range of expected values should be determined among the population it is going to be applied to. As we plan to correlate hair cortisol levels of people with disorders associated with high levels of cortisol in the organism, we had to compare the range obtained with local population with that assessed by other groups. Although we attempted to minimize within individual variation in hair growth by taking hair from the vertex posterior region of the head, hair growth rates may vary among individuals. Furthermore, the participants in this cohort at this phase have a mean age of 20.5 years; therefore, it may not be possible to generalize the findings of this study to older adults, even as the age-related variability appears mostly in the range 0.5–18 years (Binz et al. 2018).

The original data were log-transformed to obtain normal distribution, which was used to obtain re-transformed mean (4.76 pg/mg), standard deviation (1.88 pg/mg), and a prediction interval ($\alpha = 0.05$; 1.22–18.7 pg/mg) in the first three centimeters of hair (Table 3). The prediction interval could be defined as an estimate of an interval in which future

observations will fall, with a certain probability and it was very similar to the 2.5–97.5 quantile interval.

To reveal the relationship of the hair cortisol concentration with the physical state of the organism, we asked the participant with the value of hair cortisol, which was marked as an outlier, to be sampled again after a 3-month period. In this case, the hair sample was obtained from three posterior vertex positions approximately 2 cm from each other (left, middle, and right) in two replicates; each of the hair strands was cut into six 1 cm segments. Essentially, it could have represented hair cortisol concentrations approximately over the past 6 months (Table 4). Despite the high variability between individual sampling locations, it may be clearly stated that hair cortisol had been increased in the time of the first sampling (4–6 cm) and was probably lowered by a washing-out effect. The values from the 1–3 cm may suggest that the overall cortisol balance in the organism has been settled and that the former values had been momentarily increased. However, the participant was not able to provide any additional information on the cause of the elevated values. Careful interpretation has to be made as, according to another study, the participant could have been identified as a person with Cushing's syndrome (cut-off = 31.1 pg/mg) (Wester et al. 2017).

Materials and methods

Chemicals and calibration standards

Reagents, stock solutions of $^{13}C_3$-cortisol (2,3,4-$^{13}C_3$) (100 μg/mL), deuterated D_8-cortisone (2,2,4,6,6,9,12,12-D_8), formic acid (HCOOH), and methanol (MeOH, LC–MS) were obtained from Sigma Aldrich (Switzerland). All water used was of an ultra-pure grade supplied by an in-house Milli-Q system (Millipore, MA, USA).

A stock solution of deuterated internal standard (IS) D_8-cortisone was prepared at the final concentration of 100 ng/mL and was also used as a working solution. A stock solution of a stable isotope-labeled form of the analyte, $^{13}C_3$-cortisol, was prepared in methanol to a concentration of 50 ng/mL. Working standard solutions were prepared by diluting the stock solution $^{13}C_3$-cortisol to a

Table 3 Hair cortisol concentration (pg/mg) of the study participants ($N = 114$) containing mean (X), median (M), re-transformed mean (X_R), re-transformed standard deviation (SD_R), prediction interval (PI), and a 2.5–97.5 quantile interval (Q_{95})

Hair segment	N	%	X	M	X_R	SD_R	PI	Q_{95}
1st cm	114	100	6.02	4.86	4.85	1.84	1.44–16.3	1.45–16.5
2nd cm	101	88.6	7.13	4.90	5.00	2.03	1.22–20.6	1.35–17.8
3rd cm	95	83.3	6.63	4.20	4.59	2.09	1.05–20.0	1.13–23.1
3 cm length	310	–	6.57	4.76	4.76	1.88	1.22–18.7	1.32–19.4

Table 4 Hair cortisol concentrations (pg/mg) of a single sample cut into 6 segments in two replicates

Position	Hair segment					
	1 cm	2 cm	3 cm	4 cm	5 cm	6 cm
Left						
A	7.82	8.45	8.13	13.7	27.6	35.2
B	7.58	10.2	9.62	13.1	20.2	22.7
X	7.70	9.33	8.87	13.4	23.9	29.0
SD	0.168	1.24	1.05	0.44	5.23	8.82
RSD (%)	2.18	13.3	11.8	3.26	21.9	30.5
Middle						
A	8.82	10.2	16.0	41.0	60.2	52.4
B	11.0	28.2	23.5	51.8	73.1	61.1
X	9.90	19.2	19.7	46.4	66.7	56.8
SD	1.53	12.7	5.29	7.63	9.13	6.11
RSD (%)	15.4	66.4	26.8	16.4	13.7	10.8
Right						
A	11.4	11.1	11.4	12.6	18.9	19.0
B	10.7	12.3	13.5	14.5	21.3	19.9
X	11.1	11.7	12.5	13.6	20.1	19.5
SD	0.506	0.810	1.50	1.37	1.63	0.616
RSD (%)	4.57	6.92	12.0	10.1	8.13	3.17

Values of the mean (X), standard deviation (SD), and relative standard deviation (RSD) were calculated

concentration of 0.08, 0.4, 0.8, 1.6, and 8 ng/mL resulting in the final concentration levels in the calibration curve of 1–100 pg/mg.

All standard and stock solutions were individually diluted with methanol and stored at − 20 °C until use.

Hair sample collection and preparation

The hair samples were taken from healthy volunteers following the basic criteria for collection defined by the Society of Hair Testing (Cooper et al. 2012). The protocol was approved by the Masaryk University Ethical Committee, and all participants gave written informed consent. The hair strands with a thickness of several millimeters in diameter were cut with fine scissors from a posterior vertex position as closely as possible to the scalp. Subsequently, they were tagged on the proximal side and stored individually in a folded piece of paper in labeled foiled bags. Until the day of analysis, the hair strands were stored at room temperature in a dry environment away from direct sunlight. For the analysis, the first 3 cm of the proximal segment was cut into 1 cm segments. A minimum of 8 mg of each segment was weighted to evaluate and determine the level of cortisol.

Four centimeters of the distal end of 20 cm long human hair was used as authentic matrix. The hair was cut into snippets, homogenized and used as a hair pool during the method development.

Hair sample extraction

Prior to analysis, the hair samples were manually washed in vials by shaking them two times with 2 ml of isopropanol for 1 min at room temperature. Subsequently, they were dried on a piece of filter paper and uniformly mixed with a laboratory tweezer to ensure maximum homogeneity. Approximately 8 mg of washed and dry hair was carefully transferred into a glass tube. Sequentially, 1800 µl of methanol and 10 µl of IS from the working solution (100 ng/mL) were added.

Calibration curve standards were prepared following the same procedure using the hair pool matrix. The 8-mg hair sample was spiked with $^{13}C_3$-cortisol (100 µL from the working standard solutions resulting in final concentrations of 1–100 pg/mg) and 10 µl of IS from the working solution (100 ng/mL) was added prior to incubation. The hair was incubated for 18 h at room temperature, in darkness and without shaking. Afterward, 1600 µl of the extract was transferred into a new tube and fully evaporated at 40 °C under a constant stream of nitrogen. The residue was reconstituted in 500 µl of 20% MeOH, vortexed for 1 min, and transferred into the LC–MS vials. A volume of 50 µl was directly injected into the online SPE LC–MS/MS system for analysis.

Online SPE LC–MS

The online SPE LC–MS method for analysis of cortisol was developed using a Dionex Ultimate 3000RS (ThermoScientific, CA, USA) module, equipped with a binary

high-pressure gradient pump (HPG), a quaternary low-pressure gradient pump (LPG) connected to an auto-sampler (AS), and a column oven with a 6-port, two-way valve. The trapping column (SPE column) consisted of a mounted guard column holder (Phenomenex, CA, USA) with two pieces of a SecurityGuard[TM] cartridge (2×4 mm, C18, Phenomenex, CA, USA). With the switching valve in the sample loading position (A), the LPG pump was used to load within 2 min 50 μl of the samples on the SPE column operating at room temperature using 10% MeOH in water at 1 ml/min. From 2 to 2.5 min (Fig. 2), the valve automatically switched to its alternate position (*B*) and then back to the loading position (*A*), allowing the analytes to be transferred (in a backflush mode) from the SPE column onto the analytical column (2.1 mm×100 mm, 2.7 μm C18 Ascentis, Phenomenex, CA, USA), shielded by a guard column (C18, 2×2 mm, Phenomenex, CA, USA), both operated at 20±0.1 °C. The HPG binary mobile phase system consisted of water with 0.1% formic acid (v/v) and MeOH. The flow-rate was set

to 0.2 ml/min and the following 12-min gradient program was employed. The initial 50% of MeOH was kept constant for 2 min and then linearly increased from 50 to 85% over the next 7.5 min. It was held at 85% for 1 min, followed by equilibration under the initial conditions for another 1.5 min. From 4.0 to 8.5 min, the SPE column was regenerated using 100% MeOH and then re-equilibrated using 10% MeOH.

The outlet of the analytical column was connected to a Bruker EVOQ Qube triple quadrupole mass spectrometer (Germany) operated in the negative heated-electrospray ionization mode with the following parameters: Spray voltage 3500 V, cone temperature 350 °C, cone gas flow 20 psi, heated probe temperature 350 °C, probe gas flow 40 psi (nitrogen), and nebulizer gas flow 50 psi (nitrogen). Argon was used as collision gas. All other parameters were set at default values provided by the manufacturer. The flow from LC was diverted to waste in the range of 0–5 and 8.5–12 min. Target compounds were scanned in the selected reaction monitoring mode (SRM) as fragments of ionic adducts with
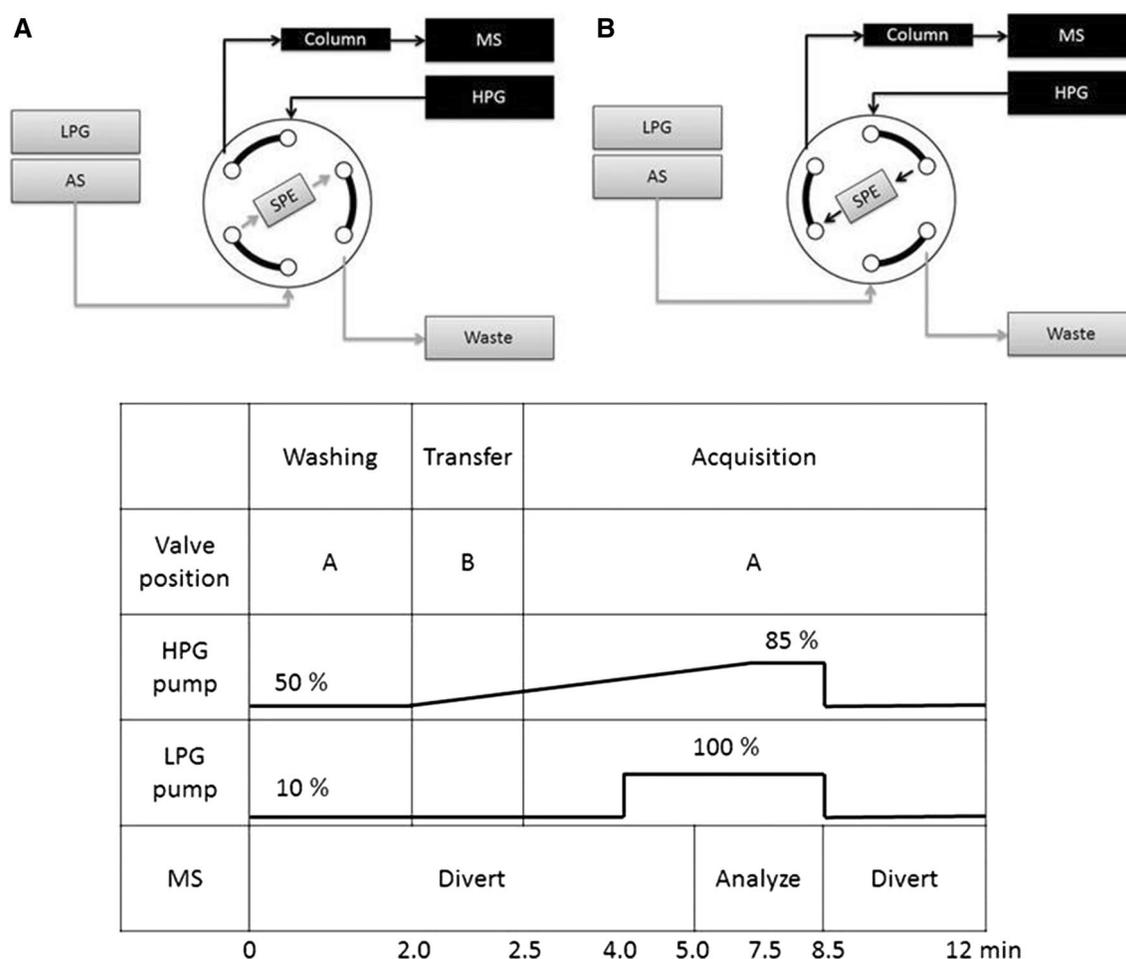

Fig. 2 Switching valves positions. **a** Loading and washing. **b** Sample transfer. The table specifies individual times of events during a single sample run

formic acid $[M+HCOO]^{-1}$: cortisol 407.1–331.1 (12 eV) and 407.1–297.1 (29 eV); cortisol $^{13}C_3$ 410.1–334.1 (12 eV) and 410.1–300.1 (29 eV); D_8-cortisone 413.3–337.1 (10 eV) and 413.1–139.1 (36 eV). Dwell time for each transition was 50 ms.

Method validation

As the validation for using the $^{13}C_3$-cortisol calibration instead of endogenous cortisol calibration was done by Binz et al. 2016, we have validated only the parameters related to the $^{13}C_3$-cortisol calibration. Statistica (v13, TIBCO Software Inc.) was used for data processing.

LOD and LOQ

Five calibration levels (1–100 pg/mg) were used. Three replicates for each calibration level (1, 5, 10, 20, 100 pg/mg) were analyzed. The calibration curve was estimated by the least-squares regression procedure. LOD and LOQ were determined for $^{13}C_3$-cortisol by analyzing the lowest calibration point of calibration and calculating a theoretical signal-to-noise ratio of 3:1 for LOD and 10:1 for LOQ. The values were verified by measuring $^{13}C_3$-cortisol samples using the calculated concentrations.

Accuracy, precision, matrix effects, and recovery

Accuracy and precision of the method were evaluated by measuring five replicates of a QC sample at three different concentration levels (low 5 pg/mg, medium 20 pg/mg, high 100 pg/mg) on 5 consecutive days. Matrix effect was measured by comparing the calculated concentration of $^{13}C_3$-cortisol spiked hair after extraction (A) to the spiked solvent at the same concentration (B) (Matrix effect $= A/B \times 100$). Recovery was measured by comparing the calculated concentration of $^{13}C_3$-cortisol from spiked hair before extraction (C) to spiked hair after extraction (D) (recovery $= C/D \times 100$). Five replicates at low (5 pg/mg), medium (20 pg/mg) and high (100 pg/mg) concentration levels were used for both parameters.

Conclusions

An online SPE LC–MS with a surrogate analyte was developed and validated to analyze the hair cortisol concentration. A range and median concentration levels of physiological values correspond to those previously published in the literature. Cortisol in hair represents a long-term value of cortisol in the organism even that the incorporation mechanism has not been fully uncovered yet. We have obtained a prediction interval for hair cortisol to help differentiate between short-term physical stress-related issues and long-term non-physiological conditions, such as Cushing's syndrome. Hence, when hair cortisol values are being determined we recommend analyzing a longer segment of a hair strand to obtain a decline curve, which might negate the enormous individual and sampling variability. Careful interpretation of hair cortisol levels within the prediction interval should be considered as well.

References

Binz TM, Braun U, Baumgartner MR, Kraemer T (2016) Development of an LC–MS/MS method for the determination of endogenous cortisol in hair using C-13(3)-labeled cortisol as surrogate analyte. J Chromatogr B Anal Technol Biomed Life Sci 1033:65–72. https://doi.org/10.1016/j.jchromb.2016.07.041

Binz TM, Rietschel L, Streit F, Hofmann M, Gehrke J, Herdener M, Quednow BB, Martin NG, Rietschel M, Kraemer T, Baumgartner MR (2018) Endogenous cortisol in keratinized matrices: systematic determination of baseline cortisol levels in hair and the influence of sex, age and hair color. Forensic Sci Int 284:33–38. https://doi.org/10.1016/j.forsciint.2017.12.032

Cirimele V, Kintz P, Dumestre V, Goulle JP, Ludes B (2000) Identification of ten corticosteroids in human hair by liquid chromatography–ionspray mass spectrometry. Forensic Sci Int 107:381–388. https://doi.org/10.1016/S0379-0738(99)00180-2

Cooper GAA, Kronstrand R, Kintz P (2012) Society of hair testing guidelines for drug testing in hair. Forensic Sci Int 218:20–24. https://doi.org/10.1016/j.forsciint.2011.10.024

Dong Z, Wang CH, Zhang JL, Wang Z (2017) A UHPLC-MS/MS method for profiling multifunctional steroids in human hair. Anal Bioanal Chem 409:4751–4769. https://doi.org/10.1007/s00216-017-0419-2

Doroschuk VO, Grogul AB, Mandzyuk YS, Makukha OG, Grytsyk NO (2016) Cloud point extraction of disulfiram for its HPLC–MS/MS determination in synthetic urine. Chem Pap 70:1316–1321. https://doi.org/10.1515/chempap-2016-0074

Gao W, Kirschbaum C, Grass J, Stalder T (2016) LC–MS based analysis of endogenous steroid hormones in human hair. J Steroid Biochem Mol Biol 162:92–99. https://doi.org/10.1016/j.jsbmb.2015.12.022

Kirschbaum C, Tietze A, Skoluda N, Dettenborn L (2009) Hair as a retrospective calendar of cortisol production-increased cortisol incorporation into hair in the third trimester of pregnancy. Psychoneuroendocrinology 34:32–37. https://doi.org/10.1016/j.psyneuen.2008.08.024

Miller R, Plessow F, Rauh M, Groschl M, Kirschbaum C (2013) Comparison of salivary cortisol as measured by different immunoassays and tandem mass spectrometry. Psychoneuroendocrinology 38:50–57. https://doi.org/10.1016/j.psyneuen.2012.04.019

Quinete N, Bertram J, Reska M, Lang J, Kraus T (2015) Highly selective and automated online SPE LC–MS3 method for determination of cortisol and cortisone in human hair as biomarker for stress related diseases. Talanta 134:310–316. https://doi.org/10.1016/j.talanta.2014.11.034

Raul JS, Cirimele V, Ludes B, Kintz P (2004) Detection of physiological concentrations of cortisol and cortisone in human hair.

Clin Biochem 37:1105–1111. https://doi.org/10.1016/j.clinbiochem.2004.02.010

Russell E, Koren G, Rieder M, Van Uum S (2012) Hair cortisol as a biological marker of chronic stress: current status, future directions and unanswered questions. Psychoneuroendocrinology 37:589–601. https://doi.org/10.1016/j.psyneuen.2011.09.009

Şener H, Anilanmert B, Cengiz S (2017) A fast method for monitoring of organic explosives in soil: a gas temperature gradient approach in LC–APCI/MS/MS. Chem Pap 71:971–979. https://doi.org/10.1007/s11696-016-0042-2

Taieb J, Benattar C, Birr AS, Lindenbaum A (2002) Limitations of steroid determination by direct immunoassay. Clin Chem 48:583–585

Tsakelidou E, Virgiliou C, Valianou L, Gika HG, Raikos N, Theodoridis G (2017) Sample preparation strategies for the effective quantitation of hydrophilic metabolites in serum by multi-targeted HILIC–MS/MS. Metabolites. https://doi.org/10.3390/metabo7020013

Vanaelst B, Rivet N, Huybrechts I, Ludes B, De Henauw S, Raul JS (2013) Measurement of cortisol and cortisone in children's hair using ultra performance liquid chromatography and tandem mass spectrometry. Anal Methods 5:2074–2082. https://doi.org/10.1039/c3ay26570f

Wennig R (2000) Potential problems with the interpretation of hair analysis results. Forensic Sci Int 107:5–12. https://doi.org/10.1016/S0379-0738(99)00146-2

Wester VL, van Rossum EFC (2015) Clinical applications of cortisol measurements in hair. Eur J Endocrinol 173:M1–M10. https://doi.org/10.1530/Eje-15-0313

Wester VL, Reincke M, Koper JW, van den Akker ELT, Manenschijn L, Berr CM, Fazel J, de Rijke YB, Feelders RA, van Rossum EFC (2017) Scalp hair cortisol for diagnosis of Cushing's syndrome. Eur J Endocrinol 176:695–703. https://doi.org/10.1530/Eje-16-0873

4.3   Therapeutic Drug Monitoring of Sunitinib in Gastrointestinal Stromal Tumors and Metastatic Renal Cell Carcinoma in Adults-A Review

Sunitinib (SUN) and its major metabolite N-desethyl sunitinib (DES), belonging to multitargeted tyrosine kinase inhibitors, exhibit a non-uniform therapeutic outcome in adult patients. In 2006, SUN was launched as a standard care treatment for metastatic cell carcinoma in adults, gastrointestinal stromal tumors, and in 2011 for pancreatic neuroendocrine tumors. Severe toxicity and adverse effects, frequently observed in clinical practice but not in type III clinical trials, could be explained by poor adherence, CYP polymorphisms, and drug-drug interactions. Therapeutic drug monitoring (TDM) could target the variable outcomes and decrease adverse effects' toxicity and/or frequency. Reviewing 73 articles related to a SUN or DES concentration-to-toxicity relationship concluded that the therapeutic trough levels should be in a range of 50–100 ng/ml for a total concentration SUN + DES. LC–MS is the method of choice for TDM as it provides unmatched sensitivity and specificity at the same time. SUN and DES may undergo Z/E-photoisomerization, forcing many laboratories and hospitals to work in the dark. Nevertheless, the light-induced isomerization is reversible, and the active (E-)isomer could be quantitatively reverted by heating the samples in the dark.[85] Quantitative determination was performed using isotopically labeled or chemically similar internal standards. As many worldwide LC–MS instruments have become available, the cost per sample could be kept relatively low. On the other hand, the high cost of therapeutic agents and molecular pathology-based indication rules should guarantee an optimal dose for each patient.

Therapeutic Drug Monitoring of Sunitinib in Gastrointestinal Stromal Tumors and Metastatic Renal Cell Carcinoma in Adults—A Review

Regina Demlová, MD, PhD,* Miroslav Turjap, PharmDr, PhD,† Ondřej Peš, PhD,‡
Katarína Kostolanská, PharmDr,‡ and Jan Juřica, PharmDr, PhD§¶

Background: Sunitinib is an inhibitor of multiple receptor tyrosine kinases and is a standard-of-care treatment for advanced and metastatic renal cell carcinoma and a second-line treatment in locally advanced inoperable and metastatic gastrointestinal stromal tumors. A fixed dose of the drug, however, does not produce a uniform therapeutic outcome in all patients, and many face adverse effects and/or toxicity. One of the possible causes of the interindividual variability in the efficacy and toxicity response is the highly variable systemic exposure to sunitinib and its active metabolite. This review aims to summarize all available clinical evidence of the treatment of adult patients using sunitinib in approved indications, addressing the necessity to introduce proper and robust therapeutic drug monitoring (TDM) of sunitinib and its major metabolite, N-desethylsunitinib.

Methods: The authors performed a systematic search of the available scientific literature using the PubMed online database. The search terms were "sunitinib" AND "therapeutic drug monitoring" OR "TDM" OR "plasma levels" OR "concentration" OR "exposure." The search yielded 520 journal articles. In total, 447 publications were excluded because they lacked sufficient relevance to the reviewed topic. The remaining 73 articles were, together with currently valid guidelines, thoroughly reviewed.

Results: There is sufficient evidence confirming the concentration–efficacy and concentration–toxicity relationship in the indications of gastrointestinal stromal tumors and metastatic renal clear-cell carcinoma. For optimal therapeutic response, total (sunitinib + N-desethylsunitinib) trough levels of 50–100 ng/mL serve as a reasonable target therapeutic range. To avoid toxicity, the total trough levels should not exceed 100 ng/mL.

Conclusions: According to the current evidence presented in this review, a TDM-guided dose modification of sunitinib in selected groups of patients could provide a better treatment outcome while simultaneously preventing sunitinib toxicity.

Key Words: sunitinib, N-desethylsunitinib, mRCC, GIST, therapeutic drug monitoring, toxicity-adjusted dosing

(*Ther Drug Monit* 2020;42:20–32)

INTRODUCTION

Sunitinib is a multitargeted receptor tyrosine kinase inhibitor (TKi), acting on signaling cascades involved in proliferation and tumor progression. It was launched in 2006 and became a standard-of-care treatment for advanced/metastatic renal cell carcinoma (mRCC) in adults and in unresectable and/or metastatic malignant gastrointestinal stromal tumor (GIST) in adults after the failure of imatinib treatment due to resistance or intolerance.[1,2] In 2011, sunitinib was additionally approved for the treatment of unresectable or metastatic, well-differentiated pancreatic neuroendocrine tumors (pNET) with disease progression in adults.[3]

Similar to other TKi, it seems that a fixed dose of sunitinib does not produce a uniform therapeutic outcome in patients. Furthermore, the frequency of adverse effects and toxicity also fluctuates.[4,5] One of the possible causes may be high interindividual variability in the systemic exposure to TKi due to the high variability in pharmacokinetics (PK) and genetic polymorphisms of specific efflux transporters.[6] In addition, a relationship has been found between plasma levels of several TKi and the treatment outcome and toxicity.[5,7–10]

In clinical practice, it has been documented that severe toxicity and adverse events occur more frequently in "real-life" patients than in phase III of clinical studies.[11] The causes of this discrepancy may be patients' nonadherence to the treatment, genetic polymorphisms of the cytochrome P450 (CYP) enzymes and transporters, or drug–drug interactions. The question of whether therapeutic drug monitoring (TDM) with an individualized dose adjustment may improve the therapeutic

outcome of sunitinib or at least improve its tolerability is yet to be answered. Hence, the main aim of this review lies in gathering maximum clinical evidence for the justification of TDM of sunitinib and its major metabolite, N-desethylsunitinib, in adult patients with approved indications in relation to an exposure/efficacy and exposure/toxicity relationship.

Pharmacodynamics of Sunitinib

Sunitinib exerts an inhibitory action on several receptor tyrosine kinase families, including receptors for PDGFR-α, PDGFR-β, VEGFR1-3, and c-KIT. Furthermore, it also inhibits FMS-like tyrosine kinase 3 (Tyrosine kinase involved in the regulation of the family of genes originally isolated from the Susan McDonough strain of feline sarcoma virus, FLT), a macrophage colony-stimulating factor receptor (CSF-1R), and a glial cell-line derived neurotrophic factor receptor (RET = rearranged during transfection; protooncogene).[12–14] Sunitinib, compared with interferon-α, placebo, or other targeted agents, showed improved progression-free survival (PFS) in randomized phase III trials.[15] Together with pazopanib and a combination of nivolumab and ipilimumab, sunitinib is currently the most preferred and used TKi in the treatment of mRCC[2,16] and according to the European Society for Medical Oncology, British Sarcoma Group, and National Comprehensive Cancer Network guidelines, also the second-line treatment of metastatic GIST.[1,16,17] Moreover, sunitinib is currently being investigated in 102 clinical trials, including for type B3 thymoma and thymic carcinoma (NCT03449173), glioblastoma (NCT03025893), genitourinary cancer (NCT02060370), urinary tract urothelial carcinoma (NCT00794950), brain metastases (NCT00981890), endometrial adenocarcinoma (NCT00478426), soft-tissue sarcoma, bone sarcoma (NCT03277924), ciliary body and choroid melanoma (NCT02068586), ovarian clear-cell adenocarcinoma (NCT00979992), prostate cancer (NCT00329043), thyroid gland carcinoma (NCT00381641), pheochromocytoma and paraganglioma (PPGL) (NCT01371201), small-cell lung carcinoma (NCT00453154), breast cancer (NCT00513695), lymphoma, non-Hodgkin lymphoma, and multiple myeloma (NCT02693535).

PK Properties

Sunitinib is absorbed slowly and reaches a maximal plasma concentration (C_{max}) within 6–12 hours (h) after oral administration.[3,14] Although the absolute bioavailability has not been assessed in humans, the preclinical experiments approximated it to reach ~50% owing to the extensive first-pass effect.[18–20] The type of meal does not seem to affect the bioavailability.[21] PK is linear in the range of doses from 50 to 350 mg/d[3,19] The steady-state concentration (c_{ss}), owing to the long elimination half-life, is reached after 10–14 days of regular administration.[22] However, a simulation made from 1205 samples taken from 70 patients determined the time to reach 90% of the steady state was 6 days for sunitinib and 8 days for N-desethylsunitinib.[23] Sunitinib and N-desethylsunitinib are bound extensively to plasmatic proteins (95% and 90%, respectively), and both have a large volume of distribution (V_d) of more than 2300 and 3000 L, respectively.[3,24] In the preclinical experiments, protein binding profiles seem

to be linear; hence, hypoalbuminemia may lead to decreased total concentrations of sunitinib and N-desethylsunitinib and an increased volume of distribution.[25]

On the other hand, sunitinib intracellular penetration is not influenced by active transport; nevertheless, it may be limited by the activity of the efflux transporters, ABCB1 and ABCG2.[19,26–30] The transporters also prevent the passage of sunitinib through the blood–brain barrier.[31] Sunitinib is subject to microsomal oxidative dealkylation through CYP3A4 to N-desethylsunitinib, which shows a similar inhibitory action on tyrosine kinases as the parent drug. It has been estimated that N-desethylsunitinib adds approximately 30% to the overall sunitinib + N-desethylsunitinib exposure.[3] N-desethylsunitinib is further metabolized through CYP3A4, and its elimination half-life is even longer, up to 80–100 hours, while its V_d is similar or greater than that of sunitinib.[19] More than 60% of the administered dose is excreted in feces, and only a small percentage appears in the urine.[32] No accumulation of sunitinib or N-desethylsunitinib was observed within 13 cycles (28 days of treatment) in patients with GIST dosed with 37.5 mg/d.[33]

Biotransformation of sunitinib is influenced by sex—female patients have up to 30% lower apparent clearance (Cl/F), but even this difference does not imply different dosing for women.[3,34] Only minor differences in sunitinib plasma concentrations within various age groups in the outpatient population have been reported.[35] Patients with mRCC older than 70 years received significantly lower doses compared with those received by younger individuals (median dose 37.5, and 50 mg/d, respectively).[36]

Mild to moderate hepatic impairment (Child–Pugh scores A and B) has no significant effect on sunitinib exposure[37]; the influences of more severe hepatic impairment have not yet been studied. In the patients with renal impairment (ClCr ≤30 mL/min), the sunitinib systemic exposure was similar to that in patients with normal renal functions. In the hemodialyzed patients, the exposure decreased to 47% of the exposure observed in patients with normal renal functions.[3,14] The influence of hemodialysis on the PK of sunitinib is somewhat inconclusive.[38] Terada et al[39] concluded that sunitinib could be used in hemodialyzed patients without any special dose adjustments since its PK, owing to its large volume of distribution, is affected by high plasma protein binding and rather extensive liver metabolism.

The effect of biorhythms was also studied, with sunitinib reported to attenuate circadian blood pressure rhythmicity.[40] Neither morning nor evening administration had any apparent effect on the therapeutic outcome or PK[41]; however, the severity of the adverse events was slightly lower in patients receiving sunitinib in the morning compared with the evening dosing.[42]

Adverse Effects and Toxicity

Sunitinib is, in the context of other targeted therapy agents for mRCC and GIST, well tolerated at recommended dosing, and most adverse effects observed were mild to moderate. Reported adverse effects (occurring in ≥20% patients) included anemia, skin discoloration, fatigue, gastrointestinal disorders (diarrhea, nausea, and vomiting), stomatitis, decreased appetite, taste disturbance, hypertension, hand-foot

syndrome (HFS), hypothyroidism, and mucosal inflammation.[3,43] Hematological disorders such as neutropenia, thrombocytopenia, and anemia are among the most common adverse effects.[44] A decline in the left ventricular ejection fraction also appeared quite often.[43] Severe but rare adverse effects of sunitinib include renal or heart failure, pulmonary embolism, gastrointestinal perforation, and hemorrhages.[3,45] In addition to the adverse effects mentioned in the summary of the product characteristics, hepatotoxicity (an increase in liver transaminases), increased creatinine, anorexia, dysgeusia, mucositis, and epistaxis have been observed in real-life patients.[46,47] Some of the aforementioned adverse effects may diminish with treatment continuation.

Dosing Schedules

In mRCC and GIST indications, sunitinib recommended dosing consists of 50 mg/d over 4 consecutive weeks followed by a 2-week rest period (4/2). An alternative dosing schedule of 50 mg/d for 2 weeks with a single-week rest period (2/1) should help in reducing the sunitinib toxicity in mRCC patients without compromising the efficacy.[48,49] In GIST, an alternative of 37.5 mg continuously has also been tested and proved to be a possible dosing strategy.[33] Recently, in a small Japanese study, an alternative to 4/2 dosing was evaluated. Administration of sunitinib in 23 patients every other day with a standard dose (50 or 37.5 mg) resulted in a better time to progression (TTP), overall survival (OS) outcomes, and tolerability (lower frequency of HFS, thrombocytopenia, and leucopenia). The total trough levels (TTLs) were significantly lower (64.83 versus 135.8 ng/mL, $P < 0.001$).[50]

The approved dose of sunitinib in the pNET indication is 37.5 mg/d administered continuously. Dose modification based on individual safety and tolerability is possible in 12.5 mg steps; however, the daily dose should be kept in a specific range (25–75 mg/d for mRCC and GIST, while the maximal studied daily dose for pNET was 50 mg/d).[3]

In special situations, such as coadministration of inducer or inhibitor of sunitinib metabolism, a dose modification has been advised. When coadministration of a CYP3A4 inducer cannot be avoided, a dose modification up to 87.5 or 62.5 mg/d is recommended for mRCC/GIST or pNET, respectively.[3]

Drug–Drug Interactions

PK interactions generally include (1) drugs influencing the main biotransformation pathway (CYP3A4) of sunitinib or (2) sunitinib theoretically influencing the effects of other drugs. Inducers of CYP3A4 enzymes, such as anticonvulsants (carbamazepine, phenobarbital, or phenytoin), rifampin, mitotane, dexamethasone, or St. John's wort might decrease plasma levels or systemic exposure of sunitinib.[14,51] On the other hand, coadministration of sunitinib with CYP3A4 enzyme inhibitors might result in supratherapeutic trough levels and increased incidence or a higher grade of toxicity. Such drugs include macrolide antibiotics (clarithromycin), azole antifungals (ketoconazole, itraconazole, voriconazole, or posaconazole), HIV protease inhibitors (indinavir, ritonavir, nelfinavir, or saquinavir), aprepitant, as well as food supplements based on citrus juice.[3,14] A few interactions were documented

in clinical studies, for example, in highly active antiretroviral therapy, where ritonavir and efavirenz increased or decreased the exposure of N-desethylsunitinib, respectively.[52] It was also reported that coadministration of sunitinib with proton-pump inhibitors is associated with higher plasma concentrations of sunitinib (+53%).[35] Sunitinib is a moderate inhibitor of CYP3A4 and, therefore, might increase plasma concentrations of drugs metabolized by this enzyme.[53,54] If concurrent administration with an enzyme inhibitor or inducer is necessary, a dose modification with TDM should be considered.[3] Sunitinib is a PgP inhibitor and, thus, may increase the toxicity of PgP substrates including colchicine.[55]

The displacement of sunitinib/N-desethylsunitinib from plasma proteins may also be theoretically relevant when administering with a drug that has a high affinity to albumin. Such interaction has yet not been reported; however, several antiretroviral treatment schedules did not show a significant change in the unbound fraction of sunitinib and/or N-desethylsunitinib.[52]

Pharmacodynamic (PD) interactions are expectable in a combination of sunitinib with drugs affecting heart rhythmicity, immune response, liver functions, and, most notably, bisphosphonates, which may increase the risk of osteonecrosis of the jaw.[14] Because of these effects, sunitinib should be used with caution in a combination with antiarrhythmics or drugs suspected of prolonging the QT interval (eg, several antipsychotics, antidepressants, 5-HT$_3$ antagonists, prokinetics, quinolones, fingolimod, vemurafenib, or nilotinib).[56] Such an interaction is dangerous and possibly the most common PD interaction.[57] Meanwhile, sunitinib should be used carefully with drugs that are hepatotoxic or may increase levels of alanine aminotransferase or aspartate aminotransferase (eg, leflunomide, acetaminophen, lomitapide, or nimesulide) since sunitinib was mentioned in the "black box warnings" by the Food and Drug Administration.[58] Since sunitinib is also thyrotoxic, particular caution should be taken when sunitinib is coadministered with amiodarone (thyrotoxic + proarrhythmic).[47] Finally, all immunosuppressants might increase the risk of opportunistic infections.[14] Interactions with immunostimulant food supplements such as *Echinacea* extracts or beta-glucans should be considered as well.[59]

METHODS

The literature search was conducted in December 2018 using the PubMed online database. Search terms used were "sunitinib" AND "therapeutic drug monitoring" OR "TDM" OR "plasma levels" OR "concentration" OR "exposure" in "all fields." Searches were limited to human studies and publications in English or German languages. The initial search provided 520 journal articles. A single author (J.J.) read the abstracts of these articles. In total, 447 publications were excluded because they lacked relevance to the reviewed topic or were focused on TDM of sunitinib in indications other than mRCC and GIST. The relevant 73 articles were revised as they contained prospective, retrospective, and cross-sectional observational studies, interventional randomized controlled trials, literature reviews, letters to editors, and case reports. Currently valid guidelines were also included in the review.[1,2,16,60]

RESULTS

Benefit of TDM of Sunitinib in the Treatment of mRCC and GIST

The most significant benefits from TDM are observed in drugs when (1) no clear or safe marker of the clinical effect may be readily measured; (2) toxicity or inefficacy may harm the patient; (3) the clinically relevant concentration–response (effect/toxicity) relationship has already been established; (4) a narrow therapeutic range exists; (5) no or poor correlation of a dose–response relationship exists, or (6) a high degree of interindividual variability of plasma concentrations exists. Other circumstances such as the presence of an active metabolite in clinically relevant concentrations, great interaction potential of the drug, or nonlinear PK might be considered as well.

In the case of sunitinib and N-desethylsunitinib, most of the criteria are perspicuous (1–4), while Lankheet et al[35] did not find any relationship between the dose and the plasma concentration (5). Therefore, as in the case of imatinib, it may prove beneficial to monitor plasma concentrations of sunitinib to avoid toxicity and/or to improve the therapeutic outcome.

A lack of correlation between the dose and the drug exposure [area under the time–concentration curve (AUC)] or predose concentration (C_{trough}) also justifies the use of TDM.[35,61] As the recommended dose of fixed 50 mg/d (dose reduction is considered only in extreme adverse effects) has been used in all patients regardless of their weight, sex, or age, the interindividual PK variability is very high (for AUC and C_{trough} up to 41% and 54%, respectively).[62] Other authors have reported the interpatient variation coefficient (CV) of C_{max}, AUC, and C_{trough} to be in the range of 20%–60%.[33,35,63–65] Faivre et al[63] have observed that differences in C_{trough} between individuals on the same dose might reach 1 order of magnitude. Similar intrapatient variability determined as CV of C_{trough} has also been reported.[65,66] On the other hand, a strong correlation between sunitinib, N-desethylsunitinib, and its combined C_{trough} (TTL) and AUC (combined $AUC_{0–24h}$) has been observed.[67]

Concentrations Achieved at Standard Dosing Schedules

Demetri et al[68] conducted a study with 79 patients with GIST; 79% of the patients on the 50 mg/d dose had TTL over 50 ng/mL by the 14th day of treatment. Lower TTL in the 2/2 schedule (32–47 ng/mL) was observed than in the 4/2 (38–66 ng/mL) or 2/1 (48–63 ng/mL) schedules. Lankheet et al[4] published a study where 42 patients with advanced solid tumors (6 mRCC, 8 neuroendocrine carcinomas, 8 colorectal carcinomas, 3 adenocarcinomas of an unknown origin, 3 uveal carcinomas, and 14 miscellaneous) had the median TTL value of 49.5 ng/mL by the 15th day of treatment when dosed with 37.5 mg continuously.

Interestingly, in toxicity-adjusted dosing (TAD), the median TTL in 45 patients with mRCC was 67.4 ng/mL, and the interindividual variability (represented by SD) was 25.8 ng/mL.[66] In the study with Chinese patients with mRCC who were administered 37.5 mg/d in the 4/2 schedule, 84%–92% of patients had C_{trough} greater than 50 ng/mL in the cycles 1–3.[69] The

latter finding could be explained by ethnic differences in the occurrence of some polymorphisms (ABCG2).[29,70,71] More frequent adverse events in the Asian population are also in line with these findings.[72]

Determination of Sunitinib in Human Plasma for TDM Purposes

Since sunitinib and its salts are of intense orange-yellow color, their concentrations are determined by liquid chromatography (LC) UV–Vis methods with satisfactory results.[73,74] However, TTLs are expected to range below the detection limit for most LC UV–Vis methods with some exceptions.[75,76] This makes liquid chromatography–mass spectrometry (LC-MS/MS), frequently based on triple quadrupole analyzers, the ideal choice for sunitinib TDM. Sunitinib is very light sensitive, and all samples should be prepared and analyzed under strict light-protected conditions,[77] determined as a sum of both isomers, or converted back to the (E)-isomer.[78]

To determine sunitinib alone or sunitinib + its metabolite, most authors use stable isotopically labeled internal standards[35,79–91] because they are generally recommended for use in quantitative MS.[92,93] However, some methods were successfully validated with the use of a chemically similar internal standard such as dasatinib,[77,94] buspirone,[95] clozapine,[96] imatinib,[97,98] sorafenib,[99] or testosterone.[100] In 1 case, an external standard calibration was used.[101]

TDM generally requires very sensitive methods to establish TTL. Methods based on LC-MS/MS provide a rapid and reliable option to monitor low concentrations of sunitinib and N-desethylsunitinib in patient plasma. Even as the number of LC/MS instruments worldwide has increased, it still demands a high initial cost and a skilled operator. Such facts may significantly contribute to whether the TDM can be successfully performed at a specific institution.

Exposure–Efficacy Relationship and Therapeutic Target Range

The primary focus of the preclinical in vitro/in vivo studies performed by Mendel et al[102] was to develop a quantitative understanding of the plasma levels of sunitinib exposure required to achieve target inhibition (for each of its primary targets). It might be defined as the extent to which the targets need to be inhibited to have some biologic activity and the fraction of the dosing interval the targets need to be inhibited to achieve optimal antitumor activity. In the preclinical experiments, sunitinib selectively inhibited VEGFR2 and PDGFRβ phosphorylation in a time- and dose-dependent manner, achieving strong inhibition of both targets when plasma concentrations reached or exceeded 50–100 ng/mL.[3,79,102,103] Moreover, constant inhibition of VEGFR2 and PDGFRβ phosphorylation was not required for the efficacy; at highly efficacious doses, the inhibition was sustained for 12 hours of a 24-hour dosing interval.[102,104] Hence, even complete in vitro inhibition of phosphorylation was not reflected in clinical outcomes.

Objective measures of treatment outcomes, such as TTP, OS, PFS, time to treatment failure, time to next treatment, or frequencies and severity of adverse effects, are

recorded in clinical studies to demonstrate the real benefit of TDM. These are often recorded simultaneously, especially when there are some drawbacks to distinct measures (eg, time to treatment failure does not sufficiently reflect toxicity) or because they require large population samples (eg, OS).

Such preclinical PK–PD relationship has been tested and confirmed in early clinical trials. As an example, a phase I dose-escalation study by Faivre et al[63] was undertaken in patients with advanced solid malignancies. PK data from the study indicated that doses of 50 mg/d led to TTL ranging from 50 to 100 ng/mL. The clinical activity was observed once the patients achieved daily doses of sunitinib that resulted in steady-state TTL of 50–100 ng/mL. The most convincing evidence for a correlation between exposure and the treatment response in humans came from a PK–PD analysis performed by Houk et al.[61] The authors investigated the relationship between clinical end points and sunitinib exposure in patients with advanced solid tumors. PD data were available for 639 patients of whom 434 had PK data (146 with mRCC, 219 with GIST, and 69 with solid tumors). The results indicated that the increased exposure to sunitinib was associated with an improved clinical outcome (longer TTP, longer OS, and higher chance of antitumor response), as well as with an increased risk of adverse effects in patients with mRCC and GIST.[61] Low sunitinib exposure was associated with a reduced response rate, TTP, and OS in both patients with mRCC and GIST. The exposure–response relationship in sunitinib has been reported in mRCC, GIST, and in other solid tumors in the 4/2 sunitinib dosing schedule. In particular, sunitinib AUC_{0-24} greater than 800 and 600 ng/mL·h were associated with higher rates of OS, TTP, and overall response rate in patients with mRCC and GIST.[61,65] When these AUCs were extrapolated to TTL, the levels of 36.4, 24.6, and 30.5 ng/mL were obtained, which were lower than the recommended target TTL (50–100 ng/mL).

When sunitinib was dosed continuously at 37.5 mg/d, a lower C_{trough} of 37.5 ng/mL is considered a reasonable target value in patients with pNET.[65] Correspondingly, it has been shown that exposure correlated with the treatment outcome; the patients with combined AUC_{0-24} above the median had greater OS (35.2 months) than patients with combined AUC_{0-24} below the median (16.7 months).[105] Yu et al[106] proposed practical guidelines for TKi TDM in GIST with a continuous dosing schedule of 37.5 mg/d with TTL 37.5–50 ng/mL. Analogously, the authors proposed a dosing schedule 4/2 of 50 mg/d, with TTL being higher than 50 ng/mL in RCC.

It has been recommended that dose increments should be undertaken in patients with TTL below 50 ng/mL.[4,5,35,106,107] In recent clinical studies, TTLs were reached in up to 50% of the patients at a fixed dose.[4,35] Similar percentages of patients who did not reach TTL were also estimated by a PK-based simulation.[107]

In a prospective study by Narjoz et al,[105] 55 patients with mRCC were assessed for an exposure-survival analysis. Patients with high combined AUC had a longer survival than patients with low AUC. In a retrospective observational clinical study in Japanese patients with RCC (n = 21), Noda et al[38] reported worse clinical outcomes in patients with

TTL ≥ 100 ng/mL. Most of these patients experienced unacceptable toxicity. A dose reduction might be needed in such cases to avoid unnecessary early discontinuation of the treatment due to toxicity.[38] The exposure–efficacy relationship studies with sunitinib are summarized in Table 1.

The phase II TAD study of Uemura et al[108] aimed to assess the efficacy and safety of sunitinib in Japanese patients with mRCC. Sunitinib was self-administered at a starting dose of 50 mg daily (mRCC, 4/2, n = 51). Doses were reduced to 37.5 mg/d in cases of treatment-related grade ≥3 adverse events and by additional 12.5 mg/d to a minimum dose of 25 mg/d if toxicity persisted. All 51 patients experienced treatment-related adverse events, the majority of which were grade 1 or 2 in severity. At final dose levels, median TTL reached therapeutic levels (>50 ng/mL) on day 14 of the first cycle. Nine patients experienced treatment-related adverse events that led to discontinuation.[108] In the TAD study by Sabanathan et al[66] with patients with mRCC (n = 45), the sunitinib dose was increased/decreased to ensure only grade 1 or 2 toxicity on 10–20 days of each 42-day cycle. Eventually, 91% of the patients achieved the target toxicity with a final sunitinib dose of 25 mg (18%), 37.5 mg (27%), 50 mg (50%), and 62.5 or 75 mg (7%). At TAD, the mean TTL of the study group was 72.0 ng/mL (median 67.4 ng/mL; SD 25.8 ng/mL). Using TAD, the majority of patients (85%) achieved TTL above the proposed effective range of >50 ng/mL. Fifteen percent of patients had TTL > 100 ng/mL. Patients requiring the dose reduction owing to increased toxicity during the dose manipulation period had TTL of <50 ng/mL (2 patients), 50–100 ng/mL (5 patients), and >100 ng/mL (8 patients).[66]

In the observational study with an unselected cohort of outpatients with cancer in routine clinical practice (patients on sunitinib n = 31) by Lankheet et al,[35] the sunitinib C_{trough} ranged from 14.7 to 93.7 ng/mL; however, the predefined target concentration of ≥50 ng/mL was reached in only 51.4% of the patients.

The feasibility of PK-guided dosing was investigated in the following studies. A prospective study by Lankheet et al[4] was conducted to determine the safety and feasibility of sunitinib dosing based on TTL in patients with advanced solid tumors (n = 42). Patients were given sunitinib at 37.5 mg/d continuously. On days 15 and 29 of the treatment, TTL was measured. If TTL was <50 ng/mL and the patient did not show any grade ≥3 toxicity, the daily sunitinib dose was increased by 12.5 mg. If the patient suffered from grade ≥3 toxicity, the sunitinib dose was lowered by 12.5 mg. The assessment of 29 out of 42 patients revealed that grade ≥3 adverse events were experienced in 7 patients (24%) at the starting dose and in 9 patients (31%) after the dose escalation. TTL was below the proposed target in 15 patients (52%) at the starting dose. Of these, 5 patients (17%) reached target TTL after the dose escalation without any additional toxicity.

The aim of a retrospective cohort study by Lankheet et al[5] was to monitor how many patients reached the target exposure after a PK-based dose optimization in daily practice. Twenty-seven patients (23 with mRCC and 4 with GIST) were treated with sunitinib and provided 75 samples. In the study, the target range was 50–87.5 ng/mL for mRCC

TABLE 1. The Exposure–Efficacy Relationship of Sunitinib in mRCC and GIST

Tumor Type	n	PK Parameter	Outcome	Correlation	Significance	Reference
Advanced solid (preclinical)		TTL	Target inhibition	A C_{trough} of 50–100 ng/mL is the minimum plasma concentration required to inhibit Flk-1/KDR (VEGFR2) and PDGFRβ	N/A	102
mRCC	146	Sunitinib AUC_{0-24}; combined AUC_{0-24}	TTP	TTP increased with increasing AUC_{0-24}	$P = 0.001$	61
			OS	OS increased with increasing AUC_{0-24}	$P = 0.010$	
		Sunitinib AUC_{0-24}	PR or CR	PR and CR increased with increasing AUC_{0-24}	$P = 0.00001$	
			SD	SD increased with increasing AUC_{0-24}	$P = 0.002$	
mRCC	21	TTL < versus ≥ 100 ng/mL	TTF	Median TTF, 590 versus 71 d	$P = 0.04$	38
			PFS	Median PFS, 748 versus 238 d	$P = 0.02$	
mRCC	20	TTL < versus ≥ 50 ng/mL	TTF	Median TTF, 743 versus 56 d	$P < 0.001$	109
			PFS	Median PFS, 731 versus 95 d	$P < 0.001$	
mRCC	55	Combined AUC > versus < 1973 ng/mL·h at day 21	OS	Patients with high combined AUC had a longer survival than patients with low combined AUC	$P = 0.0051$	105
GIST	225	AUC_{ss}	PR and CR	Probability of PR or CR correlates with exposure	$P = 0.06$	61
			SD	Probability of SD correlates with exposure	$P = 3 \times 10^{-9}$	
			TTP and OS	Above median AUC_{ss} displayed Longer TTP and OS	N/A	
GIST	278	AUC_{0-24} > versus < 600 ng/mL·h	TTP, OS, and SD	TTP, OS, and SD increased with AUC_{0-24}	$P = 0.001$	65
			ORR	TTP, OS, and SD increased with AUC_{0-24}	$P = 0.06$	
mRCC	33	Combined AUC_{0-24}	Disease progression	In patients with disease progression, combined AUC_{ss} tends to be lower than in patients without disease progression during the first cycle (1678 versus 2004 ng/mL·h, respectively)	$P = 0.072$	11
mRCC	26	Sunitinib C_{trough}	PFS	No association of TTL with PFS or OS	$P = 0.269$	67
			OS		$P = 0.681$	
		TTL	PFS	No association of TTL with PFS or OS	$P = 0.425$ (PFS)	
			OS		$P = 0.505$ (OS)	
		N-desethylsunitinib C_{trough}	PFS	C_{trough} >15 ng/mL associated with increased PFS (61 wks versus 12 wks)	$P = 0.004$	
			OS	C_{trough} >15 ng/mL associated with increased OS (36 mo versus 8 mo)	$P = 0.040$	

CR, complete response; ORR, overall response rate; PR, partial response; SD, stable disease; TTF, time to treatment failure.

intermittent dosing (starting dose 50 mg/d) and 37.5–75 ng/mL for mRCC and GIST continuous dosing (starting dose 37.5 mg/d). For patients with TTL within the target range, the advice was to maintain the same dose level if the toxicity was manageable. For patients with TTL below the target range, it was advised to increase the dose to reach the target

TTL. If the TTL was above the target range and signs of toxicity were present, the dose was decreased to reach the target TTL range. After the start of treatment, the first mean TTL was 35.8 ng/mL (ranging from 23.9 to 53.5 ng/mL) with 14 (51.9%) patients being below and 6 patients (22.2%) above the proposed TTL target range. At the last

measurement, the mean TTL was 50.4 ng/mL (ranging from 44.2 to 57.6 ng/mL) with 5 (18.5%) and 2 (7.4%) patients being below and above the proposed TTL target range, respectively. Thus, the proportion of the patients within the target range increased from 26% to 74%. The unusually low proportion of patients in the target range at the start of the study was probably caused by the selection bias. First, only the minimal effective target levels were known from the previous studies, and at the beginning of each study period, TDM was not part of the routine care but was reserved for the cases of suspected toxicity or suboptimal drug response.[5] On the other hand, in a recent small study of Takasaki et al[109] performed on patients with mRCC, better clinical outcomes (TTP and PFS) were observed in the group with TTL <50 ng/mL than in the group with TTL >50 ng/mL.

Summary

Most studies with patients with mRCC and GIST confirmed better efficacy of sunitinib when TTLs were greater than 50 ng/mL. There were also reported better outcomes in combined AUC_{0-24h} greater than 600 and 800 ng/mL·h for patients with mRCC and GIST.

Exposure–Toxicity Relationship

Sunitinib exposure (AUC) or TTL has been associated with various kinds of toxicity. In one of the first studies with sunitinib, most patients with dose-limiting toxicity had C_{trough} greater than 100 ng/mL. Furthermore, a correlation between an advanced age and sunitinib exposure with grade ≥3 toxicity and N-desethylsunitinib exposure with grade ≥2 thrombocytopenia has been reported.[105]

In a phase I dose-escalation study conducted by Faivre et al,[63] the occurrence of dose-limiting toxicities was associated with sunitinib C_{trough} >100 ng/mL. Patients with TTL ≥100 ng/mL had a higher incidence of grade ≥3 toxicity in a retrospective observational clinical study by Noda et al.[38] Significantly higher incidence of grade ≥2 thrombocytopenia and grade ≥2 hypertension in patients with TTL ≥90 ng/mL than those with TTL <90 ng/mL was identified in a study by Mizuno et al.[29] In this study, the authors reported a hazard ratio of 3.0 for high versus low AUC with a threshold of 2600 ng/mL·h for a shorter treatment period without discontinuation or dose reduction. Similarly, a PK simulation in a study conducted by Nagata et al[110] indicated that the sunitinib C_{trough} should be <100 ng/mL to avoid severe thrombocytopenia.

In the study by Teo et al,[69] patients who manifested grade ≥2 mucositis and altered taste had higher TTLs than those who had grade 1 or no toxicity. In the prospective study, Bello et al[111] reported an association between sunitinib exposure and prolongation of the QT interval. Sunitinib C_{trough} was positively correlated with the occurrence of fatigue.[30,61] Furthermore, the increased sunitinib exposure was negatively correlated with changes in the absolute neutrophil count and positively with changes in diastolic blood pressure. However, at a dose of 50 mg/d (4/2), these effects were generally mild to moderate and easy to manage.[61] In a prospective PK study by Kloth et al,[30] patients with grade ≥3 toxicity had a significantly lower clearance of sunitinib than patients without grade ≥3 toxicities. In the review of de Wit et al,[65] there was a positive

correlation between C_{trough} and increase in diastolic blood pressure, AUC_{0-24}, and fatigue, and a negative correlation between cumulative (per cycle) AUC and grade ≥2 absolute neutrophil count. Grade ≥2 thrombocytopenia was also significantly more frequently observed in patients with sunitinib C_{trough} >90 ng/mL than in the patients with sunitinib C_{trough} <90 ng/mL (100% versus 53%). In line with these findings, a combined AUC_{0-24} value was independently associated with any grade ≥3 toxicity. Receiver operating characteristics revealed a combined AUC_{0-24} threshold of 2150 ng/mL·h for grade 3 toxicity.[11] However, in the toxicity-based dosing study of Lankheet et al,[4] the initial proportion (before any dose modification) of patients with toxicity was higher in the group with TTL <50 ng/mL than in the group with TTL >50 ng/mL. The exposure–toxicity relationship studies are summarized in Table 2.

Practical guidelines for TDM of TKi by Yu et al[106] proposed a dosing schedule of 50 mg/d (4/2) with TTL >50 ng/mL and 37.5–50 ng/mL as a PK target in RCC and GIST, respectively. Recent practical recommendations for TDM of kinase inhibitors by Verheijen et al[112] proposed a similar target TTL (≥50 ng/mL for intermittent dosing and ≥37.5 ng/mL for continuous dosing). Based on the toxicity studies, a value of 100 ng/mL should be considered as upper TTL.

Sunitinib SmPC,[3] European Society for Medical Oncology Clinical Practice Guidelines,[2] National Comprehensive Cancer Network guidelines,[16] or European Association of Urology guidelines[60] do not mention the determination of sunitinib plasma levels as a possible step in a dose individualization strategy.

The therapeutic goal in the treatment of mRCC is the prolongation of survival. Thus, it is critical to maximize the chance for response by consecutively reaching and maintaining adequate drug exposure and keeping treatment-related toxicities at an acceptable level while increasing the drug adherence and overall time on treatment. TDM may include prevention of treatment failure or severe toxicity as a consequence of inadequate drug exposure, avoidance of low exposure in renal or hepatic impairment (including patients in continuous renal replacement therapy), and management of PK variability caused, for example, by drug–drug interactions or suspected genetic polymorphism and concerns over adherence to treatment. TDM could also be helpful in unique populations, such as in age or weight extremes (children, elderly, patients with limb amputation, or obese patients), or rare ethnic/genetic groups of patients.

Summary

The promising benefit/risk ratio occurs when TTL are below 100 ng/mL or combined AUC_{0-24h} below 2150 ng/mL·h.

Population PK–PD Modeling for Prediction of Sunitinib Exposure

Several population-based PK models for individual prediction of plasmatic concentrations of sunitinib have been developed. They involve either a 1- or 2-compartment model for sunitinib or a 2-compartment model for N-desethylsunitinib.[23,61,107,113] Some of these models also include various

TABLE 2. An Overview of Exposure–Toxicity Relationship Studies

Tumor Type	n	PK Parameter	Outcome	Correlation	Significance	Reference
Solid	28	TTL >100 ng/mL	Dose-limiting toxicity (DLT)	Most patients with DLT had TTL >100 ng/mL	N/A	63
mRCC	19	TTL > or ≤90 ng/mL	Grade ≥2 thrombocytopenia	100% versus 55.6%	$P = 0.033$	29
			Grade ≥2 hypertension	90% versus 22.2%	$P = 0.0055$	
Solid, GIST, and mRCC	443	Combined AUC_{0-24}	Fatigue	A positive correlation between AUC_{0-24} and the incidence of fatigue	N/A	61
		Combined AUC_{cum28}	ANC	ANC decreased linearly with increasing AUC_{cum28}	N/A	
		TTL	dBP	dBP increased linearly with increasing TTL	N/A	
Solid	24	TTL ≥ versus < 180 ng/mL	QTc prolongation	15.4 versus 9.6 milliseconds	N/A	111
pNET, GIST, and mRCC	52	CL/F	Grade 3 toxicity	34.4 versus 41.4 L/h for patients with versus without grade 3 toxicity	$P = 0.025$	30
		TTL	Fatigue	A positive correlation between C_{trough} and the occurrence of fatigue	$P = 0.007$	
mRCC	36	TTL	Grade ≥2 versus grade ≤1 mucositis	126.46 versus 84.81 ng/mL for patients with grade ≥2 versus grade ≤1 toxicity	$P = 0.04$	69
			Altered taste	159.91 versus 105.22 ng/mL for patients with grade ≥2 versus grade ≤1 toxicity	$P = 0.05$	
RCC	21	TTL > or <100 ng/mL	Grade ≥3 toxicities	Patients with >100 ng/mL TTL (n = 8), compared with patients with <100 ng/mL (n = 13), had a greater incidence of grade ≥3 toxicities (6 patients, ie, 75.0% versus 3 patients, ie, 23.1%).	N/A	38
RCC	6	TTL	Grade ≥2 thrombocytopenia	PK/PD simulations indicate that TTL should be <100 ng/mL to avoid severe thrombocytopenia	N/A	110
Advanced	29	TTL	Grade ≥3 toxicity (CTCAE 4.02)	TTL <50 ng/mL	N/A	4
				17.2% no severe toxicity, 34.5% severe toxicity		
				TTL ≥50 ng/mL 28.6% no severe toxicity		
				20.7% severe toxicity		
mRCC, GIST	29	TTL	Serum AST and ALT activity	Higher plasma concentration associated with higher AST and ALT activity	N/A	35
Advanced solid	105	Combined AUC_{0-24}	Any grade ≥3 toxicity	Combined AUC_{0-24} associated with grade 3–4 toxicity	$P < 0.0001$	11
Advanced/metastatic solid	92	Sunitinib AUC	Any grade ≥3 toxicity	Sunitinib AUC independently associated with any grade ≥3 toxicity [OR = 1.16 (1.05–1.28)]	$P = 0.005$	105
		N-desethylsunitinib AUC	Grade ≥2 thrombocytopenia	N-desethylsunitinib AUC independently associated with any grade ≥3 toxicity [OR = 1.27 (1.03–1.57)]	$P = 0.028$	
mRCC	26	Sunitinib C_{trough}	Grade ≥1 HFS	Higher sunitinib C_{trough} associated with HFS (89.5 versus 48.3 ng/mL)	$P < 0.01$	67

TABLE 2. (*Continued*) An Overview of Exposure–Toxicity Relationship Studies

Tumor Type	n	PK Parameter	Outcome	Correlation	Significance	Reference
		Sunitinib C_{trough}	Grade ≥1 thrombocytopenia	Higher sunitinib C_{trough} associated with thrombocytopenia (89.5 versus 50.8 ng/mL)	$P = 0.02$	
		TTL	Grade ≥1 HFS	Higher TTL associated with HFS (75.2 versus 64.2 ng/mL)	$P < 0.01$	
		TTL	Grade ≥1 thrombocytopenia	Higher TTL associated with thrombocytopenia (64.4 versus 75.2 ng/mL)	$P = 0.01$	

ANC, absolute neutrophil count; ALT, alanine aminotransferase activity; AST, aspartate aminotransferase activity; AUC_{cum28}, cumulative 0–28 day AUC of sunitinib + N-desethylsunitinib; dBP, diastolic blood pressure; OR, odds ratio.

covariates, which help in the explanation of interindividual variability in plasmatic concentrations, for example, gene polymorphism of ABCG2 and lean body mass.[29,105] The univariate analysis showed that single nucleotide polymorphisms of CYP3A4, CYP3A5, and ABCB1 affected sunitinib and N-desethylsunitinib clearance, but the effect was lower than the interindividual variability.[6] A study of Theo et al[114] confirmed that CYP3A5 did not play a significant role in sunitinib exposure. This was not surprising since CYP3A5 barely contributes to the overall sunitinib clearance.[53] PK–PD models were also developed to predict the clinical benefit of sunitinib TDM.

Goulooze et al[107] performed Monte Carlo simulations with modified Weibull models to generate an individual survival function (TTP) in virtual patients receiving 37.5 mg/d of sunitinib continuously. The simulation revealed that about half of the patients on a daily continuous dose of 37.5 mg had C_{trough} below the target values and decreased to 16% after a 2-step dose increase based on TDM. The authors also included covariates of the dose-limiting toxicity and the dropout rate in the model. These virtual patients were not meant to be eligible for the TDM-guided dose increase despite the predicted C_{trough} below the target 50 ng/mL value. The authors finally concluded that TDM might increase the TTP by approximately 1–2 months in eligible patients and estimated that the number of patients required in the clinical study to prove their results using real data was approximately 1600.

These simulations were partially confirmed by a small study with advanced solid tumor patients (n = 43, PK data evaluated in 29 subjects), of which, 15 (52%) had TTL below the target 50 ng/mL.[4] Target TTL without any additional toxicity was reached in 5 patients (17%).

The models mentioned above, provided they are implemented in related software tools (eg, MWPharm, BestDose, TDMx, DoseMe, NextDose, and TUCUXI), may significantly help with dose individualization according to the observed plasma concentration levels (model-based dosing). None of the studies included in this review used such tools to individualize sunitinib dosing before the measurement of real plasma levels. Unfortunately, because of the occasional reporting of high intraindividual variabilities in C_{trough},[35] dose modification or routine TDM based on a single-point concentration remains challenging. However, as sunitinib exposure strongly correlates with the midazolam exposure,[54] midazolam might be used as a phenotypic probe to predict the metabolic clearance of sunitinib. Nevertheless, such a prediction remains a rough estimate of real sunitinib and N-desethylsunitinib exposure.

Summary

Population models may become a valuable tool in the prediction and dose adjustment based on TDM. However, currently, there is no valid PK model for sunitinib implemented as a software tool.

CONCLUSIONS

The widely accepted definition for personalized pharmacotherapy emphasizes treating the right patient with the right drug in the right time using the right dose. In a clinically apparent malignant disease, we need to identify the disease/tumor-dependent variables as well as the host dependent variables, as each plays a key role during the clinical course of the disease. Both variables are essential, and the concept of personalized medicine is, therefore, needed to be perceived as the "all-in-one" concept. A definition of personalized medicine either as "targeted therapy" with tumor-dependent variables or "targeted dosing" based solely on pharmacogenomics would be an oversimplification.[115]

In real clinical practice, the statement to administer "the right drug to the right patient" refers mainly to the tumor-dependent variables, which nowadays are one of the most studied pathological parameters and treatment predictive biomarkers. With current technologies enabling an examination of the cancer genome and interpatient variation in germline DNA, we are in a much better position than ever in terms of selecting patients for targeted therapies.[116]

Not only "the right drug to the right patient" but also tailoring drug dosages and schedules to optimize the PK profiles is equally important. This part of the treatment individualization is assessed mainly in the early phase of the drug development but is usually missing in clinical practice. In the review of de Wit et al,[65] the authors concluded that sunitinib would, after imatinib, be another great candidate, and with the most evidence, for dose individualization based on TDM. Despite the evidence-based clinical efficacy of sunitinib, its

severe toxicity in some patients has become an essential issue in clinical decisions regarding proper treatment. High exposure to sunitinib might be one of the reasons for the severe toxicity of sunitinib. Hence, TDM should/could be undertaken in all patients or at least in a subset of patients subjected to dose extremes and/or in patients with an "unmatched" toxicity (high dose-low toxicity or low dose-high toxicity).[66]

Another proposed method for dose individualization using toxicity as a replacement for systemic exposure is TAD.[117,118] Such a method has been suggested for axitinib using hypertension as the target toxicity, and for sunitinib using a broader range of toxicities.[119,120] A similar approach was used in the study of Maráz et al,[121] in which the dose escalation was conducted in patients with a slight disease progression. The clinical outcome (PFS and OS) was better in the group undergoing the dose escalation strategy than in the control group ($P = 0.009$ and 0.016 for PFS and OS hazard ratio, respectively).

Similar results were also obtained in the study of Raphael et al,[122] where an additional benefit was observed after the dose escalation in patients who had previously progressed from the disease. The occurrence of targeted toxicity from sunitinib (HFS, neutropenia, hypertension, or thyroid dysfunction) was associated with greater OS. Thus, toxicity may serve as a surrogate marker of the treatment outcome, and TAD may thus be an alternative to TDM-guided dosing.[47,119,123]

In our opinion, the approach of TAD would not be the best option in the light of the currently known therapeutic reference range in the treatment of GIST and mRCC, at least for patients who do not perceive any toxicity. Another group which could also benefit from TDM, instead of TAD, includes patients with severe toxicity (≥ 3), where the TDM-guided dose de-escalation could be achieved more precisely and preserve therapeutically relevant plasma concentrations.

In our opinion, and in agreement with other authors,[35] the greatest benefits of TDM could be achieved in patients above the target C_{trough}, with or without toxicity, and in patients below the target C_{trough} experiencing no toxicity. These groups are perfectly eligible for TDM-guided dose modification. The question is whether the patients with plasma levels above the target C_{trough} range and no toxicity would benefit from a TDM-guided dose decrease or whether TAD would be a sufficient alternative.

There is probably no benefit of TDM in patients with or without toxicity while within the target C_{trough}. In the group of patients experiencing toxicity while below the target C_{trough}, dose modification is inadequate and alternative drug treatment would be optional. The groups of the patients which could benefit from TDM of sunitinib are summarized in the Table 3. Sunitinib TDM should/could be performed if drug–drug interactions were present.

Despite drug exposure definitely being one of the key factors influencing treatment outcomes, many other factors, such as time from diagnosis to treatment, genetic polymorphisms (both tumor and "host-related"), pretreatment levels of circulating ligands of regulating receptors, some clinical factors (activity of the lactate dehydragenase, hemoglobin concentration, and performance status), or complex clinical score MSKCC ("Motzer score" defined by Motzer et al[124] at the Memorial Sloan Kettering Cancer Center) may play a role.

TABLE 3. Groups of Patients Who Could Benefit From TDM-Guided Dosing With Target TTL 50–100 ng/mL

	Below Target	On Target	Above Target
Toxicity grade ≥ 3	—	TAD	TDM
No toxicity/toxicity grade ≤ 2	TDM	—	TDM

The high cost of targeted agents and the increasing use of indications based on tumor molecular pathology rather than its location provide another reason to ensure an optimal dose for each patient. There has been sufficient evidence that TDM-guided dose modifications of sunitinib could provide considerably better treatment outcomes while simultaneously preventing its toxicities. TTLs should be used as a response for sunitinib exposure, with the target range being 50–100 ng/mL.

REFERENCES

1. Group ESMO/European Sarcoma Network Working Group. Gastrointestinal stromal tumours: ESMO Clinical Practice Guidelines for diagnosis, treatment and follow-up. *Ann Oncol.* 2014;25(suppl 3):21–26.
2. Escudier B, Porta C, Schmidinger M, et al. Renal cell carcinoma: ESMO Clinical Practice Guidelines for diagnosis, treatment and follow-up. *Ann Oncol.* 2016;27:v58–v68.
3. *Electronic Medicines Compendium SmPC: SUTENT 25 Mg Hard Capsules*. 2019. Available at: https://www.medicines.org.uk/emc/product/7968/smpc. Accessed April 15, 2019.
4. Lankheet NAG, Kloth JSL, Gadellaa-van Hooijdonk CGM, et al. Pharmacokinetically guided sunitinib dosing: a feasibility study in patients with advanced solid tumours. *Br J Cancer.* 2014;110:2441–2449.
5. Lankheet NAG, Desar IME, Mulder SF, et al. Optimizing the dose in cancer patients treated with imatinib, sunitinib and pazopanib. *Br J Clin Pharmacol.* 2017;83:2195–2204.
6. Diekstra MHM, Klumpen HJ, Lolkema MPJK, et al. Association analysis of genetic polymorphisms in genes related to sunitinib pharmacokinetics, specifically clearance of sunitinib and SU12662. *Clin Pharmacol Ther.* 2014;96:81–89.
7. Gotta V, Widmer N, Decosterd LA, et al. Clinical usefulness of therapeutic concentration monitoring for imatinib dosage individualization: results from a randomized controlled trial. *Cancer Chemother Pharmacol.* 2014;74:1307–1319.
8. Larson RA, Druker BJ, Guilhot F, et al. Imatinib pharmacokinetics and its correlation with response and safety in chronic-phase chronic myeloid leukemia: a subanalysis of the IRIS study. *Blood.* 2008;111:4022–4028.
9. Blasdel C, Egorin MJ, Lagattuta TF, et al. Therapeutic drug monitoring in CML patients on imatinib. *Blood.* 2007;110:1699–1701. author reply 1701.
10. Verheijen RB, Swart LE, Beijnen JH, et al. Exposure-survival analyses of pazopanib in renal cell carcinoma and soft tissue sarcoma patients: opportunities for dose optimization. *Cancer Chemother Pharmacol.* 2017;80:1171–1178.
11. Cabel L, Blanchet B, Thomas-Schoemann A, et al. Drug monitoring of sunitinib in patients with advanced solid tumors: a monocentric observational French study. *Fundam Clin Pharmacol.* 2017;32:98–107.
12. Schmid TA, Gore ME. Sunitinib in the treatment of metastatic renal cell carcinoma. *Ther Adv Urol.* 2016;8:348–371.
13. Papaetis GS, Syrigos KN. Sunitinib: a multitargeted receptor tyrosine kinase inhibitor in the era of molecular cancer therapies. *BioDrugs.* 2009;23:377–389.
14. American Society of Health System Pharmacists Inc. *DynaMed.* Ipswich (MA): EBSCO Information Services; 1995. Available at: http://www.dynamed.com/resultlist?q=sunitinib&filter=all. Accessed April 15, 2019. Record No. 233006, Sunitinib. Feb 18, 2016.
15. Rodriguez-Vida A, Hutson TE, Bellmunt J, et al. New treatment options for metastatic renal cell carcinoma. *ESMO Open.* 2017;2:e000185.

16. Kidney Cancer, Version 4.2018, NCCN Clinical Practice Guidelines in Oncology. 2018:1–62. Available at: https://www2.tri-kobe.org/nccn/guideline/urological/english/kidney.pdf. Accessed November 22, 2018.

17. Soft Tissue Sarcoma, Version I.2018, NCCN Clinical Practice Guidelines in Oncology. *J Natl Compr Canc Netw.* 2017:1–137. Available at: http://nlmsf.org/wp-content/uploads/2018/03/NCCN-sarcoma-guidelines-for-physicians.pdf. Accessed October 9, 2018.

18. Haznedar JO, Patyna S, Bello CL, et al. Single- and multiple-dose disposition kinetics of sunitinib malate, a multitargeted receptor tyrosine kinase inhibitor: comparative plasma kinetics in non-clinical species. *Cancer Chemother Pharmacol.* 2009;64:691–706.

19. Di Gion P, Kanefendt F, Lindauer A, et al. Clinical pharmacokinetics of tyrosine kinase inhibitors: focus on pyrimidines, pyridines and pyrroles. *Clin Pharmacokinet.* 2011;50:551–603.

20. European Medicines Agency. *Assessment Report for Sutent (Sunitinib) Procedure No.* London, United Kingdom: EMA; 2010. EMA/H/C/000687/II/0021.

21. Bello CL, Sherman L, Zhou JH, et al. Effect of food on the pharmacokinetics of sunitinib malate (SU11248), a multi-targeted receptor tyrosine kinase inhibitor: results from a phase I study in healthy subjects. *Anticancer Drugs.* 2006;17:353–358.

22. Goodman VL, Rock EP, Dagher R, et al. Approval summary: sunitinib for the treatment of imatinib refractory or intolerant gastrointestinal stromal tumors and advanced renal cell carcinoma. *Clin Cancer Res.* 2007;13:1367–1373.

23. Yu H, Steeghs N, Kloth JS, et al. Integrated semi-physiological pharmacokinetic model for both sunitinib and its active metabolite SU12662. *Br J Clin Pharmacol.* 2015;79:809–819.

24. FDA. Approval package for NDA 21-938 (GIST) and NDA 21-968 (mRCC). In: *Clinical Pharmacology and Biopharmaceutics Review.* San Diego, CA: Center for Drug Evaluation and Research; 2005:1–190.

25. Toyama Y, Ueyama J, Nomura H, et al. Contribution of plasma proteins, albumin and alpha 1-acid glycoprotein, to pharmacokinetics of a multi-targeted receptor tyrosine kinase nhibitor, sunitinib, in analbuminemic rats. *Anticancer Res.* 2014;34:2283–2289.

26. Kunimatsu S, Mizuno T, Fukudo M, et al. Effect of P-glycoprotein and breast cancer resistance protein inhibition on the pharmacokinetics of sunitinib in rats. *Drug Metab Dispos.* 2013;41:1592–1597.

27. van der Veldt AAM, Eechoute K, Gelderblom H, et al. Genetic polymorphisms associated with a prolonged progression-free survival in patients with metastatic renal cell cancer treated with sunitinib. *Clin Cancer Res.* 2011;17:620–629.

28. Miura Y, Imamura CK, Fukunaga K, et al. Sunitinib-induced severe toxicities in a Japanese patient with the ABCG2 421 AA genotype. *BMC Cancer.* 2014;14:964.

29. Mizuno T, Fukudo M, Terada T, et al. Impact of genetic variation in breast cancer resistance protein (BCRP/ABCG2) on sunitinib pharmacokinetics. *Drug Metab Pharmacokinet.* 2012;27:631–639.

30. Kloth JS, Klümpen HJ, Yu H, et al. Predictive value of CYP3A and ABCB1 phenotyping probes for the pharmacokinetics of sunitinib: the ClearSun study. *Clin Pharmacokinet.* 2014;53:261–269.

31. Tang SC, Lagas JS, Lankheet NAG, et al. Brain accumulation of sunitinib is restricted by P-glycoprotein (ABCB1) and breast cancer resistance protein (ABCG2) and can be enhanced by oral elacridar and sunitinib coadministration. *Int J Cancer.* 2012;130:223–233.

32. Sherman L, Peng G, Patyna S, et al. Open-label, single-dose, phase I study evaluating the mass balance and pharmacolkinetics (PKs) of sunitinib (SU) in healthy male subjects. *EJC Suppl.* 2007;5:116.

33. George S, Blay JY, Casali PG, et al. Clinical evaluation of continuous daily dosing of sunitinib malate in patients with advanced gastrointestinal stromal tumour after imatinib failure. *Eur J Cancer.* 2009;45:1959–1968.

34. Houk BE, Bello CL, Kang DW, et al. Population pharmacokinetic meta-analysis of sunitinib malate (SU11248) and its primary metabolite (SU12662) in healthy volunteers and oncology patients. *Clin Cancer Res.* 2009;15:2497–2506.

35. Lankheet NAG, Knapen LM, Schellens JHM, et al. Plasma concentrations of tyrosine kinase inhibitors imatinib, erlotinib, and sunitinib in routine clinical outpatient cancer care. *Ther Drug Monit.* 2014;36:326–334.

36. Crombag MBS, van Doremalen JGC, Janssen JM, et al. Therapeutic drug monitoring of small molecule kinase inhibitors in oncology in a real-world cohort study: does age matter? *Br J Clin Pharmacol.* 2018;84:2770–2778.

37. Bello CL, Garrett M, Sherman L, et al. Pharmacokinetics of sunitinib malate in subjects with hepatic impairment. *Cancer Chemother Pharmacol.* 2010;66:699–707.

38. Noda S, Otsuji T, Baba M, et al. Assessment of sunitinib-induced toxicities and clinical outcomes based on therapeutic drug monitoring of sunitinib for patients with renal cell carcinoma. *Clin Genitourin Cancer.* 2015;13:350–358.

39. Terada T, Noda S, Inui K, et al. Management of dose variability and side effects for individualized cancer pharmacotherapy with tyrosine kinase inhibitors. *Pharmacol Ther.* 2015;152:125–134.

40. Kappers MHW, van Esch JHM, Sluiter W, et al. Hypertension induced by the tyrosine kinase inhibitor sunitinib is associated with increased circulating endothelin-1 levels. *Hypertension.* 2010;56:675–U216.

41. Kloth JSL, Binkhorst L, De Bruijn P, et al. Effect of dosing time on sunitinib pharmacokinetics. *Eur J Cancer.* 2013;49:S152.

42. Escudier B, Roigas J, Gillessen S, et al. Phase II study of sunitinib administered in a continuous once-daily dosing regimen in patients with cytokine-refractory metastatic renal cell carcinoma. *J Clin Oncol.* 2009;27:4068–4075.

43. Eisen T, Sternberg CN, Robert C, et al. Targeted therapies for renal cell carcinoma: review of adverse event management strategies. *J Natl Cancer Inst.* 2012;104:93–113.

44. Guo J, Jin J, Oya M, et al. Safety of pazopanib and sunitinib in treatment-naïve patients with metastatic renal cell carcinoma: Asian versus non-Asian subgroup analysis of the COMPARZ trial. *J Hematol Oncol.* 2018;11:69.

45. Motzer RJ, Hutson TE, Tomczak P, et al. Sunitinib versus interferon alfa in metastatic renal-cell carcinoma. *N Engl J Med.* 2007;356:115–124.

46. Ibrahim EM, Kazkaz GA, Abouelkhair KM, et al. Sunitinib adverse events in metastatic renal cell carcinoma: a meta-analysis. *Int J Clin Oncol.* 2013;18:1060–1069.

47. Kollmannsberger C, Soulieres D, Wong R, et al. Sunitinib therapy for metastatic renal cell carcinoma: recommendations for management of side effects. *Can Urol Assoc J.* 2007;1:S41–S54.

48. Bracarda S, Iacovelli R, Boni L, et al. Sunitinib administered on 2/1 schedule in patients with metastatic renal cell carcinoma: the RAINBOW analysis. *Ann Oncol.* 2016;27:366.

49. Lee JL, Kim MK, Park I, et al. RandomizEd phase II trial of Sunitinib four weeks on and two weeks off versus two weeks on and one week off in metastatic clear-cell type REnal cell carcinoma: RESTORE trial. *Ann Oncol.* 2015;26:2300–2305.

50. Ohba K, Miyata Y, Yasuda T, et al. Efficacy and safety of sunitinib alternate day regimen in patients with metastatic renal cell carcinoma in Japan: comparison with standard 4/2 schedule. *Asia Pac J Clin Oncol.* 2018;14:153–158.

51. Thomas-Schoemann A, Blanchet B, Bardin C, et al. Drug interactions with solid tumour-targeted therapies. *Crit Rev Oncol Hematol.* 2014;89:179–196.

52. Rudek MA, Moore PC, Mitsuyasu RT, et al. A phase 1/pharmacokinetic study of sunitinib in combination with highly active antiretroviral therapy in human immunodeficiency virus-positive patients with cancer: AIDS Malignancy Consortium trial AMC 061. *Cancer.* 2014;120:1194–1202.

53. Sugiyama M, Fujita K, Murayama N, et al. Sorafenib and sunitinib, two anticancer drugs, inhibit CYP3A4-mediated and activate CY3A5-mediated midazolam 1'-hydroxylation. *Drug Metab Dispos.* 2011;39:757–762.

54. de Wit D, Gelderblom H, Sparreboom A, et al. Midazolam as a phenotyping probe to predict sunitinib exposure in patients with cancer. *Cancer Chemother Pharmacol.* 2014;73:87–96.

55. Abodunde OA, LevakaVeera RR, Desai R, et al. Colchicine toxicity precipitated by interaction with sunitinib. *J Clin Pharm Ther.* 2013;38:243–245.

56. van Leeuwen RWF, van Gelder T, Mathijssen RHJ, et al. Drug-drug interactions with tyrosine-kinase inhibitors: a clinical perspective. *Lancet Oncol.* 2014;15:E315–E326.

57. Kruse V, Somers A, Van Bortel L, et al. Sunitinib for metastatic renal cell cancer patients: observational study highlighting the risk of important drug-drug interactions. *J Clin Pharm Ther.* 2014;39:259–265.

58. Karczmarek-Borowska B, Salek-Zan A. Hepatotoxicity of molecular targeted therapy. *Contemp Oncol.* 2015;19:87–92.

59. Zhang M, Kim JA, Huang AYC. Optimizing tumor microenvironment for cancer immunotherapy: beta-glucan-based nanoparticles. *Front Immunol.* 2018;9:341.

60. Ljungberg B, Albiges L, Bensalah K, et al. EAU Guidelines on Renal Cell Carcinoma. 2018;2018:1–62. Available at: https://uroweb.org/wp-content/uploads/EAU-RCC-Guidelines-2018-large-text.pdf. Accessed October 9, 2018.

61. Houk BE, Bello CL, Poland B, et al. Relationship between exposure to sunitinib and efficacy and tolerability endpoints in patients with cancer: results of a pharmacokinetic/pharmacodynamic meta-analysis. *Cancer Chemother Pharmacol.* 2010;66:357–371.

62. Gao B, Yeap S, Clements A, et al. Evidence for therapeutic drug monitoring of targeted anticancer therapies. *J Clin Oncol.* 2012;30:4017–4025.

63. Faivre S, Delbaldo C, Vera K, et al. Safety, pharmacokinetic, and antitumor activity of SU11248, a novel oral multitarget tyrosine kinase inhibitor, in patients with cancer. *J Clin Oncol.* 2006;24:25–35.

64. Britten CD, Kabbinavar F, Hecht JR, et al. A phase I and pharmacokinetic study of sunitinib administered daily for 2 weeks, followed by a 1-week off period. *Cancer Chemother Pharmacol.* 2008;61:515–524.

65. de Wit D, Guchelaar HJ, den Hartigh J, et al. Individualized dosing of tyrosine kinase inhibitors: are we there yet? *Drug Discov Today.* 2015; 20:18–36.

66. Sabanathan D, Zhang A, Fox P, et al. Dose individualization of sunitinib in metastatic renal cell cancer: toxicity-adjusted dose or therapeutic drug monitoring. *Cancer Chemother Pharmacol.* 2017;80:385–393.

67. Numakura K, Fujiyama N, Takahashi M, et al. Clinical implications of pharmacokinetics of sunitinib malate and N-desethyl-sunitinib plasma concentrations for treatment outcome in metastatic renal cell carcinoma patients. *Oncotarget.* 2018;9:25277–25284.

68. Demetri GD, Heinrich MC, Fletcher JA, et al. Molecular target modulation, imaging, and clinical evaluation of gastrointestinal stromal tumor patients treated with sunitinib malate after imatinib failure. *Clin Cancer Res.* 2009;15:5902–5909.

69. Teo YL, Chue XP, Chau NM, et al. Association of drug exposure with toxicity and clinical response in metastatic renal cell carcinoma patients receiving an attenuated dosing regimen of sunitinib. *Targeted Oncol.* 2015;10:429–437.

70. Liu X, Fiocco M, Swen JJ, et al. Assessment of ethnic differences in sunitinib outcome between Caucasian and Asian patients with metastatic renal cell carcinoma: a meta-analysis. *Acta Oncol.* 2017;56:582–589.

71. Houk BE, Bello CL, Michaelson MD, et al. A population pharmacokinetic/pharmacodynamic (PK/PD) analysis of exposure-response for sunitinib in metastatic renal cell carcinoma (mRCC). *EJC Suppl.* 2007;5:300.

72. Lee SH, Bang YJ, Mainwaring P, et al. Sunitinib in metastatic renal cell carcinoma: an ethnic Asian subpopulation analysis for safety and efficacy. *Asia Pac J Clin Oncol.* 2014;10:237–245.

73. Chew CC, Ng S, Chee YL, et al. Diclofenac sex-divergent drug-drug interaction with Sunitinib: pharmacokinetics and tissue distribution in male and female mice. *Invest New Drugs.* 2017;35:399–411.

74. Lahti S, Ludwig JM, Xing MZ, et al. In vitro biologic efficacy of sunitinib drug-eluting beads on human colorectal and hepatocellular carcinoma—a pilot study. *PLoS One.* 2017;12:e0174539.

75. Garrido-Cano I, Garcia-Garcia A, Peris-Vicente J, et al. A method to quantify several tyrosine kinase inhibitors in plasma by micellar liquid chromatography and validation according to the European Medicines Agency guidelines. *Talanta.* 2015;144:1287–1295.

76. Helvenstein M, Hambye S, Blankert B. Determination of three tyrosine kinase inhibitors and one active metabolite by an identical and validated ultra-performance liquid chromatography-DAD method in human plasma. *Curr Pharm Anal.* 2014;10:161–168.

77. Oberoi RK, Mittapalli RK, Fisher J, et al. Sunitinib LC-MS/MS assay in mouse plasma and brain tissue: application in CNS distribution studies. *Chromatographia.* 2013;76: 1–18.

78. Posocco B, Buzzo M, Giodini L, et al. Analytical aspects of sunitinib and its geometric isomerism towards therapeutic drug monitoring in clinical routine. *J Pharm Biomed Anal.* 2018;160:360–367.

79. Keil C, Götze L, Olbert P, et al. Metastasized renal cell carcinoma. Measurement of plasma levels of the tyrosine kinase inhibitors sunitinib, sorafenib and pazopanib. *Urologe A.* 2015;54:811–818.

80. Bouchet S, Chauzit E, Ducint D, et al. Simultaneous determination of nine tyrosine kinase inhibitors by 96-well solid-phase extraction and ultra performance LC/MS-MS. *Clin Chim Acta.* 2011;412:1060–1067.

81. Couchman L, Birch M, Ireland R, et al. An automated method for the measurement of a range of tyrosine kinase inhibitors in human plasma or serum using turbulent flow liquid chromatography-tandem mass spectrometry. *Anal Bioanal Chem.* 2012;403:1685–1695.

82. Henry H, Sobhi HR, Scheibner O, et al. Comparison between a high-resolution single-stage Orbitrap and a triple quadrupole mass spectrometer for quantitative analyses of drugs. *Rapid Comm Mass Spectrom.* 2012;26:499–509.

83. Lankheet NAG, Hillebrand MJX, Rosing H, et al. Method development and validation for the quantification of dasatinib, erlotinib, gefitinib, imatinib, lapatinib, nilotinib, sorafenib and sunitinib in human plasma by liquid chromatography coupled with tandem mass spectrometry. *Biomed Chromatogr.* 2013;27:466–476.

84. Rodamer M, Elsinghorst PW, Kinzig M, et al. Development and validation of a liquid chromatography/tandem mass spectrometry procedure for the quantification of sunitinib (SU11248) and its active metabolite, N-desethyl sunitinib (SU12662), in human plasma: application to an explorative study. *J Chromatogr B Analyt Technol Biomed Life Sci.* 2011;879:695–706.

85. Lankheet NA, Blank CU, Mallo H, et al. Determination of sunitinib and its active metabolite N-desethylsunitinib in sweat of a patient. *J Anal Toxicol.* 2011;35:558–565.

86. Rais R, Zhao M, He P, et al. Quantitation of unbound sunitinib and its metabolite N-desethyl sunitinib (SU12662) in human plasma by equilibrium dialysis and liquid chromatography-tandem mass spectrometry: application to a pharmacokinetic study. *Biomed Chromatog.* 2012;26: 1315–1324.

87. de Bruijn P, Sleijfer S, Lam MH, et al. Bioanalytical method for the quantification of sunitinib and its N-desethyl metabolite SU12662 in human plasma by ultra performance liquid chromatography/tandem triple-quadrupole mass spectrometry. *J Pharm Biomed Anal.* 2010;51: 934–941.

88. Musijowski J, Piórkowska E, Rudzki PJ. Determination of sunitinib in human plasma using liquid chromatography coupled with mass spectrometry. *J Sep Sci.* 2014;37:2652–2658.

89. Lankheet NAG, Steeghs N, Rosing H, et al. Quantification of sunitinib and N-desethyl sunitinib in human EDTA plasma by liquid chromatography coupled with electrospray ionization tandem mass spectrometry: validation and application in routine therapeutic drug monitoring. *Ther Drug Monit.* 2013;35:168–176.

90. Herbrink M, de Vries N, Rosing H, et al. Quantification of 11 therapeutic kinase inhibitors in human plasma for therapeutic drug monitoring using liquid chromatography coupled with tandem mass spectrometry. *Ther Drug Monit.* 2016;38:649–656.

91. Merienne C, Rousset M, Ducint D, et al. High throughput routine determination of 17 tyrosine kinase inhibitors by LC-MS/MS. *J Pharm Biomed Anal.* 2018;150:112–120.

92. Krautbauer S, Büchler C, Liebisch G. Relevance in the use of appropriate internal standards for accurate quantification using LC-MS/MS: tauro-conjugated bile acids as an example. *Anal Chem.* 2016;88:10957–10961.

93. De Nicolo A, Cantu M, D'Avolio A. Matrix effect management in liquid chromatography mass spectrometry: the internal standard normalized matrix effect. *Bioanal.* 2017;9:1093–1105.

94. van Erp NP, de Wit D, Guchelaar HJ, et al. A validated assay for the simultaneous quantification of six tyrosine kinase inhibitors and two active metabolites in human serum using liquid chromatography coupled with tandem mass spectrometry. *J Chromatogr B Analyt Technol Biomed Life Sci.* 2013;937:33–43.

95. Qiu F, Bian W, Li J, et al. Simultaneous determination of sunitinib and its two metabolites in plasma of Chinese patients with metastatic renal cell carcinoma by liquid chromatography-tandem mass spectrometry. *Biomed Chromatogr.* 2013;27:615–621.

96. Chen X, Wang Z, Liu MP, et al. Determination of sunitinib and its active metabolite, N-desethyl sunitinib in mouse plasma and tissues by UPLC-MS/MS: assay development and application to pharmacokinetic and tissue distribution studies. *Biomed Chromatogr.* 2015;29:679–688.

97. Andriamanana I, Gana I, Duretz B, et al. Simultaneous analysis of anticancer agents bortezomib, imatinib, nilotinib, dasatinib, erlotinib,

31

lapatinib, sorafenib, sunitinib and vandetanib in human plasma using LC/MS/MS. *J Chromatogr B Analyt Technol Biomed Life Sci.* 2013; 926:83–91.

98. Takasaki S, Tanaka M, Kikuchi M, et al. Simultaneous analysis of oral anticancer drugs for renal cell carcinoma in human plasma using liquid chromatography/electrospray ionization tandem mass spectrometry. *Biomed Chromatogr.* 2018;32:e4184.

99. Götze L, Hegele A, Metzelder SK, et al. Development and clinical application of a LC-MS/MS method for simultaneous determination of various tyrosine kinase inhibitors in human plasma. *Clin Chim Acta.* 2012;413:143–149.

100. He Y, Zhou L, Gao S, et al. Development and validation of a sensitive LC-MS/MS method for simultaneous determination of eight tyrosine kinase inhibitors and its application in mice pharmacokinetic studies. *J Pharm Biomed Anal.* 2018;148:65–72.

101. Honeywell R, Yarzadah K, Giovannetti E, et al. Simple and selective method for the determination of various tyrosine kinase inhibitors used in the clinical setting by liquid chromatography tandem mass spectrometry. *J Chromatogr B Analyt Technol Biomed Life Sci.* 2010;878:1059–1068.

102. Mendel DB, Laird AD, Xin X, et al. In vivo antitumor activity of SU11248, a novel tyrosine kinase inhibitor targeting vascular endothelial growth factor and platelet-derived growth factor receptors: determination of a pharmacokinetic/pharmacodynamic relationship. *Clin Cancer Res.* 2003;9:327–337.

103. Teo YL, Chue XP, Chau NM, et al. Association of drug exposure with clinical response and toxicities in metastatic renal cell carcinoma patients (mRCC) receiving an alternative dosing (AD) regimen of sunitinib. *J Clin Oncol.* 2013;31:e13582.

104. Mendel DB, Cherrington JM, Laird AD. CCR 20th anniversary commentary: determining a pharmacokinetic/pharmacodynamic relationship for sunitinib—a look back. *Clin Cancer Res.* 2015;21:2415–2417.

105. Narjoz C, Cessot A, Thomas-Schoemann A, et al. Role of the lean body mass and of pharmacogenetic variants on the pharmacokinetics and pharmacodynamics of sunitinib in cancer patients. *Invest New Drugs.* 2015;33:257–268.

106. Yu H, Steeghs N, Nijenhuis CM, et al. Practical guidelines for therapeutic drug monitoring of anticancer tyrosine kinase inhibitors: focus on the pharmacokinetic targets. *Clin Pharmacokinet.* 2014;53:305–325.

107. Goulooze SC, Galettis P, Boddy AV, et al. Monte Carlo simulations of the clinical benefits from therapeutic drug monitoring of sunitinib in patients with gastrointestinal stromal tumours. *Cancer Chemother Pharmacol.* 2016;78:209–216.

108. Uemura H, Shinohara N, Yuasa T, et al. A phase II study of sunitinib in Japanese patients with metastatic renal cell carcinoma: insights into the treatment, efficacy and safety. *Jpn J Clin Oncol.* 2010;40:194–202.

109. Takasaki S, Kawasaki Y, Kikuchi M, et al. Relationships between sunitinib plasma concentration and clinical outcomes in Japanese patients with metastatic renal cell carcinoma. *Int J Clin Oncol.* 2018; 23:936–943.

110. Nagata M, Ishiwata Y, Takahashi Y, et al. Pharmacokinetic-pharmacodynamic analysis of sunitinib-induced thrombocytopenia in Japanese patients with renal cell carcinoma. *Biol Pharm Bull.* 2015; 38:402–410.

111. Bello CL, Mulay M, Huang X, et al. Electrocardiographic characterization of the QTc interval in patients with advanced solid tumors: pharmacokinetic-pharmacodynamic evaluation of sunitinib. *Clin Cancer Res.* 2009;15:7045–7052.

112. Verheijen RB, Yu H, Schellens JHM, et al. Practical recommendations for therapeutic drug monitoring of kinase inhibitors in oncology. *Clin Pharmacol Ther.* 2017;102:765–776.

113. Houk BE, Bello C, Cohen DP, et al. Efficacy of sunitinib in patients with gastrointestinal stromal tumor (GIST): an exposure-response based meta-analysis. *Mol Cancer Ther.* 2007;6:3589S.

114. Teo YL, Wee HL, Chue XP, et al. Effect of the CYP3A5 and ABCB1 genotype on exposure, clinical response and manifestation of toxicities from sunitinib in Asian patients. *Pharmacogenomics J.* 2016;16:47–53.

115. Demlova R, Zdrazilova-Dubska L, Sterba J, et al. Host-dependent variables: the missing link to personalized medicine. *Eur J Surg Oncol.* 2018;44:1289–1294.

116. Mateo J, Chakravarty D, Dienstmann R, et al. A framework to rank genomic alterations as targets for cancer precision medicine: the ESMO Scale for Clinical Actionability of molecular Targets (ESCAT). *Ann Oncol.* 2018;29:1895–1902.

117. Gurney H. Dose calculation of anticancer drugs: a review of the current practice and introduction of an alternative. *J Clin Oncol.* 1996;14:2590–2611.

118. Gurney H. How to calculate the dose of chemotherapy. *Br J Cancer.* 2002;86:1297–1302.

119. Rini BI, Cohen DP, Lu DR, et al. Hypertension as a biomarker of efficacy in patients with metastatic renal cell arcinoma treated with sunitinib. *J Natl Cancer Inst.* 2011;103:763–773.

120. Kollmannsberger C, Bjarnason G, Burnett P, et al. Sunitinib in metastatic renal cell carcinoma: recommendations for management of non-cardiovascular toxicities. *Oncologist.* 2011;16:543–553.

121. Maráz A, Cserháti A, Uhercsák G, et al. Dose escalation can maximize therapeutic potential of sunitinib in patients with metastatic renal cell carcinoma. *BMC Cancer.* 2018;18:296.

122. Raphael J, Thawer A, Bjarnason GA. Sunitinib dose-escalation after disease progression in metastatic renal cell carcinoma. *Urol Oncol.* 2018;36:12.e1–12.e6.

123. Klumpen HJ, Samer CF, Mathijssen RHJ, et al. Moving towards dose individualization of tyrosine kinase inhibitors. *Cancer Treat Rev.* 2011; 37:251–260.

124. Motzer RJ, Bacik J, Schwartz LH, et al. Prognostic factors for survival in previously treated patients with metastatic renal cell carcinoma. *J Clin Oncol.* 2004;22:454–63.

5 Conclusion

Mass spectrometry has been part of modern chemistry regardless of the focus field. Its capability to identify, characterize, quantify, and hyphenate is unparalleled across other methods. Although no mass spectrometer can provide maximum performance in all tasks simultaneously, a suitable combination of a ionization technique and a mass analyzer helps overcome the significant challenges of current science. It is worth noting that possession of the instrument itself is not sufficient; a skillful operator capable of acquiring, interpreting, and maintaining the entire workflow is mandatory.

All the data gathered by applying mass spectrometry in this work represent a collection of individual inferences and conclusions, which would have taken much longer if mass spectrometry had not been accessible. The first part dealt with the hyphenation capabilities of MS and demonstrated that even in the world where majority of LC is online-coupled to ESI MS, the offline coupling has its place, and it is irreplaceable in specific types of applications. The second part employed MS in the molecular composition and structure investigation to uncover either new molecules or novel processes associated with them. MS is perfectly suited for identification of known unknowns with the help of computational *in silico* database matching and prediction. The third part utilized MS as a sensitive and a specific detector, which could substitute several different detection techniques simultaneously. Mass spectrometry helped to reject the long-term downtrend that if a detection technique is universal (such as refractometric or conductometric detection) it is associated with low sensitivity and specificity. Nevertheless, quantitation studies using any method provides inferences in the small world only; navigation to the large world via generalization remains the central challenge of statistical modeling.[86]

6 References

(1)   Thomson, J. J. XL. Cathode Rays. *The London, Edinburgh, and Dublin Philosophical Magazine and Journal of Science* **1897**, *44* (269), 293–316. https://doi.org/10.1080/14786449708621070.

(2)   Thomson, J. J. Rays of Positive Electricity. *Proceedings of the Royal Society of London. Series A, Containing Papers of a Mathematical and Physical Character* **1913**, *89* (607), 1–20. https://doi.org/10.1098/rspa.1913.0057.

(3)   Nier, A. O.; Bardeen, J. The Production of Concentrated Carbon (13) by Thermal Diffusion. *J. Chem. Phys.* **1941**, *9* (9), 690–692. https://doi.org/10.1063/1.1750978.

(4)   Paul, W.; Steinwedel, H. Notizen: Ein Neues Massenspektrometer Ohne Magnetfeld. *Zeitschrift fur Naturforschung A* **1953**, *8* (7), 448–450. https://doi.org/10.1515/zna-1953-0710.

(5)   Biemann, K.; Gapp, G.; Seibl, J. APPLICATION OF MASS SPECTROMETRY TO STRUCTURE PROBLEMS. I. AMINO ACID SEQUENCE IN PEPTIDES. *J. Am. Chem. Soc.* **1959**, *81* (9), 2274–2275. https://doi.org/10.1021/ja01518a069.

(6)   McLafferty, F. W. Mass Spectrometric Analysis. Molecular Rearrangements. *Anal. Chem.* **1959**, *31* (1), 82–87. https://doi.org/10.1021/ac60145a015.

(7)   Budzikiewicz, H.; Wilson, J. M.; Djerassi, Carl. Mass Spectrometry in Structural and Stereochemical Problems. XXXII.1 Pentacyclic Triterpenes. *J. Am. Chem. Soc.* **1963**, *85* (22), 3688–3699. https://doi.org/10.1021/ja00905a036.

(8)   Comisarow, M. B.; Marshall, A. G. Fourier Transform Ion Cyclotron Resonance Spectroscopy. *Chemical Physics Letters* **1974**, *25* (2), 282–283. https://doi.org/10.1016/0009-2614(74)89137-2.

(9)   Hipple, J. A.; Sommer, H.; Thomas, H. A. A Precise Method of Determining the Faraday by Magnetic Resonance. *Phys. Rev.* **1949**, *76* (12), 1877–1878. https://doi.org/10.1103/PhysRev.76.1877.2.

(10)   Stephens, William E. A Pulsed Mass Spectrometer with Time Dispersion. *Phys. Rev.* **1946**, *69* (11-12), 674–674. https://doi.org/10.1103/PhysRev.69.674.

(11)   Houk, R. S.; Fassel, V. A.; Flesch, G. D.; Svec, H. J.; Gray, A. L.; Taylor, C. E. Inductively Coupled Argon Plasma as an Ion Source for Mass Spectrometric Determination of Trace Elements. *Anal. Chem.* **1980**, *52* (14), 2283–2289. https://doi.org/10.1021/ac50064a012.

(12)   Fenn, J. B.; Mann, M.; Meng, C. K.; Wong, S. F.; Whitehouse, C. M. Electrospray Ionization for Mass Spectrometry of Large Biomolecules. *Science* **1989**, *246* (4926), 64–71. https://doi.org/10.1126/science.2675315.

(13)   Tanaka, K.; Waki, H.; Ido, Y.; Akita, S.; Yoshida, Y.; Yoshida, T.; Matsuo, T. Protein and Polymer Analyses up to m/z 100 000 by Laser Ionization Time-of-Flight Mass Spectrometry. *Rapid Communications in Mass Spectrometry* **1988**, *2* (8), 151–153. https://doi.org/10.1002/rcm.1290020802.

(14)   Dole, M.; Mack, L. L.; Hines, R. L.; Mobley, R. C.; Ferguson, L. D.; Alice, M. B. Molecular Beams of Macroions. *J. Chem. Phys.* **1968**, *49* (5), 2240–2249. https://doi.org/10.1063/1.1670391.

(15) Karas, Michael.; Bachmann, Doris.; Hillenkamp, Franz. Influence of the Wavelength in High-Irradiance Ultraviolet Laser Desorption Mass Spectrometry of Organic Molecules. *Analytical Chemistry* **1985**, *57* (14), 2935–2939. https://doi.org/10.1021/ac00291a042.

(16) Rashed, M. S.; Bucknall, M. P.; Little, D.; Awad, A.; Jacob, M.; Alamoudi, M.; Alwattar, M.; Ozand, P. T. Screening Blood Spots for Inborn Errors of Metabolism by Electrospray Tandem Mass Spectrometry with a Microplate Batch Process and a Computer Algorithm for Automated Flagging of Abnormal Profiles. *Clinical Chemistry* **1997**, *43* (7), 1129–1141. https://doi.org/10.1093/clinchem/43.7.1129.

(17) Singhal, N.; Kumar, M.; Kanaujia, P. K.; Virdi, J. S. MALDI-TOF Mass Spectrometry: An Emerging Technology for Microbial Identification and Diagnosis. *Front Microbiol* **2015**, *6*, 791. https://doi.org/10.3389/fmicb.2015.00791.

(18) Takats, Z.; Wiseman, J. M.; Gologan, B.; Cook, R. G. Mass Spectrometry Sampling Under Ambient Conditions with Desorption Electrospray Ionization. *Science* **2004**, *306* (5695), 471–473. https://doi.org/10.1126/science.1104404.

(19) Cody, R. B.; Laramee, J. A.; Durst, H. D. Versatile New Ion Source for the Analysis of Materials in Open Air Under Ambient Conditions. *Anal. Chem.* **2005**, *77* (8), 2297–2302. https://doi.org/10.1021/ac050162j.

(20) Makarov, A. Orbitrap Journey: Taming the Ion Rings. *Nat Commun* **2019**, *10* (1, 1), 3743. https://doi.org/10.1038/s41467-019-11748-y.

(21) Makarov, A.; Denisov, E.; Kholomeev, A.; Balschun, W.; Lange, O.; Strupat, K.; Horning, S. Performance Evaluation of a Hybrid Linear Ion Trap/Orbitrap Mass Spectrometer. *Anal. Chem.* **2006**, *78* (7), 2113–2120. https://doi.org/10.1021/ac0518811.

(22) Thomson, J. J.; Rutherford, E. XL. On the Passage of Electricity Through Gases Exposed to Rontgen Rays. *The London, Edinburgh, and Dublin Philosophical Magazine and Journal of Science* **1896**, *42* (258), 392–407. https://doi.org/10.1080/14786449608620932.

(23) Pringle, S. D.; Giles, K.; Wildgoose, J. L.; Williams, J. P.; Slade, S. E.; Thalassinos, K.; Bateman, R. H.; Bowers, M. T.; Scrivens, J. H. An Investigation of the Mobility Separation of Some Peptide and Protein Ions Using a New Hybrid Quadrupole/Travelling Wave IMS/Oa-ToF Instrument. *International Journal of Mass Spectrometry* **2007**, *261* (1), 1–12. https://doi.org/10.1016/j.ijms.2006.07.021.

(24) Dodds, J. N.; Baker, E. S. Ion Mobility Spectrometry: Fundamental Concepts, Instrumentation, Applications, and the Road Ahead. *J Am Soc Mass Spectrom* **2019**, *30* (11), 2185–2195. https://doi.org/10.1007/s13361-019-02288-2.

(25) *Ion Mobility Spectrometry - Mass Spectrometry: Theory and Applications*, 1st edition.; Wilkins, C. L., Trimpin, S., Eds.; CRC Press: Boca Raton, FL, 2010.

(26) Rankin-Turner, S.; Heaney, L. M. Applications of Ambient Ionization Mass Spectrometry in 2020: An Annual Review. *Analytical Science Advances* **2021**, *2* (3-4), 193–212. https://doi.org/10.1002/ansa.202000135.

(27) Li, L.; Schug, K. A. On- and Off-Line Coupling of Separation Techniques to Ambient Ionization Mass Spectrometry. *LC GC N. AM.* **2011**, 8–14.

(28)   Coufalikova, K.; Benesova, I.; Vaculovic, T.; Kanicky, V.; Preisler, J. LC Coupled to ESI, MALDI and ICP MS A Multiple Hyphenation for Metalloproteomic Studies. *Analytica Chimica Acta* **2017**, *968*, 58–65. https://doi.org/10.1016/j.aca.2017.03.016.

(29)   Foltynova, P.; Kanicky, V.; Preisler, J. Diode Laser Thermal Vaporization Inductively Coupled Plasma Mass Spectrometry. *Anal. Chem.* **2012**, *84* (5), 2268–2274. https://doi.org/10.1021/ac202884m.

(30)   Bednarik, A.; Tomalova, I.; Kanicky, V.; Preisler, J. Thin-Layer Chromatography Combined with Diode Laser Thermal Vaporization Inductively Coupled Plasma Mass Spectrometry. *Journal of Chromatography A* **2014**, *1364*, 271–275. https://doi.org/10.1016/j.chroma.2014.08.069.

(31)   Domin, M.; Cody, R. *Ambient Ionization Mass Spectrometry*; Royal Society of Chemistry, 2014.

(32)   Foret, F.; Preisler, J. Liquid Phase Interfacing and Miniaturization in Matrix-Assisted Laser Desorption/Ionization Mass Spectrometry. *Proteomics* **2002**, *2* (4), 360–372. https://doi.org/10.1002/1615-9861(200204)2:4%3C360::AID-PROT360%3E3.0.CO;2-Y.

(33)   Preisler, J.; Hu, P.; Rejtar, T.; Karger, B. L. Capillary Electrophoresis–Matrix-Assisted Laser Desorption/Ionization Time-of-Flight Mass Spectrometry Using a Vacuum Deposition Interface. *Anal Chem* **2000**, *72* (20), 4785–4795. https://doi.org/10.1021/ac0005870.

(34)   Pes, O.; Preisler, J. Off-Line Coupling of Microcolumn Separations to Desorption Mass Spectrometry. *J. Chromatogr. A* **2010**, *1217* (25), 3966–3977. https://doi.org/10.1016/j.chroma.2010.02.058.

(35)   Jungova, P.; Navratilova, J.; Pes, O.; Vaculovic, T.; Kanicky, V.; Smarda, J.; Preisler, J. Substrate-Assisted Laser Desorption Inductively-Coupled Plasma Mass Spectrometry for Determination of Copper in Myeloid Leukemia Cells. *J. Anal. At. Spectrom.* **2010**, *25* (5), 662–668. https://doi.org/10.1039/b919811c.

(36)   Stiborek, M.; Preisler, J.; Shekargoftar, M.; Kanicky, V.; Kela, J. Cold Plasma: The Way to Improve the Repeatability of Sald ICP-MS Analysis. *Hungarian Journal of Industry and Chemistry* **2018**, *46* (1), 19–22. https://doi.org/10.1515/hjic-2018-0005.

(37)   Benesova, I.; Dlabkova, K.; Zelenak, F.; Vaculovic, T.; Kanicky, V.; Preisler, J. Direct Analysis of Gold Nanoparticles from Dried Droplets Using Substrate-Assisted Laser Desorption Single Particle-ICPMS. *Anal. Chem.* **2016**, *88* (5), 2576–2582. https://doi.org/10.1021/acs.analchem.5b02421.

(38)   Vrbkova, B.; Roblova, V.; Yeung, E. S.; Preisler, J. Determination of Sterols Using Liquid Chromatography with Off-Line Surface-Assisted Laser Desorption/Ionization Mass Spectrometry. *Journal of Chromatography A* **2014**, *1358*, 102–109. https://doi.org/10.1016/j.chroma.2014.06.077.

(39)   De Vijlder, T.; Valkenborg, D.; Lemiere, F.; Romijn, E. P.; Laukens, K.; Cuyckens, F. A Tutorial in Small Molecule Identification via Electrospray Ionization-Mass Spectrometry: The Practical Art of Structural Elucidation. *Mass Spectrometry Reviews* **2018**, *37* (5), 607–629. https://doi.org/10.1002/mas.21551.

(40)   Meija, J. Mathematical Tools in Analytical Mass Spectrometry. *Anal Bioanal Chem* **2006**, *385* (3), 486–499. https://doi.org/10.1007/s00216-006-0298-4.

(41) Zaia, J. Mass Spectrometry of Oligosaccharides. *Mass Spectrometry Reviews* **2004**, *23* (3), 161–227. https://doi.org/10.1002/mas.10073.

(42) Prasad, B.; Garg, A.; Takwani, H.; Singh, S. Metabolite Identification by Liquid Chromatography-Mass Spectrometry. *TrAC Trends in Analytical Chemistry* **2011**, *30* (2), 360–387. https://doi.org/10.1016/j.trac.2010.10.014.

(43) Vogel, V. J. *American Indian Medicine*, Reprint edition.; University of Oklahoma Press, 2013.

(44) Slavik, J.; Slavikova, L. Alkaloide Der Mohngewachse (Papaveraceae) VI. Uber Die Alkaloide Aus Macleaya Microcarpa (MAXIM.) FEDDE. *Collect. Czech. Chem. Commun.* **1955**, *20* (2), 356–362. https://doi.org/10.1135/cccc19550356.

(45) Hammerova, J.; Uldrijan, S.; Taborska, E.; Slaninova, I. Benzo[c]phenanthridine Alkaloids Exhibit Strong Anti-Proliferative Activity in Malignant Melanoma Cells Regardless of Their P53 Status. *J Dermatol Sci* **2011**, *62* (1), 22–35. https://doi.org/10.1016/j.jdermsci.2011.01.006.

(46) Hammerova, J.; Uldrijan, S.; Taborska, E.; Vaculova, A. H.; Slaninova, I. Necroptosis Modulated by Autophagy Is a Predominant Form of Melanoma Cell Death Induced by Sanguilutine. *Biological Chemistry* **2012**, *393* (7), 647–658. https://doi.org/10.1515/hsz-2011-0279.

(47) Hosek, J.; Sebrlova, K.; Kaucka, P.; Pes, O.; Taborska, E. The Capability of Minor Quaternary Benzophenanthridine Alkaloids to Inhibit TNF-alpha Secretion and Cyclooxygenase Activity. *Acta Vet. BRNO* **2017**, *86* (3), 223–230. https://doi.org/10.2754/avb201786030223.

(48) Slaninova, I.; Slunska, Z.; Sinkora, J.; Vlkova, M.; Taborska, E. Screening of Minor Benzo(c.)phenanthridine Alkaloids for Antiproliferative and Apoptotic Activities. *Pharmaceutical Biology* **2007**, *45* (2), 131–139. https://doi.org/10.1080/13880200601113099.

(49) Cui, Z.-M.; Zhou, B.-H.; Fu, C.; Chen, L.; Fu, J.; Cao, F.-J.; Yang, X.-J.; Zhou, L. Simple Analogues of Quaternary Benzo[c]phenanthridine Alkaloids: Discovery of a Novel Antifungal 2-Phenylphthalazin-2-ium Scaffold with Excellent Potency Against Phytopathogenic Fungi. *J. Agric. Food Chem.* **2020**, *68* (52), 15418–15427. https://doi.org/10.1021/acs.jafc.0c06507.

(50) Lasak, P.; Motyka, K.; Krystof, V.; Styskala, J. Synthesis, Bacteriostatic and Anticancer Activity of Novel Phenanthridines Structurally Similar to Benzo[c]phenanthridine Alkaloids. *Molecules* **2018**, *23* (9, 9), 2155. https://doi.org/10.3390/molecules23092155.

(51) Matkar, S. S.; Wrischnik, L. A.; Hellmann-Blumberg, U. Production of Hydrogen Peroxide and Redox Cycling Can Explain How Sanguinarine and Chelerythrine Induce Rapid Apoptosis. *Archives of Biochemistry and Biophysics* **2008**, *477* (1), 43–52. https://doi.org/10.1016/j.abb.2008.05.019.

(52) Kucera, J.; Pes, O.; Janovic, T.; Hofr, C.; Kubinyiova, L.; Toth, J.; Kana, S.; Taborsky, P. Enhancement of Luminescence Signal by Deuterated Water – Practical Implications. *Sensors and Actuators B: Chemical* **2022**, *352*, 131029. https://doi.org/10.1016/j.snb.2021.131029.

(53) Shimomura, O. *Bioluminescence: Chemical Principles and Methods*; World Scientific, 2006.

(54) Pitt, J. J. Principles and Applications of Liquid Chromatography-Mass Spectrometry in Clinical Biochemistry. *The Clinical Biochemist Reviews* **2009**, *30* (1), 19–34.

(55) Ho, C.; Lam, C.; Chan, M.; Cheung, R.; Law, L.; Lit, L.; Ng, K.; Suen, M.; Tai, H. Electrospray Ionisation Mass Spectrometry: Principles and Clinical Applications. *The Clinical Biochemist Reviews* **2003**, *24* (1), 3–12.

(56) Iyer, S. S.; Zhang, Z.-P.; Kellogg, G. E.; Karnes, H. T. Evaluation of Deuterium Isotope Effects in Normal-Phase LC-MS-MS Separations Using a Molecular Modeling Approach. *Journal of Chromatographic Science* **2004**, *42* (7), 383–387. https://doi.org/10.1093/chromsci/42.7.383.

(57) Trufelli, H.; Palma, P.; Famiglini, G.; Cappiello, A. An Overview of Matrix Effects in Liquid Chromatography–mass Spectrometry. *Mass Spectrometry Reviews* **2011**, *30* (3), 491–509. https://doi.org/10.1002/mas.20298.

(58) Zhou, W.; Yang, S.; Wang, P. G. Matrix Effects and Application of Matrix Effect Factor. *Bioanalysis* **2017**, *9* (23), 1839–1844. https://doi.org/10.4155/bio-2017-0214.

(59) Annesley, T. M. Ion Suppression in Mass Spectrometry. *Clinical Chemistry* **2003**, *49* (7), 1041–1044. https://doi.org/10.1373/49.7.1041.

(60) Matuszewski, B. K.; Constanzer, M. L.; Chavez-Eng, C. M. Strategies for the Assessment of Matrix Effect in Quantitative Bioanalytical Methods Based on HPLC-MS/MS. *Analytical Chemistry* **2003**, *75* (13), 3019–3030. https://doi.org/10.1021/ac020361s.

(61) Taylor, P. J. Matrix Effects: The Achilles Heel of Quantitative High-Performance Liquid Chromatography–electrospray–tandem Mass Spectrometry. *Clinical Biochemistry* **2005**, *38* (4), 328–334. https://doi.org/10.1016/j.clinbiochem.2004.11.007.

(62) Harrington, D.; D'Agostino, R. B.; Gatsonis, C.; Hogan, J. W.; Hunter, D. J.; Normand, S.-L. T.; Drazen, J. M.; Ham, M. B. New Guidelines for Statistical Reporting in the Journal. *New England Journal of Medicine* **2019**. https://doi.org/10.1056/NEJMe1906559.

(63) Gelman, A.; Hill, J.; Vehtari, A. *Regression and Other Stories*; Cambridge University Press, 2020.

(64) Lindquist, E. F. *Statistical Analysis in Educational Research*; Houghton Mifflin Co.: Boston; New York, 1940.

(65) Neyman, J.; Pearson, E. S. On the Use and Interpretation of Certain Test Criteria for Purposes of Statistical Inference: Part I. *Biometrika* **1928**, *20A* (1/2), 175–240. https://doi.org/10.2307/2331945.

(66) Fisher, R. A. Inverse Probability and the Use of Likelihood. *Mathematical Proceedings of the Cambridge Philosophical Society* **1932**, *28* (3), 257–261. https://doi.org/10.1017/S0305004100010094.

(67) Tukey, J. W. The Philosophy of Multiple Comparisons. *Statistical Science* **1991**, *6* (1), 100–116. https://doi.org/10.1214/ss/1177011945.

(68) Kruschke, J. K. *Doing Bayesian Data Analysis: A Tutorial with R, JAGS, and Stan*; Academic Press, 2014.

(69)   Greenland, S.; Senn, S. J.; Rothman, K. J.; Carlin, J. B.; Poole, C.; Goodman, S. N.; Altman, D. G. Statistical Tests, P Values, Confidence Intervals, and Power: A Guide to Misinterpretations. *Eur J Epidemiol* **2016**, *31* (4), 337–350. https://doi.org/10.1007/s10654-016-0149-3.

(70)   Sedgwick, P. Understanding P Values. *BMJ* **2014**, *349*, g4550. https://doi.org/10.1136/bmj.g4550.

(71)   Clayton, A. *Bernoulli's Fallacy: Statistical Illogic and the Crisis of Modern Science*; Columbia University Press, 2021.

(72)   Bayes, T.; Price, null. LII. An Essay Towards Solving a Problem in the Doctrine of Chances. By the Late Rev. Mr. Bayes, F. R. S. Communicated by Mr. Price, in a Letter to John Canton, A. M. F. R. S. *Philosophical Transactions of the Royal Society of London* **1763**, *53*, 370–418. https://doi.org/10.1098/rstl.1763.0053.

(73)   Hilbe, J. M.; de Souza, R. S.; Ishida, E. E. O. *Bayesian Models for Astrophysical Data: Using R, JAGS, Python, and Stan*; Cambridge University Press: Cambridge, 2017. https://doi.org/10.1017/CBO9781316459515.

(74)   Laplace, P. S. Memoir on the Probability of the Causes of Events. *Statistical Science* **1986**, *1* (3), 364–378. https://doi.org/10.1214/ss/1177013621.

(75)   McGrayne, S. B. *The Theory That Would Not Die: How Bayes' Rule Cracked the Enigma Code, Hunted down Russian Submarines, & Emerged Triumphant from Two Centuries of Controversy*; Yale University Press, 2012.

(76)   Gill, J.; Witko, C. Bayesian Analytical Methods: A Methodological Prescription for Public Administration. *Journal of Public Administration Research and Theory* **2013**, *23* (2), 457–494. https://doi.org/10.1093/jopart/mus091.

(77)   Kruschke, J. K.; Liddell, T. M. Bayesian Data Analysis for Newcomers. *Psychon Bull Rev* **2018**, *25* (1), 155–177. https://doi.org/10.3758/s13423-017-1272-1.

(78)   McElreath, R. *Statistical Rethinking: A Bayesian Course with Examples in R and Stan*, 2nd ed.; Chapman and Hall/CRC: New York, 2020. https://doi.org/10.1201/9780429029608.

(79)   Ioannidis, J. P. A. Why Most Published Research Findings Are False. *PLOS Medicine* **2005**, *2* (8), e124. https://doi.org/10.1371/journal.pmed.0020124.

(80)   Cirimele, V.; Kintz, P.; Dumestre, V.; Goulle, J. P.; Ludes, B. Identification of Ten Corticosteroids in Human Hair by Liquid Chromatography-Ionspray Mass Spectrometry. *Forensic Science International* **2000**, *107* (1-3), 381–388. https://doi.org/Doi%2010.1016/S0379-0738(99)00180-2.

(81)   Wennig, R. Potential Problems with the Interpretation of Hair Analysis Results. *Forensic Science International* **2000**, *107* (1-3), 5–12. https://doi.org/Doi%2010.1016/S0379-0738(99)00146-2.

(82)   Casals, G.; Hanzu, F. A. Cortisol Measurements in Cushing's Syndrome: Immunoassay or Mass Spectrometry? *Ann Lab Med* **2020**, *40* (4), 285–296. https://doi.org/10.3343/alm.2020.40.4.285.

(83)   Binz, T. M.; Braun, U.; Baumgartner, M. R.; Kraemer, T. Development of an LC-MS/MS Method for the Determination of Endogenous Cortisol in Hair Using C-13(3)-Labeled Cortisol as Surrogate Analyte. *Journal of Chromatography B-Analytical Technologies in the Biomedical and Life Sciences* **2016**, *1033*, 65–72. https://doi.org/10.1016/j.jchromb.2016.07.041.

(84)   Kostolanska, K.; Siprova, H.; Bartecku, E.; Jurica, J.; Rihacek, I.; Taborska, E.; Soucek, M.; Pes, O. Longitudinal Monitoring of Hair Cortisol Using Liquid Chromatography-Mass Spectrometry to Prevent Hypercortisolism in Patients Undergoing Glucocorticoid Replacement Therapy. *Therapeutic Drug Monitoring* **2021**. https://doi.org/10.1097/FTD.0000000000000946.

(85)   Posocco, B.; Buzzo, M.; Giodini, L.; Crotti, S.; D'Aronco, S.; Traldi, P.; Agostini, M.; Marangon, E.; Toffoli, G. Analytical Aspects of Sunitinib and Its Geometric Isomerism Towards Therapeutic Drug Monitoring in Clinical Routine. *J Pharm Biomed Anal* **2018**, *160*, 360–367. https://doi.org/10.1016/j.jpba.2018.08.013.

(86)   Savage, L. J. *The Foundations of Statistical Inference*; Methuen, 1962.